REMOTE SENSING SERIES 73

JÖRG WEYERMANN

Reflectance Anisotropy Effects in Optical Remote Sensing Data

Remote Sensing Laboratories
Department of Geography
University of Zurich, 2016

REMOTE SENSING SERIES 73

JÖRG WEYERMANN

Reflectance Anisotropy Effects in Optical Remote Sensing Data

Remote Sensing Laboratories
Department of Geography
University of Zurich, 2016

Front page: APEX mosaic of flight lines covering the Zurich area and the Irchel campus of the University of Zurich. The location where two flight lines adjoin can easily be identified as vertical line.

Weyermann, Jörg

Reflectance Anisotropy Effects in Optical Remote Sensing Data.

Remote Sensing Series, Vol. 73
Remote Sensing Laboratories, Department of Geography, University of Zurich
Switzerland, 2016

ISBN: 978-3-906894-02-7

This work was approved as a PhD thesis by the Faculty of Science of the University of Zurich in the spring semester 2016. Doctorate committee: Prof. Dr. Michael E. Schaepman (chair), Dr. Stefan Dangel, Dr. Gabriela Schaepman-Strub, Dr. Mathias Kneubühler.

Summary

The quantification of reflectance anisotropy and their correction in optical remote sensing data has a long history, dating back to the 1970s and 1980s when the first spaceborne data were analyzed for the Earth's surface properties. Early papers on such techniques were published on the correction of effects in Landsat or airborne AVIRIS data, when data were to be mosaicked and the visible brightness gradients were visually disturbing the mosaic. Reflectance anisotropy describes the dependence of the reflection of light in a specific wavelength on the illumination and observation direction. The effect is caused by the structure of the observed surface, and is termed commonly the "Bi-directional Reflectance Distribution Function" (BRDF) effect.

Predominantly, the first efforts towards modeling the BRDF seem to have been forced by visual motivation. The long evolution of methods for BRDF modeling and compensation of its effects in remote sensing data, however, emphasizes both the importance of this correction step as well as its complexity, which due to its dependence on surface structural properties increases with the spatial resolution of modern optical instruments. Nowadays, applications for high spatial and spectral resolution optical instruments are the quantification of biochemical contents, assessment of biophysical variables for phenological studies or biodiversity research. The compensation for directional effects which influence the information content of a pixel is a requirement for accurate quantitative data analysis. In the airborne case the starting situation for BRDF modeling is considerably more intricate than for spaceborne instruments with multi-angular capabilities, because only a single observation exists for each point on the surface. An exception is given for optional overlapping of flight lines where eventually two angular observations are present for modeling.

Ignoring the effects of reflectance anisotropy in optical remote sensing data has consequences for the accuracy of parameter retrieval, first and foremost for statistical and empirical/index-based data products and parameters. Depending on the effective flight geometry, deviations of product values of up to 100% can be observed.

The primary goal of this thesis is therefore the quantification of BRDF effects in optical remote sensing data with a special focus on imaging spectrometer data, and the evaluation and further advancement of methods for BRDF modeling and compensation.

This thesis consists of five peer-reviewed scientific publications. Two papers focus on the presentation of methodological advancements, while a chapter comprising three publications explores the application to Earth system science related research. These three publications are presented as excerpts in chapter 4, while the full publications are printed in the appendix (A-C).

The first publication aims at quantifying the effect of reflectance anisotropy at HDRF level and its propagation into products. It adapts an established approach for multi-angular observations to airborne imaging spectroscopy data where only a single observation exists for a single pixel, where the appropriate aggregation of pixels of similar

scattering behavior is the key. Both a suite of standard vegetation indices and inversion products of a coupled leaf-canopy radiative transfer model (Prospect/Sail) are evaluated for sensitivity to reflectance anisotropy effects in the underlying data. With only few exceptions a very high sensitivity with product value deviations up to 60% from the nadir values is measured. The application of the semi-empirical Ross-Li model can effectively reduce these deviations to few percent only. To account for scattering differences caused by surface structure differences, the surface is stratified in discrete classes. Vegetation is separated in two structural types (complex and simple structure), allowing to address the scattering differences of e.g. forests and meadow appropriately. The discrete classification was, however, found to be the major drawback of the method, as it does not account for the typical structural complexity of natural surfaces. The stratification concept is extended in the following publication, accounting for the fact that a single pixel is typically composed of smaller elements with different scattering behavior. A spectral unmixing approach is employed to calculate abundances of individual BRDF effective surface components. The Ross-Li model is inverted on the purest angular observations for each component, and the correction is then applied according to the individual component fractions for each pixel.

Publications three to five apply the aforementioned methods to data of forest, snow, and crop type surface, with an Earth System Science focus. The research objectives are on accurate parameter and surface characteristics retrieval rather than the in-depth evaluation of the BRDF correction method itself. The results of these papers demonstrate the successful application of the method. Publication three is on successful application to norway spruce forest data from the Hymap sensor, for vegetation health status assessment. The anisotropy effects in the data can be removed sufficiently, enabling more accurate data analysis. The fourth publication deals with the calculation of an albedo proxy based on airborne laser scanning data. The non-lambertian reflectance behaviour of fresh snow can be successfully modeled with the Ross-Li method. The goal of the last publication is the simulation of a Sentinel-2 scene from airborne APEX data, requiring reliable correction for anisotropy effects. Remaining anisotropy effects in the mosaic of APEX flight lines can be ascribed the lack of correction for solar zenith, and solar-angle-induced relative azimuth angle changes. The paper further provides the reader with a comparison of directional signatures as calculated with a physical model and the semi-empirical Ross-Li model. Differences are systematic but small. The major criticism in the general methodology of the approach was the fact that a physical model was employed on top of (semi-) empirically transformed data, where the physical information was necessarily destroyed.

Finally, the limitations and future potential of the Ross-Li approach as evaluated in the course of this PhD work are treated in the synthesis and outlook section.

Zusammenfassung

Direktionale Effekte in optischen Fernerkundungsdaten wurden bereits in den 70er und 80er Jahren beobachtet, als die ersten Missionen wie Landsat für Erdbeobachtungszwecke ausgewertet wurden. Diese Effekte erzeugten in den Daten einen sichtbaren Helligkeitsgradienten, der vor allem optisch störte wenn Bilder mosaikiert werden sollten. Die ersten Techniken zur Korrektur zielten auch in erster Linie darauf ab, optisch “schöne” Bildmosaike erzeugen zu können. Schnell begann man aber auch, die physikalischen Mechanismen der Reflektanzanisotropie zu erforschen. Ein solch typisches Reflektanzverhalten natürlicher Oberflächen entsteht durch eine sich innerhalb eines Bildstreifens ändernde Geometrie aus Beleuchtungsquelle, Sensor und dem Objekt am Boden, und zeigt ausgeprägte bodenstrukturelle sowie Wellenlängenabhängigkeit.

Die Tatsache, dass das “BRDF-Problem” immer noch nicht durch Standardverfahren gelöst und auch immer wieder in der Fernerkundungsgemeinschaft thematisiert wird, beweist die Wichtigkeit und gleichzeitig Komplexität der Thematik. Es ist ein Fakt, dass mit räumlich immer höher auflösenden Instrumenten die direktionalen Effekte komplexer werden und immer weniger mit statistischen und empirischen Methoden korrigiert werden können. Für flugzeuggestützte Datenerhebung ergibt sich weiterhin das Problem, dass zur Modellierung der direktionalen Effekte lediglich eine einzige Aufzeichnung pro Auflösungszelle am Boden unter einer fixen Beobachtungs- und Beleuchtungsgeometrie vorhanden ist, was eine Aggregierung der Daten in Klassen repräsentativer BRDF-Eigenschaften notwendig macht.

Werden die Effekte ignoriert ist eine verringerte Genauigkeit und Zuverlässigkeit quantitativer Auswertungen die Folge. Dies gilt vor allem für statistisch-empirische Auswertung, zum Beispiel bei der Berechnung von Vegetationsindizes. Studien haben gezeigt, dass bei ungünstiger Fluggeometrie (relativ zur Sonnenhauptebene) die Abweichung einzelner Produkte in den Randbereichen des Sehfelds orthogonal zur Flugrichtung bis zu 100% des Wertes im Nadir betragen kann.

Das Hauptziel dieser Dissertation ist die Untersuchung von Methoden zur operationellen Korrektur von direktionalen Effekten in optischen Fernerkundungsdaten, ihre Anpassung an die Eigenheiten von flugzeuggetragenen Scannern und eine Einstufung ihrer Eignung für die Anwendung auf unterschiedlichen natürlichen Oberflächen.

Diese Dissertation besteht aus fünf wissenschaftlichen Publikationen (alle peer reviewed). Zwei Publikationen haben ihren Schwerpunkt in der Methodenentwicklung und -verbesserung, drei weitere präsentieren Anwendungen der Methoden. Die drei Anwendungspublikationen sind in diesem Manuskript in einem Kapitel zusammengefasst, im Appendix (A-C) aber voll abgedruckt.

Die erste Publikation quantifiziert die Effekte der Reflektanzanisotropie auf dem Prozessierlevel “HDRF”-Daten und beschreibt die Fehlerpropagation in Produkte. Es werden sowohl Standard-Vegetationsindizes als auch Inversionsprodukte eines physikalischen Modells (Prospect/Sail) evaluiert. Mit wenigen Ausnahmen wird eine sehr hohe

Sensitivität auf die Anisotropien der Reflektanzdaten festgestellt. Die Abweichungen der Werte im Randbereich des Sensorblickfelds liegen in der Grössenordnung von bis zu 60% der Werte im Nadir, dies sowohl für die Indizes als auch die Inversionsprodukte. Die Arbeit stellt weiter eine semi-empirische Methode (Ross-Li) zur Korrektur vor. Mit einer relativ einfachen Vorklassifikation der Daten in zwei Vegetationsstrukturtypen (komplexe und einfach strukturierte Vegetation) kann eine Reduktion der Anisotropieeffekte bis auf wenige Prozent mittlere Abweichung von den Nadirwerten erzielt werden. Die Methode ist somit für eine operationelle Korrektur von Spektroskopie- und anderen optischen Daten flugzeuggetragener Sensoren geeignet, als grosser Schwachpunkt lässt sich aber die Abhängigkeit von einer guten Vorklassifikation festhalten, da diese manuell erstellt werden muss und fehleranfällig ist. Weiter entspricht eine Klassifikation in diskrete Klassen in vielen Fällen nicht den realen strukturellen Verhältnissen am Boden.

Die zweite Publikation erweitert das Konzept der ersten, indem eben diesem Umstand Rechnung getragen wird, dass eine Auflösungszelle am Boden sich in der Regel aus einer Mischung BRDF-effektiver Strukturen zusammensetzt. Ein Entmischungsansatz wird verwendet, um die Anteile an unterschiedlichen Oberflächenkomponenten festzustellen. Das Ross-Li Modell wird auf den Werten der reinsten Pixel für jede Komponente invertiert, und Korrekturfaktoren schliesslich anteilmässig angewendet. Der Korrekturerfolg liegt quantitativ in vergleichbarer Grössenordnung der in der ersten Publikation vorgestellten Methode, mit dieser "kontinuierlichen" Klassifikation können Unterschiede im Streuverhalten aber räumlich feiner aufgelöst behandelt werden.

Im Anwendungsteil (Kapitel 4) werden die Korrekturmethoden in unterschiedlichen Kontexten für Fragestellungen der Erdsystemwissenschaften angewendet. In der ersten Publikation wird eine BRDF-Korrektur auf flugzeuggetragenen optischen Hymap-Daten über Fichtenwald durchgeführt, was eine genauere Analyse des Gesundheitszustands des Bestandes ermöglicht. Die BRDF-Effekte können mit der Ross-Li Methode stark reduziert werden. Die zweite Publikation beschäftigt sich mit der Berechnung eines Albedo-Proxy basierend auf Laserscannerdaten. Das nicht-lambertiane Reflexionsverhalten von frischem Schnee wird hier ebenfalls mit Ross-Li erfolgreich modelliert. In der dritten Publikation schliesslich wird die Methode auf APEX Radianzdaten angewendet und auf landwirtschaftlichen Nutzflächen unterschiedlicher Feldfrüchte evaluiert. Es wird ein räumlicher Ausschnitt einer Sentinel-2 Szene simuliert. Hier wird auch der direkte Vergleich zu direktionalen Signaturen eines gekoppelten physikalischen Modells hergestellt. Es gibt systematische Abweichungen beider Modelle, die aber gering sind. Eine wesentliche Kritik an der Methode ist, dass die Anwendung einer semi-empirischen Vor-Transformation die Sinnhaftigkeit der Anwendung eines physikalischen Modells im Prinzip zunichte macht, da die originalen, physikalisch korrekten Daten zerstört wurden.

Nach der Vorstellung der Forschungsarbeiten in den Kapiteln 2-4 schliesst sich eine Synthese an, welche wesentliche Diskussionspunkte im Kontext behandelt. Im Ausblick werden schliesslich Lösungsansätze für bestehende Unzulänglichkeiten der Methoden vorgestellt.

Structure of the thesis

This thesis consists of five chapters:

Chapter 1 places the work in the scientific context and familiarizes the reader with important concepts and terminology.

Chapter 2 and **Chapter 3** present first-authored peer-reviewed original research articles. The focus in these publications is on method development, basic application to data, and the presentation of representative results.

Chapter 4 presents three co-authored peer-reviewed original research articles. These articles deal with applications of the methods presented in Chapters 2 and 3 to objectives of the Earth System Science. The contribution of the author of this thesis to the publications is hightlighted in the form of excerpts, while introductorial sections familiarize the reader with the research context and objectives of the paper.

Chapter 5 synthesizes research results of all publications and discusses selected aspects in more detail. Conclusions and an outlook provide the reader with possible future research directions.

Contents

1. INTRODUCTION

1.1. Optical Remote Sensing

Optical remote sensing denotes the technology and science of measuring and interpreting the intensity of light reflected from a surface of interest (e.g., the Earth) without physical connection between the sensor and the observed object. In the context of Earth observation, the illumination source is usually decoupled from the observer and not controllable in its radiometric and spectral properties (like the Sun). The whole processing chain from the raw measurement to a unit of information (product) can be separated in two logical parts, both having significant influence on the end product.

While measuring the light intensity is predominantly an engineering task driven in its capabilities by sensor technology and calibration knowledge, interpreting the measurements in a quantitative manner requires knowledge of the underlying physics of the processes, thus is more a scientific part. Retrieval of useful information requires thorough understanding of scattering mechanisms of arbitrary natural surfaces and both quality and quantity of interaction with the medium the light is traveling through before received by the sensor. In addition, the characteristics of the illumination source should be known or at least be modelable with good accuracy. These prerequisites are valid independently from the distance between object and observer, thus must be considered equally in a laboratory experiment (distance $<$ 2m) or in the airborne or spaceborne case (distances between several hundred meters and 400km above surface).

Optical remote sensing has evolved in its applications from imaging (e.g. aerial photography) and topographical mapping to measurement of quantitative surface properties including helping to understand time variant processes like phenology which became possible by repeated measurements. Retrieval algorithms were developed or enhanced, but progress in remote sensing capabilities in recent years was often technology-driven, being the result of increased detector sensitivity (better radiometric efficiency), better spatial resolution, and narrower spectral bandwidth.

While better sensors enable to acquire more accurate and higher resolved data the limitations are increasingly on the science side. Data interpretation by algorithms can become more difficult with higher spatial resolution and requires better process understanding (and models) with respect to scattering of light at the surface of interest.

1.2. Surface reflectance anisotropy

Natural surfaces feature a mainly structure-driven property to scatter light unequally in different directions. The reason for this behavior is in the surface structure at different spatial scales: i) the microstructure of single surface components (like leaves or soil particle aggregations), and ii) in the architectural organization of these surface components (the macrostructure) (Stenberg et al. (2008); Li and Strahler (1992, 1986)).

On microstructure level the surface roughness determines the degree of forward- versus backward scattering of light. Leaf tissue for example can have a more or less pronounced coating, protecting it from too intensive solar irradiation, which effectuates in a mirror-like effect when illuminated. These leaves when looking at them in isolation behave predominantly as forward-scatterers. Leaf thickness and biochemical properties further determine the degree of light absorbtion and transmission, modifying the scattering mechanism on leaf level.

Leaves are usually organised along branches, possibly stacked in arbitrary height and density and angular distribution, depending on the species. On macrostructure level, multiple-scattering effects come into play. Irradiant light passing through a leaf can be reflected by another leaf back to an observer, or just be scattered multiple times from leaf surfaces. Three-dimensional objects containing these leaf collections (e.g., 'Trees', 'Shrubs') grow at variable spatial (horizontal) density, forming clearings, so that with increasing solar zenith angle larger shaded areas on ground/understorey are generated, or shadow is cast on adjacent trees. Shadowing will decrease the intensity of light visible to an observer. Depending on the scale differences between the sensor's ground-instantaneous field-of-view (GIFOV) and the vegetation structure either the reflectance of a pixel is decreased (GIFOV $>>$ structure scale), or fully shaded pixels will be present in the data (structure scale $>>$ GIFOV). The impact of shadowing on remote sensing data usually depends on the observation and solar zenith angle and the relative azimuth difference between the light source and observation vectors.

A typical scanning instrument (like a push-broom sensor) features a system-specific variation in the observation angle (within the FOV, with a typical observation zenith angle for each across-track pixel). Assuming a homogeneous forest canopy with regular tree density and shaded clearings, a sensor will observe different fractions of shadow at the extremes of the FOV. Likewise, for a fixed observer position and homogeneous leaf angle distribution the light scattered into the FOV will depend on the solar angular position relative to the instrument. These mechanisms will generate a pattern of variation in received light over the FOV even for an absolutely homogeneous surface. Reflectance anisotropy becomes only manifest through change in a component of the whole observing system. This can be either a change in observation angle, a change in solar zenith/azimuth angle, or a combination of both. Such a pattern is typically visible as brightness gradient in a flight line, as depicted in the second publication (on page 28 of this thesis).

Also the atmosphere contributes to anisotropy, which is of measureable impact (in the order of up to 10% reflectance). Non-lambertian diffuse irradiation, while not treated in this thesis, must not be disregarded for highly accurate modeling of illumination effects. A small contribution of at-sensor measured radiance comes from photons that are multiply scattered at the geosphere-atmosphere boundary (so several times scattered upward from the surface before reaching the sensor). Another component of scattering often neglected is the one of horizontal radiation transfer within canopies (Widlowski et al. (2006)). These scattering components are small in terms of absolute, measureable radiation, but even smaller in terms of their contribution to reflectance anisotropy.

Reflectance anisotropy is not exclusively an unwanted effect in remote sensing data. Several studies (Schaepman (2007); Liang et al. (2000); Diner et al. (1999); Asner et al. (1998)) on multi-angular data acquisitions have shown that there is potential to use the reflectance variation through an enhanced angular observation space to retrieve surface parameters with higher accuracy, or gain new insights that were not possible with a single view angle, or the comparably limited range offered by wide-FOV airborne instruments.

Surface reflectance anisotropy is the factor contributing most to the overall uncertainty of remote sensing products in the optical solar reflective domain, given a sensor is well-calibrated. Various studies reported its average impact on atmospherically corrected data to be in the order of 2-7% with 15% in worst case (Hu et al. (1999), on satellite data), or up to 20% for airborne IS data (Richter and Schläpfer (2002)).

1.3. Concepts and definitions

Remote sensing in the optical domain typically denotes the quantification of light emitted by the sun and reflected from a surface of interest to the sensor. This sensor is defined to be an imaging spectrometer in the context of this introduction. Exeptions in the optical domain are active remote sensing instruments like airborne laser scanners (ALS) that act as light source themselves; they are supposed to only measure radiation sent out by the scanner with the sun having negligible impact due to the signal intensity. Definitions for ALS systems are treated briefly in the application chapter of this thesis.

1.3.1. Atmospheric processing

The primary purpose of remote sensing activities is to acquire qualitative and quantitative information about either the surface or the atmosphere itself. Spectrometers like the APEX instrument act as "photon counting" instruments, where the number of photons captured per spectral band for each spatial pixel can be regarded as "raw data". According to spectral and radiometric sensor characteristics these raw data need to be converted to physical units (sensor calibrated spectral radiance, measured in [W m^{-1} sr^{-1} nm^{-1}] (spectral calibration, e.g., Hueni et al. (2013)). While retaining all the effects of surface reflectance anisotropy, radiance data still do not exactly represent surface-only properties. Photons that are received by a detector element pointing at an explicit ground location are partly scattered into the sensor's field of view (FOV) from the atmosphere (path radiance) or the neighborhood of the ground location (adjacency radiance). Characterizing the atmosphere (including the quantification of absorbing gases (water vapor, CO2), and aerosol scattering) is necessary to remove spectrally dependent modifications of irradiance, transforming the data to represent true surface optical properties (reflectance data, e.g., Richter and Schläpfer (2002)). All these effects are spatially explicit and variable due to the anisotropy of the atmosphere, but the diffuse component is not explicitly treated in most atmospheric processing schemes.

Reflectance anisotropy becomes manifest in raw as well as in calibrated radiance and reflectance data. Its compensation can be performed on all data processing levels (while being less reasonable on raw data, which contain too many uncertainties originating from sensor effects like vignetting). The literature recommends an iterative approach of first performing anisotropy correction on radiance level, then correcting for the influence of the atmosphere and then performing another iteration of anisotropy correction (Hu et al. (1999)). This scheme is e.g. implemented in the MODIS operational processing chain for various products.

1.3.2. BRDF and associated geometric-optical concepts

Declaring reflectance quantities correctly for a specific application is essential.

Schaepman-Strub et al. (2006) provide an extensive study on the proper use of reflectance definitions and conversion between reflectance quantities, the most relevant of which are introduced in this section of this thesis.

The physical phenomenon 'reflectance anisotropy' is often paraphrased in the literature as 'bi-directional reflectance distribution function' (BRDF) effect. The according compensation step is usually called 'BRDF-correction'. BRDF denotes a quantity measured as ratio from directional illumination and directional reflection (both as 'parallel beam of light' with no angular extent). Airborne and spaceborne optical instruments measure light reflected within a small cone according to the sensor's instantaneous field-of-view (IFOV) where the photons reflected within that cone stem from hemispherical illumination onto the surface. Hemispherical illumination can be separated in a directional and a diffuse component, where directional illumination $>>$ diffuse illumination holds true for the majority of optical data acquisitions. As the cone is very small, and, in addition, atmospheric correction schemes do not explicitly correct at-sensor measured radiance for the angular impact of the diffuse component, a directional reflection is approximated. The data typically used in this thesis can be termed 'hemispherical-directional reflectance factor (HDRF)' data. So in most applications we are trying to model and correct HDRF data for the effects of reflectance anisotropy. However, for convenience, and because this term is established in literature, 'BRDF' will be used in the following as representative for the manifold mechanisms associated with reflectance anisotropy.

ALS data form an exception: they do basically fulfill the specifications of a bi-directional configuration, and contributions from other light sources like the sun (at the corresponding wavelength) can barely be received due to sensor sensitivity characteristics. These scanning systems do, if not completely, highly approximate true BRDF measurements (Li et al. (2014)).

1.3.3. Albedo quantities and concepts

Albedo simply denotes the ratio of reflected radiation to incoming radiation. Without any specifications, albedo refers to an energy-weighted average as integration over all wavelengths in the Earth's reflective domain of the electromagnetic spectrum (broadband albedo). This is just the spectral domain of albedo. With respect to the directionality, 'albedo' refers to a bi-hemispherical configuration (bi-hemispherical reflectance, BHR, or 'blue-sky albedo'), meaning that an angular integration of incoming radiation and outgoing radiation over the viewing hemisphere is required to calculate the albedo value, if not already measured, e.g. by traditional albedometers. It also means that there are contributions of both direct and diffuse illumination. Technically, the integration of the at-surface HDRF over the viewing hemisphere leads to the BHR (= albedo). Separating direct and diffuse contributions to the overall illumination field requires modeling; ground-based sun photometer measurements can be used as local information. The resulting directional-hemispherical reflectance (DHR) quantity (direct illumination only) is also called 'black-sky albedo' whereas the diffuse counterpart (BHR under perfect diffuse illumination conditions) is called 'white-sky albedo'. These are notably conceptual quantities only, which require modeling the BRDF for their calculation (Schaepman-Strub et al. (2006)).

1.4. BRDF models

Three conceptual classes of models are described in literature. Empirical (statistical) models must be distinguished from physical models; approximations to the latter, the so-called semi-empirical approaches, form a third class of models. Major properties of all model types will be discussed in the next sections.

1.4.1. Empirical models

A BRDF model is called purely empirical, when it consists of a mathematical term or a combination of terms that seem to reproduce the shape of BRDF quite well (Wanner et al. (1995b)). Such a model does not have physical basis at all; it is thus not possible to derive any surface properties from inversion. Purely empirical methods were found suitable for various land cover types like vegetation and soil (Walthall et al. (1985); Nilson and Kuusk (1989); Walthall (1997); Kennedy (1997); Kennedy et al. (1997)), or urban surfaces (Schiefer et al. (2006)) but have limitations with respect to extrapolation and normalization for illumination angle effects (as opposed to view angle effects). In their most basic form empirical models are purely statistical and try to fit a polynomial expression to the data. This can be very effective, but bears high risks to distort data due to the large degrees of freedom. Higher weight has then to be put into a-priori knowledge on surface properties, introduced e.g. by providing an appropriate surface classification. Results from empirical modeling are barely transferable to other situations, which can be stated as a second major drawback of this type of model.

1.4.2. Physical models

A second class of approaches is represented by purely physical models. Physical models (e.g., INFORM (Schlerf and Atzberger (2006)), FRT (Kuusk and Nilson (2000)), or the canopy bidirectional reflectance model SAIL (Jacquemoud et al. (2009); Verhoef and Bach (2003)) require an accurate description of the surface in terms of structure and biochemistry to model the interaction of radiation with vegetation and background components for an arbitrary illumination and observation geometry configuration.

Model coupling allows to combine different hierarchical levels of radiative transfer in the bio-geosphere and atmosphere into a comprehensive description of scattering effects (Liang and Strahler (1995)). SAIL is e.g. often coupled with the leaf optical properties model PROSPECT (Jacquemoud et al. (1996)). The Soil-Leaf-Canopy (SLC) model (Verhoef and Bach (2007)) was coupled with the MODTRAN atmospheric transfer code to support simulations of absolute sensor responses at a given angular relative location and observation height (Laurent et al. (2011)).

One of the most comprehensive and versatile models available today is the 3-d radiative transfer model DART (Grau and Gastellu-Etchegorry (2013)), which incorporates an atmosphere module in the latest version, and allows for both voxel-based and discrete scatterer based calculations. An exhaustive comparison of model's performances is given in Widlowski et al. (2013).

Physical models, while the reference for accurate modeling of scattering, are hard to employ when complete flight lines over heterogeneous surface are in focus of the BRDF correction. The reasons can be summarized as follows:

- The input parameter space is usually large and can barely be collected for each pixel in a flight line (20 to 50 parameters per pixel).
- A single model is usually not able to deal with all surface types present in a typical flight line.
- Inversion can be unstable, or leave uncertainties in unknown magnitude when model parameters are unknown.
- Inversion is computationally expensive (while this is less relevant these days).
- It is hard to apply most physical models in an automated and operational way on binary imaging spectroscopy data (thus requiring tedious manual work).

1.4.3. Semi-empirical models

Semi-empirical approaches like the kernel-based class of models combine elements of the aforementioned types. They are usually composed of mathematical simplifications (approximation) to radiative transfer equations with an empirical component acting as 'tie function'. Some of their parameters still may have physical meaning. Thus, they have less degrees of freedom, i.e. less uncertainties than purely empirical approaches. They can be considered as a good compromise between operational applicability (inversion stability) and soundness of their physical basis to reduce effects of reflectance anisotropy. Kernel-based methods have been widely used for spaceborne data product generation (Schaaf et al. (2002); Lucht et al. (2000)). When linear, another tremendous advantage is that they are easy and efficiently to invert with limited computational cost. The kernel-based family of models based on Ross's theory of light scattering in vegetation canopies and the Li-Strahler geometric-optical (physical) model (e.g., Roujean et al. (1992a); Wanner et al. (1995a); Hu et al. (1997); Chopping (1999); Lucht et al. (2000)), on which the focus is in this thesis, belong to this class.

An example for a popular non-linear model is the Rahman-Pinty-Verstraete (RPV) model (Rahman et al. (1993)), which is in use for MISR BRDF/albedo processing and for which a robust inversion scheme was developed (Biliouris et al. (2009); Lavergne et al. (2007)).

1.4.4. Operational considerations

Empirical and semi-empirical methods were proposed for modeling and correction of reflectance anisotropy effects, when the focus is on correcting a full flight line or the majority of its pixels. The major advantages of linear semi-empirical models are

- the limited a-priori knowledge required for inversion,

- the stable invertibility,
- performance through a numerical solution for linear models

From possible models, the Ross-Li model was selected for application due to its high profile and acceptance in the scientific community.

1.5. The Ross-Li model

A linear, semi-empirical, kernel-based three-parameter model as first introduced in section 1.4.3 is used for the majority of work in this thesis. Important properties of the three kernels are described here, while the reader is referred to the literature for explicit kernel formulae. The basic idea of the kernel-based approach is that the general shape of anisotropy can be decomposed in the dominant scattering mechanisms (volume scattering, geometric-optical scattering), individually for each spectral band or wavelength. The shape of these 'sub-models' can be described with non-linear mathematical functions (the so-called kernels). These kernels depend on the illumination and observation geometry only. Kernels can be linearly combined (as weighted sum). An isotropic scattering constant is finally added to 'lift' the gradient to the reflectance level of the respective wavelength. Let R be the reflectance at wavelength λ for a certain illumination and observation geometry, then the weighted linear combination of kernels K with weight f describes the shape of anisotropy, thus R at an arbitrary combination of illumination and observation angle:

$$R{=}f_{iso}(\lambda) + f_{geo}(\lambda) + f_{vol}(\lambda)$$

Basic shapes for volume scattering and geometric-optical scattering must depend on surface structural characteristics like the number of scattering elements within a vegetation canopy, or the spatial distribution (sparsity) of 3-d objects like trees, generating shadow effects. For this reason, different kernels were derived from radiative transfer modeling and geometric optics to allow good model fit to different configurations of surface structure. The kernels relevant for this thesis are described in the next section. The shape of the mentioned four kernels plus the Roujean kernel (Roujean et al. (1992b)) are further compared in Figure 1.1 on the following page. Negative view zenith angles are in the backscatter direction. A clear hotspot is visible in the Li Kernels at 30 degree backscatter position.

1.5.1. Volume scattering kernels

A first volume scattering kernel (**Ross-thick**) was developed by (Roujean et al. (1992a)) as approximation to Ross's theory of light scattering from a horizontally homogeneous plant canopy (Ross (1981)). Bi-directional reflectance is modeled here in single-scattering approximation, meaning that photons are scattered only once, either from leaves or the surface (Wanner et al. (1995b)). Surface reflectance is assumed to be lambertian (no directionality). A further assumption is that leaf reflectance equals transmission (Wanner et al. (1995b)). The 'thick' refers to the fact that the assumptions made in the simplification to radiative transfer theory are only valid for high leaf density, i.e. high values of LAI (>1).

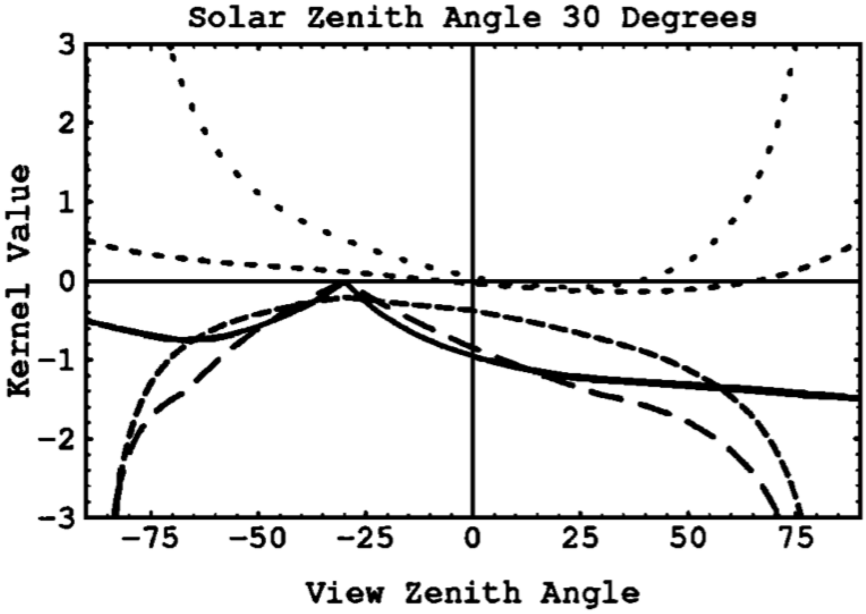

Figure 1.1.: Principle plane kernel values for a solar zenith angle of 30 deg. With increasing dash length: Ross-thin, Ross-thick, Roujean, Li-sparse, Li-dense. From Wanner et al. (1995b).

When the canopy is thin (small values of LAI) photons can travel through the canopy and may be scattered either at the surface or a denser canopy layer beneath the layer of scattering maxima (Wanner et al. (1995c)). The formula of the 'thick' kernel is modified to account for contributions from a second scattering layer, while these contributions are assumed to suffer multiple scattering and thus become lambertian (if the photons are not absorbed in that lower layer completely). The resulting kernel function is then called '**Ross-thin**'.

1.5.2. Geometric-optical scattering kernels

The formulation of geometric-optical scattering kernels is based on the work of Li and Strahler (1986). The so-called 'Li' kernels model the reflectance of a scene based on areal fractions of sunlit crown, sunlit background, shaded crown and shaded background (Li and Strahler (1986)). The discrete 3-d objects casting shadows have the shape of an ellipsoid, with configurable crown height to total height and crown height to crown diameter relationships (Li and Strahler (1992)). The fraction of shadow cast on the ground or on other objects has angular dependence, both in the viewing and illumination domain. As simplification to reality, shadows are assumed to be perfectly black, and canopy reflectance (when illuminated) is assumed to equal the illuminated background reflectance. The fact that there are configurable parameters within the otherwise only illumination- and observation geometry dependent functions let the Li kernels actually be a 'family' of kernels. Apart from that configuration, a kernel was developed for sparse objects (tree stands) with random tree height (**Li-sparse**), another one (**Li-**

dense) accounting for the fact that mutual shadowing cannot be ignored when trees are located in close distance to each other.

1.5.3. Scientific application of the Ross-Li scheme

The Ross-Li scheme gained most of its scientific profile and acceptance through its operational application in the generation of the spaceborne MODIS BRDF/Albedo product (e.g., Schaaf et al. (2000, 2002)). It is by design perfectly suited for global application on multiangular data with a spatial resolution of several hundred meters. While the kernels are per se scale independent, a constraint of normal distribution of scattering elements within a resolution cell poses a lower boundary condition on its application in practice. Circumnavigating this constraint for high spatial resolution data is one of the subjects of this thesis.

1.6. Research outline

1.6.1. Research questions

The major research topic of this thesis can be structured in i) method development oriented analyses (METH) and ii) application oriented analyses (APPL). The topics are presented here with the associated research questions:

1. [METH] What is the impact of reflectance anisotropy on remotely measured single observation HDRF data and empirically and physically based vegetation products?

2. [METH] To which degree can the view-angle effects be reduced with the Ross–Li model?

3. [METH] How is the surface to be stratified to enable application of the Ross-Li model?

4. [METH] How can the Ross-Li model be used with a continuous field surface stratification to avoid spatial artefacts in the corrected solution?

5. [APPL] Is the Ross-Li model capable of modeling anisotropy effects in forest data for enhanced estimation of ecosystem health?

6. [APPL] Can the Ross-Li model be used to reduce reflectance anisotropy effects of snow in airborne laser scanning data?

7. [APPL] Is the Ross-Li model suited to minimize reflectance anisotropy effects on high-resolution radiance data in order to simulate a Sentinel-2 top-of-atmosphere calibrated radiance image? How does it perform compared to a physical model in the anisotropy correction of different crop types?

1.6.2. Order of presentation

These research questions are answered and discussed in the five peer-reviewed publications presented from chapter 2 to chapter 4. The first two publications in the order of presentation are first-authored publications. Research objectives for these publications were defined as follows:

a) **Assessing the impact of reflectance anisotropy on airborne HDRF data and products, and the effectiveness of the Ross-Li method for compensation.**

In the first paper we developed a classification strategy for operational application of the Ross-Li model on airborne spectroscopy data. We evaluated the impact of anisotropy effects for two vegetation structural types and assessed the effect of Ross-Li correction on empirical (index-based) and physically-derived products (PROSPECT/SAIL inversion derived biochemical vegetation parameters).

b) **Developing a novel method for correction of anisotropy effects by combining spectral mixture analysis derived continuous surface stratification with the Ross-Li approach.**

In this publication we performed continuous-field surface stratification into BRDF effective scattering types and trained the Ross-Li model individual for pure observations of each individual type. The Ross-Li model was inverted on this subset of angular observations and correction factors were applied according to a pixel's fractions of each scattering type.

While the research objectives in the method-oriented papers are always in the area of anisotropy correction this is not necessarily the case for the application oriented publications. Here, anisotropy correction is more of a side-aspect providing an unbiased data basis to reach the individual research objectives of the papers. In this thesis the original research questions of the papers are only treated specifically if they are not directly related to reflectance anisotropy.

c) **Applying the method developed in a) to large areas of forest type land surface**

In this publication we applied the Ross-Li approach to forest pixels of Norway spruce trees.

d) **Transferring the approach to ALS measured snow reflectance data and assessing its effectiveness.**

In this publication we transferred the Ross-Li approach to retrieve anisotropies of snow in ALS measured intensity data.

e) **Applying the method developed in a) to APEX radiance data for generation of a simulated Sentinel-2 scene**

In this publication we applied the Ross-Li model to APEX radiance data over the Swiss midlands and compared the angular signatures for different crop types quantitatively with those retrieved by a coupled SLC/MODTRAN-4 physical model.

2. CORRECTION OF REFLECTANCE ANISOTROPY EFFECTS OF VEGETATION ON AIRBORNE SPECTROSCOPY DATA AND DERIVED PRODUCTS

© 2013 IEEE. Reprinted, with permission from Weyermann, J., Damm, A., Kneubühler, M. & Schaepman, M. E. (2013). Correction of reflectance anisotropy effects of vegetation on airborne spectroscopy data and derived products. *IEEE Transactions on Geoscience and Remote Sensing*, Vol. 52, Issue 1, January 2014.

Contribution of first author and co-authors:

Michael Schaepman designed the study.

Jörg Weyermann, Alexander Damm and Mathias Kneubühler and Michael Schaepman developed the methodology.

Jörg Weyermann collected the data.

Jörg Weyermann and Alexander Damm performed the analysis.

Jörg Weyermann, Alexander Damm, Mathias Kneubühler and Michael Schaepman wrote the manuscript.

Correction of Reflectance Anisotropy Effects of Vegetation on Airborne Spectroscopy Data and Derived Products

Jörg Weyermann, Alexander Damm, Mathias Kneubühler, and Michael E. Schaepman, *Senior Member, IEEE*

***Abstract*—Directional effects in airborne imaging spectrometer (IS) data are mainly caused by anisotropic reflectance behavior of surfaces, commonly described by bi-directional reflectance distribution functions (BRDF). The radiometric and spectral accuracy of IS data is known to be highly influenced by such effects, which prevents consistent comparison of products. Several models were developed to approximate surface reflectance anisotropy for multi-angular observations. Few studies were carried out using such models for airborne flight lines where only a single observation is available for each ground location. In the present work, we quantified and corrected reflectance anisotropy on a single airborne HyMap flight line using a Ross–Li model. We stratified the surface in two vegetation structural types (different in vertical structuring) using spectral angle mapping, to generate a structure dependent set of angular observations. We then derived a suite of products [indices (structure insensitive pigment index, normalized difference vegetation index, simple ratio index, and anthocyanin reflectance index) and inversion-based (SAIL/PROSPECT—leaf area index, Cw, Cdm, Cab)] from corrected and uncorrected images. Non-parametric analysis of variance (Kruskal–Wallis test) showed throughout significant improvements in products from corrected images. Data correction resulting in airborne nadir BRDF adjusted reflectance (aNBAR) showed uncertainty reductions from 60 to 100% (p-value $= 0.05$) as compared to uncorrected and nadir observations. Using sparse IS data acquisitions, the use of fully parametrized BRDF models is limited. Our normalization scheme is straightforward and can be applied with illumination and observation geometry being the only a priori information. We recommend aNBAR generation to precede any higher level airborne IS product generation based on reflectance data.**

***Index Terms*—Airborne imaging spectroscopy, bi-directional reflectance distribution functions (BRDF), directional effects, HyMap, pre-processing, PROSPECT/SAIL, reflectance anisotropy, Ross–Li.**

I. INTRODUCTION

IN THE past decades, airborne and spaceborne imaging spectroscopy (IS) has gained importance in the field of Earth system science and ecosystem process modeling, ranging from local to global scales [1]. Assessing the status and monitoring the development of the Earth's vegetated surface are typical strengths of IS, relevant for many ecologic applications. Recent studies on ecotone mapping [2], assessment of biodiversity and canopy biochemistry [3], [4], or determination of plant functional types [5], emphasize the importance of high-quality measurements. Optical measurements are, however, affected by several influencing factors disturbing the measured signal and consequently impacting the parameter retrieval.

TABLE I
DOMAINS OF UNCERTAINTY IN QUANTITATIVE IMAGING SPECTROMETRY AND THEIR IMPACT ON PRODUCT ACCURACY

Domain of uncertainty	Expected uncertainty	Source
Sensor calibration	27%	(Jiang et al. 2008)
Atmospheric correction	2-5%	(Richter and Schlaepfer 2002)
Anisotropy of the atmosphere	< 10%	(Clevers et al. 2001)
Ground reflectance anisotropy	20%	(Richter and Schlaepfer 2002)

Uncertainties in parameter retrieval can originate from the sensor and calibration side, issued for example by an inappropriate sensor model. The uncertainties can equally be introduced in subsequent data processing, when environmental conditions like the atmosphere cannot be modeled with sufficient accuracy. This article quantifies the uncertainty caused by surface reflectance anisotropy, which has considerable negative influence on the accuracy of IS data. Table I summarizes major domains of uncertainty and quantifies individual contributions.

Reflectance anisotropy describes the intrinsic property of natural surfaces to scatter radiation unequally into all directions. The effect is mainly driven by canopy structural and architectural properties [6], [7] and thus is surface specific. While surface reflectance anisotropy can be considered as an intrinsic information source, it causes a wavelength-dependent variation on hemispherical–directional reflectance factor (HDRF) data in the order of up to 20% [8]. Thus, it hinders a consistent estimation of HDRF within a scene and across scenes. Relevant parameters controlling the angular distribution of reflected radiation in vegetation are the leaf area index (LAI) and the leaf angle distribution (LAD). The scattering regime is additionally influenced by the canopy architecture, i.e., tree-shaped parameters, clumping, the gap fraction [9], and leaf level reflectance anisotropy. LAD and LAI significantly influence

---

Manuscript received August 24, 2012; revised January 7, 2013; accepted January 9, 2013. Date of publication March 19, 2013; date of current version November 26, 2013.

The authors are with the Remote Sensing Laboratories (RSL), Department of Geography, University of Zurich, CH-8057 Zurich, Switzerland (e-mail: joerg.weyermann@geo.uzh.ch; alexander.damm@geo.uzh.ch; Mathias.Kneubuehler@geo.uzh.ch; michael.schaepman@geo.uzh.ch).

Digital Object Identifier 10.1109/TGRS.2013.2242898

the multiple scattering occurring in tree crowns [10], while the gap fraction controls the shadow regime of the observed canopy [11]. The angular impact of the gap fraction can be explained with changes in visibility of shadowed and sunlit trees and background in dependence on the view zenith angles, causing changes of the measured radiance at differing viewing directions [12], [13]. The impact of shadow in IS data depends further on the sensor's instantaneous field of view (IFOV). A larger IFOV effectuates a mixture signal of fully illuminated and shaded areas and thus damps the magnitude of reflectance anisotropy [14]. Smaller ground sampling size increases the contribution of geometric-optical scattering to the total anisotropy. Canopy structural and architectural properties can be considered as the main driver of reflectance anisotropy in IS data [6], [7].

Uncertainties in HDRF data can translate into considerable errors in IS products if spectral bands highly affected by reflectance anisotropy are used for retrieval [15], [16]. Other studies found that reflectance anisotropy biases the retrieval of biophysical and biochemical surface properties or causes mis-classifications [17]–[20]. Thus, reliable retrieval of surface parameters from IS data is only possible from data free of directional effects. Correction can be applied either on HDRF level or directly on the subsequently derived products. The latter technique is product specific and not transferable between different products [16]. Correcting at HDRF level minimizes uncertainties caused by reflectance anisotropy for all subsequently derived products and makes this strategy superior.

Empirical and semi-empirical correction methods were proposed in the past. Purely empirical methods [21]–[24] were found suitable for various land cover types but have limitations with respect to extrapolation and normalization for illumination angle effects. Semi-empirical approaches like the kernel-based class of models [25]–[29] have less degrees of freedom than empirical approaches. They can be considered as a good compromise between operational applicability and soundness of their physical basis to reduce effects of reflectance anisotropy. Kernel-based methods are robust and have been widely used for spaceborne data product generation [30]. The MODIS NBAR (nadir bi-directional reflectance distribution functions (BRDF) adjusted reflectance) product, to give an example, is a widely accepted product, used for many global applications [31]–[36]. Stable model inversion requires a number of angular observations for each target, i.e., accurately co-registered pixels of scenes taken from different view and/or under different illumination angles.

Few studies only demonstrated the concept of using such a method for anisotropy correction of airborne imagery [37]. In addition, the impact of reflectance anisotropy on higher level products from airborne IS data, as well as the influence of a kernel-based transformation on these products, has rarely been investigated. For our study, we chose a set of semi-empirical Li and Ross kernels [27], [28].

The goal of the present study is to systematically evaluate the impact of reflectance anisotropy on remotely measured single observation HDRF data and empirically and physically based vegetation products (e.g., vegetation indices (VIs) or PROSPECT/SAIL inversion results). Further, the correction of view-angle effects using the Ross–Li model will be assessed. Results are considered as one important component of the uncertainty budget related to evaluate the reliability and accuracy of airborne IS-data and state-of-the-art thematic products. Specific objectives of this study are: 1) to adapt an established semi-empirical correction approach to correct airborne based IS data; 2) to evaluate uncertainties in measured HDRF data in response to reflectance anisotropy; 3) to evaluate the impact of reflectance anisotropy on product level by investigating different vegetation products derived from either empirical or physical approaches.

The findings of this work are intended as a step toward standardization of IS data pre-processing with the aim to make view-angle correction a standard step before any higher level products are generated.

TABLE II
ILLUMINATION GEOMETRY FOR THE FLIGHT LINES

Flight line	Solar Azimuth [deg]	Solar Zenith [deg]	Heading [deg]
Hy-NS	124.3	39.4	179.23
Hy-WE	130.3	36.9	89.64

II. MATERIAL

The data used in this study were acquired over the "Vordemwald" test site located in the Swiss Midlands, Switzerland ($7°52'16.88''$E/$47°16'20.41''$N). The test site features a rural landscape with roughly 55% homogeneously dense mixture forest [38] and 45% agricultural fields with various crops in different phenological stages.

IS data were acquired with the HyMap imaging spectrometer (IS) [39]. HyMap is a whiskbroom IS, recording 512 pixels per scan line with a FOV of 61.4°. The solar reflective wavelength region between 450 and 2500 nm is recorded in 126 contiguous spectral bands. Two airborne HyMap flight lines were acquired on the 29 July 2004. One flight line is aligned in north-south direction (heading = 180°, "Hy-NS"); the second data set was recorded normal to the first one in west-east direction (heading = 90°, "Hy-WE"). The overlapping area is dominated by a patchwork of agricultural fields with a broad range of vegetation abundances. The data were recorded from a flight altitude of 2500 m above ground, which results in a raw data ground sampling distance of 7.2 m in along-track and 6.0 m in across-track direction. Table II indicates the solar angles for the flight lines.

Atmospheric correction using the ATCOR-4 software [8] was carried out with a rural standard atmosphere and a terrain model of equal ground pixel size. Effects of view angle-dependent path radiance as well as the adjacency effect are estimated and removed assuming lambertian surface reflectance. The output of atmospheric correction can be described as "Top-Of-Canopy HDRF" [40]. For better readability, the terminology "HDRF" is used in the following chapters. Reflectance anisotropy induced by the target is not accounted for during atmospheric correction.

Reflectance anisotropy has strongest influence when the sensor is scanning in the solar principle plane (SPP, relative azimuth of 0 deg) and least influenced when scanning perpendicular to the SPP [41]. The maximum influence is thus not reached in the data used for this study. No validation field measurements were available from representative locations.

III. METHODS

A. Ross–Li BRDF Model

The semi-empirical, kernel-based Ross–Li BRDF model [27], [28] was used to quantify the reflectance anisotropy and assess its correction. Illumination/observation geometry and crown-shaped parameters are the only input required in inversion [25], [28]. The Ross–Li model decomposes measured HDRF into radiation components originating from three scattering types. Isotropic scattering (ISO) is the radiation fraction, which has no angular dependence. Volumetric scattering (VOL) can be described as radiation fraction with an angular dependence as function of small inter-leaf gaps within a horizontally homogeneous vegetation canopy [42]. Geometric scattering (GEO) generates an angular dependence as function of large gaps within a canopy or sparse stand structure [7]. K_{VOL} and K_{GEO} are a nonlinear function (so-called "kernel" K) of the observation and illumination geometry, while the kernels are linearly combined, using a waveband specific weighting parameter f. Considering these components, the reflectance R can be then described as

$$R = f_{ISO}(\mathbf{\Lambda}) + f_{VOL}(\mathbf{\Lambda})K_{VOL} + f_{GEO}(\mathbf{\Lambda})K_{GEO}. \quad (1)$$

The Ross–Li model incorporates a set of kernels [27], [43], which were found to be more reliable and accurate in reproducing BRDF's than other kernel-based models [44]. Individual kernels were developed for different vegetation structural properties. Two kernels can be selected in the present model to describe volume scattering and two to model the geometric optical scattering regime.

The Ross Thick (R_tk) volume scattering kernel is specifically adapted to high LAI values (> 1), whereas Ross Thin (R_tn) is designed for less dense vegetation with LAI values smaller than 1 [45]. Ross kernels rely on the single scattering approximation [27]. Li kernels model the surface geometric-optical scattering regime in terms of sunlit and shadowed crowns and background [6]. Two different kernels were implemented for sparse (Li_s) and dense (Li_d) vegetation canopies. The Li kernel canopy shape parameters were fixed according to the MODIS BRDF/Albedo product as $b/r = 1(2.5)$ and $h/b = 2(2)$ for the sparse (dense) kernel. The weighting of scattering components was determined empirically, based on a stratification of the data, as multi-angular information is not available in airborne data.

The application of the Li–Ross model is shown in Fig. 1.

We first generated a set of angular observations by stratifying the surface in two vegetation structural types. For each type, all permutations of kernels (R_tk-Li_s, R_tn-Li_s, R_tk-Li_d, R_tn-Li_d) were then tested toward their capability to reproduce the measured HDRF angular shape. The kernel combination with a minimum Root Mean Squared Error between modeled and measured HDRF for all spectral bands was finally selected for the structural type under consideration.

We performed matrix inversion using UL decomposition to obtain the kernel weights for isotropic, volumetric, and geometric scattering. We then applied the model in forward mode to calculate reflectances for each view angle. According to [37], correction factors were calculated as gain, keeping for each pixel, band, and structural class a constant factor between the modeled HDRF for the current geometry to the modeled HDRF in the normalization geometry (i.e., nadir). The resulting data, corrected with the obtained correction factors, were termed as "airborne nadir BRDF adjusted reflectance" (aNBAR) data. Similar correction factors have been applied by [46] for the retrieval of intrinsic albedo from nadir-looking sensors (e.g., ETM+).

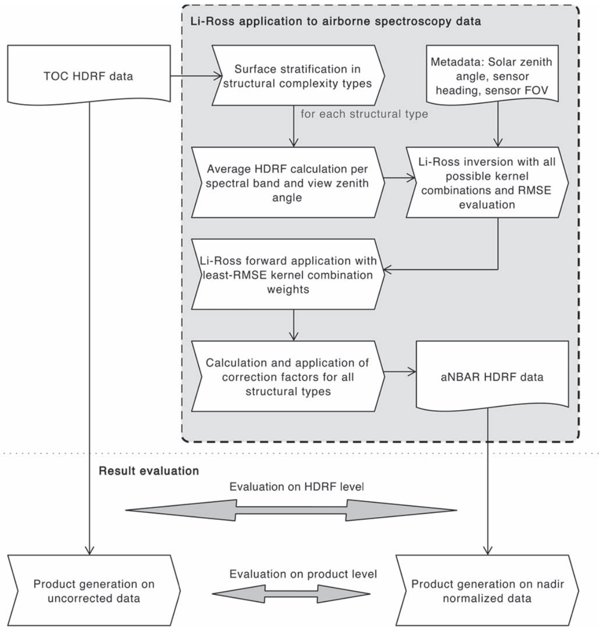

Fig. 1. Schematic overview of the Li–Ross BRDF correction and product evaluation.

TABLE III
VEGETATION STRUCTURAL CANOPY TYPES IN HY-NS AND THEIR SCATTERING PROPERTIES [ADOPTED FOLLOWING (KIMES 1983)]

Structural class	Percentage of pixels	Volume scattering	Forward/Backward scattering	Shadowing behavior
Simple scattering type	20.99	low	Forward ≈ Backward (i.e. bowl shape)	Subpixel level
Complex scattering type	55.79	high	Backward >> Forward (i.e. bell shape)	Subpixel to pixel level

B. Surface Stratification

We applied the standard Spectral Angle Mapper (SAM) classification algorithm [47] to spectrally distinguish two different vegetation structural types, soil, and water as the main surface structural types. The two vegetation types (the "simple scattering type" and the "complex scattering type") represent two species compositions that significantly differ in their horizontal and vertical structures, assuming a specific "scattering regime" for each type. Comparing with the global biome definition of the MODIS LAI/fPAR algorithm [48], the "simple scattering type" encompasses grasses, cereals, broad-leaved crops, and shrubs, the "complex scattering type" consists of broadleaved and coniferous tree species with a varying composition of both species (mixed forest). Table III summarizes basic properties of the vegetation structural types in the Hy-NS scene and their basic scattering properties.

SAM reference spectra were obtained from Hy-NS itself, by averaging homogeneous regions around or close to the nadir line. Radiometric thresholds were additionally used to discriminate the two structural types. The empirical thresholds were applied in a post-classification step, based on the view-angle specific averaged HDRF values at 500 nm. Ross–Li correction was independently applied to each structural type.

C. Product Generation

This study focuses on evaluating the impact of surface anisotropy and correction on IS level 3 products. These products comprise two- and multiband VIs and biochemical products retrieved through the inversion of the coupled radiative transfer models PROSPECT and SAIL [49], [50].

VIs: Four standard VIs were calculated from uncorrected HDRF data and the aNBAR product of flight line Hy-NS. The standard broadband *simple ratio index* (SRI) [51] relates the NIR to the RED HDRF $(R_{\mathrm{NIR}}/R_{\mathrm{RED}})$ and was selected because of its significant dependency on angular anisotropy, which was found particularly for coniferous forests and meadows [16]. The normalized difference vegetation index (NDVI) $(R_{\mathrm{NIR}} - R_{\mathrm{RED}}/R_{\mathrm{NIR}} + R_{\mathrm{RED}})$[51], [52] is still frequently applied as proxy for biomass and productivity estimation. The structure insensitive pigment index (SIPI) [53] was developed as proxy for light use efficiency. SIPI was particularly designed to provide structure independent measurements of the relation between carotenoids (alpha-carotene and beta-carotene) and chlorophyll content. SIPI is calculated as $(R_{800} - R_{445})/(R_{800} - R_{680})$. Last, the anthocyanin reflectance index (ARI1) [54] was investigated as it showed very distinct angular dependence. ARI1 is a narrow-band leaf pigment VI and relates the green to the red edge reflectance $((R_{550})^{-1} - (R_{700})^{-1})$.

PROSPECT/SAIL Inversion Products: Three biochemical and one structural product were inferred from the uncorrected HDRF data and the aNBAR product of Hy-NS and Hy-WE, applying the coupled radiative transfer models PROSPECT and SAIL (PROSAIL). PROSPECT allows simulating hemispherical leaf reflectance and transmittance as function of the leaf chlorophyll- (CAB), water- (CW) and dry matter content (CDM), and the leaf structural parameter (N) [55]. Leaf optical properties simulated with PROSPECT are incorporated in the canopy reflectance model SAIL to calculate canopy reflectance. Simulation of canopy optical properties requires additional parameters, i.e., the LAI, LAD, background reflectance, sun-observation geometry, and basic information on atmospheric properties [50]. CAB, CW, CDM, and LAI were estimated in this study through PROSAIL inversion.

Parameters were estimated applying PROSAIL in quasi-inverse mode using a look-up table (LUT) approach [56]. For simulating the LUT entries, the four parameters of interest were kept free within the following parameter ranges (i.e., CAB: 10.0–70.0 $\mu\mathrm{g\,cm}^{-2}$; CW: 0.001–0.03 $\mathrm{g\,cm}^{-2}$; CDM: 0.001–0.01 $\mathrm{g\,cm}^{-2}$; LAI: 0.1–8 $\mathrm{m}^2\mathrm{m}^{-2}$) based on [57]. All other parameters were kept constant (i.e., N: 1.8; LAD: planophile). The applied value ranges and constant values were defined considering published results and personal experience gathered during field campaigns. For inversion, we did not use the probability distribution function to generate the LUTs as constraining the parameter space too rigorously would introduce additional uncertainties. While creating the LUT, a constant view angle was considered and set to nadir view (i.e., viewing zenith of 0°). This strategy allows identifying the impact of surface anisotropy on the product retrieval and the improvements related to the proposed anisotropy correction, without any superimposing effects caused by assumptions implemented in PROSAIL to account for BRDF effects. Background reflectances were extracted from the image by calculating an average reflectance signature of existing bare soil surfaces.

The model combination of PROSPECT/SAIL was developed to simulate optical properties of broad-leaved canopies [55]. To avoid violating model assumptions, the modeling approach was only applied on pixels covering the simple scattering type vegetation, which are homogeneous structured canopies like crops or grass.

For direct comparison of angular responses, we first calculated the median in along-track direction and then normalized all products to a nadir value of 1. Offsets at nadir between corrected and uncorrected version were equally translated in normalized values, with the aNBAR-derived version as [16] demonstrated a product specific distinct curvature over the FOV. A second-order polynomial fit was therefore applied to the across-track product gradients, to allow comparison of the gradient's shape to the results of this work.

A subset of the data covering the overlapping area of the Hy-NS and Hy-WE data set was incorporated for cross-comparison and relative validation purposes. The across-track gradient of each Hy-NS product was compared to the along-track gradient of the according Hy-WE product. This gradient is used as reference, as the view angle remains constant in along-track direction and solar angle changes are assumed negligible.

D. Statistical Evaluation of Uncertainty Budgets

We tested the statistical significance of the angular dependence and the impact of correction for each product, employing a non-parametric analysis of variance (Kruskal–Wallis test [58]). The Kruskal–Wallis test evaluates the null hypothesis that two samples come from populations sharing the same median against the alternative hypothesis that the medians are not the same. A Kruskal–Wallis p-value close to 1 indicates that there is not enough evidence to reject the null hypothesis while $p < 0.005$ indicates significant differences between samples.

Two independent test runs were performed. The first compares all off-nadir angular positions to the nadir (both for uncorrected and corrected data). The second test compares populations of uncorrected data to corrected data drawn from equal off-nadir position. To achieve equal test sample sizes, pixels of each test sample were randomly excluded. While still numerically accurate, the results of the statistical tests should be assessed on a comparative, relative basis rather than valued absolutely.

IV. RESULTS

A. Quantification of Reflectance Anisotropy on HDRF Data

This section describes the wavelength-dependent sensitivity of HDRF data to reflectance anisotropy. HDRF across-track

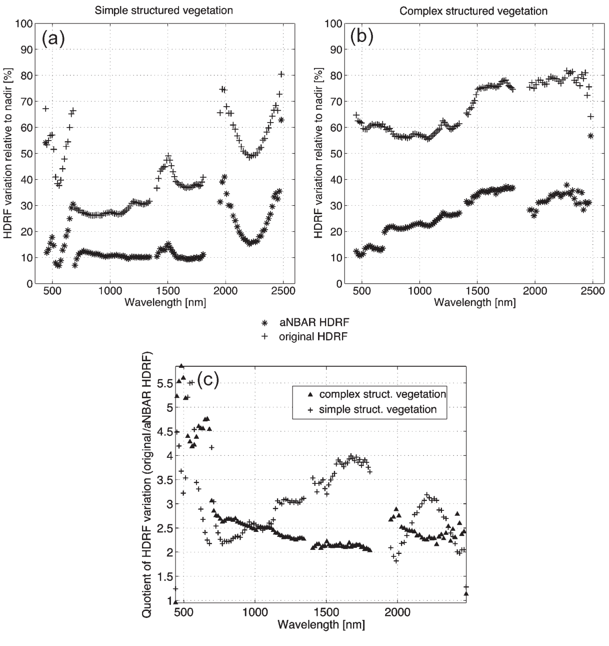

Fig. 2. Variability of HDRF relative to nadir (a), (b) and nonlinearity of the effect of Ross–Li transformation on HDRF variability (c).

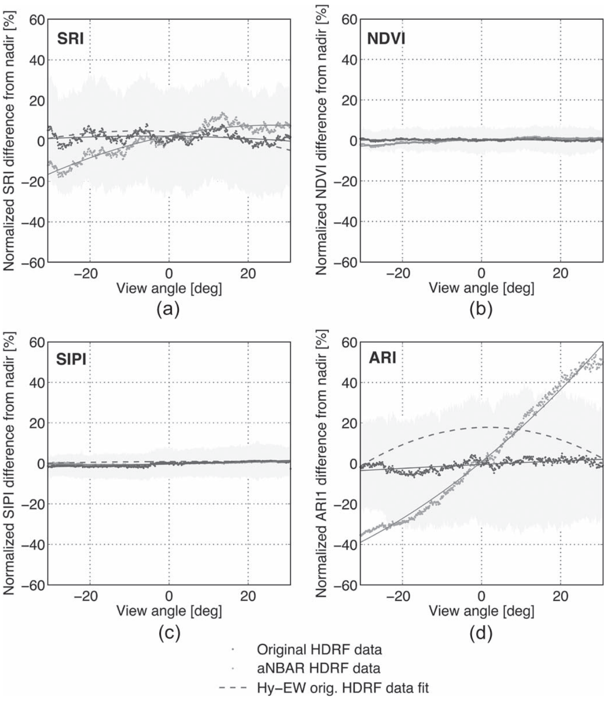

Fig. 3. Across-track gradient of investigated spectral indices before and after correction, compared to the original gradient in Hy-WE. Negative view angles refer to the backscatter direction; positive view angles to the forward-scatter direction.

variation is plotted as the maximum deviation from nadir HDRF for each spectral band (Fig. 2). In the following, the term "HDRF variation" refers to variation measured in across-track direction. Throughout this paper, a negative view-angle indicator ("−" sign) is used for the backscatter direction.

Both scattering types show similar angular behavior in the uncorrected data. HDRF variability is moderate in the VIS, decreases in the NIR and reaches its maximum in the SWIR.

For the simple scattering type, the HDRF variation before correction ranges from 37% in the VIS to 80% in the SWIR around 2500 nm [Fig. 2(a)], with an average of about 50%. After the Ross–Li correction, the general shape of HDRF variation is unaltered but its magnitude drops to an average of 18%. HDRF variation in the aNBAR product ranges from 5% in the VIS to 40% in the SWIR around 2000 nm.

HDRF variation is higher for the complex structured type. Before correction, it ranges from 56% in the VIS–NIR to 80% in the SWIR between 2000 and 2500 nm [Fig. 2(b)], with an average of about 65%. This variation drops significantly to an average of 30% in the aNBAR product, ranging from 10% in the VIS to 40% in the SWIR.

The Ross–Li correction reduces the across-track HDRF variation for both scattering types remarkably [Fig. 2(a) and (b), asterisk symbols]. Still, HDRF varies notably after correction. Remaining variation results from the large radiometric variability within a structural type and the results presented in the figure express the combined effect of two factors: 1) changes in view angles, and 2) structural and biochemical differences of species subsumed in one structural type.

The effect of the Ross–Li transformation differs between the two canopy types, particularly in the VIS. The simple structured HDRF variation drops almost linearly, conserving the features of the variability shape [Fig. 2(a)], while the variability for the complex type is reduced relatively stronger such that variability increases with the wavelength up to 1800 nm [Fig. 2(b)]. Following on a discontinuity, a second variability peak is in the SWIR around 2250 nm.

The difference between corrected and uncorrected data is not linear for both scattering types [Fig. 2(c)]. This indicates that some components of scattering can be treated better than others through the Ross–Li transformation.

B. *Impact of Reflectance Anisotropy on Products*

Standard VIs: All VIs differ considerably in the magnitude of angular dependence while the shape of the gradient is comparable [Fig. 3(a)–(d), results shown are only for the complex structured scattering type]. With exception of the ARI1, the anisotropy can be described by a tilted bell-shaped curve with the maximum shifted toward the forward-scattering direction. The ARI1 anisotropy gradient is rather flat and slightly bowl shaped. SRI and NDVI anisotropy is larger for the simple scattering type, while SIPI and ARI1 angular dependence is considerably larger for the complex scattering type.

The across-track variation of SRI for the complex scattering type derived from uncorrected HDRF values [Fig. 3(a), gray symbols] ranges from 8% in the forward- to −17% in the backscatter direction. NDVI is far less sensitive to reflectance anisotropy [1% to −3%, Fig. 3(b)], while SIPI shows nearly no angular dependence [Fig. 3(c)], uncertainties in the order of +/−1%). ARI1 is highly sensitive to reflectance anisotropy [Fig. 3(d)]. For the complex scattering type, deviations range from 59% in forward scatter to—39% in backward scatter direction. For the simple scattering type, deviations are considerably lower (20% to -33%).

Applying the Ross–Li correction considerably reduces the product across-track variation. Remaining uncertainties are in the order of a few percent (SIPI: 0%, NDVI: 2%) up to 12% (SRI) for the simple scattering type. Differences can be observed between the scattering types. For most aNBAR-derived products, the across-track variation is in good agreement with the gradient retrieved from Hy-WE. The Ross–Li correction slightly increases initial SIPI deviation to -2% in the backscatter direction for the complex scattering type. For the simple scattering type, any angular trends are eliminated after the Ross–Li correction.

The corrected ARI1 gradients are perfectly balanced with respect to nadir values for both structural types. However, comparing the Hy-NS with the Hy-WE flight line reveals considerable differences between the structural types. While the Hy-WE ARI1 gradient for the complex structured type is bell shaped, it is rather bowl shaped for the simple structured type. Thus, corrected Hy-NS gradients seem to be under-/overestimated when compared to that relative reference.

The Kruskal–Wallis test confirms the visual observations [Fig. 4(a)–(d)]. With exception of SIPI [Fig. 4(c)], across-track p changes of the uncorrected products are remarkable with lowest p-values in the extreme backscatter direction (beyond—20° view angle, off-nadir minima of 10^{-50} to 10^{-200}). In the forward-scattering direction, p-values start dropping to values of around 10^{-40} for view angles $> 10°$. The impact of reflectance anisotropy is significantly reduced in aNBAR-derived products and p-values are close to 1 even at extreme off-nadir view angles. Comparing p-values of corrected and uncorrected data [Fig. 4(e)–(g)] reveals a distinct asymmetry. Kruskal–Wallis p is lower in the backscatter direction and decreases continuously with increasing off-nadir view angles. In the forward-scatter direction, p reaches a local minimum around 20° off-nadir view angle and increases slightly to larger view angles.

The SIPI p gradients both from uncorrected and aNBAR data [Fig. 4(c)] do not reveal angles with low p-values. However, off-nadir angles can be identified where p-values are lower after correction than before. A slight p asymmetry is visible when comparing equal off-nadir positions of the corrected and uncorrected SIPI product [Fig. 4(g)], but less accentuated than for SRI or NDVI. Also, for the highly sensitive ARI1 index, p-values increased from around 10^{-200} at extreme off-nadir angles to values close to 1 after correction.

CAB, CW, CDM: The biochemical parameters are more sensitive to reflectance anisotropy than any other product evaluated in this work (Fig. 5). In uncorrected products, the across-track variation is important with highest deviations from nadir in forward-scatter direction. Across-track changes range from 58% (CW) up to 155% (CDM) [Fig. 5(a)–(c), Table IV]. CDM varies considerably within small changes in view angle, even close to nadir. Considering the results of the statistical test [Fig. 6(f) and (g)], CW features the highest uncertainty caused by angular effects and CDM the lowest. Across-track changes of CAB and CW retrieved from uncorrected data are comparable, while across-track changes of CDM are considerably higher in the extreme backscatter direction [Fig. 5(a)–(c)].

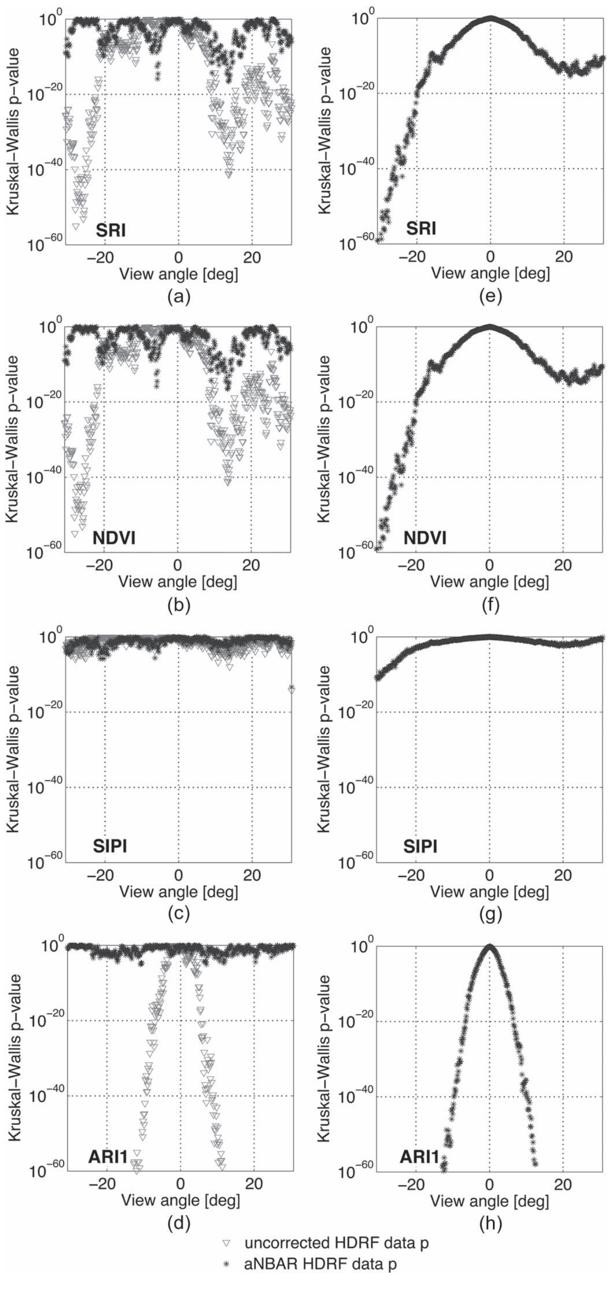

Fig. 4. Results of the Kruskal–Wallis non-parametric analysis of variance for the vegetation indices. X-axis depicts the FOV, y-axis p-values. Plots A–D: Off-nadir samples are compared to nadir samples for products from aNBAR and original HDRF data. Plots E–H: product values of equal off-nadir view angle from aNBAR and original HDRF data were tested against each other. The p-value indicates the probability for the tested samples to belong to the same population or populations with the same median.

Applying the Ross–Li correction significantly reduces the angular trends. A discrepancy in the order of 5% (CW) up to 40% (CDM) compared to Hy-NS remains after correction [Fig. 5(a)–(c)]. CDM is extremely variable and has very high standard deviation over the FOV. In addition, only a limited number of pixels of the simple structured type could be used for the cross-comparison. According to the Kruskal–Wallis

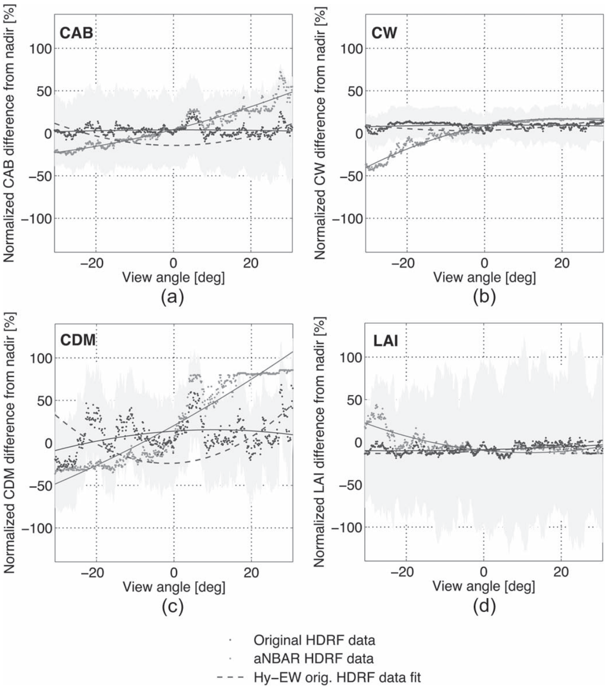

Fig. 5. Across-track gradient of the PROSPECT/SAIL inversion products before and after correction, compared to the original gradient in Hy-WE. Negative view angles refer to the backscatter direction; positive view angles to the forward-scatter direction.

test, across-track p profiles of all biochemical products retrieved from aNBAR data feature considerably higher p-values [Fig. 6(a)–(c)]. This finding indicates an important reduction in uncertainty on Ross–Li corrected data [Fig. 6(e)–(g)].

LAI: Directional effects cause LAI overestimation up to 22% in backscatter direction [Fig. 5(d)]. This is in contrast with the results for the biochemical vegetation products. The impact of reflectance anisotropy can be considerably reduced (up to 80%) when deriving LAI from Ross–Li corrected data.

The Kruskal–Wallis test, however, shows minor differences between LAI retrieved from uncorrected and aNBAR data [Fig. 6(d)]. Comparing equal view angles [Fig. 6(h)], the variation in p-value is rather small for LAI. It is particularly small in forward-scatter direction (p between 1 and 10^{-2}). The biochemical products are characterized by p-values smaller than 10^{-15} at comparable off-nadir angles.

V. DISCUSSION

A. Anisotropy Effects on HDRF Data

The impact of reflectance anisotropy on airborne IS HDRF data is as expected and often documented considerable. Geometric-optical scattering effects cause a large fraction of anisotropy in discontinuous vegetation canopies of any vertical structure complexity, but will more severely affect canopies with pronounced 3-D structure, where the height of vegetation is larger than its horizontal extent within a pixel and shaded canopy gaps can sum up to a considerable fraction of an observed surface area. This manifests itself in the continuously high HDRF across-track variation in complex structured vegetation [Fig. 2(b)].

Geometric-optical effects have less influence in the NIR due to increased multiple scattering [59]. This effect typically balances across-track variation of HDRF signals of homogeneously structured vegetation canopies [59], [60]. Our analysis fully supports these findings. HDRF angular sensitivity is larger for the VIS than for the NIR spectral region before Ross–Li transformation. The very high variability in angular sensitivity, predominantly for the simple structured vegetation [Fig. 2(a), cross symbols], can most likely be ascribed to species heterogeneity, as individual patches of this canopy type are comparably homogeneous at pixel level of the observation scale [14], [61].

The comparably strong reduction of HDRF variability through Ross–Li application in the VIS of the complex structured type [Fig. 2(b), comparing both curves] is associated with the effect of volume scattering, which has less influence in the simple structured vegetation canopy but is very intense in complex structured tree canopies.

The location of discontinuities indicates that either Ross–Li cannot successfully reproduce the rapid increase of volume scattering in these spectral regions, or that the within-class HDRF variability is significantly higher in these spectral regions. In addition, discontinuities could be an effect of an inappropriate observation scale. However, the high absolute number of observations should provide statistically sufficient samples even with the small ground-projected IFOV (GIFOV) of the Hymap instrument.

More than 60% of HDRF variation can be eliminated through correction for both canopy types (on average over all bands). Remaining across-track HDRF variations can be ascribed to the within-class HDRF variability. This fraction of the variation is not related to reflectance anisotropy, but arising from the surface stratification scheme. Stratification into more structural scattering types is, however, assumed to introduce additional uncertainties, while barely enhancing the correction result.

B. Anisotropy Effects on Products

The least angular dependence was found for SIPI. SIPI calculation involves wavelengths in the shorter NIR (800 nm, strong multiple scattering of photons) and the VIS (445 nm, 680 nm, weak multiple scattering). The formed ratio allows minimizing the sensitivity of the SIPI to structural effects as both the numerator and denominator are similarly influenced by canopy biophysical parameters like LAI. SIPI is equally sensitive to reflectance anisotropy for the complex and the simple structured type, which is in line with the results of [16], at least for the angular range where both studies can be compared.

While NDVI uses the same spectral bands in the NIR and RED as the SRI, its angular sensitivity is only about 30% of the SRI sensitivity. The ratio (NIR-RED/NIR+RED) is much more driven by the constant (higher) NIR reflectance than the anisotropic RED reflectance, making this index considerably more robust than the SRI.

The direct ratio forming of the SRI formula, in contrast, amplifies the structural dependence of this index. The observed strong SRI angular sensitivity is consistent with the findings made in [16]. In their work, however, minimal SRI values were

TABLE IV

SUMMARY OF PRODUCT UNCERTAINTIES (BASED ON MIN/MAX OF THE PRODUCT FIT VALUES)

	Simple scattering type							Complex scattering type						
	Backscatter		Forward scatter		Overall			Backscatter		Forward scatter		Overall		
Product	orig. HDRF uncertainty	aNBAR uncertainty	orig. HDRF uncertainty	aNBAR uncertainty	orig. HDRF uncertainty	aNBAR uncertainty	Uncertainty reduction [%]	orig. HDRF uncertainty	aNBAR uncertainty	orig. HDRF uncertainty	aNBAR uncertainty	orig. HDRF uncertainty	aNBAR uncertainty	Uncertainty reduction [%]
SRI	-39	-19	-6	-7	33	12	63.6	-17	0	8	2	25	2	92.0
NDVI	-9	-4	-1	-1	8	3	62.5	-3	0	1	0	4	0	100
SIPI	1	1	3	1	2	0	100	-1	-2	1	1	2	3	-50
ARI1	-33	-7	20	-3	53	4	92.5	-39	-4	59	2	98	6	99.4
CAB	-23	-2	49	4	72	6	91.7	n/a	n/a	n/a	n/a	n/a	n/a	n/a
CW	-41	8	17	10	58	2	96.6	n/a	n/a	n/a	n/a	n/a	n/a	n/a
CDM	-48	-9	107	15	155	24	84.5	n/a	n/a	n/a	n/a	n/a	n/a	n/a
LAI	22	-3	-12	-10	34	7	79.4	n/a	n/a	n/a	n/a	n/a	n/a	n/a

found close to the nadir. This contradicts the findings of this study for the complex structured type, where highest SRI values were found close to the nadir. A possible explanation is the species composition of the forest. Their study was carried out on homogeneous, evergreen coniferous forest dominated by *Pinus arborea* and *Pinus cembra*. The angular behavior of a mixed species forest is expected to be different as a deciduous tree canopy differs from a coniferous canopy in the contribution of individual scattering components [62]. For the simple structured type, results of the present study match the results of [16].

ARI1 is characterized by a very high sensitivity to angular effects. This finding is consistent with the results of [16]. The ARI1 index is designed for leaf level applications and exploits the NIR (700 nm) and GREEN (550 nm) spectral region. The pronounced angular sensitivity in complex structured vegetation can be related to varying fractions of photosynthetic (PV) and non-photosynthetic (NPV) parts of vegetation visible from different viewing angles. At larger off-nadir angles, the visible fraction of NPV increases and reduces the green plant material reflective proportion, limiting its applicability at canopy level [54]. Increased NPV visibility at extreme off-nadir angles combines with higher reflectance in the red edge due to an increase of multiple scattering. For the simple structured type, NPV does play a minor role, while increased red-edge reflectance at larger off-nadir angles is caused by the obscuration of sunlit soil. This effectuates stronger ARI1 angular dependence in complex structured canopies.

The high CAB angular sensitivity can be directly related to across-track HDRF changes in the VIS. These are not considered during model inversion, which leads to misinterpretation of the signal as changing CAB contents. The same explanation holds true for the CW sensitivity to reflectance anisotropy. Lower HDRF due to reflectance anisotropy in water absorptions regions between 700 and 2500 nm are misinterpreted as higher water absorption.

The derivation of CDM from IS data suffers from ambiguities. The wavelength region affected by the absorption of dry matter (lignin and cellulose) notably overlaps with the wavelength region affected by water absorption. Further, CDM absorption is small compared to the water absorption or the impact of varying LAI on the canopy reflectance signal. This explains the noise fraction of 10% up to 50% in CDM absorption measured over the FOV. In addition, the value range of existing CDM contents is very low, which further increases this effect.

Structure drives anisotropic reflectance behavior; as LAI is influenced by vegetation structure, it is supposed to be rather sensitive to reflectance anisotropy [63]. In fact, from all PROSPECT-SAIL inversion products, LAI features the highest standard deviation (approximately 80%), which partly explains the low influence of the measured anisotropic response on the statistical results.

C. Using Ross–Li for Reflectance Anisotropy Quantification and Correction

We demonstrated that a correction of view-angle effects in a single airborne flight line using the Ross–Li transformation significantly reduces the angular dependencies. While not being designed for a particular GIFOV, the kernel functions describe the BRDF for sub-pixel influences of volume- and geometric-optical scattering. Thus, the geometric-optical kernel can correct for a certain shadow fraction within a vegetation pixel, while it is not capable of removing shadow from a completely shaded pixel. This has to be considered when high-resolution data are corrected using this method. The correction coefficients

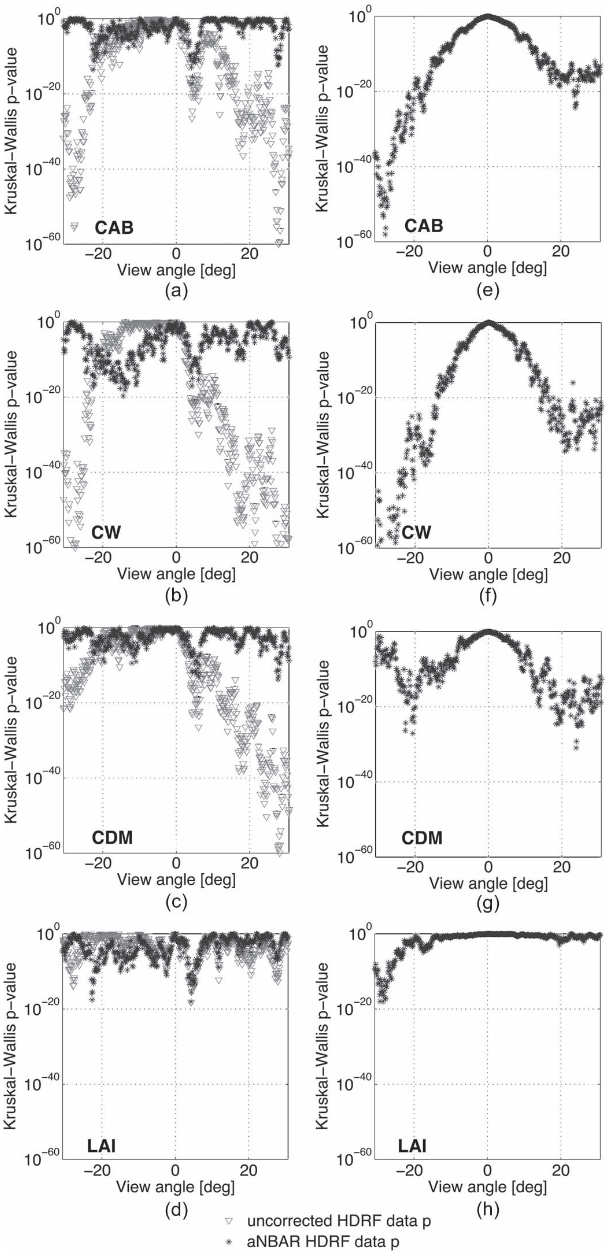

Fig. 6. Results of the Kruskal–Wallis non-parametric analysis of variance for the PROSPECT/SAIL inversion products. X-axis depicts the FOV, y-axis the p-value. Plots A–D: Off-nadir samples are compared to nadir samples for products from aNBAR and original HDRF data. Plots E–H: product values of equal off-nadir view angle from aNBAR and original HDRF data were tested against each other. p-values indicate the probability for the tested samples to belong to the same population or populations with the same median.

applied, however, are based on averaged observations for a given view angle, comprising a wide range of completely shadowed pixels to completely illuminated pixels. Thus, correction coefficients applied to the HDRF data are based on an average volume- and geometric-optical scattering regime that is comparable to the scattering regime of a lower resolution data set. We can recommend using the Ross–Li approach also for high-resolution data sets when the model is inverted against a representative number of illuminated and shaded pixels.

The empirical part of the Ross–Li model can be considered as the "bottleneck" of the whole approach, when only a single observation per pixel is available. No information on the magnitude and distribution of volume scattering and shading effects can be retrieved directly from a single flight line. Consequently, there is no means to limit the range of possible kernel weights for the semi-empirical approach. Attempts to derive image-based information about the canopy specific scattering characteristics, e.g., by using different error metrics, or by determining representative kernel weights using a forward modeling approach [64] are only possible for multi-angular data (AirMISR, Polder, CAR, ASAS) where the observations are well distributed over the hemisphere [65]. The empirical estimation of volume scattering information from airborne data, however, is ill posed. The fraction of volume scattering of the total reflected radiation increases with a larger "volume" filled with scattering elements, which is, for a forest canopy, equivalent to larger trees with more trunks and leaves where photon scattering can occur. The thickness of the volume scattering medium is measured directly in the line of sight of the sensor. In case of a tilted view, it must be a function of both canopy height and the view angle. Thus, any assumptions on the volume scattering fraction of the reflected radiation can be disturbed if the height of a canopy strongly varies in across-track direction.

The Ross–Li kernel formulations are based on simplified physical reflectance functions for which the physical parameters have been fixed. Because of the separation of individual scattering mechanisms, a certain kernel combination allows representing canopies that are characterized by, e.g., varying density, height, or gap fraction. This variation is accounted for through individual weighting of the geometric and volumetric scattering kernel. The Ross–Li model, however, presumes constant canopy characteristics for the set of observations used to invert the model [27]. In case of airborne acquisition, the set of observations is constrained by the stratification of the data set into structural types. If the canopy characteristics considerably change in across-track direction, the pre-defined weighted kernel combinations might be less representative and consequently lead to unrealistic estimations of the BRDF. For high-resolution data, the absolute number of angular observations must balance a potentially unrepresentative observation scale.

Two steps are critical with respect to the stratification of data. 1) The definition of spectral classes must map the dominating scattering effective structural types, and 2) a suitable classification algorithm is required. SAM was proven to be appropriate for the present investigation. Nevertheless, classification errors will bias the aNBAR HDRF calculation. Correction factors for the vegetation structural types were found to differ by a maximum of 21% (RED) and 18% (NIR) at very large off-nadir view angles, which is about the order of magnitude of maximum error to expect for mis-classified vegetation pixels (detailed analysis not shown).

A general drawback of the approach lies in its dependence on land cover types, thus relying on an accurate classification. This concept does not allow accounting for horizontal radiation transfer, e.g., between a (high) forest and an adjacent meadow. Horizontal radiation transfer particularly modifies the scattering regime when the height differences between low and high objects with individual scattering properties are in the order of or larger than the size of a ground resolution cell [66].

VI. CONCLUSION

We discuss a potential pathway correcting directional effects present in airborne IS data. The impact of surface reflectance anisotropy was found to be present and substantially different for two selected structural vegetation classes, both on HDRF level and for derived products. A significant across-track variation was observed for the majority of products derived from uncorrected HDRF data. An anisotropy correction of the HDRF data allows compensating the sensitivity of almost all IS data products. This indicates that the shape of BRDF for the investigated land cover structural types can be reproduced by the Ross–Li method with sufficient accuracy. The proposed aNBAR product is a step toward the minimization of uncertainties in quantitative spectroscopy data analysis.

Remaining gradients in the products can be further reduced by an empirical correction directly applied on product level. Such correction on product level is highly unphysical and should be considered only when residual errors can be confined and quantified by ground measurements or an investigation of the overlapping area of two flight lines.

Future efforts will go toward a continuous description of the surface to better model individual contributors (e.g., geometric-optical, volumetric, and isotropic) to the overall scattering regime. The required information could be extracted from co-registered external data sources like maps of surface structural properties as generated from active remote sensing technologies like ground-based or airborne LIDAR [67], [68] or through SAR tomography [69]. Alternatively, scale-invariant approaches are emerging and consistent databases of single scattering albedo or phase functions would allow scaling approaches from leaf to canopy and finally help to estimate anisotropy better [9], [70].

However, inclusion of a priori information like canopy structure and height can enhance the robustness of the retrieval, but will rely on externally available data sources. The cost of such externally available data for operational airborne IS data normalization seems today be too high, while the added dimensionality of spectroscopy data has not yet been fully explored.

A future reliable estimate of the effective magnitude of the volume scattering and geometric scattering regime per resolution cell, forming continuous fields allowing to describing basic BRDF shape parameters, will help significantly to provide operational and physically sound solutions for anisotropy correction in spectrometry data and thus to improve the general product quality.

REFERENCES

[1] M. E. Schaepman, S. L. Ustin, A. J. Plaza, T. H. Painter, J. Verrelst, and S. Liang, "Earth system science related imaging spectroscopy—An assessment," *Remote Sens. Environ.*, vol. 113, no. Suppl. 1, pp. S123–S137, Sep. 2009.

[2] K. Lucas and G. Carter, "The use of hyperspectral remote sensing to assess vascular plant species richness on Horn Island, Mississippi," *Remote Sens. Environ.*, vol. 112, no. 10, pp. 3908–3915, Oct. 2008.

[3] L. Kooistra, W. Wamelink, G. Schaepman-Strub, M. Schaepman, H. Vandobben, U. Aduaka, and O. Batelaan, "Assessing and predicting biodiversity in a floodplain ecosystem: Assimilation of net primary production derived from imaging spectrometer data into a dynamic vegetation model," *Remote Sens. Environ.*, vol. 112, no. 5, pp. 2118–2130, May 2008.

[4] R. F. Kokaly, G. P. Asner, S. V. Ollinger, M. E. Martin, and C. A. Wessman, "Characterizing canopy biochemistry from imaging spectroscopy and its application to ecosystem studies," *Remote Sens. Environ.*, vol. 113, no. Suppl. 1, pp. S78–S91, Sep. 2009.

[5] S. L. Ustin and J. A. Gamon, "Remote sensing of plant functional types," *New Phytologist*, vol. 186, no. 4, pp. 795–816, Jun. 2010.

[6] X. Li and A. Strahler, "Geometric-optical bidirectional reflectance modeling of a conifer forest canopy," *IEEE Trans. Geosci. Remote Sens.*, vol. GRS-24, no. 6, pp. 906–919, Nov. 1986.

[7] X. Li and A. H. Strahler, "Geometric-optical bidirectional reflectance modeling of the discrete crown vegetation canopy: Effect of crown shape and mutual shadowing," *IEEE Trans. Geosci. Remote Sens.*, vol. 30, no. 2, pp. 276–292, Mar. 1992.

[8] R. Richter and D. Schläpfer, "Geo-atmospheric processing of airborne imaging spectrometry data. Part 2: Atmospheric/topographic correction," *Int. J. Remote Sens.*, vol. 23, no. 13, pp. 2631–2649, 2002.

[9] D. S. Kimes, "Dynamics of directional reflectance factor distributions for vegetation canopies," *Appl. Opt.*, vol. 22, no. 9, p. 1364, May 1983.

[10] W. Ni, X. Li, C. E. Woodcock, R. Caetano, and A. H. Strahler, "An analytical hybrid GORT Model for bidirectional reflectance over discontinuous plant canopies," *IEEE Trans. Geosci. Remote Sens.*, vol. 37, no. 2, pp. 987–999, Mar. 1999.

[11] A. H. Strahler and D. L. B. Jupp, "Modeling bidirectional reflectance of forests and woodlands using boolean models and geometric optics," *Remote Sens. Environ.*, vol. 34, no. 3, pp. 153–166, Dec. 1990.

[12] C. L. Walthall, "Field and landscape BRDF optical wavelength measurements: Experience, techniques and the future," *Remote Sensing Reviews*, vol. 18, no. 2–4, pp. 503–532, 2000.

[13] D. W. Deering, T. F. Eck, and B. Banerjee, "Characterization of the reflectance anisotropy of three boreal forest canopies in spring-summer," *Remote Sens. Environ.*, vol. 67, no. 2, pp. 205–229, Feb. 1999.

[14] M. O. Román, C. K. Gatebe, C. B. Schaaf, R. Poudyal, Z. Wang, and M. D. King, "Variability in surface BRDF at different spatial scales (30 m–500 m) over a mixed agricultural landscape as retrieved from airborne and satellite spectral measurements," *Remote Sens. Environ.*, vol. 115, no. 9, pp. 2184–2203, Sep. 2011.

[15] F. Gemmell and A. J. Mcdonald, "View zenith angle effects on the forest information content of three spectral indices," *Remote Sens. Environ.*, vol. 158, no. 2, pp. 139–158, May 2000.

[16] J. Verrelst, M. E. Schaepman, B. Koetz, and M. Kneubühler, "Angular sensitivity analysis of vegetation indices derived from CHRIS/PROBA data," *Remote Sens. Environ.*, vol. 112, no. 5, pp. 2341–2353, May 2008.

[17] S. Collings, P. Caccetta, N. Campbell, and X. Wu, "Techniques for BRDF correction of hyperspectral mosaics," *IEEE Trans. Geosci. Remote Sens.*, vol. 48, no. 10, pp. 3733–3746, Oct. 2010.

[18] B. Holben, D. Kimes, and R. S. Fraser, "Directional reflectance response in AVHRR red and near-IR bands for three cover types and varying atmospheric conditions," *Remote Sens. Environ.*, vol. 19, no. 3, pp. 213–236, Jun. 1986.

[19] R. D. Jackson, P. M. Teillet, P. N. Slater, G. Fedosejevs, M. F. Jasinski, J. K. Aase, and M. S. Moran, "Bidirectional measurements of surface reflectance for view angle corrections of oblique imagery," *Remote Sens. Environ.*, vol. 32, no. 2/3, pp. 189–202, May/Jun. 1990.

[20] P. J. Mouginis-Mark, H. Garbeil, and P. Flament, "Effects of viewing geometry on AVHRR observations of volcanic thermal anomalies," *Remote Sens. Environ.*, vol. 48, no. 1, pp. 51–60, Apr. 1994.

[21] R. E. Kennedy, "Empirical methods to compensate for a view-angle-dependent brightness gradient in AVIRIS imagery," *Remote Sens. Environ.*, vol. 62, no. 3, pp. 277–291, Dec. 1997.

[22] R. E. Kennedy, W. B. Cohen, and G. Takao, "A BRDF-related brightness gradient in AVIRIS imagery: Lessons from an empirical compensation method," in *Proc. Summaries 7th JPL Airborne Earth Science Workshop*, 1998, pp. 225–231.

[23] S. Schiefer, P. Hostert, and A. Damm, "Correcting brightness gradients in hyperspectral data from urban areas," *Remote Sens. Environ.*, vol. 101, no. 1, pp. 25–37, Mar. 2006.

[24] C. L. Walthall, "A study of reflectance anisotropy and canopy structure using a simple empirical model," *Remote Sens. Environ.*, vol. 61, no. 1, pp. 118–128, Jul. 1997.

[25] B. Hu, W. Lucht, X. Li, and A. H. Strahler, "Validation of kernel-driven semiempirical models for the surface bidirectional reflectance distribution function of land surfaces," *Remote Sens. Environ.*, vol. 62, no. 3, pp. 201–214, Dec. 1997.

[26] W. Lucht, C. B. Schaaf, and A. H. Strahler, "An algorithm for the retrieval of Albedo from space using semiempirical BRDF models," *IEEE Trans. Geosci. Remote Sens.*, vol. 38, no. 2, pp. 977–998, Mar. 2000.

[27] J. L. Roujean, M. Leroy, and P. Y. Deschamps, "A bidirectional reflectance model of the Earth's surface for the correction of remote sensing data," *J. Geophys. Res.*, vol. 97, no. D18, pp. 20 455–20 468, Jan. 1992.

[28] W. Wanner, X. Li, and A. H. Strahler, "A new class of geometric-optical semiempirical kernels for global BRDF and albedo modeling," in *Proc. IEEE Geosci. Remote Sens.*, 1995, pp. 15–17.

[29] M. J. Chopping, "Testing a LiSK BRDF model with in situ bidirectional reflectance factor measurements over semiarid grasslands," *Remote Sens. Environ.*, vol. 74, no. 2, pp. 287–312, Nov. 2000.

[30] C. B. Schaaf, F. Gao, A. H. Strahler, W. Lucht, X. Li, T. Tsang, N. C. Strugnell, X. Zhang, Y. Jin, J. Muller, P. Lewis, M. Barnsley, P. Hobson, M. Disney, G. Roberts, M. Dunderdale, C. Doll, P. Robert, B. Hu, S. Liang, J. L. Privette, and D. Roy, "First operational BRDF, albedo nadir reflectance products from MODIS," *Remote Sens. Environ.*, vol. 83, no. 1/2, pp. 135–148, Nov. 2002.

[31] S. Liang, H. Fang, M. Chen, C. J. Shuey, C. Walthall, C. Daughtry, J. Morisette, C. Schaaf, and A. Strahler, "Validating MODIS land surface reflectance and albedo products: Methods and preliminary results," *Remote Sens. Environ.*, vol. 83, no. 1/2, pp. 149–162, Nov. 2002.

[32] L. He, J. M. Chen, J. Pisek, C. B. Schaaf, and A. H. Strahler, "Global clumping index map derived from the MODIS BRDF product," *Remote Sens. Environ.*, vol. 119, pp. 118–130, Apr. 2012.

[33] J. Pisek, M. Rautiainen, J. Heiskanen, and M. Mõttus, "Retrieval of seasonal dynamics of forest understory reflectance in a Northern European boreal forest from MODIS BRDF data," *Remote Sens. Environ.*, vol. 117, pp. 464–468, Feb. 2012.

[34] D. J. Weiss and R. L. Crabtree, "Percent surface water estimation from MODIS BRDF 16-day image composites," *Remote Sens. Environ.*, vol. 115, no. 8, pp. 2035–2046, Aug. 2011.

[35] Q. Zhang, X. Xiao, B. Braswell, E. Linder, S. Ollinger, M.-L. Smith, J. P. Jenkins, F. Baret, A. D. Richardson, B. Moore, and R. Minocha, "Characterization of seasonal variation of forest canopy in a temperate deciduous broadleaf forest, using daily MODIS data," *Remote Sens. Environ.*, vol. 105, no. 3, pp. 189–203, Dec. 2006.

[36] A. Cescatti, B. Marcolla, S. K. Santhana Vannan, J. Y. Pan, M. O. Román, X. Yang, P. Ciais, R. B. Cook, B. E. Law, G. Matteucci, M. Migliavacca, E. Moors, A. D. Richardson, G. Seufert, and C. B. Schaaf, "Intercomparison of MODIS albedo retrievals and in situ measurements across the global FLUXNET network," *Remote Sens. Environ.*, vol. 121, pp. 323–334, Jun. 2012.

[37] U. Beisl, *Correction of Bidirectional Effects in Imaging Spectrometer Data*. Zurich, Switzerland: Univ. Zurich, 2001.

[38] S. Huber, M. Kneubühler, A. Psomas, K. Itten, and N. Zimmermann, "Estimating foliar biochemistry from hyperspectral data in mixed forest canopy," *Forest Ecol. Manage.*, vol. 256, no. 3, pp. 491–501, Jul. 2008.

[39] T. Cocks, R. Jenssen, A. Stewart, I. Wilson, and T. Shields, "The HyMap airborne hyperspectral sensor: The system, calibration and performance," in *Proc. EARSeL Workshop Imag. Spectrosc.*, 1998, pp. 1–6.

[40] G. Schaepman-Strub, M. E. Schaepman, T. H. Painter, S. Dangel, and J. V. Martonchik, "Reflectance quantities in optical remote sensing—Definitions and case studies," *Remote Sens. Environ.*, vol. 103, no. 1, pp. 27–42, Jul. 2006.

[41] R. B. Myneni, R. Ramakrishna, R. Nemani, and S. W. Running, "Estimation of global leaf area index and absorbed par using radiative transfer models," *IEEE Trans. Geosci. Remote Sens.*, vol. 35, no. 6, pp. 1380–1393, Nov. 1997.

[42] J. Ross, *The Radiation Regime and Architecture of Plant Stands*. New York, NY, USA: Springer-Verlag, 1981.

[43] W. Lucht, A. H. Hyman, A. H. Strahler, M. J. Barnsley, P. Hobson, and J. Muller, "A comparison of satellite-derived spectral albedos to ground-based broadband Albedo measurements modeled to satellite spatial scale for a semidesert landscape," *Remote Sens. Environ.*, vol. 74, no. 1, pp. 85–98, Oct. 2000.

[44] F. Maignan, F.-M. Bréon, and R. Lacaze, "Bidirectional reflectance of Earth targets: Evaluation of analytical models using a large set of spaceborne measurements with emphasis on the Hot Spot," *Remote Sens. Environ.*, vol. 90, no. 2, pp. 210–220, Mar. 2004.

[45] W. Wanner, X. Li, and A. H. Strahler, "On the derivation of kernels for kernel-driven models of bidirectional reflectance," *J. Geophys. Res.*, vol. 100, no. D10, pp. 21 077–21 089, Jan. 1995.

[46] Y. Shuai, J. G. Masek, F. Gao, and C. B. Schaaf, "An algorithm for the retrieval of 30-m snow-free albedo from Landsat surface reflectance and MODIS BRDF," *Remote Sens. Environ.*, vol. 115, no. 9, pp. 2204–2216, Sep. 2011.

[47] F. A. Kruse, A. B. Lefkoff, J. B. Boardman, K. B. Heidebrecht, A. T. Shapiro, P. J. Barloon, and A. F. H. Goetz, "The spectral image processing system (SIPS)—Interactive visualization and analysis of imaging spectrometer data," *Remote Sens. Environ.*, vol. 44, no. 2/3, pp. 145–163, May/Jun. 1993.

[48] R. B. Myneni, S. Hoffman, Y. Knyazikhin, J. L. Privette, J. Glassy, Y. Tian, Y. Wang, X. Song, Y. Zhang, G. R. Smith, A. Lotsch, M. Friedl, J. T. Morisette, P. Votava, R. R. Nemani, and S. W. Running, "Global products of vegetation leaf area and fraction absorbed PAR from year one of MODIS data," *Remote Sens. Environ.*, vol. 83, no. 1/2, pp. 214–231, Nov. 2002.

[49] S. Jacquemoud, W. Verhoef, F. Baret, C. Bacour, P. J. Zarco-Tejada, G. P. Asner, C. François, and S. L. Ustin, "PROSPECT+SAIL models: A review of use for vegetation characterization," *Remote Sens. Environ.*, vol. 113, no. Suppl. 1, pp. S56–S66, Sep. 2009.

[50] W. Verhoef and H. Bach, "Simulation of hyperspectral and directional radiance images using coupled biophysical and atmospheric radiative transfer models," *Remote Sens. Environ.*, vol. 87, no. 1, pp. 23–41, Sep. 2003.

[51] C. J. Tucker, "Red and photographic infrared linear combinations for monitoring vegetation," *Remote Sens. Environ.*, vol. 8, no. 2, pp. 127–150, May 1979.

[52] S. O. Los, C. O. Justice, and C. J. Tucker, "A 1° by 1° global NDVI data set for climate studies derived from the GIMMS continental NDVI data," *Int. J. Remote Sens.*, vol. 15, no. 17, pp. 3493–3518, 1994.

[53] J. Peñuelas, F. Baret, and I. Filella, "Semi-empirical indices to assess carotenoids/chlorophyll a ratio from leaf spectral reflectance," *Photosynthetica*, vol. 31, no. 2, pp. 221–230, 1995.

[54] A. A. Gitelson, M. N. Merzlyak, and O. B. Chivkunova, "Optical properties and nondestructive estimation of anthocyanin content in plant leaves," *Photochem. Photobiol.*, vol. 74, no. 1, pp. 38–45, Jul. 2001.

[55] S. Jacquemoud, S. L. Ustin, J. Verdebout, G. Schmuck, and G. Andreoli, "Estimating leaf biochemistry using the PROSPECT leaf optical properties model," *Remote Sens. Environ.*, vol. 56, no. 3, pp. 194–202, Jun. 1996.

[56] B. Combal, F. Baret, M. Weiss, A. Trubuil, D. Macé, A. Pragnère, R. Myneni, Y. Knyazikhin, and L. Wang, "Retrieval of canopy biophysical variables from bidirectional reflectance using prior information to solve the Ill-posed inverse problem," *Remote Sens. Environ.*, vol. 84, no. 1, pp. 1–15, Jan. 2003.

[57] V. C. E. Laurent, W. Verhoef, M. E. Schaepman, A. Damm, and J. G. P. W. Clevers, "Mapping LAI and chlorophyll content from at-sensor APEX data using a bayesian optimisation of a coupled canopy-atmosphere model," in *Proc. Geosci. Remote Sens.*, 2012, pp. 5685–5688.

[58] J. D. Gibbons, *Nonparametric Statistical Inference*. New York, NY, USA: Marcel Dekker, 1985.

[59] F. Gao, "Detecting vegetation structure using a kernel-based BRDF model," *Remote Sens. Environ.*, vol. 86, no. 2, pp. 198–205, Jul. 2003.

[60] P. Guillevic, F. Zagolski, V. Demarez, V. Trichon, D. Deering, and M. Leroy, "Modeling BRF and radiation regime of boreal and tropical forests: I. BRF," *Remote Sens. Environ.*, vol. 68, no. 3, pp. 281–316, Jun. 1999.

[61] J.-L. Widlowski, B. Pinty, N. Gobron, M. M. Verstraete, and A. B. Davies, "Characterization of surface heterogeneity detected at the MISR/TERRA subpixel scale," *Geophys. Res. Lett.*, vol. 28, no. 24, pp. 4639–4642, Dec. 2001.

[62] M. Rautiainen, M. Lang, M. Mõttus, A. Kuusk, T. Nilson, J. Kuusk, and T. Lükk, "Multi-angular reflectance properties of a hemiboreal forest: An analysis using CHRIS PROBA data," *Remote Sens. Environ.*, vol. 112, no. 5, pp. 2627–2642, May 2008.

[63] P. Bicheron and M. Leroy, "A method of biophysical parameter retrieval at global scale by inversion of a vegetation reflectance model," *Remote Sens. Environ.*, vol. 67, no. 3, pp. 251–266, Mar. 1999.

[64] J. Susaki, K. Hara, K. Kajiwara, and Y. Honda, "Robust estimation of BRDF model parameters," *Remote Sens. Environ.*, vol. 89, no. 1, pp. 63–71, Jan. 2004.

[65] F. Gao, C. B. Schaaf, A. H. Strahler, and W. Lucht, "Using a multikernel least-variance approach to retrieve and evaluate albedo from limited bidirectional measurements," *Remote Sens. Environ.*, vol. 76, no. 1, pp. 57–66, Apr. 2001.

[66] J. Widlowski, B. Pinty, T. Lavergne, M. M. Verstraete, and N. Gobron, "Horizontal radiation transport in 3-D forest canopies at multiple spatial resolutions: Simulated impact on canopy absorption," *Remote Sens. Environ.*, vol. 103, no. 4, pp. 379–397, Aug. 2006.

[67] F. Morsdorf, C. Nichol, T. Malthus, and I. H. Woodhouse, "Assessing forest structural and physiological information content of multispectral LiDAR waveforms by radiative transfer modelling," *Remote Sens. Environ.*, vol. 113, no. 10, pp. 2152–2163, Oct. 2009.

3. MINIMIZING REFLECTANCE ANISOTROPY EFFECTS IN AIRBORNE SPECTROSCOPY DATA USING ROSS-LI MODEL INVERSION WITH CONTINUOUS FIELD LAND COVER STRATIFICATION

© 2015 IEEE. Reprinted, with permission from Weyermann, J., Kneubühler, M., Schläpfer, D. & Schaepman, M. E.: Minimizing reflectance anisotropy effects in airborne spectroscopy data using Ross-Li model inversion with continuous field land cover stratification. *IEEE Transactions on Geoscience and Remote Sensing*, Vol. 53, Issue 11, November 2015.

Contribution of first author and co-authors:

Michael Schaepman designed the study.

Jörg Weyermann, Mathias Kneubühler and Michael Schaepman developed the methodology.

Jörg Weyermann collected the data.

Jörg Weyermann and Daniel Schläpfer performed the analysis.

Jörg Weyermann, Daniel Schläpfer, Mathias Kneubühler and Michael Schaepman wrote the manuscript.

Minimizing Reflectance Anisotropy Effects in Airborne Spectroscopy Data Using Ross–Li Model Inversion With Continuous Field Land Cover Stratification

Jörg Weyermann, Mathias Kneubühler, Daniel Schläpfer, *Member, IEEE*, and
Michael E. Schaepman, *Senior Member, IEEE*

***Abstract*—The spectral and radiometric quality of airborne imaging spectrometer data is affected by the anisotropic reflectance behavior of the imaged surface. Illumination and observation angle-dependent patterns of surface reflected radiation propagate into products, hinder quantitative assessment of biophysical/biochemical parameters, and decrease the comparability of data from multiple flight lines. The Ross–Li model, originally developed for multiangular observations, can be inverted to estimate and correct for surface anisotropy effects. This requires land cover be stratified into distinct types of scattering behavior. When the observations subsumed in these classes cover a range of view angles, a pseudo multiangular view on the surface can be employed to invert the Ross–Li model. A discrete land cover classification, however, bears the risk of inappropriate scattering correction resulting in spatial artifacts in the corrected data, predominantly in transition regions of two land cover types (e.g., soil and sparse vegetation with varying fractions). We invert the Ross–Li model on continuous land cover fraction layers. We decompose land cover in dominating structural types using linear spectral unmixing. Ross–Li kernel weights and formulations are estimated for each type independently; the correction is then applied pixel-wise according to the fractional distribution. The corrected Airborne Prism EXperiment imaging spectrometer data show significant reduction of anisotropic reflectance effects of up to 90% (average 60% to 75%, $p = 0.05$), measured in the overlapping regions of adjacent flight lines. No spatial artifacts or spectral irregularities are observed after correction.**

***Index Terms*—Airborne Prism EXperiment (APEX), imaging spectroscopy (IS), reflectance anisotropy, Ross–Li, spectral mixture analysis.**

I. INTRODUCTION

AIRBORNE imaging spectroscopy (IS) is increasingly used for precision applications in the context of biochemical and biophysical land surface parameter estimation [1]–[3], atmospheric trace gas retrievals [4], or calibration/validation activities for spaceborne missions [5]. Applications of such type require accurate sensor and data calibration to provide the customer with reliable products. Basically all optical data recorded with scanner-type airborne spectrometers are affected by the anisotropic reflectance behavior of natural and artificial surfaces of the Earth, which needs to be corrected for [6]. The function to be modeled is usually described as bidirectional reflectance distribution function (BRDF) [7], [8]. The BRDF depends on the illumination and observation geometry and features a surface specific shape.

Physical-based approaches such as radiative transfer models (RTMs) are barely applicable to full IS flight lines because a description of the surface in terms of structural and biochemical properties is usually missing at the detail level required by RTM. Semiempirical approaches such as the kernel-based class of models [9]–[13] were found to be a good compromise between operational applicability and soundness of their physical basis to reduce effects of reflectance anisotropy. Kernel-based methods are robust and have been widely used for spaceborne data product generation [14]. Stable model inversion requires a number of angular observations for each target, i.e., accurately coregistered pixels taken from different view and/or under different illumination angles. A method based on the well-known Ross and Li kernels is also applicable to anisotropy correction of airborne imagery, when the surface is stratified into structural scattering types and the view-angle-dependent reflectance is used to model the BRDF separately for individual types [15]. As a semiempirical model generally can be regarded as a constrained fit to measured observations, the surface stratification defining the set of observations is of high relevance for the quality of correction. Application to airborne data based on stratification of surface is an active field of research; one of the authors published work with a conceptually different approach recently in this journal [16].

A discrete surface classification, allowing a single spectral or structural class per pixel, has limitations, when the surface represents a continuously changing mix of different scattering types, as e.g., soil and a spatially varying layer of short vegetation [17]–[19]. A classification strategy accounting for the fractional amount of scattering effective surface components should better account for heterogeneous surface structure at the spatial scale of the sensor's ground instantaneous field-of-view (GIFOV).

Manuscript received November 11, 2014; revised February 12, 2015; accepted March 11, 2015.

J. Weyermann, M. Kneubühler, and M. E. Schaepman are with the Remote Sensing Laboratories, Department of Geography, University of Zürich, CH-8057 Zürich, Switzerland (e-mail: joerg.weyermann@geo.uzh.ch).

D. Schläpfer is with ReSe Applications, CH-9500 Wil SG, Switzerland (e-mail: daniel@rese.ch).

Color versions of one or more of the figures in this paper are available online at http://ieeexplore.ieee.org.

Digital Object Identifier 10.1109/TGRS.2015.2415872

TABLE I
FLIGHT LINE PARAMETERS

Flight line ID	Heading [°]	Solar zenith [°]	Solar azimuth [°]
1	358.5	35.7	120.6
2	178.9	34.7	122.7

The goal of this paper is to evaluate a Ross–Li-based correction method where the influence of reflectance anisotropy is estimated for surface constituents individually and correction factors are applied according to the individual fractions within a single pixel.

The specific objectives of this study are: i) to combine the established Ross–Li method with spectral mixture analysis; ii) to quantify the effectiveness of the new method in the overlapping area of two adjacent flight lines in terms of reflectance units and on product level for two spectral vegetation indices sensitive to reflectance anisotropy; and iii) to discuss the sensitivity of the spectral mixture analysis to reflectance anisotropy.

The need for anisotropy correction is commonly accepted [20], [21]. The method presented in this paper can be regarded as a contribution toward a more reliable correction of angular effects with respect to the typical mixed pixel situation at arbitrary sensor spatial resolution. Its application is possible for a broad range of optical remote sensing image data, given a spectral mixture model can be established and the angular distribution of observations within a cover type is sufficient. Its application is foreseen predominantly when statistical or index-based data analysis at regional scale is intended.

II. IMAGING SPECTROMETER DATA

Spectroscopy data for this study were acquired on June 26, 2011 at a test site close to the city of Zürich in northern Switzerland (8° $32'$ $40''$E/47° 22’ 2"N) (two partly overlapping flight lines). Fig. 3(a) shows the orientation of the flight lines and the overlap. Rural landscape is the dominating land cover type with roughly 44% homogeneously dense mixture forest, 25% agricultural fields with various crops in different phenological stages, 17% bare soil surface, 13% lake and river water areas, and 1% sealed (urban) surface.

Data were acquired with the Airborne Prism EXperiment (APEX) imaging spectrometer (IS) [22]. APEX is a pushbroom scanner, recording 1000 pixels per scan line with a total FOV of 28.0°. The solar reflective wavelength region between 380 and 2500 nm was recorded in 301 contiguous spectral bands. The flight lines are oriented in north–south direction (heading about $360^{\circ}/180^{\circ}$). The overlapping area at the main test site is dominated by a patchwork of agricultural fields with a broad range of vegetation abundances. The data were recorded from a flight altitude of about 6000 m above ground, resulting in a raw data ground sampling distance of 3 m both in along-track and across-track direction. Table I indicates the flight geometry and solar angles for all flight lines.

APEX data were atmospherically corrected using the ATCOR-4 standard approach [23]. Atmospheric correction was carried out with a rural standard atmosphere, removing effects of view-angle-dependent path radiance and adjacency effects as well as incidence angle and terrain dependencies of the illumination. The output of atmospheric correction approximates the so-called “Top-Of-Canopy Hemispherical-Directional-Reflectance-Factor” (HDRF) [24]. The anisotropy correction was then carried out on HDRF data in image acquisition geometry with an effective ground sampling distance of 3 m. The image data were then orthorectified to the digital terrain model using a direct geocoding approach (PARGE standard approach) [25].

Reflectance anisotropy has strongest influence when the sensor is scanning in the solar principal plane (SPP, relative azimuth of 0°) and least influence when scanning perpendicular to the SPP [26]. The maximum influence is by far not reached in the data used for this study. No validation field measurements were available from representative locations.

III. METHODS

A. Linear Spectral Unmixing

Linear spectral unmixing (LSU) [27] allows to quantify the radiometric contribution of subpixel surface components to the total reflectance signal, assuming that the total reflectance of a single pixel can be expressed as a linear combination of the reflected radiation of all its components (called endmembers). The general equation for the linear spectral mixture model at a single image position i,j can be written as [27]

$$R_{ij,\lambda,dir} = \sum_{n=1}^{N} g_{ij,n} E_{n,\lambda} \tag{1}$$

where $R_{ij,\lambda,dir}$ is the reflectance factor at image row i and column j at wavelength λ, dir indicates that we are dealing with a directional reflectance quantity, $g_{ij,n}$ is the fraction of endmember n at the respective image location, and $E_{n,\lambda}$ is the reflectance of endmember n at wavelength λ.

The assumption of a linear mixture model can only be an approximation to the reality, however, sufficiently accurate for the majority of applications [28]. Due to its simplifying nature with respect to nonlinear effects and ignorance of the instrument’s point spread function LSU can provide only a proxy for the areal fractions of surface components within a single pixel. For BRDF studies the radiometric decomposition through LSU has a so far unexploited potential to discriminate BRDF cover types.

We performed LSU with the three basic structural surface elements at the spatial scale of APEX, represented by two vegetation structural types (vertically and horizontally complex vegetation such as forest, and low vegetation such as meadow or agricultural crops) and a ‘soil’ type, including bare soil, gravel, and sand. Spectral signatures of these three endmembers were averaged directly from representative regions of interest (ROIs) in the IS data. ROIs were chosen close to nadir to prevent angular effects to have significant influence on the endmembers. The respective abundances f were resolved with a least squares method in an unconstrained manner, i.e., no normalization to sum unity was invoked. Abundance maps of two vegetation structural types and "soil" resulted from the LSU procedure.

LSU with more spectral bands than endmembers is an overdetermined system, possibly leading to unreliable abundances adding to a sum of more than 100% or even negative abundances [28]. Some type of normalization is always required to gain reliable radiometric contributions of single endmembers. We applied a two-step pixel-wise normalization, first applying an offset (additively) if negative abundances were present, then normalizing the total reflectance to a value of 100%, including residual reflectance (multiplicatively). After this normalization, the surface reflectance could be described as a linear superposition of at least a subset of the spectral endmembers including residual, adding to 100% for each pixel.

B. Ross–Li BRDF Model

We used the semiempirical, kernel-based Ross–Li BRDF model [11], [12] to correct reflectance anisotropy effects. The Ross–Li model allows decomposing measured HDRF into radiation components originating from three surface scattering types. Isotropic scattering (ISO) is the radiation fraction without angular dependence. Volumetric scattering (VOL) has angular dependence as a function of small inter-leaf gaps within a horizontally homogeneous vegetation canopy [29]. Geometric scattering (GEO) generates angular dependence as function of large gaps within a canopy or sparse stand structure [30]. KVOL and KGEO are nonlinear functions (so-called "kernel" K) of observation and illumination geometry only. The kernels themselves are linearly combined, using a waveband specific weighting parameter f. This weighting parameter is retrieved by model inversion. Considering the mentioned components, the reflectance R can be then described as

$$R = f_{ISO}(\lambda) + f_{VOL}(\lambda)K_{VOL} + f_{GEO}(\lambda)K_{GEO}. \quad (2)$$

Individual kernels were developed for different vegetation structural properties [11], [31]. Four kernels are implemented in the present correction chain (two modeling the volume-scattering (K_{VOL}, Ross kernels) and two the geometric-optical scattering (K_{GEO}, Li kernels)): The Ross Thick (R_tk) volume scattering kernel is specifically adapted to high LAI values (> 1), whereas Ross Thin (R_tn) is designed for less dense vegetation with LAI values smaller than 1 [32]. Ross kernels rely on the single scattering approximation [11]. Li kernels model the surface geometric-optical scattering regime in terms of sunlit and shadowed crowns and background [33]. Two different kernels were implemented for sparse (Li_s) and dense (Li_d) vegetation canopies. The Li kernel canopy parameters (defining canopy-to-total-height and canopy spheroidal shape) were fixed according to the MODIS BRDF/Albedo product as crown vertical to horizontal radius ratio $(\mathrm{h/b}) = 1$ (2.5) and center of crown height to horizontal radius ratio $(\mathrm{b/r}) = 2$ (2) for the sparse (dense) kernel [14]. Fig. 1 shows the kernel values for all kernels and the observation/illumination geometry of the data under investigation.

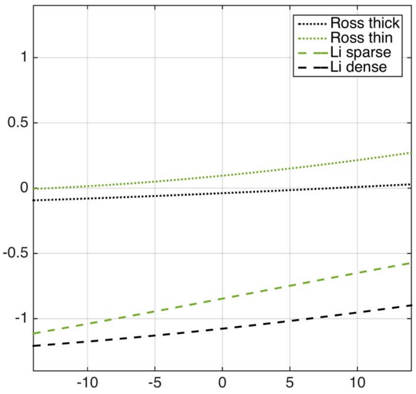

Fig. 1. Kernel values for the Ross and Li kernels for the solar geometry defined in Table I, and the APEX FOV (±14°).

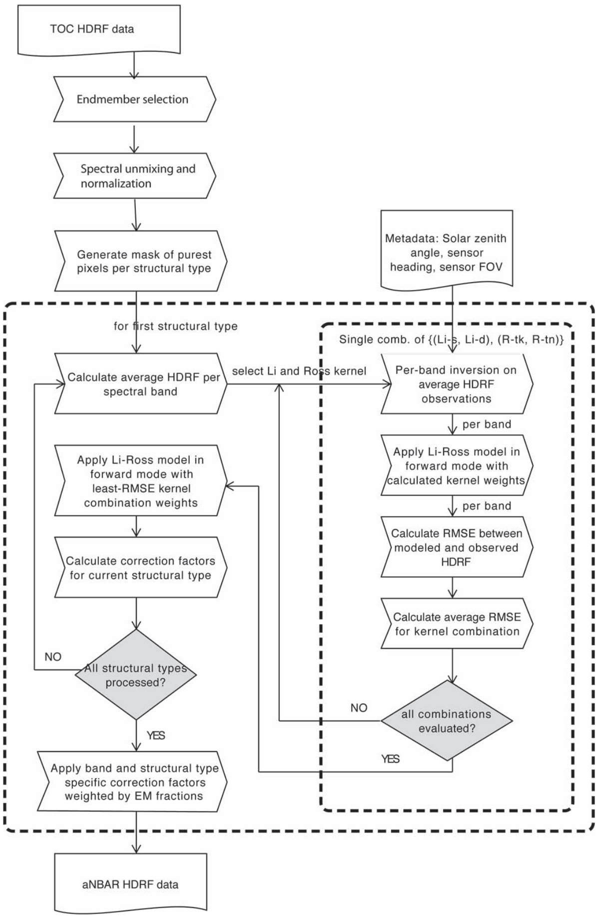

Fig. 2. Flowchart of the method.

The kernels to be employed for a certain surface type are selected based on a fit-RMSE criterion. The method thus dynamically adapts to a multitude of natural surface types. The processing chain of the Ross–Li model is depicted in Fig. 2.

TABLE II
KERNELS SELECTED FOR EACH STRUCTURAL TYPE THROUGH RMSE ANALYSIS

Structural type	Complex veg.	Simple veg.	Soil	Residual
Kvol	Ross thin	Ross thin	Ross thin	Ross thin
Kgeo	Li sparse	Li sparse	Li dense	Li sparse

We first performed LSU as described in the previous section. Based on the normalized abundance maps for each spectral endmember, we generated a mask of the purest pixels by applying a threshold in abundance. For each spectral endmember we tested the threshold levels from 70% to 95% in steps of 5% and fixed the threshold at the maximum value that fulfilled the following constraints: i) angular observations for that endmember were distributed over the full or near-full FOV; ii) the mask pixel count per view angle unit (i.e., per spatial pixel in across-track direction) was at least ten times the number of pixels required to fulfill the spatial homogeneity criterion for Ross and Li kernel functions; and iii) the spatial structure of the scene (i.e., the main land cover types) was visible in the set of observations after the threshold was applied. When, e.g., only single pixels without spatially contiguous structure were included the threshold was considered too high. At the APEX GIFOV of 3 m, we fixed the number of observations required to fulfill the homogeneity criterion to be 100 for forest (a patch of e.g., 30 by 30 m) and ten for crops, soil and other surfaces. The effective number of angular observations per view angle unit was much higher for the majority of angular positions.

For each of the pure pixel masks all permutations of kernels were then tested toward their capability to reproduce the measured HDRF angular shape. The kernel combination with a minimum root-mean-squared error (RMSE) between modeled and measured HDRF for all spectral bands was finally selected for the structural type under consideration. Kernel combinations effectively applied for each structural type are shown in Table II. RMSE differences between kernel combinations were on the order of only 2%–5%, however.

We performed numerical matrix inversion to obtain the kernel weights for isotropic, volumetric and geometric scattering. We then applied the model in forward mode to calculate reflectances for each view angle and spectral band. According to [35], correction factors were calculated as gain, keeping for each pixel, band and structural type a constant factor between the modeled HDRF for the current geometry to the modeled HDRF in the normalization geometry (i.e., nadir view and a mean solar zenith angle of 35.2°). The output of the method can be termed “airborne nadir-BRDF-adjusted reflectance (aNBAR), as presented first in [15].

C. Rationale of Method

According to the theory of LSU the reflected signal of a single pixel is a linear superposition of the reflectance signal of all components within this pixel's area, weighted by their individual areal fractions [27], [36]. This is an approximation because multiple scattering effects [28], [37] are not accounted for. The general equation for the linear spectral mixture model was introduced earlier in this paper as (1) (Section III-A).

Furthermore, the subpixel effects of surface reflectance anisotropy on the reflectance R of a pixel can be formulated by decomposing the total reflectance of this pixel into the contribution of basic scattering types according to (2) (Section III-B).

Assuming that the areal fractions of subpixel surface components directly influence the anisotropic reflectance behavior of a single pixel one can thus write

$$R_{ij,\lambda,dir} = \sum_{n=1}^{N} g_{ij,n}(f_{ISO} + f_{VOL}K_{VOL} + f_{GEO}K_{GEO})_{n,\lambda}. \tag{3}$$

The correction for reflectance anisotropy effects can then be performed independently for each of the surface components (endmembers). Correction factors are calculated for each endmember as quotient from the modeled reflectance at pixel location ij and the modeled reflectance at nadir

$$c_{i,j,\lambda} = \frac{R_{ij,mod}}{R_{ij,nad}}. \tag{4}$$

Correction factors can then be applied as a weighted sum of the contribution of all endmembers for a certain pixel and wavelength

$$R_{ij,\lambda,anbar} = \sum_{n=1}^{N} g_{ij,n} c_{i,j,n,\lambda}. \tag{5}$$

D. Evaluation of Results

For quantitative evaluation we defined 52 regions of natural land cover types (crop fields with different soil fraction, bare soil, forest patches) in the overlapping part of the two APEX IS data sets. We compared these regions before and after correction both on HDRF and on product level for two vegetation indices known as sensitive to reflectance anisotropy [15], i.e., the Normalized Difference Vegetation Index (NDVI) [38] and the Anthocyanin Reflectance Index (ARI1) [39] for each region. ARI1 is a narrow-band leaf pigment VI, relating the green to the red edge reflectance$((\mathrm{R}_{550})^{-1} - (\mathrm{R}_{700})^{-1})$. Reflectance values in selected wavebands in the blue, green, red and NIR region ($\lambda = 461.1$ nm, 551.5 nm, 621.6 nm and 811.3 nm) were compared. For both reflectance values and index products we expected the differences between flight lines in the corrected versions to be considerably lower than in the uncorrected data sets. A difference of zero would represent a perfect BRDF correction.

We performed nonparametric analysis of variance (Kruskal–Wallis test) individually for each plot in the main dataset to assess the effectiveness of the correction statistically. The null hypothesis is that after correction the medians of the compared samples do not significantly differ (with $\mathrm{p} = 0.05$). While absolute statistical significance is an important indicator of the

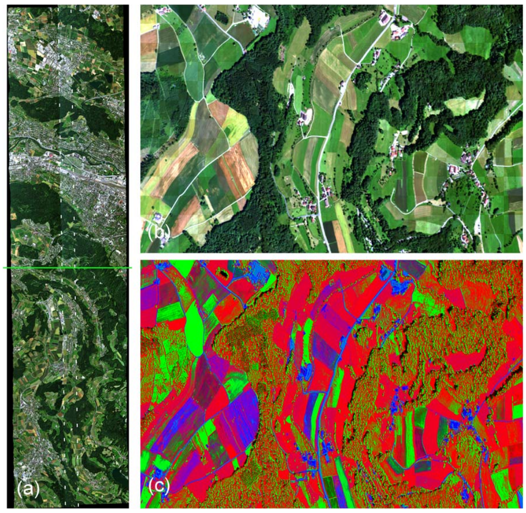

Fig. 3. True-color mosaic of two flight lines. The northern part (indicated with the green horizontal line) is not corrected for anisotropy, the southern is corrected. The overlapping area is indicated with dashed lines (a). True-color RGB checkerboard image showing for a single flight line the reduction of off-nadir variations by the correction (b) and RGB representation of normalized abundances for the vegetation types and soil (c) for the same subset. Red color represents the complex structured vegetation endmembers (high fraction of volume scattering), green color the simple structured vegetation (low volume scattering), and blue color the soil endmember (predominance of geometric-optical effects).

quality of correction the main quality indicator used in this study is the increase in p when comparing uncorrected and corrected data samples. Additional statistical Kruskal–Wallis tests were performed comparing off-nadir to nadir samples of the NDVI and ARI1 product before and after correction for both flight lines of the main dataset to evaluate the effectiveness of the method in forested areas, based on an independent classification in distinct forest pixels.

IV. RESULTS

From a visual point of view the correction was very effective for all flight lines. Fig. 3(a) depicts a true-color RGB mosaic of the two flight lines, where the northern part is uncorrected and the southern is corrected with the presented method.

No residual brightness gradient within the flight lines and the characteristic edge in the intersection line can be observed after correction. Fig. 3(b) shows a checkerboard composite of corrected and uncorrected data (subset of a single flight line) in a true-color RGB representation, visualizing the effectiveness of the correction in more detail. The correction was based on the unmixing-derived normalized abundance distribution visualized for the same spatial subset in Fig. 3(c). Per-pixel abundances are expressed as RGB color value. Red color represents the complex structured vegetation endmembers (high fraction of volume scattering), green color the simple structured vegetation (low volume scattering), and blue color the soil endmember (predominance of geometric-optical effects through micro-scale shading effects on the ground). Aspects of the abundance distribution are subject to the discussion.

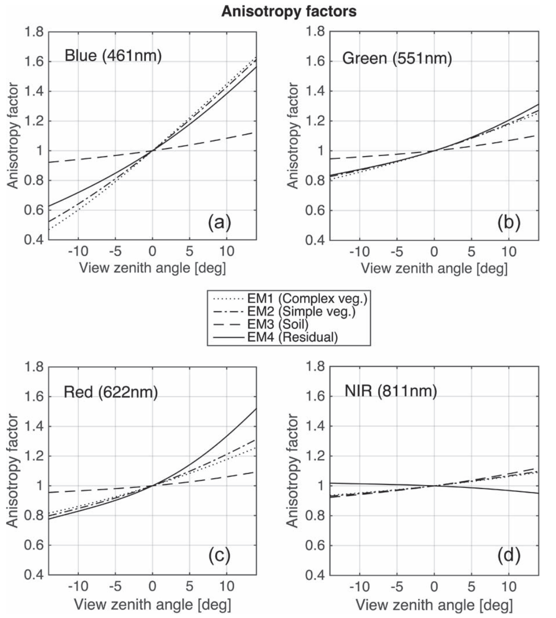

Fig. 4. Comparison of anisotropy factors for the spectral endmembers and four spectral bands.

The Ross–Li modeled anisotropies are shown in Fig. 4.

The per-endmember anisotropy is presented here as factor with respect to nadir observations, valid for "pure" pixels of the respective type. The two vegetation types show rather similar angular behavior across the investigated wavelengths, whereas soil deviates strongly. This implies that vegetation and soil surface types, and particularly mixtures among them need to be treated separately for angular effects correction. A global correction thus can never correct satisfactory for view angular effects on soil and vegetation surfaces at the same time. The correction factor finally applied to a single pixel at a certain wavelength thus is calculated from a weighted sum of usually 2 to 3 of these components, as defined in (5). The anisotropy of the residual is comparatively high. Again, it is calculated here for the most pure pixels of the "residual" type, which is represented by pixels that do not fit in vegetation or soil-similar type. Few natural pixels only have considerable fractions of the "residual" type such that its overall impact is very small.

Quantitative evaluation of the effectiveness of the correction was accomplished with an initial number of 52 plots within the overlapping area of the two flight lines.

Three of these 52 validation plots within the overlapping region of the two flight lines were excluded because of their small spatial size. From the remaining 49 plots (of size larger than 1200 pixels), 12 showed a distinct negative impact of the presented correction method in the vegetation index products. This was in contrast to the visually positive effect. Investigation showed that these regions were mostly forest patches with distinct vertical structure and strong shading effects, where a large fraction of illuminated and shaded pixels does not match in the coregistered data. The correction obviously has negative impact on pixels that are fully shaded. Five other plots represented bare soil patches where standard vegetation

TABLE III

CORRECTION GAINS AS AVERAGE REDUCTION IN DIFFERENCE IN THE OVERLAPPING AREA BETWEEN TWO FLIGHT LINES

Product	HDRF blue (λ = 461.1nm)	HDRF green (λ = 551.5nm)	HDRF red (λ = 621.6nm)	HDRF NIR (λ = 811.3nm)	NDVI	ARI1
Avg. reduction [%]	75.4	64.3	64.3	58.7	60.4	62.2
Stdev [%]	23.0	20.6	20.2	23.5	23.0	18.9

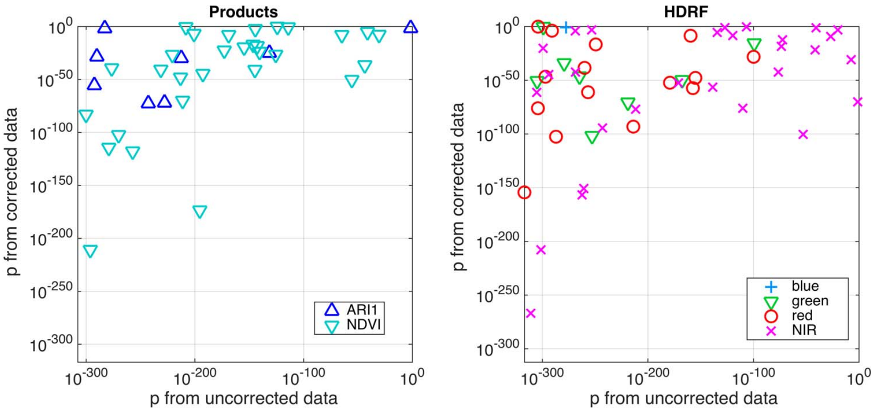

Fig. 5. Scatter plot of Kruskal–Wallis p-values for the investigated samples and products. X-axis: p from uncorrected data. Y-axis: p from corrected data. This plot compares the statistical relationship of product values in the overlapping area of the two flight lines of the main dataset before and after application of the correction method.

indices do not necessarily contain meaningful values. These areas are not included in the following presentation of results, which consists of 33 plots after exclusion of those with limited validity.

A. *Quantitative Effect of the Correction on HDRF Data and Products*

We compared the per-plot average differences in HDRF value before (off-nadir HDRF) and after correction (nadir HDRF) in the overlapping area of two coregistered flight lines for four (narrow) spectral bands in the VIS and NIR range. Quality gain through the correction is measured as reduction in plot-averaged differences in corrected data relative to the differences in uncorrected data. Results and basic statistics are depicted in Table III. Average reduction refers to the arithmetic mean of all investigated plots in the overlap.

The per-plot differences were reduced after correction by 64% on average, depending on the product, with a mean standard deviation of 21%.

In the visible range, the average reduction (arithmetic mean of a single blue, green and red channel as declared above) was 68%, whereas 21% of the plots showed a difference reduction of more than 90%. The HDRF agreement in the plots increased by more than 70% in half of the plots and by more than 50% in 80% of the plots.

In the NIR, numbers are slightly different. The average reduction was at 59% with 13% of the plots with 90% better agreement (i.e., plots having a residual of 10% of the original difference). In 37% of the plots the difference was reduced by more than 70%, and in 53% by more than 50%.

NDVI (incorporating red and NIR bands) and ARI1 (green and red bands) feature comparable values for the estimation metrics. The average difference reduction is 60.4% (NDVI) and 62.2% (ARI1). For both indices about 10% of the plots show a reduction of uncorrected difference of more than 90%. In about one-third of the plots the reduction is better than 70% and in about 80% more than half of the anisotropy effect could be removed.

Despite the overall positive influence of the correction, the statistical test results as presented in Fig. 5 do not allow accepting the null hypothesis for the majority of the samples, i.e., also after correction the medians of the compared samples do differ significantly. Fig. 5 plots for each product the Kruskal–Wallis p-value from uncorrected data (x-axis) against the p-value from corrected data (y-axis). Each data point represents one of the 33 evaluated sample plots. Fig. 5 shows the p distribution logarithmically on both axes, focusing on the exact value of p in the uncorrected data. In many cases, there is no statistical relationship at all before correction ($\mathrm{p} = 0$), resulting in data points not presentable as "0" is not an element of the logarithmic scale.

The increase in Kruskal–Wallis p-value as drawn from Fig. 5 is remarkable, indicating that the correction has a widely positive effect on the quality of the data and products, even if a perfect correction cannot be achieved.

Similar statistical results for the comparison of forest off-nadir to nadir pixels confirm that the presented correction method has significant positive effect on the data. The increase

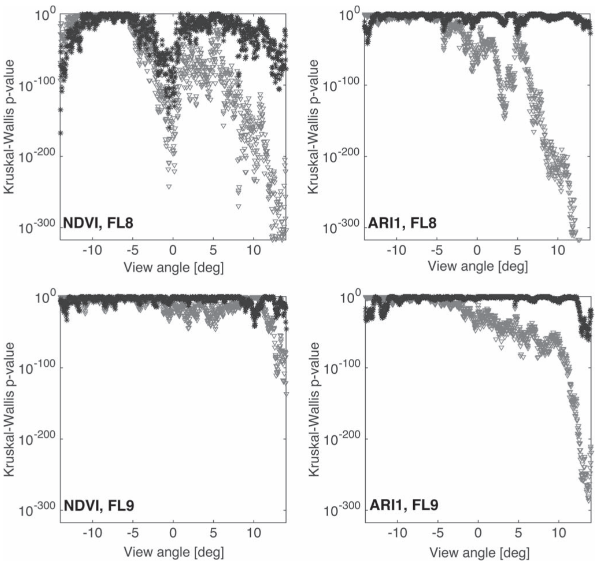

Fig. 6. Results of the Kruskal–Wallis nonparametric analysis of variance for forest pixels of the two flight lines (main dataset). X-axis depicts the FOV, y-axis p-values. Off-nadir samples are compared with nadir samples for products from aNBAR and original HDRF data.

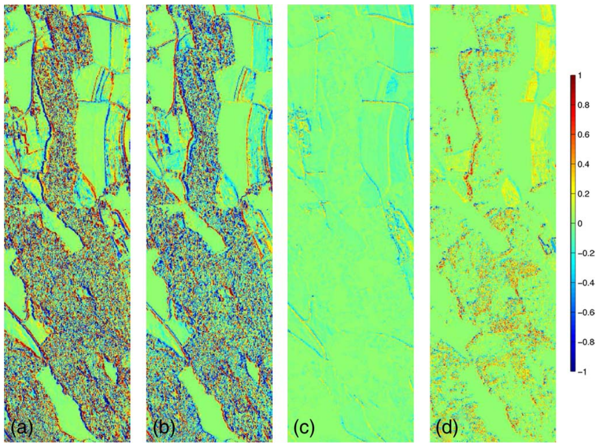

Fig. 7. Differences in the normalized abundances for all endmembers (subset of the overlapping area between the two flight lines). (a) Complex structured vegetation (forest). (b) Simple structured vegetation (crops, meadow). (c) Soil. (d) Residual.

in the Kruskal–Wallis p-value through correction comparing off-nadir to nadir values is depicted in Fig. 6.

The statistical relationship increases remarkably for both flight lines and products over the full FOV and approaches a value of “1” except for the NDVI product at angles beyond 10 deg off-nadir view angle.

V. DISCUSSION

A. General Effectiveness of the Method

The wavelength dependence of BRDF could be well modeled and corrected appropriately, such that anisotropy effects were reduced by 60% to 75% in the calculated products. The general performance of the method is comparable to results of previous research [15]. Retrieved spectral anisotropies are further comparable to the work of [16].

The absolute reduction in anisotropy varies slightly between plots (compare standard deviation in Table III), and is further specific to the spectral band or product. While minor differences between e.g., spectral bands are expected due to the nonlinear spectral behavior of BRDF, larger offsets might indicate that either the fractions of BRDF-effective land cover components (as retrieved from LSU procedure) are not representative for the true scattering behavior, or that the estimation of the anisotropy is not modeled accurately for these surface structures during the Li–Ross inversion. Differences between plots of similar spectral characteristics are weak, however, and can be partly deduced from the nonperfect coregistration of the images.

B. Sensitivity of Spectral Mixture Analysis to Reflectance Anisotropy

Reflectance anisotropy may affect spectral mixture analysis due to the nonlinearity in the spectral domain. For the method presented in this study it is, however, important that there is no significant systematic error introduced on the distribution of fractions for the individual endmembers, originating from reflectance anisotropy effects. Such errors would harm both the estimation of BRDF shape and magnitude from the purest pixels, and the application of calculated correction factors according to the calculated abundances for each mixed pixel.

An evaluation of the overlapping area in terms of differences between the LSU derived abundances (normalized according to Section III-A) showed that there is a distinct, but rather small effect of reflectance anisotropy on the final abundances. Fig. 7 compares these abundances for each spectral endmember.

The spatial linear structures indicate (known) coregistration insufficiencies, whereas spatially homogeneous areas (at the spatial scale of the instrument) feature very small differences between the two flight lines. This holds true for all endmembers. The distribution of abundance differences in the forested areas, again, can be considered on the one hand an effect of the imperfect coregistration of the two flight lines, which is further modified by the fact that due to the maximum offset in observation angle (APEX: Δ FOV $\sim 30^\circ$) the sensor potentially observes different fractions of shadow in the two flight lines. Furthermore, the unmixing results make evident that particularly in forested areas the mapping of two vegetation spectral endmembers to the multitude of individual species in the forest is a challenge, which is basically due to the spatial heterogeneity and mixture effects occurring not only within different species but also with illuminated or shaded background or shaded parts of trees. It is therefore questionable whether the pattern of abundances, as presented in Fig. 3(b) accurately represents the distribution of the two individual scattering types. The major difference between the scattering types (for which the endmembers act as proxies) is the wavelength dependent influence of multiple scattering effects. A well-known characteristic of the NIR is the increased presence of multiple scattering effects, flattening the BRDF in this spectral region. Underestimating the abundance of complex structured

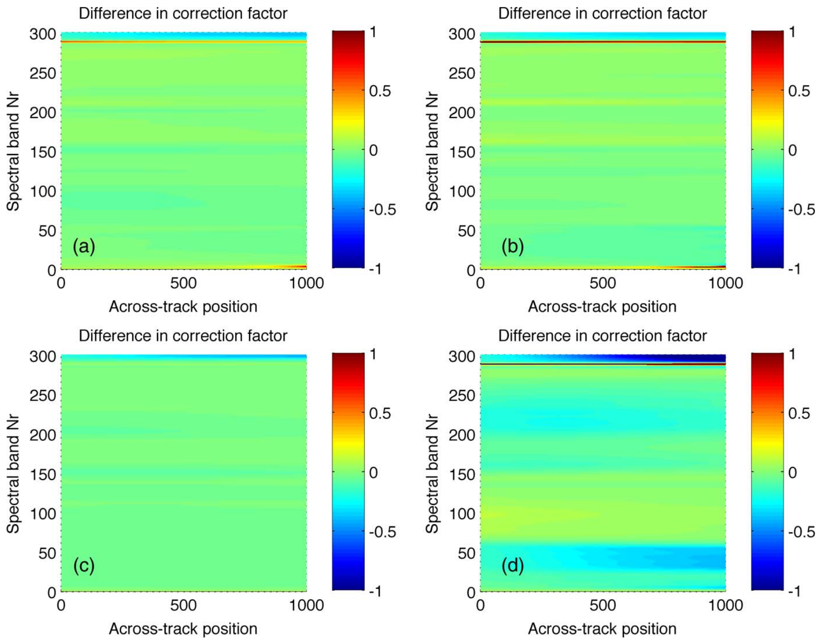

Fig. 8. Differences in correction factor between the two flight lines for all endmembers. (a) Complex structured vegetation (forest). (b) Simple structured vegetation (crops, meadow). (c) Soil. (d) Residual.

vegetation (which is the case when the other vegetation endmember has significant abundance in the forest as well) thus should lead to an overcorrection in the NIR range with limited influence in the visible range. The maximum error can then be quantified as the difference in correction factor calculated for the respective land cover type, observation/illumination geometry and spectral band, multiplied with the reflectance factor for that band at the respective location. The maximum error occurs when a pixel has 100% abundance of the "wrong" endmember, which is very unlikely.

Apart from these effects, abundance differences in overlapping areas of the flight lines are restricted to a range of ±20% in more homogeneous regions within the forests.

C. *Robustness of the Li–Ross Correction*

An important factor determining the robustness of the presented method is the reproducibility of correction factors when both the LSU and the subsequent estimation of anisotropic reflectance are performed individually on two flight lines featuring similar surface structural and spectral characteristics and recorded under comparable illumination conditions. The expectation would be that correction factors are highly comparable.

In order to evaluate this we i) calculated a set of correction factors individually for the two flight lines (the results of which were presented in the results section); and ii) transferred a set of correction factors, estimated for a single flight line, to the adjacent one to perform a correction and evaluate the transferability of the factors. The matrices of correction factors derived independently on the two flight lines showed only marginal differences, which are visualized in Fig. 8.

The color representation was scaled to the range $[-1, 1]$ and singular outliers were excluded for better visualization. In general (for most spectral bands and view angles) the differences between correction factors for the same surface structural type and view angle were on the order of 5%–10% of the absolute range. However, the spatial distribution of the correction factor differences is of major interest. Changes in difference within a single endmember plot occur in the spectral domain (y-axis) rather than in the spatial domain (x-axis), indicating that the shape of the anisotropy-introduced gradient is estimated consistently between the two flight lines. Differences that do not change significantly between forward- and backward scattering direction only effectuate in the final 'brightness' level for a waveband and surface spectral component, but not in shape differences with respect to the brightness gradient in across-track direction. The areas of larger difference values in Fig. 8 are all located in either very short or very long wavelengths, mostly in those with low reflectance level and thus rather small signal-to-noise ratio. Atmospheric correction artifacts possibly cause irregularities in these spectral regions. In general, we can conclude that the correction parameters can be retrieved in a stable manner and the correction is transferable between flight lines recorded under comparable illumination conditions.

D. *Selection of Spectral Endmembers*

Endmember selection is a required task for this method, at the same time critital and hard to constrain, both with respect to the number of endmembers and the quality. The major difficulty is the proper mapping of vegetation structural types (and their individual scattering properties) to spectral endmembers. The uncertainties related with improper abundance retrieval in unmixing are, however, less critical than the effect of a wrong class assignment in the case of a distinct classification.

Fig. 4 also supports the thesis that partially improper endmember abundances for vegetation are compensated by the fact that the anisotropies for the two vegetation structural types are rather similar and thus still lead to a good correction result.

The use of generic spectral endmembers would make the correction more operational and transferable and is subject to current research within the topic of BRDF correction.

VI. CONCLUSION

The correction of reflectance anisotropy effects in airborne spectroscopy data is an inevitable task becoming more and more critical with increased accuracy requirements on radiance, reflectance, or value-added (level-3) products. In this paper, we presented a novel method, which combines the (methodically) established semiempirical Ross–Li inversion method with the advantages of a continuous description of land cover stratification in terms of abundances of BRDF-effective structural components. The method proved to be very effective and could reduce the uncertainty for the investigated products by 60% to 75%. In a true-color RGB visualization of the data there was barely a gradient or sharp edge visible after correction and subsequent mosaicking. Major weaknesses of the method include the manual selection of representative regions-of-interest for endmember generation and the selection of thresholds for the "purest pixels mask" generation. Establishing a hard constraint for the threshold is method and scene specific. Whether a fully automatic endmember selection method would be capable of generating an equally effective set of spectral endmembers requires further investigation, as well as the impact of different threshold values on the Ross–Li inversion and on the resulting anisotropy correction. A further potential enhancement to the presented method would be the inclusion of library spectra for typical BRDF cover types to allow unsupervised anisotropy correction.

Our analysis showed that shadowed areas, specifically in forests, are disturbing a BRDF correction or at least their evaluation in many aspects. Due to these problems in evaluation, the BRDF correction of shaded pixels with their strongly differing illumination field needs to be treated separately. A coupling of the BRDF correction as presented in this paper with the calculation of the complete illumination field on a pixel scale would be the only, however challenging, approach to solve this issue.

The overall results achieved with the correction method presented in this paper were highly satisfactory and we can recommend the method for correction of airborne IS data. It is notable that the rather narrow view angular range of ±14 deg and a single solar zenith/azimuth angle are sufficient to invert a Ross–Li model on data of the given surface structural complexity. The presented methodological idea is of generic applicability to wide FOV airborne IS data, as the underlying theory is not tied to the presented validation case. Validation on different imagery is ongoing and shows well comparable results.

We would, however, limit the usage of the presented method to applications where empirical or semiempirical IS data analysis (e.g., index-based product generation, regression analysis, etc.) is intended. RTM's usually incorporate illumination- and view geometry and should resolve for the according effects more specific, given the surface can be described with sufficient accuracy.

REFERENCES

[1] S. L. Ustin, D. A. Roberts, J. A. Gamon, G. P. Asner, and R. O. Green, "Using imaging spectroscopy to study ecosystem processes and properties," *Bioscience*, vol. 54, no. 6, pp. 523–534, Jun. 2004.

[2] M. E. Schaepman *et al.*, "Earth system science related imaging spectroscopy—An assessment," *Remote Sens. Environ.*, vol. 113, pp. S123–S137, Sep. 2009.

[3] L. Homolová, Z. Malenovský, J. G. P. W. Clevers, G. García-Santos, and M. E. Schaepman, "Review of optical-based remote sensing for plant trait mapping," *Ecol. Complexity*, vol. 15, pp. 1–16, Sep. 2013.

[4] C. Popp *et al.*, "High-resolution NO 2 remote sensing from the Airborne Prism EXperiment (APEX) imaging spectrometer," *Atmos. Meas. Tech.*, vol. 5, no. 9, pp. 2211–2225, Sep. 2012.

[5] V. C. E. Laurent, M. E. Schaepman, W. Verhoef, J. Weyermann, and R. O. Chávez, "Bayesian object-based estimation of LAI and chlorophyll from a simulated sentinel-2 top-of-atmosphere radiance image," *Remote Sens. Environ.*, vol. 140, pp. 318–329, Jan. 2014.

[6] S. R. Sandmeier, "Acquisition of bidirectional reflectance factor data with field goniometers," *Remote Sens. Environ.*, vol. 73, no. 3, pp. 257–269, Sep. 2000.

[7] F. E. Nicodemus, J. C. Richmond, and J. J. Hsia, "Geometrical considerations and nomenclature for reflectance," *Sci. Technol.*, Oct. 1977.

[8] G. Schaepman-Strub, M. E. Schaepman, T. H. Painter, S. Dangel, and J. V. Martonchik, "Reflectance quantities in optical remote sensing—definitions and case studies," *Remote Sens. Environ.*, vol. 103, no. 1, pp. 27–42, Jul. 2006.

[9] B. Hu, W. Lucht, X. Li, and A. H. Strahler, "Validation of kernel-driven semiempirical models for the surface bidirectional reflectance distribution function of land surfaces," *Remote Sens. Environ.*, vol. 62, no. 3, pp. 201–214, Dec. 1997.

[10] W. Lucht, C. B. Schaaf, and A. H. Strahler, "An algorithm for the retrieval of albedo from space using semiempirical BRDF models," *IEEE Trans. Geosci. Remote Sens.*, vol. 38, no. 2, pp. 977–998, May 2000.

[11] J. L. Roujean, M. Leroy, and P. Y. Deschamps, "A bidirectional reflectance model of the Earth's surface for the correction of remote sensing data," *J. Geophys. Res.*, vol. 97, no. D18, pp. 20455–20468, Dec. 1992.

[12] W. Wanner, X. Li, and A. H. Strahler, "A new class of geometric-optical semiempirical kernels for global BRDF and albedo modeling," in *Proc. Int. Geosci. Remote Sens. Symp.*, pp. 15–17, 1995.

[13] M. J. Chopping, "Testing a lisk BRDF model with in situ bidirectional reflectance factor measurements over semiarid grasslands," *Remote Sens. Environ.*, vol. 74, no. 2, pp. 287–312, Nov. 2000.

[14] C. B. Schaaf *et al.*, "First operational BRDF, albedo nadir reflectance products from MODIS," *Remote Sens. Environ.*, vol. 83, no. 1/2, pp. 135–148, Nov. 2002.

[15] J. Weyermann, A. Damm, M. Kneubühler, and M. E. Schaepman, "Correction of reflectance anisotropy effects of vegetation on airborne spectroscopy data and derived products," *IEEE Trans. Geosci. Remote Sens.*, vol. 52, no. 1, pp. 616–627, Jan. 2014.

[16] D. Schläpfer, R. Richter, and T. Feingersh, "Operational BRDF effects correction for wide field of view optical scanners (BREFCOR)," *IEEE Trans. Geosci. Remote Sens.*, vol. 53, no. 4, pp. 1855–1864, Apr. 2014.

[17] R. S. DeFries, J. R. G. Townshend and M. C. Hansen, "Continuous fields of vegetation characteristics at the global scale at 1-km resolution," *J. Geophys. Res.*, vol. 104, no. D14, pp. 16911–16924, Jul. 1999.

[18] M. Schwarz and N. E. Zimmermann, "A new GLM-based method for mapping tree cover continuous fields using regional MODIS reflectance data," *Remote Sens. Environ.*, vol. 95, no. 4, pp. 428–443, Apr. 2005.

[19] S. L. Ustin and J. A. Gamon, "Remote sensing of plant functional types," *New Phytologist*, vol. 186, no. 4, pp. 795–816, Jun. 2010.

[20] J.-L. Roujean, M. Leroy, and P. Y. Deschamps, "A bidirectional reflectance model of the Earth's surfaces for the correction of remote sensing data," *J. Geophys. Res.*, vol. 97, no. D18, pp. 20455–20468, Dec. 1992.

[21] B. Hu, W. Wanner, X. Li, and A. H. Strahler, "Validation of kernel-driven semiempirical BRDF models for application to MODIS/MISR Data," in *Proc. IEEE Int. Geosci. Remote Sens. Symp.*, pp. 1669–1671.

[22] M. E. Schaepman *et al.*, "Advanced radiometry measurements and Earth science applications with the Airborne Prism EXperiment (APEX)," *Remote Sens. Environ.*, vol. 158, pp. 207–219, Mar. 2015

[23] R. Richter and D. Schläpfer, "Geo-atmospheric processing of airborne imaging spectrometry data. Part 2: Atmospheric/topographic correction," *Int. J. Remote Sens.*, vol. 23, no. 13, pp. 2631–2649, 2002.

[24] G. Schaepman-Strub, M. E. Schaepman, T. H. Painter, S. Dangel, and J. V. Martonchik, "Reflectance quantities in optical remote sensing-definitions and case studies," *Remote Sens. Environ.*, vol. 103, no. 1, pp. 27–42, Jul. 2006.

[25] D. Schläpfer and R. Richter, "Geo-atmospheric processing of airborne imaging spectrometry data. Part 1: Parametric orthorectification," *Int. J. Remote Sens.*, vol. 23, no. 13, pp. 2609–2630, 2002.

[26] R. B. Myneni, R. Ramakrishna, R. Nemani, and S. W. Running, "Estimation of global leaf area index and absorbed par using radiative transfer models," *IEEE Trans. Geosci. Remote Sens.*, vol. 35, no. 6, pp. 1380–1393, Nov. 1997.

[27] F. Van Der Meer and S. M. de Jong, "Improving the results of spectral unmixing of landsat thematic mapper imagery by enhancing the orthogonality of end-members," *Int. J. Remote Sens.*, vol. 21, no. 15, pp. 2781–2797, 2000.

[28] J. M. Bioucas-Dias *et al.*, "Hyperspectral remote sensing data analysis and future challenges," *IEEE Geosci. Remote Sens. Mag.*, vol. 1, no. 2, pp. 6–36, Jul. 2013.

[29] J. Ross, *The Radiation Regime and Architecture of Plant Stands*. Dordrecht, The Netherlands: Springer-Verlag, 1981.

[30] X. Li and A. H. Strahler, "Geometric-optical bidirectional reflectance modeling of the discrete crown vegetation canopy: Effect of crown shape and mutual shadowing," *IEEE Trans. Geosci. Remote Sens.*, vol. 30, no. 2, pp. 276–292, Mar. 1992.

[31] W. Lucht *et al.*, "A comparison of satellite-derived spectral albedos to ground-based broadband albedo measurements modeled to satellite spatial scale for a semidesert landscape," *Remote Sens. Environ.*, vol. 74, no. 1, pp. 85–98, Oct. 1997.

[32] W. Wanner, X. Li, and A. H. Strahler, "On the derivation of kernels for kernel-driven models of bidirectional reflectance," *J. Geophys. Res.*, vol. 100, no. D10, pp. 21077–21089, Oct. 1995.

[33] X. Li and A. Strahler, "Geometric-optical bidirectional reflectance modeling of a conifer forest canopy," *IEEE Trans. Geosci. Remote Sens.*, vol. GE-24, no. 6, pp. 906–919, Nov. 1986.

[34] M. Galassi, *GNU Scientific Library Reference Manual*, 3rd ed. Surrey, U.K.: Network Theory Ltd., 2009.

[35] U. Beisl, "Correction of bidirectional effects in imaging spectrometer data," Ph.D. dissertation, Dept. Geograph. Univ. Zürich, Zürich, Switzerland, 2001.

[36] J. Boardman, "Automated spectral unmixing of AVIRIS data using convex geometry concepts," in *Proc. Summaries, 4th JPL Airborne Geosci. Workshop*, 1993, pp. 11–14.

[37] J. M. Bioucas-Dias *et al.*, "Hyperspectral Unmixing Overview?: Geometrical, Statistical, and Sparse Regression-Based Approaches," *IEEE J. Sel. Topic Appl. Earth Observ. Remote Sens.*, vol. 5, no. 2, pp. 354–379, Apr. 2012.

[38] C. J. Tucker, "Red and photographic infrared linear combinations for monitoring vegetation," *Remote Sens. Environ.*, vol. 8, no. 2, pp. 127–150, May 1979.

[39] A. A. Gitelson, M. N. Merzlyak, and O. B. Chivkunova, "Optical properties and nondestructive estimation of anthocyanin content in plant leaves," *Photochem. Photobiol.*, vol. 74, no. 1, pp. 38–45, Jul. 2001.

Jörg Weyermann received the M.Sc. degree in geography from the University of Erlangen, Erlangen, Germany, in 2005. Since 2008, he has been working toward the Ph.D. thesis with the Spectroscopy Group, focusing on operational methods for bidirectional reflectance distribution function correction in airborne spectroscopy data.

From 2006 to 2008, he was Research Associate with the Radar Remote Sensing Group of the Remote Sensing Laboratories RSL, University of Zürich, Switzerland. His particular research interests are in data normalization for the effects of reflectance anisotropy and topography with a focus on high-resolution data.

Mathias Kneubühler received the M.S. degree in geography and the Ph.D. degree (Dr.Sc.Nat.) in remote sensing with emphasis on spectral assessment of crop phenology, from the University of Zürich, Zürich, Switzerland, in 1996 and 2002, respectively.

He is currently the Head of the Spectroscopy Laboratory of the Remote Sensing Laboratories (RSL), University of Zürich. He is particularly interested in spectrodirectional data analysis and spectral assessment of phenological processes in vegetated ecosystems. He is experienced in organizing and coordinating ground measurement campaigns and field experiments in the line of spectrodirectional data acquisition and vicarious calibration.

Daniel Schläpfer (M'10) was born in St. Gallen, Switzerland. He received the M.Sc. degree in geography and the Dr.Sc.Nat. and teaching degrees in physics and geography from the University of Zürich, Zürich, Switzerland, in 1994, 1998, and 1999, respectively.

He received the Teaching Professor degree from the State of St. Gallen in 2009. From 1998 to 2008, he was Research Scientist with the Remote Sensing Laboratories, University of Zürich. He is currently with ReSe Applications Schläpfer, Wil, Switzerland. In addition, he holds a physics teaching position with Kantonsschule, Wil. His major fields of research are the geometric preprocessing of airborne scanner data on the basis of the PARGE software, the application of radiative transfer models in imaging spectroscopy, and the advancement of radiometric and atmospheric compensation in the framework of the ATCOR atmospheric correction solution.

Michael E. Schaepman (M'05–SM'07) received the M.Sc. degree and the Ph.D. degree in geography from the University of Zürich (UZH), Zürich, Switzerland, in 1993 and 1998, respectively.

In 1999, he spent his postdoctoral time at the Optical Sciences Center, The University of Arizona, Tucson, AZ, USA. In 2000, he was appointed Project Manager of the European Space Agency Airborne Prism Experiment spectrometer. In 2003, he accepted a position of Full Chair of geoinformation science and remote sensing at Wageningen University, Wageningen, The Netherlands. In 2009, he was appointed Full Chair of remote sensing at UZH, where he is currently heading the Remote Sensing Laboratories, Department of Geography. His interests are in computational Earth sciences using remote sensing and physical models, with particular focus on the land–atmosphere interface using imaging spectroscopy.

4. EARTH SYSTEM SCIENCE APPLICATIONS

This chapter presents applications of the developed methods for correction of reflectance anisotropy effects in the context of Earth System Sciences. Three co-authored scientific publications are considered; they are not re-printed in full-length, but relevant aspects and results are presented together with figures. When there are complete paragraphs relevant for the thesis they are cited here in full length, instead of re-formulating the content.

4.1. Reflectance anisotropy effects in forests

This section is based on a scientific research article published as (Mišurec et al. (2012)):

Jan Mišurec, Veronika Kopačková, Zuzana Lhotáková, Jan Hanuš, **Jörg Weyermann**, Petya Entcheva-Campbell, and Jana Albrechtová. **Utilization of hyperspectral image optical indices to assess the Norway spruce forest health status.** *Journal of Applied Remote Sensing*, 6(1):063545, 2012.

Contribution of first author and co-authors:

Jana Albrechtová designed the study.

Jan Mišurec, Veronika Kopačková, Jan Hanuš and Jana Albrechtová developed the methodology.

Jan Mišurec collected the data.

Jan Mišurec, Zuzana Lhotáková, Jörg Weyermann and Petya Entcheva-Campbell performed the analysis.

Jan Mišurec, Veronika Kopačková, Zuzana Lhotáková, Jan Hanuš, Jörg Weyermann, Petya Entcheva-Campbell and Jana Albrechtová wrote the manuscript.

4.1.1. Abstract

The work is concerned with assessing the health status of trees of the Norway spruce species using airborne hyperspectral (HS) data (HyMap). The study was conducted in the Sokolov basin in the western part of the Czech Republic. First, statistics were employed to assess and validate diverse empirical models based on spectral information using the ground truth data (biochemically determined chlorophyll content). The model attaining the greatest accuracy (D718/D704:RMSE 0.2055 mg/g, R2 0.9370) was selected to produce a map of foliar chlorophyll concentrations (Cab). The Cab values retrieved from the HS data were tested together with other nonquantitative vegetation indicators derived from the HyMap image reflectance to create a statistical method allowing assessment of the condition of Norway spruce. As a result, we integrated the following HyMap derived parameters (Cab, REP, and SIPI) to assess the subtle changes in physiological status of the macroscopically undamaged foliage of Norway

spruce within the four studied test sites. Our classification results and the previously published studies dealing with assessing the condition of Norway spruce using chlorophyll contents are in a good agreement and indicate that this method is potentially useful for general applicability after further testing and validation.

4.1.2. Earth System Science context

Forests have manifold functions impacting global climate dynamics, as they act as biosphere - atmosphere interface e.g. for exchange of carbon (sequestration), water (evapotranspiration) and radiant energy. They play an important role in the regulation of the water cycle and the conservation/restauration of soil. As an ecosystem they provide humans with so-called services (ecosystem services) in the form of food and wood supply.

As anthropogenic influence is known to have considerable impact on the quality of these forest-provided services, observing and monitoring their health status has become increasingly important especially for policy makers. Defining the right variables that mirror the health status or act as proxies, together with reliable retrieving methods, and selection of high quality data/sensors have become critical tasks on the way to operational, stable, and long-term monitoring of forest ecosystems. Remote sensing (especially in the optical domain) has been found to be a useful and reliable tool for this project. The paper presented in this section deals with the retrieval of indicators for assessing the health status of Norway spruce forests based on imaging spectroscopy data from the HyMap sensor. A quantitative result from the study overlaid to anisotropy-corrected HyMap spectroscopy data is depicted in Figure 4.1.2.

4.1.3. Spectroscopy data

Wide-FOV, high-resolution imaging spectroscopy data from the HyMap sensor was used for the present study. All image data (9 flight lines) were atmospherically corrected using the airborne ATCOR (ATCOR-4, version 5.0) software, with reflectance factors calibrated to field-measured at-surface reflectance factors. Data were then orthorectified using a parametric approach (PARGE software) to an effective ground pixel size of 5 meter.

The imagery used for the study was found to contain considerable view and illumination angle effects, which needed to be corrected in order to derive surface parameters accurately and homogeneously over the sensor's across-track FOV.

4.1.4. Reflectance anisotropy effects

In this study the Ross-Li correction method as developed in Chapter 2 on page 11 was applied to HyMap pixels of Norway spruce (Picea abies) species landcover type (monoculture). Norway spruce is an evergreen coniferous tree. Four test sites for the study were selected to only contain (spatially, and age-wise) homogeneous patches of visually undamaged Norway spruce trees.

The explicit 3-d structure of a needle leaf forest with cone-shaped objects generates anisotropy driven by shadow casting, the magnitude of which strongly depends on the

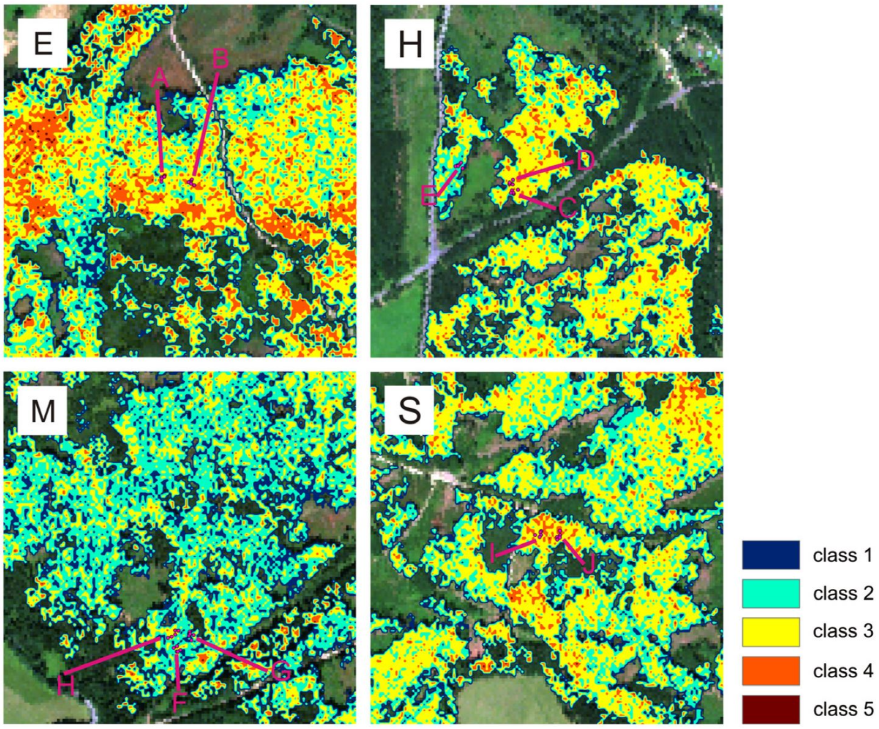

Figure 4.1.: Statistical classification of the Norway spruce health status by integrating the Cab, REP, and expSIPI. E=Erika; H=Habartov; M=Mezihorská; S=Studenec study sites; A through J; 10 defined tree groups. Color scale 1 through 5—health status classes for the trees without visible damage symptoms; 1 the worst and 5 the best result

solar angular position. This pattern of geometric-optical effects is superimposed by scattering effects within the individual tree crowns. With respect to reflectance anisotropy effects the surface is rather heterogeneous at the spatial scale of the observing instrument. The homogeneity criterion inherent to the Ross-Li kernel definitions is not per-se fulfilled as the structure scale of the scattering objects within a single resolution cell on ground is not significantly smaller than the sensor's GIFOV.

4.1.5. Results of anisotropy correction

The Ross-Li method could well model the anisotropy effects in Norway spruce forest. The evaluation criterion here was a considerable reduction of reflectance differences in overlapping patches of the flight lines. The impact of the correction was not absolutely quantified or analyzed in the frame of this publication; it was employed as one of several steps to homogenize the data for further analysis. An extensive discussion of the anisotropy effects in forests and their correction can be found in the synthesis chapter.

4.2. Reflectance anisotropy effects in snow

This section is based on a scientific research article published as (Joerg et al. (2015)):

Joerg, P.C., **Weyermann, J.**, Morsdorf, F., Zemp, M., & Schaepman, M.E. (2015). **Computation of a distributed glacier surface albedo proxy using airborne laser scanning intensity data and in-situ spectro-radiometric measurements**. Remote Sensing of Environment, 160, 31-42.

Contribution of first author and co-authors:

Philip Claudio Jörg and Michael Schaepman designed the study.

Philip Claudio Jörg, Jörg Weyermann and Michael Schaepman developed the methodology.

Philip Claudio Jörg collected the data.

Philip Claudio Jörg, Jörg Weyermann and Felix Morsdorf performed the analysis.

Philip Claudio Jörg, Jörg Weyermann, Felix Morsdorf, Michael Zemp and Michael Schaepman wrote the manuscript.

4.2.1. Abstract

In recent years, multi-temporal topographic measurements from airborne laser scanning (ALS) have been increasingly used as a source of spatially explicit and accurate information to calculate geodetic glacier mass balances. Simultaneously to collecting topographic data, most ALS instruments record the backscattered intensity for each laser emission and therefore provide additional information on the reflectance characteristics of the surveyed surface. Along with air temperature, the surface albedo of snow and ice was identified as a major driving factor of glacier melt. Consequently, better knowledge on the spatial distribution of the glacier albedo could substantially improve energy balance based glacier melt modeling. In this study, we collected on-glacier spectro-radiometric and albedometer measurements to serve as ground reference to radiometrically calibrate high resolution ALS intensity data into a distributed albedo proxy map. This method resulted in an albedo proxy with values between 0.6 on the glacier tongue and 0.9 on fresh snow in high altitudes. 99.6% of all values fell within the albedo boundary conditions, i.e. values between 0 and 1. Corrected near-infrared ALS intensity data provided a distributed product that allows simulating albedo in glacier energy and mass balance models more realistically. Remaining challenges are (i) a different surface albedo response in the visual part of the electro-magnetic spectrum, (ii) the low radiometric resolution of the ALS system for higher intensity values, and (iii) an insufficient correction of the snow bi-directional reflectance distribution function (BRDF).

4.2.2. Earth System Science context

Year-averaged changes in glacier melting intensity even if delayed by decades in time are an indicator for climate change. Understanding the mechanisms and driving factors of glacier ice melt is critical to correlating annual glacier water runoff measurements to climate variables. This includes modeling the direct response of glacier surface snow and ice to solar irradiation with respect to snow metamorphosis and surface snow melt dynamics. The magnitude of solar energy, which is absorbed by an arbitrary surface,

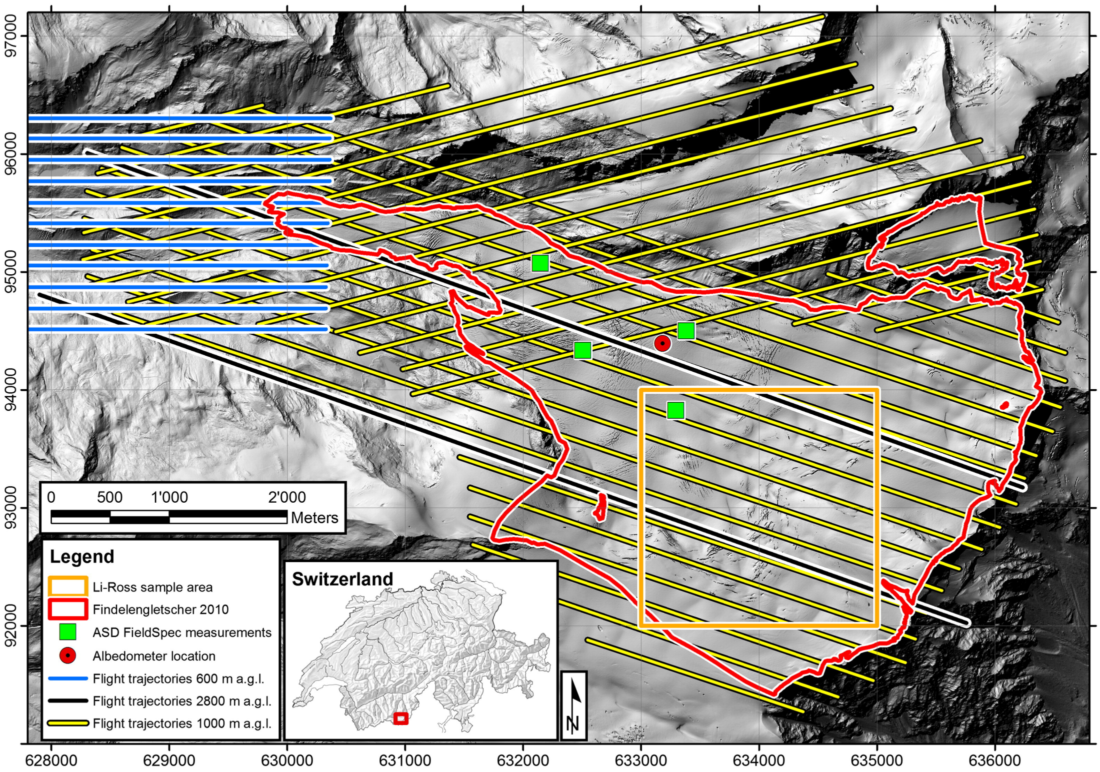

Figure 4.2.: Shaded relief of the study site with flight trajectories and in-situ reference locations. Coordinates used are in meters in the Swiss national grid (CH1903).

and thus, can readily be used for transformation of materials, highly depends on the albedo (bi-hemispherical reflectance) of a surface. The primary goal of the present study is to evaluate an airborne LiDAR dataset over the Findelengletscher to provide a spatially resolved proxy for surface albedo on snow surfaces over very undulated terrain, based on the Laser intensity measurements.

4.2.3. LiDAR data

An airborne Laser Scanning System (Optech Inc., ALTM Gemini), was employed to record range distances and intensities.

The following section is cited from the publication:

The entire glacier area was surveyed from a flight altitude of 1000 m above ground (cf. Table 1 and Fig. 4.2). A second acquisition at a lower flying altitude of 600 m above ground and a higher pulse repetition frequency (PRF) was performed as well, but only covering the lower parts of the glacier with a higher resolution. Additionally, two flight trajectories at a higher altitude of 2800 m above ground were acquired for a large portion of the glacier area to investigate effects on the accuracy of this lower point density digital elevation model (DEM) and the behavior of the recorded intensity compared to the standard setup flown at 1000 m above ground.

4.2.4. Reflectance anisotropy effects

The description of reflectance anisotropy effects is cited from the publication:

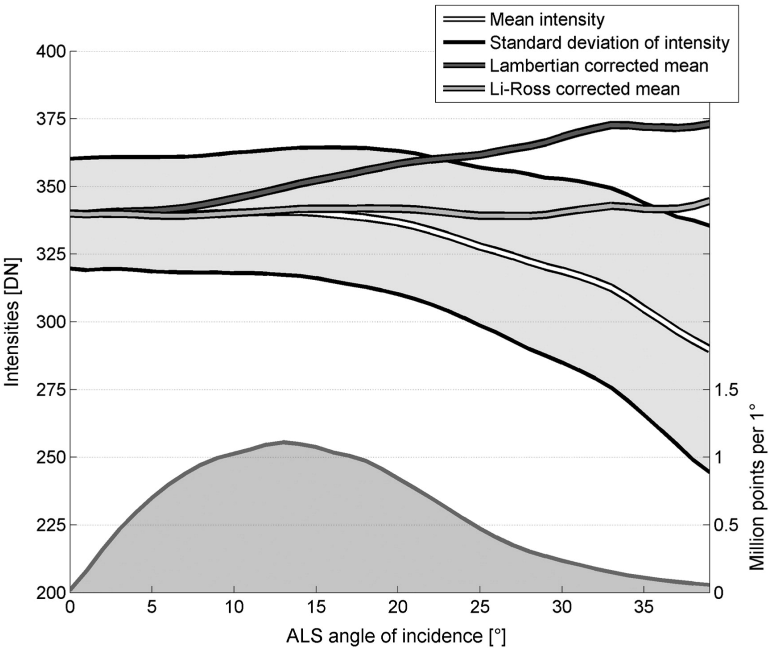

Figure 4.3.: Effects of the topographic correction for a 2 × 2 km sample patch of snow (cf. Fig. 4.2). The mean intensity and standard deviation show the decline of intensity with larger angles of incidence before the topographic correction was applied. Correcting for the topography using the Lambertian approach shows an overcorrection, while the Li–Ross correction was able to shift the average intensities to a similar value independent of the angle of incidence. The number of points per degree (angle of incidence) is shown below.

'A secondary effect of the intensity being proportional to the peak power is the dependence of the angle of incidence at the target. An inclined target surface relative to the emitted laser pulse vector leads to receiving an elongated version of the sent pulse with reduced peak amplitude. If the scattering behavior of the target's surface is assumed to be Lambertian, the peak power is reduced by with i as the local angle of incidence. However, the scattering of snow is known to be non-Lambertian, i.e. has a distinctive directional scattering behavior (e.g., Li et al. (2007); Lyapustin et al. (2010)). Due to the monostatic measurement setup, an ALS system always measures in the hot spot region of the BRDF, generating its own "solar" principle plane. Snow reflectance measurements are thus characterized by high backscatter and a large single (direct) scattering component. We employed a kernel-based approach for normalization of the anisotropic reflectance behavior of snow. Li-Ross kernels (Roujean et al. (1992a); Wanner et al. (1995a)) model the individual influence of volume- and geometric-optical scattering effects on the angular reflectance behavior of surfaces. Initially designed for vegetation, these functions were shown to be applicable to a multitude of natural surface types, including snow (e.g., Stroeve et al. (2005)). Derived from physical principles, such an

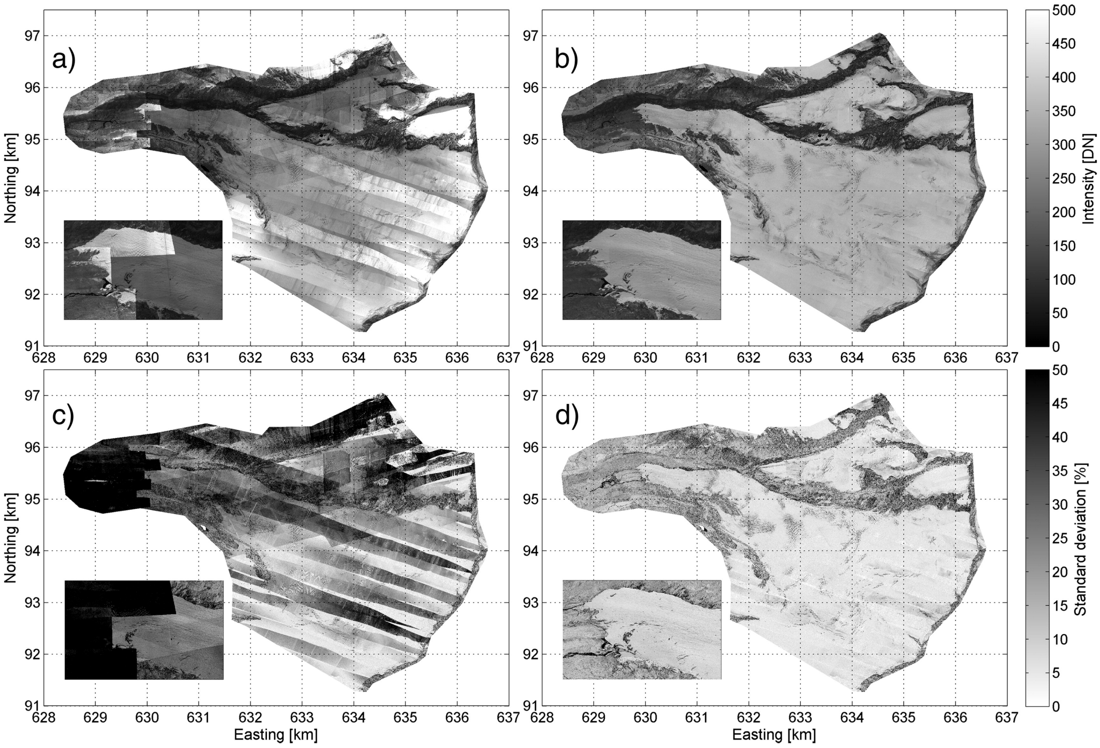

Figure 4.4.: Raw (a) and physically corrected ALS intensity data (b, topography correction: Li–Ross) show the need for intensity corrections. The corrected intensity (b) presents an albedo proxy where different surface characteristics and features (e.g. crevasses, see insets of the tongue) are visible. The relative change in the per raster cell standard deviations is visualized before (c) and after (d) the intensity corrections. Note that the lowest standard deviations in the corrected raster (d) are areas where only data from one flight strip are present. Values exceeding the color bar range are reduced to the maximum values' color to preserve a high contrast in the image. Coordinates used are in kilometers in the Swiss national grid (CH1903).

approach dramatically reduces the degrees of freedom over purely statistical-empirical approaches (Wanner et al. 1995). The present work shows the applicability also in the case of ALS measurements. We used a patch of 2 x 2 km of snow on the higher part of the Findelengletscher to train a Li-Ross based correction method dependent on the intensities with their respective angle of incidences (also Fig. 4.2). A combination of the Li-sparse geometric-optical kernel and the Ross-thick volumetric kernel provided a good fit to the measured ALS intensities in the used range of local incidence angles from 0 to 40 degrees. The local incidence angle was employed as angular offset between illumination and observation direction, assuming observation in the forward scatter direction and solar principle plane.'

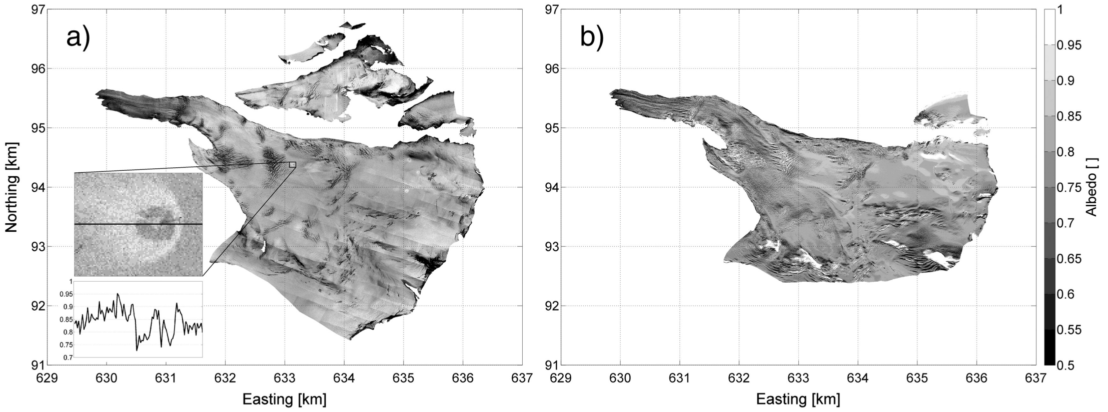

Figure 4.5.: Distributed albedo proxy map derived from ALS intensity values and ground reference measurements (a; topographic correction: Li-Ross) of Findelengletscher (south) and a contributing glacier (Adlergletscher, north). The inset shows a detail of the halo pattern where the helicopter landed (approaching from the west). Below are the albedo proxy values of the transect across the landing site. Note the areas of the deposition of fine grained snow (high albedo), the dark circular area where the fine grained snow was blown away, and the center part showing a higher albedo again, possibly due to the protected zone directly below the helicopter's fuselage. The ADS 80 reference albedo of Findelengletscher (b) is shown for comparison. Shadow areas were excluded and therefore visible as gaps in the map, as is an area to the south, which was not covered by the sensor.

4.2.5. Results

We used four pre-processing steps on the ALS intensity data to reduce physical and sensor-dependent effects before converting the intensity data into albedo proxy values. Additionally, to qualitatively check the influence of each correction step on the generated intensity maps (Fig. 4), we calculated the standard deviation of all intensity values within a raster cell. As the correction steps in the processing chain also changed the mean value in a raster cell, we normalized the standard deviations with the mean of the raster cell and therefore present the standard deviations as a percentage of the mean value. The changes from raw, uncorrected intensity values to a fully corrected, more homogeneous intensity raster can be seen in Figure 4. In the corresponding Table 2, we present the changes in average per raster cell standard deviations for snow-free terrain, the area of the glacier tongue and the glacier area excluding the tongue for a number of corrections applied. For example, after range normalization, the relative standard deviation at the glacier tongue was reduced to 59% of the initial standard deviation, meaning that the influence of the range accounts for 41% of the originally present variability. Further corrections for different PRFs, atmospheric influences and two types of topographic corrections showed an additional decrease of the relative standard deviations in most cases. The lowest variability of intensity values for the glacier tongue and snow-free area was achieved when applying all correction steps, including the Lambertian topographic correction. On the other hand, for the higher glacier area only, the topographic corrections did not further decrease the standard deviations. Figure 5 shows the influence of variations of the angle of incidence on the recorded intensity of snow, after being corrected for range, PRF, and atmospheric effects for a 2 x 2 km snow area (Li-Ross sample area in Fig. 1). As expected, with increasing angles of incidence, the values of the return intensity were decreasing. After a perfect topographic correction, the new average was expected to be a horizontal line. However, after the Lambertian correction was applied, the resulting average values per degree angle of incidence exhibited an increasing trend, showing an overcorrection of the data. Having trained Li-Ross kernels on the same test area provided a better correction of the mean values, i.e. produced an almost horizontal line.

An in-depth analysis and discussion of the anisotropy effects in snow can be found in the synthesis chapter.

4.3. Reflectance anisotropy effects in agricultural fields

This section is based on a scientific research article published as (Laurent et al. (2014)):

Valérie C.E. Laurent, Michael E. Schaepman, Wout Verhoef, **Jörg Weyermann**, and Roberto O. Chávez. **Bayesian object-based estimation of LAI and chlorophyll from a simulated Sentinel-2 top-of-atmosphere radiance image**. *Remote Sensing of Environment*, 140:318–329, January 2014.

Contribution of first author and co-authors:

Michael Schaepman and Wout Verhoef designed the study.

Michael Schaepman, Wout Verhoef and Jörg Weyermann developed the methodology.

Valérie Laurent collected the data.

Valérie Laurent, Michael Schaepman, Jörg Weyermann and Roberto O. Chavez performed the analysis.

Valérie Laurent, Michael Schaepman and Jörg Weyermann wrote the manuscript.

4.3.1. Abstract

Leaf area index (LAI) and chlorophyll content (Cab) are important vegetation variables which can be monitored using remote sensing (RS). Physically-based approaches have higher transferability and are therefore better suited than empirically-based approaches for estimating LAI and Cab at global scales. These approaches, however, require the inversion of radiative transfer (RT) models, which is an ill-posed and underdetermined problem. Four regularization methods have been proposed, allowing finding stable solutions: 1) model coupling, 2) using a priori information (e.g. Bayesian approaches), 3) spatial constraints (e.g. using objects), and 4) temporal constraints. For mono-temporal data, only the first three methods can be applied. In an earlier study, we presented a Bayesian object-based algorithm for inverting the SLC-MODTRAN4 coupled canopy-atmosphere RT model, and compared it with a Bayesian LUT inversion. The results showed that the object-based approach provided more accurate LAI estimates. This study, however, heavily relied on expert knowledge about the objects and vegetation classes. Therefore, in this new contribution, we investigated the applicability of the Bayesian object-based inversion of the SLC-MODTRAN4 model to a situation where no such knowledge was available. The case study used a 16 × 22 km2 simulated top-of-atmosphere image of the upcoming Sentinel-2 sensor, covering the area near the city of Zurich, Switzerland. Seven APEX radiance images were nadir-normalized using the parametric Li–Ross model, spectrally and spatially resampled to Sentinel-2 specifications, geometrically corrected, and mosaicked. The atmospheric effects between APEX flight height and top-of-atmosphere level were added based on two MODTRAN4 simulations. The vegetation objects were identified and delineated using a segmentation algorithm, and classified in four levels of brightness in the visible domain. The LAI and Cab maps obtained from the Bayesian object-based inversion of the coupled SLC-MODTRAN4 model presented realistic spatial patterns. The impact of the parametric Li–Ross nadir-normalization was evaluated by comparing 1) the angular signatures of the SLC-MODTRAN4 and Li–Ross models, and 2) the LAI and Cab maps obtained from a Li–Ross nadir-normalized image (using nadir viewing geometry) and from the original image (using the original viewing geometry). The differences in angular signatures were small but systematic, and the differences between the LAI and Cab maps

increased from the center towards the edges of the across-track direction. The results of this study contribute to preparing the RS community for the arrival of Sentinel-2 data in the near future, and generalize the applicability of the Bayesian object-based approach for estimating vegetation variables to cases where no field data are available.

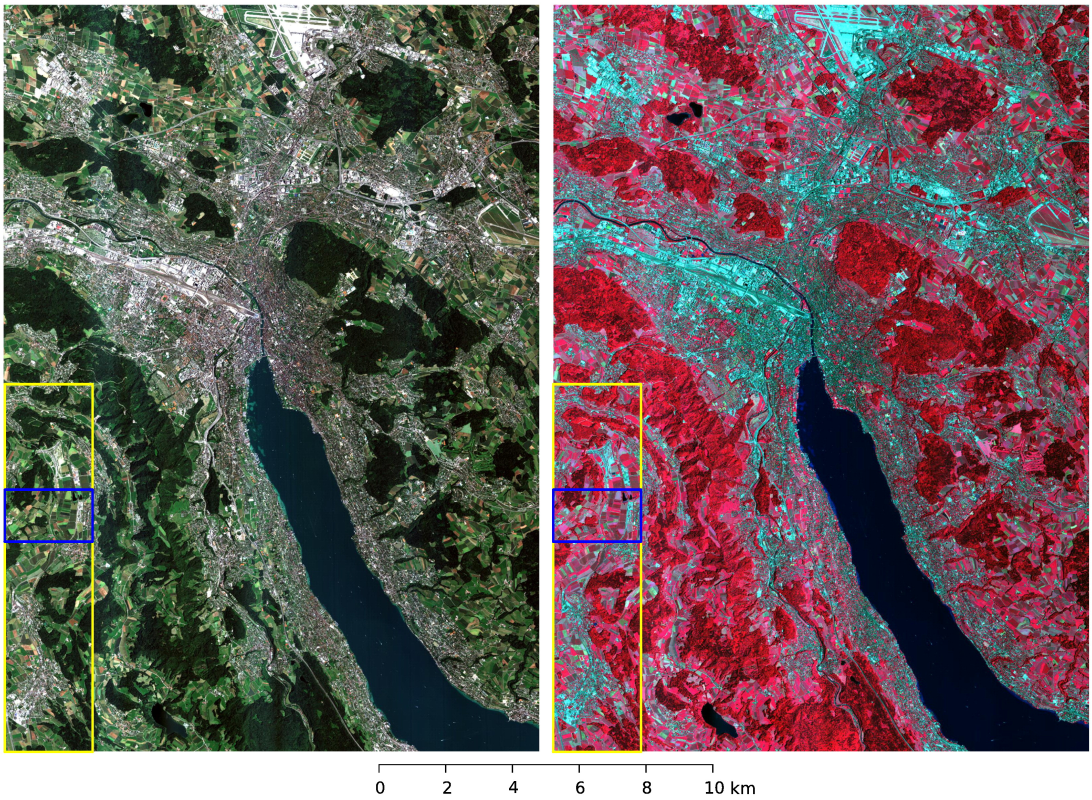

Figure 4.6.: True (R: band 4, G: band 3, B: band 2) and false (R: band 8, G: band 4, B: band 3) colour composites of the simulated Sentinel-2 image with 10 m resolution. The blue rectangle indicates the area used for Figs. 2 and 4 (not shown in this manuscript), and the yellow rectangle indicates the area of FL9 used for Fig. 4.8.

4.3.2. Earth System Science context

The Earth's biosphere has considerable influence on the global carbon cycle and, as consequence, on the climate. Mapping relevant biochemical and structural properties of vegetation surfaces in a spatial and temporal continuous manner is inevitable for monitoring the factors driving the processes. Spaceborne remote sensing has evolved as the tool of choice for global monitoring tasks, and the upcoming Sentinel-2 sensor offers challenging opportunities due to its spectral and spatial setup. The present scientific contribution thus has both methodical and data-driven objectives by presenting a novel processing scheme on simulated data from an upcoming instrument.

4.3.3. Imaging Spectroscopy data

The data for this study consist of seven APEX IS flight lines that were spectrally and spatially processed according to the Sentinel-2 specifications. Ross-Li modeling and correction as discussed in this thesis was performed on the APEX data in full spatial and spectral resolution, while the rescaling and resampling was done later.

The assessment focused on crop fields with four different types. Basic surface parameters are compiled in Table 4.1.

Table 4.1.: A priori mean, standard deviation, minimum and maximum values of the canopy and green leaves variables for the four vegetation classes.

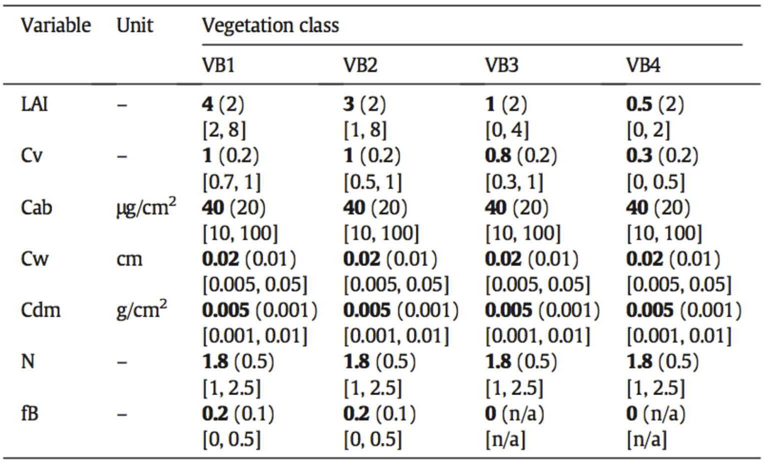

Variable	Unit	Vegetation class			
		VB1	VB2	VB3	VB4
LAI	–	**4** (2) [2, 8]	**3** (2) [1, 8]	**1** (2) [0, 4]	**0.5** (2) [0, 2]
Cv	–	**1** (0.2) [0.7, 1]	**1** (0.2) [0.5, 1]	**0.8** (0.2) [0.3, 1]	**0.3** (0.2) [0, 0.5]
Cab	μg/cm^2	**40** (20) [10, 100]	**40** (20) [10, 100]	**40** (20) [10, 100]	**40** (20) [10, 100]
Cw	cm	**0.02** (0.01) [0.005, 0.05]	**0.02** (0.01) [0.005, 0.05]	**0.02** (0.01) [0.005, 0.05]	**0.02** (0.01) [0.005, 0.05]
Cdm	g/cm^2	**0.005** (0.001) [0.001, 0.01]	**0.005** (0.001) [0.001, 0.01]	**0.005** (0.001) [0.001, 0.01]	**0.005** (0.001) [0.001, 0.01]
N	–	**1.8** (0.5) [1, 2.5]	**1.8** (0.5) [1, 2.5]	**1.8** (0.5) [1, 2.5]	**1.8** (0.5) [1, 2.5]
fB	–	**0.2** (0.1) [0, 0.5]	**0.2** (0.1) [0, 0.5]	**0** (n/a) [n/a]	**0** (n/a) [n/a]

4.3.4. Methods: Correction of reflectance anisotropy effects

The following sections (without headings) are cited from the publication:

Evaluating the effects of the parametric nadir-normalization

There is a conceptual issue when using a parametric RT model, like the Li–Ross model, to normalize the radiance data to nadir viewing, and then estimating the variables from the nadir-normalized data using a physically-based RT model, like the coupled SLC-MODTRAN4 model. Indeed, the radiance values are corrected to nadir-viewing according to the angular behavior of the parametric model, which may differ from that of the physically-based model, and therefore reduce the performance of the inversion of the physically-based model. First, the discrepancy between the Li–Ross and SLC-MODTRAN4 angular signatures was investigated, and second the impact of the Li–Ross nadir-normalization on the LAI and Cab estimates was evaluated. These two analyses were performed at APEX flight height, before applying Eq. (1). The results are easily transferred to TOA level, because the TOA radiance is a linear transformation of the radiance at APEX flight height (Eq. (1)). The westernmost image (flight line 9, FL9) was selected because it had the most vegetation. The solar zenith angle for FL9 was 34.7° and the solar azimuth angle was 122.7°. MODTRAN4 was run in advance, between the average altitude of the study area and the APEX flight height, for viewing zenith angles (VZA) between $-14°$ and $+14°$ (APEX FOV) in steps of 2°. The outputs were stored in an atmospheric database. Positive VZA values indicate viewing directions opposite to the sun (forward direction).

Angular signatures

The angular signatures simulated by the SLC-MODTRAN4 and Li-Ross models were compared for the four vegetation classes for the four 10 m bands of Sentinel-2. For each class, the SLC-MODTRAN4 was run using the default parameter values (Table 2) and the a priori values (Table 3), for each of the 1000 across-track APEX pixels, interpolating the MODTRAN4 outputs from the atmospheric database. The obtained angular signatures were then fed to the Li–Ross nadir-normalization algorithm (see Section 2.2). The kernels and associated weights chosen by the algorithm were then used to simulate the Li–Ross angular signatures.

4.3.5. Results: Comparing Li-Ross and SLC angular signatures

Effects of the parametric nadir normalization on angular signatures

For the Li–Ross simulations, the nadir normalization algorithm selected the same kernels for all four vegetation classes and for all four 10 m resolution bands: Ross-thin for the volumetric scattering and Li-dense for the geometric scattering (see Section 2.2). For all bands and vegetation classes, the spectral profiles of the kernel weights were similar (not shown). The weights of the isotropic scattering kernel were the highest, while the weights of the geometric kernel were close to zero, and the weights for the volumetric kernel were negative.

The relative differences between the Li-Ross and SLC-MODTRAN4 angular signatures for the four 10 m resolution bands are presented in Fig. 4.3.5. The difference curves for all four vegetation classes present the same sinusoidal shape for the four bands, revealing systematic differences between the two models. The Li–Ross simulations were lower than the SLC-MODTRAN4 simulations for $\mathrm{VZA} < -11°$ and for $\mathrm{VZA} \in [1°, 12°]$, and higher than the SLC-MODTRAN4 simulations for $\mathrm{VZA} \in [-11°, 1°]$ and $\mathrm{VZA} > 12°$. The Li–Ross simulations therefore differed from the SLC-MODTRAN4 simulations for nadir viewing. For the VB1 and VB2 vegetation classes, the relative differences were lower in the NIR than in the visible bands, whereas for the VB3 and VB4 vegetation classes, the relative differences were lowest in the red bands. All absolute difference values were smaller than 0.15 mW/(m2 sr nm) in absolute value.

Effects of the parametric nadir normalization on products

The LAI, Cab and cost maps obtained from the NN and OG approaches (not shown) had R2 values of 0.96 for LAI, 0.98 for Cab and 0.93 for the cost, showing a good consistency between the two approaches.

The maps in Figure 4.8 show the spatial distribution of the differences. The objects are much more visible on the LAI and cost difference maps than on the Cab difference map, which appears more scattered. For all three maps, as expected, the differences are smallest in the across-track center of the image, and increase towards the edges. The highest LAI differences are found in objects having very high structural complexity (VB1, very low brightness in the visible), where LAI values are higher. The spatial

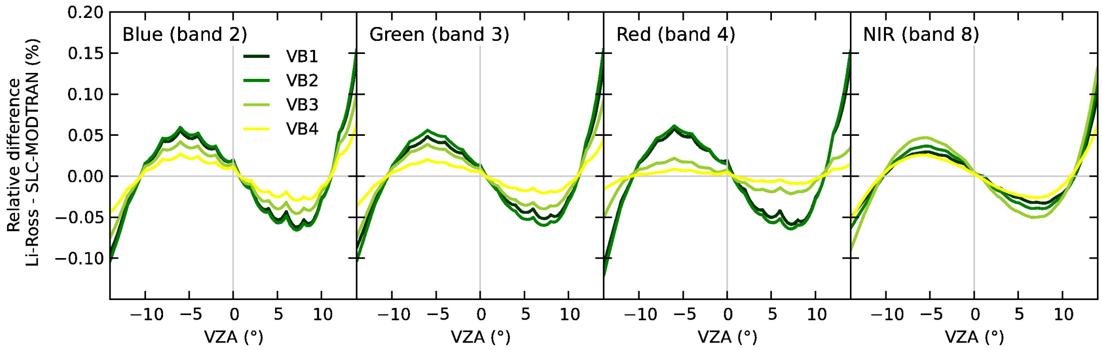

Figure 4.7.: Relative difference between the Li–Ross and SLC-MODTRAN4 angular signatures for the four 10 m bands and for the four vegetation classes.

pattern of very high cost differences roughly follows the pattern of the VB1 and VB2 objects.

4.3.6. Discussing Li-Ross and SLC angular signatures differences

Both Li–Ross and SLC-MOSTRAN4 models are simplified representations of the BRDF effects. In the parametric Li–Ross model each wavelength is treated independently, which may result in different kernels and kernel weights for each band, whereas the physically-based SLC-MODTRAN4 model uses the same values of the canopy parameters for all bands. In addition, the volume scattering component of the Li–Ross model is based on the assumption of a spherical LIDF and equal leaf reflectance and transmittance. The latter assumption is better satisfied in the NIR than in the visible domain, so one would expect smaller angular deviations between Li–Ross and SLC-MODTRAN4 in the NIR than in the visible bands. This expectation was only fulfilled for the VB1 and VB2 vegetation classes. The deviations between the SLC-MODTRAN4 and Li–Ross model were expected to be small because the spherical LIDF assumption used in the Li–Ross volumetric scattering component matches the spherical LIDF used for defining the vegetation classes (Table 2). Although the deviations between the two models were small in radiance units, they were systematic, which might be due to the much smaller number of degrees of freedom of the Li–Ross model.

These systematic deviations may have impacted the quality of the nadir-normalization of the APEX images. The main limitation, however, was that the changes in solar geometry over the two-hour acquisition period were not accounted for in the Li–Ross BRDF correction algorithm. This explains the trend of increasing brightness from the east to the west (Fig. 1) of the Sentinel-2 mosaic. Another important issue is that the nadir-normalization algorithm relies on a 5-classes land cover classification, only two of which concerning vegetation. This implies that the quality of the results depend on the spatial distribution of pixels of each class over the sensor's FOV. If observations of a scattering type are rather sparse and not well distributed over the FOV, the Li–Ross kernel weights can be less stable and correction may become less reliable. Another interfering effect is caused by topography, which is not accounted for in the algorithm. The brighter vertical stripe in the western part may be due to a combination of the described uncertainties. The Li–Ross BRDF correction cannot distinguish between the anisotropy of the surface and that of the atmosphere, and therefore corrected them both simultaneously. This is consistent with the nadir viewing convention used for creating the simulated Sentinel-2 image. Enhancements on the BRDF correction approach are subject to current work. A more robust correction could be achieved by inverting the model on a set of observations generated from several flight lines if not from all. Applying different error metrics than least-RMSE for the inversion process, e.g. the least median of error squares (Susaki et al. (2004)) or least variance of white-sky albedo (Gao et al. (2001)) could further enhance the quality of the mosaic.

A deeper discussion of the anisotropy effects in agricultural fields and their correction can be found in the synthesis chapter.

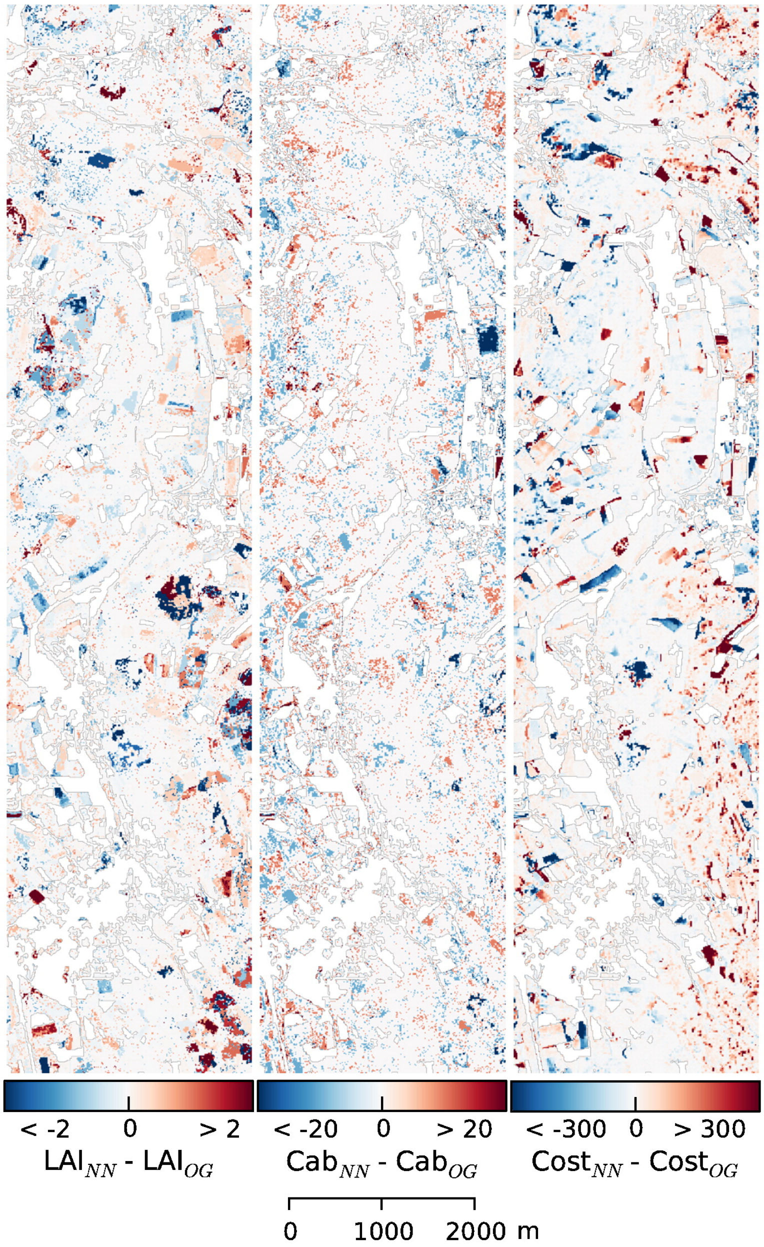

Figure 4.8.: Maps of the difference between the LAI, Cab, and cost obtained from the NN and OG approaches for the south part of FL9 (area in the yellow rectangle of Fig. 4.3.1). Blue colors indicate areas where the NN approach gave lower values than the OG approach.

5. SYNTHESIS

5.1. Main results and discussion

Main results of this dissertation are summarized and discussed in this chapter, following the research questions in the order of their introduction in the research outline.

5.1.1. Method development

As outlined in chapter 1.6 on page 9, I discuss first the four research questions related to method development:

Research question 1: What is the impact of reflectance anisotropy on remotely measured single observation HDRF data and empirically and physically based vegetation products?

This question is answered here separatly for the reflectance data and derived products part:

HDRF data: the sensitivity of HDRF data to reflectance anisotropy was found to be wavelength dependent, as often described in literature. The magnitude of this sensitivity depends on structural and biochemical surface properties, thus is different for each of the declared (distinct) surface types. In the analyis, the focus was placed on the two vegetation structural types (simple type, like meadow or crops, and complex type like forests). While different in magnitude, the shape of angular effects was very similar for both types. The HDRF variability was moderate in the VIS, decreased in the NIR and reached its maximum in the SWIR.

For the simple scattering type, the HDRF variation before correction ranged from 37% in the VIS to 80% in the SWIR (close to 2500 nm wavelength) with an average of about 50%. HDRF variation was higher for the complex structured type. Before correction, it ranged from 56% in the VIS–NIR to 80% in the SWIR (in the region between 2000 and 2500 nm), with an average of about 65%.

The results concerning the impact of reflectance anisotropy on HDRF data were found to be basically consistent with results found in literature. The increase in multiple scattering in the NIR decreased the magnitude of angular effects, an observation which could be made for both vegetation scattering types. It has stronger effect, however, in the complex vegetation where more intense multiple scattering is possible. Multiple scattering as such brightens shaded fractions of pixels and thus impacts the geometric-optical scattering regime. The reasons for discontinuities in the graph on HDRF variability (Fig. 2 in the publication) are not completely clarified. Possibly they are subject to an inappropriate (too large) observation scale compared to the Ross-Li kernel definition.

Products: as expected, the sensitivity to reflectance anisotropy depends on the individual product. The (across-track) shape of anisotropy, according to HDRF data, was generally comparable between the products. Comparing the index-based products, with the exception of ARI1, the anisotropy was found to resemble a tilted bell-shaped curve with the maximum shifted toward the forward-scattering direction. The ARI1 anisotropy gradient, in contrast, was slightly bowl shaped. SRI and NDVI anisotropies were larger in the case of the simple scattering type, while SIPI and ARI1 angular dependence was considerably larger in the case of the complex scattering type. The across-track variation of SRI for the complex scattering type derived from uncorrected HDRF values ranged from 8% in the forward- to 17% in the backscatter direction. NDVI was comparably robust to reflectance anisotropy (1% to -3%), while SIPI showed nearly no angular dependence. ARI1 was most sensitive to reflectance anisotropy with deviations ranging from 59% in forward scatter to -39% in backward scatter direction, for the complex type. For the simple scattering type, deviations were considerably lower (20% to −33%).

The PROSPECT/SAIL (physical-based) inversion products CAB, CW and CDM showed generally higher sensitivities than those based on spectral indices. These products were calculated on the simple structural type only. Across-track variation ranged from 58% (CW) up to 155% (CDM). Taking the results of the statistical test into account, CW featured the highest uncertainty caused by angular effects and CDM the lowest. This conclusion can be drawn from the very high standard deviation of the CW across-track profile. The shape of CAB and CW anisotropies retrieved from uncorrected data was comparable, while across-track changes of CDM were different, and considerably higher in the extreme backscatter direction. LAI showed a somewhat special behavior with respect to the angular dependence. Directional effects caused LAI overestimation up to 22% in backscatter direction, while the remaining biochemical vegetation products usually had lower values in the backscatter than at nadir.

Differences in index product angular behavior could be directly explained with mathematical properties of the explicit formulae, which either balanced (for NDVI, SIPI) or amplified (SRI, ARI) angular effects of the individual spectral bands from which the index is designed. In the case of the ARI1 index calculated on complex structured vegetation, it was additionally the changing ratio of photosynthetic and non-photosynthetic vegetation, which had a strong impact. This is a general problem when indices designed for leaf level are applied to canopy reflectance data.

Research question 2: To which degree can the view-angle effects be reduced with the Ross–Li model?

Again, different answers are provided for the HDRF data and the products part of the question:

HDRF data: the Ross–Li correction was able to considerably reduce the across-track HDRF variation for both scattering types by about 50% (averaged over the wavelength range). The correction was more effective in the visible range, where the uncertainty was reduced by more than 80%. However, HDRF still varied notably after correction (compare Figure 2 of the original publication). The reason for this was found in the evaluation methodology rather than in weaknesses of the correction method itself: the results express the combined effect of two factors: 1) changes in view angles, and 2) structural and biochemical differences of species subsumed in one structural type.

Products: Ross-Li was able considerably to reduce the effects of reflectance anisotropy. Remaining across-track variations were in the order of a few percent for both scattering types. This is valid also for the PROSPECT/SAIL products. In this case remaining uncertainties after correction were around of 5%, with the exception of CDM. However, CDM (and LAI results, too), should be treated with caution because of the very high standard deviation. In general, differences in the effectiveness of the Ross-Li method were observed between the scattering types, potentially indicating non-physical kernel weighting. This would effectuate that one of the components (either volume, or geometric-optical scattering) was overrated in the Ross-Li model, suppressing the impact of the other component.

For most aNBAR-derived products, the across-track variation complied with the gradient retrieved from the Hy-WE (perpendicular flight line), which was used as a reference. The Ross-Li method was therefore found to be well suited to correct for the effects of reflectance anisotropy in the investigated data.

As airborne data are acquired employing only a single observation per view angle, data have to be aggregated to simulate a multi-angular scenario, which is required for modeling the BRDF. Research question 3 deals with the methodology and impact of the surface stratification:

Research question 3: How is the surface to be stratified to enable application of the Ross-Li model?

Ross-Li is a well-tested and thus established approach for modeling reflectance anisotropy of natural surfaces in the optical domain. It was, however, developed for true multi-angular observations (spaceborne, repeat-pass), at a larger spatial scale (i.e., spatially larger pixels). The method was evaluated to be reliably applicable to airborne imaging spectroscopy and even ALS systems. For successful application to airborne optical systems (“mono-angular” configuration), the stratification of the surface was identified both as critical and non-trivial.

The goal of any surface stratification in the context of anisotropy correction is to compose surface reflectance observations (or scale-bound: pixels of data) sharing an equal scattering regime with the largest possible variation in observation and illumination geometry. As scattering types are not directly deducible from the data, a different separating criterion (spectral, textural, object-based, hybrid) needs to be chosen to generate the collection of angular observations. In the discrete case, specific classes then will act as proxy for scattering types. The separation into scattering types is not sufficient, as will be discussed below in more detail. Classes, however, have to be defined carefully bearing two aspects in mind: they need to cover the large majority of scattering types present in the scene, while at the same time assuring sufficient angular coverage for each scattering type. Classification needs to assure that enough angular observations can be employed for anisotropy statistics. Thus, granularity is a critical issue. This implies that some form of “generalization” of all possible “real-world” scattering mechanisms must take place, and only per-class average anisotropies can be measured and corrected for.

Vegetation structural types will be discussed first. Figure 4 of Chapter 3 gives evidence that the effective anisotropies of different structural vegetation types can be quite similar. The question arises whether there needs to be a separation of these structural types at all. A quick answer can be given as 'it depends', but the derivation of possible consequences of not implementing this separation is not straight-forward. The empirical part of the Ross-Li model performs essentially a fit to observations, driven by "unsupervised" a-priori knowledge on the equality of the (subpixel) scattering regime of individual pixels (incorporated into the classification). Ross-Li measures and inverts gradients in spectral reflectance, assuming that these gradients are only driven by changes in observation and/or illumination geometry. Changes in the across-track spectral reflectance which are NOT deducible from angular effects thus need to be handled by the classification, i.e. by separating the surface type in more types, even if their scattering properties (and thus: angular effects) are largely comparable. An extreme case is presented in the following (theoretical) experiment:

An airborne spectroscopy dataset has been recorded over deciduous forest where only two different species are present, growing in homogeneously high tree density, with only few cast shadow present. One species features (visually) very bright leaves, the other very dark ones. The majority of 'bright' trees is located in the backward-scattering direction of the flight line, the majority of 'dark' trees in the forward scatter. This configuration will increase the typical anisotropies for vegetated surfaces over a scanner's FOV. The general structure of the two tree species, which forces the scattering regime, is comparable. If biochemistry, which has additional impact on spectral leaf optical properties, is neglected, a single structural scattering class seems appropriate for the whole flight line. Ross-Li will then invert on this set of observations with the given angular geometry and generate kernel weights that best fit the observed gradient. This gradient, however, does not reflect the pure anisotropies, but rather represents a biochemically forced gradient, superimposed by reflectance anisotropy effects. In comparison, Ross-Li will produce a different kernel weighting if only the pure gradient derived from anisotropy had been given as input. This effect will produce uncertainty in the quality of the correction predominantly in the visible range.

The advantage of the semi-empirical concept is that the possible error associated with this type of "empirical uncertainty" is very much limited by the physically-derived core of the Ross-Li model. Ross-Li will only model anisotropies that are physically reliable, as it is hard-coded in its kernels. This is the major advantage of a semi-empirical model, as opposed to a purely empirical fit to observations using e.g. a polynomial. This small case study emphasizes the importance and responsibility of the classification to not only account for structural but also biochemical properties of the surface, at least in the case of photosynthetically active vegetation.

These conceptual ideas are implemented in the separation of complex and simple structured vegetation as developed in Chapter 2, while an important concept of the Ross-Li model is additionally taken into account. The two vegetation structural types often (but not necessarily) feature differences in the 'brightness' in the spatial scale in which they are employed as valid observation (due to the inclusion of shadowing effects, following the homogeneity criterion). Therefore, complex structured vegetation like forests of deciduous or coniferous type or shrubs often appears visually darker in remote sensing data than simple structured vegetation like meadow and crops. Calling to mind again the point made by the imagined set-up of the case(-study) outlined earlier, with only two species of trees growing in a homogeneously dense forest, this is the first reason why vegetation should be separated in the surface stratification. In addition, complex structured vegetation, independently of the horizontal homogeneity or density, will show more complex patterns of photon scattering, driven by the orientation distribution of scattering facets (=leaves), their individual transmissive properties, and the total height of the scattering layer. Conceptually, the complex pattern of scattering occurring in a layer of scattering facets is referred to as 'volume scattering'. Contributions to the overall anisotropy by this type of scattering are captured by the volume-scattering kernel adopting Ross's theory and radiative transfer approximation. The complex vegetation type is expected to show a different volume scattering behavior (thus volume scattering kernel weight) as compared to the structurally simpler type. Practical experience has shown, however, that the kernel weights do not differ extremely. A reason for this is that there is only a single counterpart balancing the anisotropy caused by a dominant volume scattering regime: the influence of subpixel surface-scattering effects. Depending on the effective structural properties of the simple vegetation type, the anisotropy of which can also be considerably controlled by shadow casting, the final ratio of volume/geometric optical scattering can be comparable. Ross-Li does not give absolute numbers, it rather models the weighting of two different scattering mechanisms. Therefore, the weight of the volume scattering kernel does not necessarily increase with a larger volume of scattering facets, it will rather be adjusted to be appropriate to the impact of subpixel surface scattering and shadow casting (the geometric-optical kernel weight).

The third important surface type to be separated is soil. Again, from Figure 4 of Chapter 3 it becomes evident that soil features an anisotropy pattern other than vegetation, controlled predominantly by geometric-optical surface scattering effects like micro-scale shadow due to the 3d structure of the soil compartments which are clumped together. Separating soil from vegetation can be done easily with any classification algorithm - it is rather a conceptual issue to decide how much vegetation on a given crop field is still acceptable for the field to be classified as soil and not vegetation. A focus-driven answer should be: as long as the anisotropy of a soil with vegetation cover still follows the typical pattern of soil anisotropy it must be treated as soil. This, however, is difficult to decide. Leaving the decision of a threshold to the classifier is the practical but potentially unphysical solution. In case of an enforcement of distinct surface classes (which we discuss here) the classification bears the risk of a fragmented solution, which means that a rather homogeneous surface can be partitioned in two different classes when the impact of vegetation is close to the selected threshold.

Research question 4: How can the Ross-Li model be used with a continuous field surface stratification to avoid spatial artefacts in the corrected solution?

In the discussion for Publication 1 it was mentioned that a classification into distinct surface classes bears the risk of producing a fragmented solution. This phenomenon, while not quantified, was observed several times in a visual representation of the corrected data. A continuous description of the surface is a solution to mitigate this potential problem. As described in Chapter 3, the surface can be described by a composition of an arbitrary number of surface cover types (or technically: spectral endmembers). Each of the predefined cover types can theoretically have abundance from 0 to 100%, and the sum of abundances is again 100% for each pixel. This allows to decompose the angular signature of a single pixel into component angular signatures, where Ross-Li is used to model anisotropies for each pure component. The final anisotropy factor estimated for a pixel is then defined as the fraction of each component contributing to this pixel multiplied with their individual anisotropy factor. The major advantage of a continuous description of the surface is the ability to deal with the situation of two interfering surface structural/spectral types both contributing to the total anisotropy with considerable fraction. This strategy - while introducing minor uncertainty in the context of unmixing reliability - removes large uncertainties as introduced with a distinct classification. For two components with contrasting anisotropies about equally mixed, the resulting anisotropy should be somewhere between the component angular signatures. So even if the abundances are estimated with a 10% uncertainty this is more accurate than accepting a 50% error because the pixel can be assigned to only one of the two contributing types.

The quality of unmixing was already mentioned in the discussion of the publication itself. It will strongly depend on the effective set of spectral endmembers, which is basically transferable between different datasets, but will most likely not generate results of equal quality, depending on the pre-processing and thus spectral quality of data. The applicability of a generic set of spectral endmembers for this purpose should be subject to further research.

It is yet to be mentioned that anisotropy correction using the weighting of component angular signatures follows a linearity assumption, which was never systematically evaluated. It is most likely that a mixed soil-plus-vegetation BRDF is not exactly equal to pure soil BRDF plus a vegetation BRDF. A sensitivity study on this subject would be hard to perform on real imaging data because of the number of observations needed and for validation reasons, but could be realized with data simulated with e.g. a radiative transfer model like DART.

There are other influences that cannot be compensated appropriately with the classification (distinct or continuous), nor with the Ross-Li model itself, e.g. spectral across-track brightness differences due to topographic effects, while independent from the surface cover. This example is roughly in line with the one given above with two differently bright tree species of otherwise similar structure. Topographic effects that modify reflectance factors of equal surface type depending on the slope and aspect need to be treated separately, either topography first and then reflectance anisotropy with the assumption of a level surface, or even iteratively.

To measure the effectiveness of the proposed correction scheme, the per-plot average differences before and after correction were calculated in the overlapping area of two co-registered flight lines. Reflectance values in selected wavebands in the blue, green, red and NIR region (λ = 461.1 nm, 551.5 nm, 621.6 nm and 811.3nm) were compared. In addition, the analysis was carried out on the ARI1 and NDVI product.

Throughout the products and spectral bands, the per-plot differences could be reduced with the Ross-Li method by 60% to 75%.

5.1.2. Application oriented studies

Research questions 5-7 relate to the application oriented research articles as presented in Chapter 4 on page 34. These studies systematically evaluate the benefits and limitations of the presented Ross-Li compensation method on different land surface types. The first research question in this context (research question 5) deals with a forest type and is phrased as follows:

Research question 5: Is the Ross-Li model capable of modeling anisotropy effects in forest data for enhanced estimation of ecosystem health?

In order to model reflectance anisotropy effects on surfaces highly structured in 3-d (like the forest stand subject to this publication), two aspects need to be taken into account carefully: the "homogeneity criterion" inherent to the Ross-Li model, and the general treatment of shadows associated with the homogeneity criterion:

Homogeneity criterion A major criticism on the application of the Ross-Li method on high spatial resolution IS data had been the obvious violation of the homogeneity criterion inherent to the Ross and Li theories. This is especially the case for surfaces with scattering-effective geometric structures horizontally and/or vertically larger than the GIFOV of the sensor. The model assumes a normal distribution of relevant scatterers within a pixel, and this is not given in forest structures and a sensor GIFOV of about 2-3 meters.

The argument to apply Ross-Li regardlessly of this violation according to specification is rooted in the way angular observations are composed. Homogeneity is implicitly generated by averaging angular observations of forest pixels composed of illuminated and shaded canopy fractions, capturing all possible illumination states. This has an effect similar to inverting Ross-Li on spatially downscaled data, which do fulfill the homogeneity criterion from the outset. Furthermore, a minimum number of observations per view angle unit (a 'column' in a flight line image, usually) was defined for each surface structural type. E.g., at the APEX GIFOV of 3 meters, we fixed the number of observations required to fulfill the homogeneity criterion to be 100 for forest (a patch of e.g. 30 by 30 meters) and 10 for crops, soil and other surfaces. When this number is not reached no observation is assumed at that angular position. The effective number of angular observations in a typical IS dataset, however, is usually much higher for the majority of angular positions.

Treatment of shadows From the rationale of the previous section it becomes obvious that we correct for the *average* impact of reflectance anisotropy in forested areas, and apply correction to illuminated and shaded pixels. This strategy has been found to work well, visually. But the approach is negotiable: another option would be to only treat the (fully) illuminated forest pixels, or to try to estimate shadow fractions and then treat shaded and illuminated forest pixels appropriately. Dealing with (partly) shaded pixels in terms of reflectance anisotropy requires modeling the complete illumination field, making a separation into fractions of direct and diffuse illumination inevitable. This information is basically accessible in reflectance data for each pixel as it can be derived from atmospheric correction by-products. There is a fraction of diffuse illumination that contributes to the overall anisotropy, the directionality of which would need to be modeled for proper correction of angular effects in fully or partly shaded pixels.

Research question 6 deals with the application of Ross-Li to a fresh snow surface. This application can be regarded as a rather "exotic" application, not only with respect to the surface type but also the data source, which was airborne laser scanning data with their associated typical scanning geometry. The research question was defined in Chapter 1.6 as follows:

Research question 6: Can the Ross-Li model be used to reduce reflectance anisotropy effects of snow in airborne laser scanning data?

Application to ALS data over snow touches several aspects critical to the Ross-Li concept. Firstly, the model was developed for vegetation surfaces and those featuring a scattering regime driven by vegetation-similar structures. Few studies only reported on application to snow, and if, anisotropy effects of larger structures of otherwise homogeneous snow in combination with a broad range of angular geometries were investigated. This study was conducted on a glacier with considerable differences in altitude within the test area so that the snow properties driving the anisotropic behavior (e.g., snow grain size) changed from lower to higher altitudes, and potentially also with the exposition. Secondly, the intensity of reflected light from an active laser scanning system was evaluated. Such a system records emitted pulses of light from a location very close to the point the pulse was sent out. This has implications for the possible angular range of illumination/observation. Only a single relative azimuth angle (of value zero) can be exploited, meaning that observations can only be made in the backscatter. The ALS geometry represents the rare case of what is generally called 'hotspot' observation in passive optical remote sensing. No shadows on the ground can be observed when the illumination source resides at the exact same location as the observer. The only geometric variable that Ross-Li can use to model anisotropies is the local slope of the surface, relative to the pointing vector of the ALS.

The shape of the anisotropy could be well modeled by Ross-Li. The uncertainty arising here is comparable to the selection of an inappropriate kernel as discussed in Section 5.1.3. A good fit to data does not necessarily mean that the relevant mechanisms of scattering are appropriately captured in the model. This is in particular the case when a model is applied that was not developed for the given application. Potential uncertainties originating from earlier processing steps (like the range, PRF, or atmospheric correction) might still be included in the data but representative only for the limited area where Ross-Li was trained on. This limits its transferability to other (lower, or differently exposed) regions on the glacier with potentially different snow properties and thus, different anisotropies. The only partly satisfactory correction result for the whole dataset can be deduced from the mentioned model incapabilities with respect to snow.

Research question 7 focuses on the application of the Ross-Li model to agricultural fields. Furthermore, the work was performed on APEX data at radiance level so that atmospheric anisotropies are incorporated in the data. The research question is defined as follows:

Research question 7: Is the Ross-Li model suited to minimize reflectance anisotropy effects on high-resolution radiance data in order to simulate a Sentinel-2 top-of-atmosphere calibrated radiance image?

This publication covers two side aspects of the Ross-Li model: i) its inversion on radiance data and ii) a comparison of calculated anisotropies with a physical model. Collectively, the study can be considered as a validation of the Ross-Li method. To achieve a systematic comparison of the model performances, firstly, angular signatures of 4 different vegetation types were simulated with the SLC-MODTRAN4 code using a structural and biochemical description of the surface (cf. Table 4.1 for reference), the APEX sensor parameters and the effective illumination geometry. This led to a set of synthetic angular observations for the four vegetation types. Secondly, the Ross-Li model was inverted on these angular observations, calculating its own parametric angular signatures. In a last step, the reproducibility of the SLC-MODTRAN simulated angular signatures with the Ross-Li model could be compared.

Applying the Ross-Li model to radiance data is a valid pathway; there is no requirement to remove atmospheric effects prior to model application. Some issues are to be mentioned, though.

At the time of writing this publication the BRDF processing software (written by the author of this thesis) was technically only able to process flight lines individually, without taking angular observations from other sources (e.g. adjacent flight lines) into account. This was a major limitation, which manifested itself in the BRDF correction quality for this publication. The fact that radiance and not reflectance data were used increased the potential error. While the intensity of reflected light in reflectance data (reflectance factor) is normalized over the incoming light intensity this is not the case in radiance data, making it show distinct diurnal variations. Such variations appear in the data for this study, because flight lines were acquired with a time delay of two hours from the first to the last recording. However, observed variations had served as an additional source of information in this context to provide a more stable Ross-Li parameterization. The brightness gradient visible in across-track should have been eliminated by this procedure, if it had been technically possible. Such a mechanism was later implemented in the BRDF correction software and and has since repeatedly been applied successfully. It allowed not only to take an arbitrary set of observations (including external) as input for Ross-Li inversion, but also to reliably normalize to a solar zenith angle different from that of the flight line subject to correction. Nevertheless, it is advisable to choose an output solar zenith angle which is in the range of input zenith angles of all observations (as opposed to one requiring extrapolation).

It is, however, controversial whether the effect previously described is a 'valid' effect to be corrected by Ross-Li in radiance data, as the general trend for higher reflected light intensity at smaller solar zenith angles (deviations from nadir) is effectuated by the role that diffuse illumination plays against the direct component. BRDF effects are different in radiance and reflectance data while the surface is exactly the same as is the illumination and observation geometry, and Ross-Li does not explicitly account for the anisotropy of diffuse illumination. Ross-Li must model these differences as different weighting between volume- and geometric-optical scattering, which does not make sense physically. It would be worth evaluating these effects in radiance and reflectance data systematically in the future.

A subquestion instantly arising from the content of this work is how the Ross-Li model performs compared to the physical SLC/Modtran model combination in the anisotropy correction of different crop types. Comparing their individual angular signatures evidenced small but systematic differences. Besides the reasons already mentioned in the paper discussion section, these differences might be directly associated with different impact of the atmosphere, the anisotropy of which is implicitly included in the Ross-Li correction, while atmospheric conditions based on a standard atmosphere are assumed in the Modtran part of the coupled physical models.

The discussion leads to an important aspect of combined usage of (semi-) empirical and physical parameter retrieval usage in remote sensing data analysis. As already mentioned in the publication conclusions, one should avoid applying an empirical or semi-empirical transformation to data when they should be further analyzed using physical models, which do have the capability to model angular effects more accurately by physical equations. Empirical transformations might corrupt the data by forcing them to fit over-simplified models.

5.1.3. Ross-Li: general aspects

This section covers several aspects of the Ross-Li semi-empirical model that are common to all studies presented so far, and cannot be targeted to a certain application type.

The role of the kernel selection

For both the volume scattering and geometric optical scattering two different kernel implementations can potentially be employed to model the reflectance anisotropy (compare Section 1.5). The approach followed in the publications in Chapters 3 and 2 is to let an RMSE criterion on measured vs. modeled observations decide on the final kernel combination to be used. Different kernels were developed for different surface structural characteristics, e.g. for dense/sparse vegetation canopies and high/low values of LAI. This implies that - when such information on the surface is available - this information should be used for a-priori kernel selection. This would be physically reasonable, as a better fit to observations does not necessarily mean that the anisotropy is corrected more effectively. In the contrary, selecting an inappropriate kernel bears the risk that effects are corrected that do not originate from reflectance anisotropy, like those mentioned in the previous section. For example, the Ross volume scattering kernels for thin and thick vegetation imply different assumptions on the reflectivity of the ground, the anisotropy of which must (in case of improper kernel selection) then be captured by the geometric scattering kernel. Even if the anisotropy as defined in the set of observations seems to be perfectly modeled with the calculated kernel weights (but unreasonable kernels) this will have effect when the desired normalization geometry enforces an extrapolation step. This is the case when a normalization solar zenith angle other than the input solar zenith angle (in case of application to a single flight line) is chosen, or one that is smaller than the smallest or larger than the larger solar zenith angle of all scenes that provide the angular observation space in case of application to multiple flight lines. It should be noted that RMSE between the four possible kernel combinations usually differed by only few percent.

The impact of kernel weights

As indicated in the previous paragraph, the kernel selection has direct influence on the final kernel weights obtained by Ross-Li inversion. But kernel weights can be questionable in any configuration of kernels. Numerous inversion procedures on single flight line observations have shown that the weights (including the constant for isotropic scattering) can diverge largely from what one would expect as 'phyically reasonable'. This includes inexplicable discontinuities in the spectral behavior of the kernel weights, which should be physically correlated between adjacent spectral bands. As mentioned above, such uncertainty will only have (negative) effect in data correction when extrapolation is performed. The inclusion of a-priori knowledge on kernel weights is a viable way to increase the quality of correction and enable proper extrapolation. Because of the 'balancing' issue between volume- and surface-scattering (and the fact that volume scattering can hardly be quantified in the sense of Ross-Li) an initial guess of the isotropic scattering was found to reliably control the kernel weight. In an (unpublished) experiment with many flight lines and illumination geometries involved, an empirically derived constant factor of 1.1 (times the average spectral reflectance factor at nadir) provided a stable and discontinuity-free distribution of kernel weights over the full spectral range except extremely noisy bands. As this measure may enforce a certain behavior of the volumetric and surface scattering kernel it is only recommended when a single or very few flight lines with few degrees of illumination angle difference can be used for composition of the angular observation space, or when the normalization geometry requires extrapolation of the input angular space.

The role of the structure scale

Ross-Li has been initially developed for global BRDF and albedo monitoring; relying on 'true' multi-angular measurements of predominantly satellite sensors, and the associated spatial characteristics. The assumption of normal distribution of scatterers in a ground resolution cell was fulfilled for all, even the most coarse textured surfaces. While this criterion is not fulfilled for higher resolution spaceborne or airborne data like the majority of data used in the studies for this thesis, it is technically not difficult to stratify data so that at least statistically the criterion is fulfilled. Nevertheless - in this step one is usually averaging observations ranging from complete illuminated canopy pixels over partly shaded to fully shaded pixels. Ross-Li when inverted on such a set of observations will perfectly correct for average angular effects and the visual result is usually good. Data are in fact corrected as if they were at lower spatial resolution. The (ensuing) problem is that the data are actually at high spatial resolution where an average BRDF effect does not represent the true angular effects. Imagine zooming onto the crown of a deciduous tree with very high leaf density, up to a resolution of 30 by 30 cm. The angle dependence of reflected light for that pixel will be mostly determined by the leaf optical properties (leaf reflectivity, absorbance and transmissivity and the reflectance anisotropy of a single leaf), and the angular distribution of leaves. Large scale shadow effects like those originating from tree density (shadows on ground and mutual shadowing) do not at all play a role for the angularity of those fully illuminated pixels, while a Ross-Li correction based on small-scale observations applies inappropriate factors to the reflectance. In other words: fully illuminated pixels are somehow corrupted, and those fully shaded are not accurately corrected either.

The simple work-around to deal with this dilemma is to preselect pixels that fulfill certain conditions on shadow fraction, and invert Ross-Li on that subset. The visual effect (e.g., in a data mosaic) will be worse, while single relevant pixels are corrected more accurately. Major uncertainties, however, arise from the empirical threshold operation to distinguish relevant pixels from others.

The better solution to this problem (actually, the only reasonable) would be to move away from the simplifying Ross-Li approach for very-high resolution data, and combine the anisotropy modeling with knowledge on the spatially explicit contribution of direct and diffuse illumination (the full hemispherical illumination field). This information could be extracted from atmospheric correction. Impacts from direct and diffuse components of scattering could then be treated separately from each other. Also the anisotropy of the atmosphere could be taken into account with such an approach, while modeling the atmosphere's anisotropy is still a challenging task.

5.2. Conclusions

The following conclusions can be drawn from my research work in the field of reflectance anisotropy effects in remote sensing data. They are presented in the order of the research question definition in Chapter 1.6, starting with the method development studies.

Reflectance anisotropy effects are severely impacting quantitative analysis of airborne imaging spectroscopy data. Depending on the product and geometic configuration, up to 100% deviation relative to nadir values must be expected. Anisotropy effects are equally arising in simple, band ratio based index products and products calculated through inversion of physical-based models, when these do not explicitly account for explicit view- and observation angles. Atmospheric correction does not reduce the unwanted effects.

Reflectance anisotropy effects can effectively and efficiently be modeled and corrected with the semi-empirical Ross-Li approach. This can remove up to 90% or even more of the angular effects. The method itself (kernel selection, weight determination, calculation and application of correction factors) can run in an automated way once a stratification of surface pixels into BRDF-effective scattering classes (or, a proxy to that) has been established. As nature is arbitrarily complex there will still be circumstances where a set of scattering classes is not sufficient to model the effects with good accuracy. Defining quality indicators would help to identify critical pixels or areas.

A very rough classification in two vegetation structural types, soil, and water is sufficient to account for the great majority of directional effects occurring in optical remote sensing data. The quality of this classification is essentially determining the quality of the BRDF correction as it is the only mechanism to introduce angular information on the scattering behavior into the model. The empirical part of the semi-empirical correction scheme can be considered as the “bottleneck” of the whole approach.

Defining the stratification of pixels in a continuous way decreases the risk of spatial artefacts due to wrong pixel assignment to classes, but even more care must be taken to select the right set of pure pixels. The reason is that the BRDF is now modeled exclusively on the pure pixels for each class which are far fewer than than the pixels used for inversion in the discrete case. So far there exists no feasible method for automatic or semi-automatic selection of pixels that can be used for Ross-Li inversion.

Once a good surface stratification has been achieved, the Ross-Li scheme can be applied to a variety of natural surface types, including snow with its forward-scattering behavior, and very structured forest types featuring a high fraction of pure shadow pixels and highly shaded pixels. It is important to remember that, using the Ross-Li approach, we can still only correct for spatially averaged effects of reflectance anisotropy even if the GIFOV is NOT considerably larger than the spatial scale of three-dimensional objects in the image (when the GIFOV is considerably larger, the image per se contains only averaged information on the angular scattering regime. A correction cannot account for explicit effects of e.g. shadow casting as this is in the subpixel domain). Limitations may arise in the correction quality in very high resolution data, where the structure scale of the objects (both vertically and horizontally) is considerably larger than a resolution cell in the data. For accurate correction of anisotropy effects in the case of very complex forest environments and very high spatial resolution data a separate treatment of direct and diffuse illumination angular effects should be taken into account. Another approach would be to label data with a defined shadow fraction as “contaminated”, invert the Ross-Li model on the remaining pixels and ignore the invalid pixels from any further analysis. This may be legitimate in some cases, in other cases an information may be desired for each and every pixel in the scene. At such high resolutions one will additionally have to take the slope and exposition of objects into account, and in last consequence make use of the full three-dimensional information if available. Whether or not a correction for reflectance anisotropy effects should be considered strongly depends on the ultimate goal and methodology of image analysis. I can generally recommend the Ross-Li scheme for correction of full flight lines when the focus of the analysis is on empirically derived surface parameters. An empirical or semi-empirical model should not be used when data are to be further analyzed with physical models which have the ability to incorporate angularity in the inversion with better accuracy. This will at least introduce additional uncertainty on the final product, or even interfere with physical model assumptions and lead to invalid results.

5.3. Outlook

Basically, the outlook emerges from the weak points which have been identified in this thesis concerning the method development and the performance of algorithms.

Directions for improvement can be identified in the following fields:

- Preparation of the classification which underlies the actual Ross-Li modeling

A classification in distinct structural surface types is not necessarily congruent with spectral types. All classification method applied so far in that context, however, assume structural classes to be a subset of spectral classes. This assumption holds true in the majority of pixels for the investigated images and structural surfaces types but there are ambiguities. Especially the two vegetation structural types can be difficult to reliably separate, while a “spectral brightness” criterion in a single spectral band was found to be sufficient in most cases. This worked well in general because of combined spectral differences between tree species and meadow/crop types, and a usually higher shadow fraction in the forest case. In contrast, complete crop fields of dark leaved plants were classified incorrectly with this simple approach. It was evident that also the anisotropy effects (like across-track brightness gradients) could bias the classification, when the threshold in spectral brightness was not selected with care. Apparently, considerably more effort would have to be put in a perfect classification, which could increase the quality of the final result because of the importance of a good stratification of the surface. There is another aspect linked with the classification, beyond its quality. Generating a classification is a highly interactive step that starts with manual pixel choice for reference spectra selection. Defining a set of sensor characteristics independent “standard” spectra would be a first step towards a more automated classification generation, while this optimization bears the risk to introduce additional uncertainties.

- The error metrics used for determining optimal kernel weights, and their physical reliability

The error metrics used for all Ross-Li inversion procedures was an RMSE criterion on the model-to-measurement fit as unweighted arithmetic mean over all spectral bands. This is a rather simplifying treatment for the underlying complexity of the model inversion, because it i) gives all spectral bands the same weight in the final kernel selection, regardlessly of the variance of angular observations; and ii) it does not account for spectral correlation between bands in the model inversion - adjacent bands should also feature similar kernel weights. The RMSE criterion simply guarantees that for each single band the modeled anisotropies best fit the angular observations, for the angular range of observations used for the inversion. Extrapolating from the retrieved kernel weights to observations beyond the typical field-of-view, or to higher/lower solar zenith angles potentially reveals a non-perfect weighting of kernels, especially when due to too sparse observations in one domain (e.g. observation solar zenith angles) ambiguous solutions are possible. The Ross-Li scheme allows to calculate white-sky-albedo directly out of the kernel weights. A very elegant approach is therefore to use its variance as a criterion for best model-to-observations fit (Gao et al. (2001)), which also facilitates reliable extrapolation of the angular space.

- Quality assessment

Another issue not discussed so far while omnipresent is the validation of any correction for reflectance anisotropy effects. Absolute validation with ground truth (e.g., Goniometer measurements) is hard to perform because of scaling issues, atmospheric correction uncertainties and so forth. Collings et al. (2010) describe a large number of metrics for relative validation (i.e., in the overlap of adjacent corrected flightlines). These could be used to better assess the quality of a correction, or to compare different configurations of e.g. the kernel.

- Treatment of high-resolution data with respect to the impact of shadowing

Mechanisms of anisotropy formation in spatial high-resolution imagery are far more complex than they are in data where the triggering spatial structures are much smaller than a resolution cell. The 'phenology' of anisotropies in the data must lead to discussions in the future, at which level of detail a correction can reliably be applied to the data, and at which level it can be omitted (because pixels can be regarded useless either way because of contamination with shadow or related effects). When the spatial resolution increases up to the point where no assumptions on the distribution of scatterers can be made anymore (because there is no distribution) one needs either to revert to physical models or needs to downscale to generate a distribution. It is argued here that there must be a definite upper resolution limit for application of such semi-empirical models as described in this thesis, beyond which one needs to make that decision. The spatial resolution at which typically APEX is operating (2 - 3 m) can be regarded to be in the uppermost range of possible spatial resolutions, for application to any possible surface type.

There are, for sure, techniques to deal with shaded or partly shaded pixels in imagery, such as implemented in recent versions in the ATCOR atmospheric correction software. This software tries to apply a modeled illumination field separated into direct and diffuse component to data and so to artificially enlighten shaded regions (Schläpfer et al. (2012)). This makes the data visually appear as if there were no shadows at all, while the information content is questionable (and would barely allow to derive quantitative information from, using physical methods).

Solving for the complete illumination field - which is a prerequisite for accurate BRDF modeling with respect to shadows - can also consist in a processing scheme relying on better integration with atmospheric correction of a semi-empirical BRDF model (Lenot et al. (2009)). These authors use several cascading physical formulations for the irradiance components and second order terms with simplifications that allow a stable inversion scheme. Angular dependencies are modeled with the RPV model (Rahman et al. (1993)). Such a processing scheme could be implemented in the framework of the Ross-Li method, too, and and would then offer several opportunities in the way that very-high resolution data and the associated effects are treated.

A conceptually different approach would be to work with BRDF databases, which would have to be populated either from modeling or from a large number of campaigns, to contain a comprising range of representative surface structural types at various spatial resolutions. Variable shadow fractions could also be taken into account within such a BRDF processing framework.

Bibliography

Asner, G. P., Braswell, H., Schimel, D., Wessman, Carol, A., 1998. Ecological Research Needs from Multiangle Remote Sensing Data. Remote Sensing of Environment 63, 155–165.

Biliouris, D., Zande, D. V. D., Verstraeten, W. W., Stuckens, J., Muys, B., Dutré, P., Coppin, P., 2009. RPV Model Parameters Based on Hyperspectral Bidirectional Reflectance measurements of Fagus Sylvatica L. leaves. Remote Sensing 1, 92–106.

Chopping, M. J., 1999. Testing a LiSK BRDF Model with in Situ Bidirectional Reflectance Factor Measurements over Semiarid Grasslands. Remote Sensing of Environment 4257 (00).

Collings, S., Caccetta, P., Campbell, N., Wu, X., Oct. 2010. Techniques for BRDF Correction of Hyperspectral Mosaics. IEEE Transactions on Geoscience and Remote Sensing 48 (10), 3733–3746.
URL `http://ieeexplore.ieee.org/lpdocs/epic03/wrapper.htm?arnumber=5483085`

Diner, D. J., Asner, G. P., Davies, R., Knyazikhin, Y., Mulle, J.-p., Nolid, A. W., Pinty, B., Schaaf, C. B., Stroeve, J., 1999. New directions in Earth observing : Scientific applications of multi-angle remote sensing (818).

Gao, F., Schaaf, C. B., Strahler, A. H., Lucht, W., Apr. 2001. Using a multikernel least-variance approach to retrieve and evaluate albedo from limited bidirectional measurements. Remote Sensing of Environment 76 (1), 57–66.
URL `http://linkinghub.elsevier.com/retrieve/pii/S0034425700001929`

Grau, E., Gastellu-Etchegorry, J.-P., 2013. Radiative transfer modeling in the Earth - Atmosphere system with DART model. Remote Sensing of Environment 139, 149–170.

Hu, B., Lucht, W., Li, X., Strahler, A. H., 1997. Validation of Kernel-Driven Semiempirical Models for the Surface Bidirectional Reflectance Distribution Function of Land Surfaces. Remote Sensing of Environment 62, 201–214.

Hu, B., Lucht, W., Strahler, A., Mar. 1999. The interrelationship of atmospheric correction of reflectances and surface BRDF retrieval: a sensitivity study. IEEE Transactions on Geoscience and Remote Sensing 37 (2), 724–738.
URL `http://ieeexplore.ieee.org/lpdocs/epic03/wrapper.htm?arnumber=752189`

Hueni, A., Lenhard, K., Baumgartner, A., Schaepman, M. E., 2013. Airborne Prism Experiment Calibration Information System. IEEE Transactions on Geoscience and Remote Sensing 51, 5169–5180.

Jacquemoud, S., Ustin, S. L., Verdebout, J., Schmuck, G., Andreoli, G., 1996. Estimating Leaf Biochemistry Using the PROSPECT Leaf Optical Properties Model 56, 194–202.

Jacquemoud, S., Verhoef, W., Baret, F., Bacour, C., Zarco-Tejada, P. J., Asner, G. P., François, C., Ustin, S. L., Sep. 2009. PROSPECT+SAIL models: A review of use for vegetation characterization. Remote Sensing of Environment 113, S56–S66.
URL `http://linkinghub.elsevier.com/retrieve/pii/S0034425709000765`

Joerg, P. C., Weyermann, J., Morsdorf, F., Zemp, M., Schaepman, M. E., 2015. Computation of a distributed glacier surface albedo proxy using airborne laser scanning intensity data and in-situ spectro-radiometric measurements. Remote Sensing of Environment 160, 31–42.

Kennedy, R. E., 1997. Empirical methods to compensate for a view-angle-dependent brightness gradient in AVIRIS imagery. Remote Sensing of Environment 62, 277–291.

Kennedy, R. E., Cohen, W. B., Takao, G., 1997. A BRDF-related brightness gradient in AVIRIS imagery: lessons from an empirical compensation method.

Kuusk, A., Nilson, T., 2000. A Directional Multispectral Forest Reflectance Model. Remote Sensing of Environment 252 (May 1999), 244–252.

Laurent, V. C., Schaepman, M. E., Verhoef, W., Weyermann, J., Chávez, R. O., Jan. 2014. Bayesian object-based estimation of LAI and chlorophyll from a simulated Sentinel-2 top-of-atmosphere radiance image. Remote Sensing of Environment 140, 318–329.
URL `http://linkinghub.elsevier.com/retrieve/pii/S0034425713003088`

Laurent, V. C., Verhoef, W., Clevers, J. G., Schaepman, M. E., Apr. 2011. Estimating forest variables from top-of-atmosphere radiance satellite measurements using coupled radiative transfer models. Remote Sensing of Environment 115 (4), 1043–1052.
URL `http://linkinghub.elsevier.com/retrieve/pii/S0034425710003470`

Lavergne, T., Kaminski, T., Pinty, B., Taberner, M., Gobron, N., Verstraete, M. M., Vossbeck, M., Widlowski, J.-L., Giering, R., Mar. 2007. Application to MISR land products of an RPV model inversion package using adjoint and Hessian codes. Remote Sensing of Environment 107 (1-2), 362–375.
URL `http://linkinghub.elsevier.com/retrieve/pii/S0034425706004147`

Lenot, X., Achard, V., Poutier, L., 2009. SIERRA : A new approach to atmospheric and topographic corrections for hyperspectral imagery. Remote Sensing of Environment 113 (8), 1664–1677.
URL `http://dx.doi.org/10.1016/j.rse.2009.03.016`

Li, W., Stamnes, K., Eide, H., Spurr, R., 2007. Bidirectional reflectance distribution function of snow: corrections for the Lambertian assumption in remote sensing applications. Optical Engineering 46 (066201).

Li, X., Liang, Y., Xu, L., 2014. Bidirectional reflectance distribution function based surface modeling of non-Lambertian using intensity data of light detection and ranging. Journal of the Optical Society of America A 31 (9), 2055–2063.
URL `http://josaa.osa.org/abstract.cfm?URI=josaa-31-9-2055`

Li, X., Strahler, A., Nov. 1986. Geometric-Optical Bidirectional Reflectance Modeling of a Conifer Forest Canopy. IEEE Transactions on Geoscience and Remote Sensing GE-24 (6), 906–919.
URL `http://ieeexplore.ieee.org/lpdocs/epic03/wrapper.htm?arnumber=4072562`

Li, X., Strahler, A. H., 1992. Geometric-Optical Bidirectional Reflectance Modeling of the Discrete Crown Vegetation Canopy : Effect of Crown Shape and Mutual Shadowing. IEEE Transactions on Geoscience and Remote Sensing 30 (2).

Liang, S., Strahler, A. H., 1995. An analytic radiative transfer model for a coupled atmosphere and leaf canopy. Journal of Geophysical Research 100 (D3), 5085–5094.

Liang, S., Strahler, A. H., Barnsley, M. J., Borel, C. C., Gerstl, S. A. W., Diner, D. J., Prata, A. J., Walthall, C. L., 2000. Multiangle remote sensing: Past, present and future. Remote Sensing Reviews 18 (2), 83–102.
URL `http://www.scopus.com/inward/record.url?eid=2-s2.0-0034261014&partnerID=tZOtx3y1`

Lucht, W., Schaaf, C. B., Strahler, A. H., 2000. An Algorithm for the Retrieval of Albedo from Space Using Semiempirical BRDF Models. IEEE Transactions on Geoscience and Remote Sensing 38 (2), 977–998.

Lyapustin, A., Gatebe, C., Kahn, R., Brandt, R., Redemann, J., Russell, P., King, M., Pedersen, C., Gerland, S., Poudyal, R., Marshak, A., Wang, Y., Schaaf, C., Hall, D., Kokhanovsky, A., 2010. Analysis of snow bidirectional reflectance from ARCTAS spring-2008 campaign. Atmospheric Chemistry and Physics 10, 4359–4375.

Mišurec, J., Kopačková, V., Lhotáková, Z., Hanuš, J., Weyermann, J., Entcheva-Campbell, P., Albrechtova, J., 2012. Utilization of hyperspectral image optical indices to assess the Norway spruce forest health status. Journal of Applied Remote Sensing 6 (1), 063545.
URL `http://link.aip.org/link/JARSC4/v6/i1/p063545/s1&Agg=doi`

Nilson, T., Kuusk, A., 1989. A reflectance model for the homogeneous plant canopy and its inversion. Remote Sensing of Environment 27 (2), 157–167.

Rahman, H., Pinty, B., Verstraete, M. M., 1993. Coupled Surface-Atmosphere Reflectance (CSAR) 2. Semiempirical surface model usable with NOAA Advanced Very High Resolution Radiometer Data. Journal of Geophysical Research 98 (D11).

Richter, R., Schläpfer, D., 2002. Geo-atmospheric processing of airborne imaging spectrometry data. Part 2 : atmospheric / topographic correction. International Journal of Remote Sensing 23 (13), 2631–2649.

Ross, J., 1981. The Radiation Regime and Architecture of Plant Stands.

Roujean, J., Leroy, M., Deschamps, P., 1992a. A bidirectional reflectance model of the Earth's surface for the correction of remote sensing data. Journal of Geophysical Research 97, 20455–20468.

Roujean, J.-L., Leroy, M., Deschamps, P. Y., 1992b. A bidirectional reflectance model of the earth's surfaces for the correction of remote sensing data. Journal of Geophysical Research 97 (D18), 20455–20468.

Schaaf, C. B., Gao, F., Strahler, A. H., Lucht, W., Li, X., Tsang, T., Strugnell, N. C., Zhang, X., Jin, Y., Muller, J.-p., Lewis, P., Barnsley, M., Hobson, P., Disney, M., Roberts, G., Dunderdale, M., Doll, C., Robert, P., Hu, B., Liang, S., Privette, J. L., Roy, D., 2002. First operational BRDF , albedo nadir reflectance products from MODIS. Remote Sensing of Environment 83, 135 – 148.

Schaaf, C. B., Gao, F., Strahler, A. H., Tsang, T., Lucht, W., Strugnell, N., Li, X., Muller, J.-p., Lewis, P., Barnsley, M., Hobson, P., Disney, M., Dunderdale, M., Roberts, G., 2000. THE MODERATE RESOLUTION IMAGING SPECTRORADIOMETER (MODIS) BRDF AND ALBEDO PRODUCT : PRELIMINARY RESULTS. IEEE Transactions on Geoscience and Remote Sensing (l), 3048–3050.

Schaepman, M. E., May 2007. Spectrodirectional remote sensing: From pixels to processes. International Journal of Applied Earth Observation and Geoinformation 9 (2), 204–223.
URL `http://www.scopus.com/inward/record.url?eid=2-s2.0-34047135508&partnerID=tZOtx3y1`

Schaepman-Strub, G., Schaepman, M., Painter, T., Dangel, S., Martonchik, J., Jul. 2006. Reflectance quantities in optical remote sensing - definitions and case studies. Remote Sensing of Environment 103 (1), 27–42.
URL `http://linkinghub.elsevier.com/retrieve/pii/S0034425706001167`

Schiefer, S., Hostert, P., Damm, a., Mar. 2006. Correcting brightness gradients in hyperspectral data from urban areas. Remote Sensing of Environment 101 (1), 25–37.
URL `http://linkinghub.elsevier.com/retrieve/pii/S0034425705004037`

Schläpfer, D., Richter, R., Kellenberger, T., 2012. Aspects Of Atmospheric And Topographic Correction Of High Spatial Resolution Imagery. In: IEEE International Geoscience and Remote Sensing Symposium, Munich. pp. 1–4.

Schlerf, M., Atzberger, C., Feb. 2006. Inversion of a forest reflectance model to estimate structural canopy variables from hyperspectral remote sensing data. Remote Sensing of Environment 100 (3), 281–294.
URL `http://linkinghub.elsevier.com/retrieve/pii/S0034425705003603`

Stenberg, P., Mõttus, M., Rautiainen, M., 2008. Modeling the spectral signature of forests: application of remote sensing models to coniferous canopies. In: Advances in Land Remote Sensing. System, Modeling, Inversion and Application. Springer Science + Business Media. pp. 147–171.

Stroeve, J., Box, J., Gao, F., Liang, S., Nolin, A., Schaaf, C., 2005. Accuracy assessment of the MODIS 16-day albedo product for snow: Comparisons with Greenland in situ measurements. Remote Sensing of Environment 94, 46–60.

Susaki, J., Hara, K., Kajiwara, K., Honda, Y., 2004. Robust estimation of BRDF model parameters. Remote Sensing of Environment 89, 63 – 71.

Verhoef, W., Bach, H., Sep. 2003. Simulation of hyperspectral and directional radiance images using coupled biophysical and atmospheric radiative transfer models. Remote Sensing of Environment 87 (1), 23–41.
URL `http://linkinghub.elsevier.com/retrieve/pii/S0034425703001433`

Verhoef, W., Bach, H., 2007. Coupled soil-leaf-canopy and atmosphere radiative transfer modeling to simulate hyperspectral multi-angular surface reflectance and TOA radiance data. Remote Sensing of Environment 109, 166–182.

Walthall, C. L., 1997. A Study of Reflectance Anisotropy and Canopy Structure Using a Simple Empirical Model. Remote Sensing of Environment 61, 118–128.

Walthall, C. L., Norman, J. M., Welles, J. M., Campbell, N., Blad, B. L., 1985. Simple equation to approximate the bidirectional reflectance from vegetation canopies and bare soil surfaces. Applied optics 24, 383–387.

Wanner, W., Li, X., Strahler, A. H., 1995a. A new class of geometric-optical semiempirical kernels for global BRDF and albedo modeling. IEEE Transactions on Geoscience and Remote Sensing, 15–17.

Wanner, W., Li, X., Strahler, A. H., 1995b. On the derivation of kernels for kernel-driven models of bidirectional reflectance. Journal of Geophysical Research 100, 21077–21089.

Wanner, W., Li, X., Strahler, A. H., 1995c. On the derivation of kernels for kernel-driven models of bidirectional reflectance. Journal of Geophysical Research 100.

Widlowski, J.-l., Pinty, B., Lavergne, T., Verstraete, M. M., Gobron, N., 2006. Horizontal radiation transport in 3-D forest canopies at multiple spatial resolutions : Simulated impact on canopy absorption. Remote Sensing of Environment 103, 379 – 397.

Widlowski, J.-L., Pinty, B., Lopatka, M., Atzberger, C., Buzica, D., Chelle, M., Disney, M., Gastellu-Etchegorry, J.-P., Gerboles, M., Gobron, N., Grau, E., Huang, H., Kallel, A., Kobayashi, H., Lewis, P., Quin, W., Scherf, M., Stuckens, J., Xie, D., 2013. The fourth radiation transfer model intercomparison (RAMI-IV): Proficiency testing of canopy reflectance models with ISO-13528. Journal of Geophysical Research: Atmosphere 118, 1–22.

Acknowledgements

The author would first like to thank all the staff and colleagues from the Remote Sensing Laboratories, for good, fruitful and enjoyable collaboration, off-work activities and friendship. The good vibes at RSL definitely formed the basis of a successful PhD. Special thanks go to Dr. Erich Meier from the SARLab for employing me as scientific staff, Prof. Dr. Klaus Itten for accepting me as PhD candidate, and Prof. Dr. Michael Schaepman for not giving up on me. I would like to also mention Dr. Mathias Kneubühler, who was always readily available for “first level support”. It was real fun to join him on field campaigns and have a beer together.

Rita Ott and Sandra Altorfer from the secretary of RSL are thanked for very very superfriendly support anytime and anywhere.

Dr. Peter Wellig and Dr. Roland Oechslin are thanked for good collaboration in the “Signaturen” project with Armasuisse, which financed a part of my PhD.

The members of the PhD promotional committee (Dr. Michael Schaepman, Dr. Stefan Dangel, Dr. Gabriela Schaepman-Strub and Dr. Mathias Kneubühler) are thanked for valuable technical input, co-authorship, and proof-reading of the full thesis manuscript.

I would like to thank Dr. Judith Böttcher for thoroughly proofreading the manuscript and compensating my incapabilities with respect to the english language.

Last but not least I would like to express infinite gratitude to my wife Andrea for all the patience, and apologize for loss of pleasures of life caused by frustrating experiment results.

Appendix

A. Utilization of hyperspectral image optical indices to assess the Norway spruce forest health status

Journal of
Applied Remote Sensing

Utilization of hyperspectral image optical indices to assess the Norway spruce forest health status

Jan Mišurec
Veronika Kopačková
Zuzana Lhotáková
Jan Hanuš
Jörg Weyermann
Petya Entcheva-Campbell
Jana Albrechtová

SPIE

Utilization of hyperspectral image optical indices to assess the Norway spruce forest health status

Jan Mišurec,[a,b] Veronika Kopačková,[a,b] Zuzana Lhotáková,[c] Jan Hanuš,[d] Jörg Weyermann,[e] Petya Entcheva-Campbell,[f] and Jana Albrechtová[c]
[a]Czech Geological Survey, Klárov 3, Prague 1, 118 21, Czech Republic
E-mail: jan.misurec@geology.cz
[b]Charles University in Prague, Faculty of Science, Department of Applied Geoinformatics and Cartography, Albertov 6, Prague 2, 128 43, Czech Republic
[c]Charles University in Prague, Faculty of Science, Department of Experimental Plant Biology, Viničná 5, Prague 2, 128 44, Czech Republic
[d]The Academy of Sciences of the Czech Republic, Global Change Research Centre, Bělidla 686/4a, Brno, 603 00, Czech Republic
[e]University of Zurich, Remote Sensing Laboratories, Wintherthurerstrasse 190, CH-8057, Zurich, Switzerland
[f]NASA Goddard Space Flight Center, Biospheric Sciences Branch, Code 614.4, building 33, Greenbelt, 20771, Maryland

Abstract. The work is concerned with assessing the health status of trees of the Norway spruce species using airborne hyperspectral (HS) data (HyMap). The study was conducted in the Sokolov basin in the western part of the Czech Republic. First, statistics were employed to assess and validate diverse empirical models based on spectral information using the ground truth data (biochemically determined chlorophyll content). The model attaining the greatest accuracy (D_{718}/D_{704}: RMSE $= 0.2055$ mg/g, $R^2 = 0.9370$) was selected to produce a map of foliar chlorophyll concentrations (C_{ab}). The C_{ab} values retrieved from the HS data were tested together with other nonquantitative vegetation indicators derived from the HyMap image reflectance to create a statistical method allowing assessment of the condition of Norway spruce. As a result, we integrated the following HyMap derived parameters (C_{ab}, REP, and SIPI) to assess the subtle changes in physiological status of the macroscopically undamaged foliage of Norway spruce within the four studied test sites. Our classification results and the previously published studies dealing with assessing the condition of Norway spruce using chlorophyll contents are in a good agreement and indicate that this method is potentially useful for general applicability after further testing and validation. © *2012 Society of Photo-Optical Instrumentation Engineers (SPIE).* [DOI: 10.1117/1.JRS.6.063545]

Keywords: chlorophyll; optical indices; Norway spruce; continuum removal; HyMap, actual physiological status; Sokolov basin, forest management.

Paper 11255 received Nov. 25, 2011; revised manuscript received May 10, 2012; accepted for publication May 11, 2012; published online Jun. 29, 2012.

1 Introduction

Forests play an important role in regulation of the global climate via the global carbon cycle, evapotranspiration, and earth surface albedo.[1,2] Moreover, forests provide humans with the whole range of ecosystem services including provision of food and forest products, regulation of the hydrological cycle, protection of soil resources, etc.[3] Forest health and ecosystem functioning have recently been influenced by anthropogenic activities and their consequences, such as air pollution, surface mining, heavy metal contamination,[4] and other biotic and abiotic stress factors such as pest invasions and soil acidification,[5] which had an especially high effect on central Europe. Therefore, large-scale monitoring of forest health and its methodologies are in the forefront of interest to scientists as well as forest managers. The condition of forests in

Europe is monitored under the International Co-operative Program on Assessment and Monitoring of Air Pollution Effects on Forests (ICP Forests).[6] The monitoring consists of two levels: monitoring Level I provides an annual overview of crown condition (defoliation, discoloration, and damage visible on the trees), soil conditions, and foliar survey (contents of nutrients in soil and foliage);[7] monitoring Level II consists of 11 additional assessments (e.g., tree growth, phenology, litterfall, and others, see http://icp-forests.net/page/level-ii), which provide a better insight into the causes affecting the condition of forest ecosystems and into the effects of various stress factors. Our study aims to contribute to improving regional methods for Level II assessments, as both surveys—remote sensing and foliar chemistry—should be included in the overall evaluation.[8]

Biochemical parameters, such as foliage leaf pigments,[9] nitrogen, lignin, and contents of other polyphenols,[10] reflect and determine physiological processes in plants, such as photosynthetic capacity and net primary production. On the other hand, foliar chemistry also governs other processes in the ecosystem, such as nutrient cycling and litter decomposition.[11] Therefore accurate estimation of the biochemical contents of vegetation is a key factor in understanding and modeling forest ecosystem functions and dynamics. The chlorophyll content is an indicator of leaf photosynthetic activity and can be directly linked to the phenology and health status of plants.[12] Leaf chlorophyll content can be used to detect actual vegetation stress; however, as shown by Ref. 12, the chlorophyll content retrieved from Proba/CHRIS images differs according to the canopy and the leaf architecture of the examined crops. Therefore, at the canopy level, the leaf area index (LAI) and also canopy architecture should be taken into account for a particular canopy. Furthermore, chlorophyll can be used to measure vegetation stress, life stage, productivity, and CO_2 sequestration. Remote sensing of the chlorophyll content has been studied extensively on both the leaf[13,14] and the canopy scales.[15–18]

Many aspects of the physiological state of trees are more or less connected with the concentrations of two main groups of leaf photosynthetic pigments: chlorophylls and carotenoids. Vegetation with a high concentration of chlorophyll is considered to be healthy, as the chlorophyll content is linked to greater light-use efficiency, photosynthetic activity, and carbon dioxide uptake.[19–21] Chlorophyll generally decreases under stress and during senescence.[20] Carotenoids play the main role in the process of incident light absorption, transportation of energy to the reaction center of the photosystems, and heat dissipation of energy in case of high irradiances.[22] The combination of the influences of chlorophylls and carotenoids is thus connected with light-use efficiency.[23] However, higher carotenoid to chlorophyll ratios indicate vegetation stress and senescence.[22,24]

Canopy reflectance depends not only on leaf chemistry but also on vegetation type and function and canopy structure and composition.[16,25] To obtain a spatially explicit vegetation biochemical content, it is necessary to scale leaf-level biochemical measurement to canopy level. Increasing availability of airborne and spaceborne hyperspectral data has enabled the development of accurate methods for scaling of biochemical properties from the leaf to the canopy scale.[26,27]

Currently, there are three remote-sensing approaches used to scale biochemical content from the leaf to the canopy level: (i) the direct extrapolation method, (ii) the canopy-integrated method, and (iii) physical models.[10,28,29] The direct extrapolation and canopy-integration methods rely on statistical analyses to establish a relationship between the targeted biochemical parameter and a spectral parameter (e.g., spectral indices, derivatives).[30,31] The direct extrapolation method (the simplest) is based on the assumptions that all the leaves in the plant have the same biochemical content and only a fine layer of the leaves covers an entire pixel in an image. The relationships between the spectral parameter and the biochemical content are applied directly. Using the canopy-integrated method, the biochemical content is obtained by multiplying the leaf content by the corresponding canopy biophysical parameter (e.g., LAI or biomass[15,29,32]). In addition, new spectral indices taking into account species heterogeneity and non-green canopy components were developed and further tested.[15] Physical methods employ inverted radiative transfer (RT) models (e.g., PROSPECT,[29] LEAFMOD,[28] SAIL,[33] SCOPE[34]) to estimate the biochemical content at the leaf level.[35] RT modeling simulates the transfer of radiation in the canopy by computing the interaction between a plant and solar radiation.[36–38] In comparison with the direct extrapolation and the canopy-integrated approaches, inversion models offer the potential of a more generic approach to quantify the biochemical parameters of vegetation based on spectral data.

The main goal of the study was retrieval of the chlorophyll content and development of a statistical classification method allowing objective assessment of the physiological status of macroscopically undamaged foliage on a regional scale. To simplify the problem, we focused on single-species (Norway spruce) homogenous forests of a similar age and tested only the direct extrapolation and canopy-integrated methods. We did not test physical models at this stage as the computation remains time-consuming and can suffer from ill-posed problems or can lead to a bias in the retrieved biophysical parameters.[39,40]

In the Sokolov area, NW Bohemia, we selected four homogenously covered Norway spruce (*Picea abies L. Karst*) forest stands with trees of similar ages (40 to 60 years) exhibiting no visible symptoms of damage. Although these forests are situated near lignite open-pit mines, they have not been directly affected by intensive mining activities or by the massive air pollution and acid rains in the late 1990s, which were factors in the Krušné Hory Mountains, part of the heavily polluted Black Triangle region. Since 1996, the atmospheric concentrations of SO_2 in Sokolov area have not exceeded 30 $\mu g.m^{-3}$ and since 2000 have not exceeded 15 $\mu g.m^{-3}$ on average (data available at Czech Hydrometeorological Institute[41]).

Statistics were employed to analyze the relationship between diverse vegetation indices and other types of spectral transformations [e.g., first derivatives, continuum removal (CR), and band-depth normalizations] and the ground truth data for the foliage sampled in stands of Norway spruce. These diverse approaches were validated, and, as a result, a map of foliar chlorophyll concentrations (C_{ab}) was derived. The C_{ab} values, together with another three optical parameters [the position of the inflection point on the spectral curve in the red-edge part of the spectrum (REP),[42] the photochemical reflectance index,[43] and the Structure Insensitive Pigment Index (SIPI)[44]], were then used to assess the actual health status of the Norway spruce forests.

2 Study Sites

The study was conducted in the Sokolov basin in the western part of the Czech Republic, in a region affected by long-term extensive mining (Fig. 1). The Sokolov basin in the Czech Republic is composed of rocks of Oligocene to Miocene age and is 8 to 9 km wide and up to 36 km long, with a total area of about 200 km^2. It contains 60% volcanic ejecta originating from fissures and volcanic cones and 40% sediments.[45] The average altitude of the study region is about 470 m. Due to the fact that the basin is surrounded by the Krušné Hory Mountains, precipitation is above the average for the Czech Republic, and the local climate in the region belongs among the more extreme conditions, characterized by colder and wetter conditions.

The selected forest stands surround the lignite open pit mines in Sokolov but have not been directly affected by the mining activities. However, the soil in all of the stands exhibits low pH and high heavy metal content. We selected four research sites dominated by mature Norway spruce forests of similar age (Table 1; Erika, Habartov, and Studenec: 40 to 60 years; Mezihorská: 60 to 80 years). The stands were located at a maximum distance of 12 km from the active lignite open pit mines (Fig. 1, Table 1). None of the selected sites showed any severe symptoms of macroscopic damage, and they were all classified as damage class 1 with total crown defoliation not exceeding 25% and average needle retention of 8 to 10 needle age classes.

In relation to soil conditions, we assume that our four study sites are good representatives of the spruce forests in the region. The pH of the study sites (2.53 to 3.31) is slightly below the average for the Czech Republic (3.2) but in accordance with local conditions (3.0).[46] In addition to Norway spruce monocultures, mixed spruce forests (with birch or pine) are characteristic of the region. We selected study sites considering the spatial resolution of the HyMap sensor (5×5 m), and thus homogeneity of spruce canopy was the main criterion for site selection.

3 Data

3.1 *Ground Truth Data*

The source for ground truth data was foliage sampled in the Norway spruce stands. The samples of Norway spruce needles were collected in each forest stand during the ground campaign

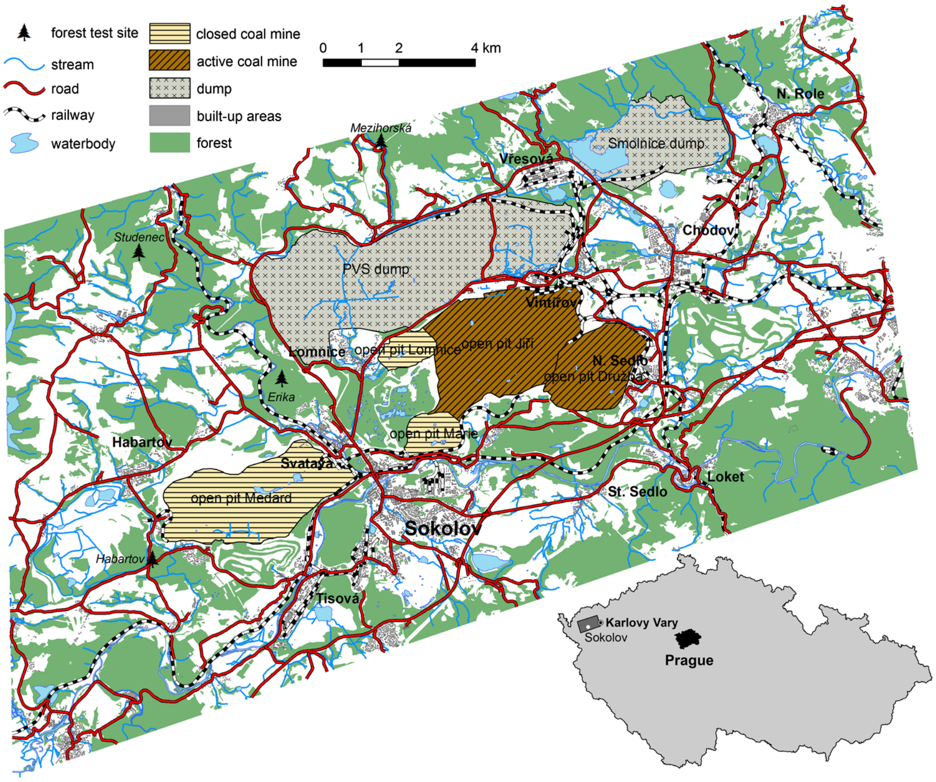

Fig. 1 Scheme of the Sokolov lignite basin with the four selected forest stands covered by homogenous Norway spruce (Picea abies L. Karst.) forests: Erika, Habartov, Mezihorská, and Studenec.

(August 27 to 30, 2009) to define statistical regression models for estimation of canopy chlorophyll content and to validate the obtained statistical models.

At each of the four test sites, 10 to 15 representative trees were selected in clearly definable groups of five (Erika: two groups A and B; Habartov: three groups C, D, and E; Mezihorská: three groups F, G, and H; and Studenec: two groups I and J). Sample branches were taken from the upper and middle portion of the sunlit canopy; the needles age classes were identified, and representative samples of the first- and third-year needles were collected. Two sample sets of the needles were generated: one for pigment determinations and one for dry matter determinations. Each set contained 200 samples (50 trees × two positions in the crown × two age classes (first- and third-year needles).

Photosynthetic pigments (e. g. chlorophyll a, b, and total carotenoids) were extracted following the procedure outlined by Ref. 47. The amounts of photosynthetic pigments were determined spectrophotometrically, using equations published by Ref. 48.

In each forest stand, five representative sampling points were chosen to collect soil samples. Material was collected from four soil horizons (two organic and two lithological horizons, the

Table 1 Norway spruce test sites and their basic characteristics.

Site	Latitude (*N*)	Longitude (*E*)	Elevation (meters above sea level)	Forest age (years)	Distance from the open-pit mines (km)
Erika	50 deg 12’25”	12 deg 36’17”	495	40 to 60	6.4
Habartov	50 deg 09’48”	12 deg 33’28”	477	40 to 60	11.2
Mezihorská	50 deg 15’50”	12 deg 38’17”	678	60 to 80	5.8
Studenec	50 deg 14’09”	12 deg 33’00”	722	40 to 60	8.5

depth of forest floor ranged between 0 and 40 cm). The four horizons have the following characteristics: horizon 1: organic horizon (largely undecomposed); horizon 2: organic horizon (poorly decomposed); horizon 3: mineral, mixed with humus, usually darkened; horizon 4: zone of maximum eluviation of clays and iron and aluminum oxides. The organic material was dried in the air prior to sieving (fraction <2 mm). Ground sub-samples were analyzed for total organic carbon and nitrogen (Perkin Elmer CHN analyzer). In addition, the pH was determined in the laboratory using an ion-selective electrode in 1M KCl solution.

3.2 *High Spectral Resolution Data*

3.2.1 *HyMap airborne hyperspectral data*

The hyperspectral image data was acquired on July 27, 2009, during the HyEUROPE 2009 flight campaign using the HyMap (HyVista Corp., Australia) airborne imaging spectrometer. The HyMap sensor records image data in 126 narrow spectral bands (with full-width half maximum ca. 15 nm) covering the entire spectral interval between 450 to 2500 nm. The resulting ground pixel resolution of the image data was 5 m. To cover the entire area of interest (approx. 15×22 km), nine cloudless flight lines were acquired in the NE-SW direction.

3.2.2 *Supportive ground measurements*

In order to successfully pre-process the hyperspectral data, a supportive calibration and validation ground campaign were organized simultaneously with the HyMap data acquisition. The ground measurements are essential to properly calibrate as well as validate the image data and to enable: (i) atmospheric correction of the airborne hyperspectral images and (ii) retrieving at surface reflectance values for the further verification. The study area was investigated in advance to find the reference targets, which must meet the following conditions: (i) spatial homogeneity for a minimum area of 5×5 image pixels and (ii) natural or artificial nearly Lambertian ground surfaces. Consequently, six appropriate targets with different values of the surface reflectance were chosen, covering the range of reflectivity from ca. 0 up to 70% (water pool, artificial grass, two asphalt plots, concrete, and beach-volleyball court). The hemispherical-conical reflectance factor (HCRF)[49] was measured by an ASD FielSpec-3 spectroradiometer for each reference target. Raw spectroradiometric data were transformed into the HCRF using the calibrated white spectralon panel.

In addition, Microtops II Sunphotometer (Solar Light Comp., USA) measurements were taken approximately every 30 s during the HyMap data acquisition. These data was used for estimation of the actual atmospheric conditions (aerosol optical thickness; water vapor content).

3.2.3 *Hyperspectral image data pre-processing*

The HyMap multiple flight-line data were atmospherically corrected using software (SW) package ATCOR-4 version 5.0,[50] which is based on the MODTRAN[51] radiative transfer model and enables atmospheric correction of the aerial hyperspectral images. The known reflectances of the specific reference target as well as of WV were utilized for fine-tuning of the model, as facilitated by ATCOR-4. The remaining reference targets were used for validation of the corrected image.

The orientation and geometry of the HyMap strips followed the SW-NE orientation of the lignite basin. However, this setting represented an optimal solution from the economic point of view; on the other hand, this setting (relative solar azimuth at the acquisition hour was about 73 deg) caused that the data suffered from strong cross-track illumination and bi-directional reflectance distribution function effects.[52,53] Therefore, in addition to the atmospheric correction, the data had to be further processed to minimize these effects, and semi-empirical nadir normalization using the kernel-based Ross-Li model[54] was performed for all the flight lines.

Direct ortho-georectification was performed using the PARGE software package.[55] Data from the on-board inertial measurement unit/global positioning system unit and digital elevation model with ground resolution of 10 m were used as the input parameters for the ortho-georectification. Finally, the hyperspectral image data was georeferenced to the UTM 33N (WGS-84) coordinate system. To assess the final accuracy the ortho-rectified HyMap, the product was compared to the very high spatial resolution aerial orthophotos (pixel size = 0.5 m) and a resulting standard positional accuracy of 3.7 m was defined.

Finally, we assessed the radiometric quality of each flight line by calculating the signal-to-noise ratios (SNR).[56] To calculate this parameter, a dark and homogenous surface (deep clean water body) was identified for each flight line and set as a region of interest (ROI). Subsequently, the ratio of the mean radiance and the standard deviation were calculated for each ROI (Table 2). In addition, we employed the minimum noise fraction transformation[57] to assess the level of noise present in each flight line image (Fig. 2). Based on this assessment, we could see that two flight lines (8 and 9) had significantly lower radiometric quality and high amounts of noise, especially flight line number 9 (Table 2), (Fig. 2).

4 Methods

The general workflow of the completed research is outlined in Fig. 3. C_{ab} was determined by testing numerous empirical models utilizing the original (nontransformed) reflectance data as well as its transformed products (see 4.3). Initially we defined the extent of the Norway spruce forests to which the further computation was applied. To create and validate the empirical models, we divided our ground truth data into training and validation datasets. The relationship between the predicted and measured values was described by the linear regression model and the coefficient of determination (R^2 and Rv^2) and root mean square errors (RMSE) were determined. To assess the vegetation health status, we also tested the following indicators: the red-edge part of spectrum (REP),[42] photosynthetic reflectance index,[43] and structure insensitive pigment index (SIPI).[44]

4.1 *Definition of the Norway Spruce Forest Extends*

We focused on homogenous Norway spruce forests, and it was thus necessary to mask out other surfaces. We used a hierarchical classification approach, which we found more efficient than simple supervised classification (Fig. 4). First we identified vegetated and non-vegetated areas using simple threshold classification of the red-edge normalized difference index ($NDVI_{705} = 0.3$).[58] The vegetated surfaces were then classified into grasslands and forest areas using the maximum likelihood classification (MLC) applied to the first five components,

Table 2 Image-derived signal-to-noise ratios (SNR) calculated for the chlorophyll absorption domain bands.

Line	SNR(646 nm)	SNR(660 nm)	SNR(675 nm)	SNR(690 nm)	SNR(704 nm)	SNR(718 nm)
1	46.61	47.50	49.77	43.19	52.98	55.67
2	37.14	33.89	34.17	30.21	28.57	24.55
3	55.01	50.30	47.76	61.63	55.29	48.38
4	36.07	35.57	36.91	34.46	36.26	38.28
5	23.90	24.57	25.34	22.91	23.77	23.89
6	38.15	35.31	36.62	44.82	53.16	40.37
7	49.98	40.20	41.47	36.82	33.42	29.52
8	19.25	19.27	19.09	19.08	20.50	21.83
9	22.03	21.03	19.76	19.46	16.69	16.69

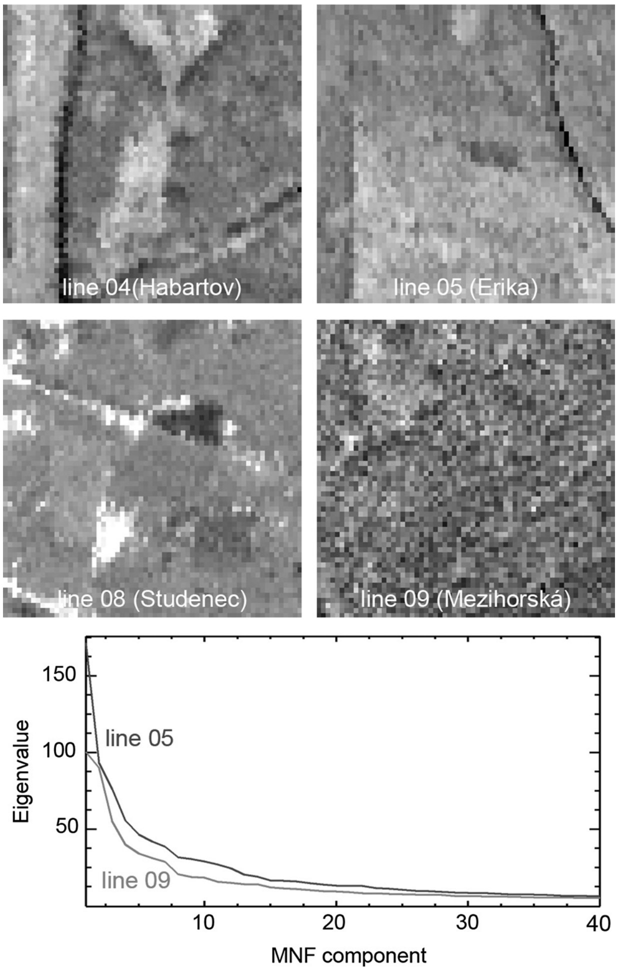

Fig. 2 Upper: The first MNF component of the studied localities, the high amount of noise is visible particularly for flight line No. 9. Bottom: MNF Eigenvalues calculated for the whole flight line images—flight lines numbers 05 and 09. They also show that flight line No. 9 suffers from significantly higher noise levels.

the results from the MNF transformation of the HyMap data. The forests were subsequently divided into coniferous and deciduous by applying the MLC method to the selected spectral ratios (R_{742}/R_{558}, R_{1062}/R_{558}, R_{1652}/R_{558}, R_{2192}/R_{558}).

To classify exclusively the Norway spruce forests, the MNF transformation and MLC were then applied again, this time only to the HyMap reflectance pixels that were previously identified as coniferous. Finally, the resultant classification was filtered using a sieve filter to remove very small clumps of pixels. The derived Norway spruce forest mask was then used for all the following calculations and transformations applied to the HyMap data.

4.2 *Statistical Background*

Although the positions of all the trees in each group were measured by a FieldMap laser rangefinder, it was not possible to distinguish individual tree crowns within the HyMap image data due to the relatively low spatial resolution (5 m). This issue needed to be resolved prior to the empirical modeling as an image pixel value could not be associated with the corresponding ground truth data value. Therefore we defined 10 tree groups as the least circumscribed rectangle defined by a cluster of trees (ROI) (Fig. 5). Then the average ground truth value (the average laboratory chlorophyll content calculated for each tree group) could be directly compared with the average pixel value falling within the defined group (ROI).

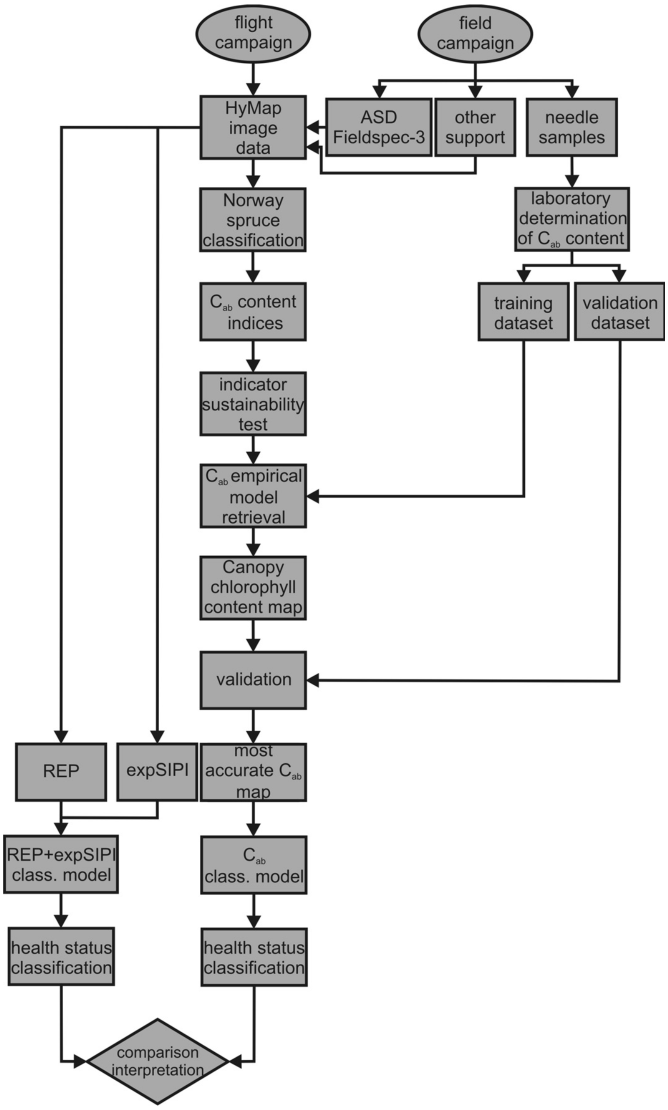

Fig. 3 Data processing workflow.

Basic statistics for each group defined in the following order (Erika: 2 groups A and B; Habartov: 3 groups C, D, and E; Mezihorská: 3 groups F, G, and H; Studenec: 2 groups, I and J, were calculated (Table 3) to ensure the proper definition of training and validation datasets. Studying the data variability within each group and spatial variability within each site, we defined the following two datasets required for further statistical treatment:

- The training dataset that was used to define the regression models: groups A, C, D, F, G, and I.
- The validation dataset that was used to validate the obtained models for C_{ab}: groups B, E, H, and J.

4.3 *Retrieval of the Chlorophyll Content*

For the further empirical modeling of chlorophyll content (C_{ab}), we used the spectral transformations as follows:

- Vegetation indices.
- Stepwise multiple regression (SMR) models.

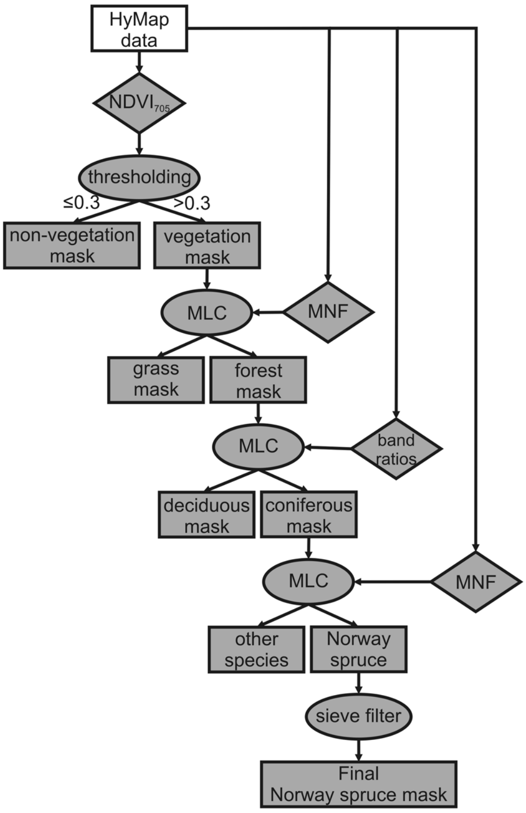

Fig. 4 HyMap data classification workflow. MNF-minimum noise fraction, MLC-maximum likelihood classifier.

- Ratio indices derived from the first-derivative spectra.
- Normalized reflectance models.

4.3.1 *Vegetation indices*

The vegetation indices models are based on the simple linear relationship between the chlorophyll content concentration and the vegetation index. The first group of vegetation indices is based on the (normalized) ratios of a few selected bands. We selected the $NDVI_{705}$[58] and a simple ratio Vogelmann red-edge index (VOG).[59]

Furthermore, we calculated the position of the inflection point of the spectral reflectance curve in red-edge part of the spectra red-edge position (REP)[42] as it allows assessing the

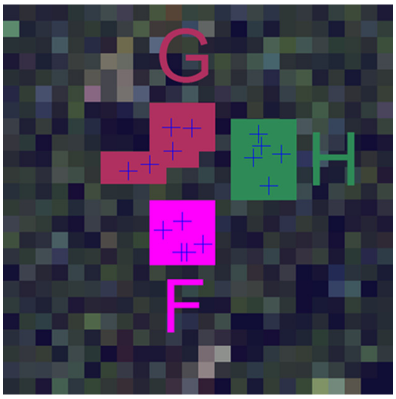

Fig. 5 Examples of the defined ROIs.

Table 3 Description statistics of the laboratory chlorophyll content values.

Group	Locality	Use	C_{ab} (min) [mg/g]	C_{ab} (max) [mg/g]	C_{ab} (mean) [mg/g]	C_{ab} (std) [mg/g]
A	Erika	calibration	1.7260	3.4439	2.7146	0.6251
C	Habartov	calibration	2.1862	3.5375	2.8805	0.4930
D	Habartov	calibration	2.0755	3.1775	2.6008	0.3646
F	Mezihorská	calibration	1.8657	2.3356	2.1417	0.1699
G	Mezihorská	calibration	1.6008	2.3668	2.0292	0.2780
I	Studenec	calibration	2.3670	3.2668	2.9070	0.3121
calibration (the whole dataset)			1.6008	3.5375	2.5456	0.5373
B	Erika	validation	2.0485	3.3826	2.5832	0.4995
E	Habartov	validation	1.8710	2.9022	2.1765	0.3738
H	Mezihorská	validation	1.5004	2.7110	2.3043	0.4260
J	Studenec	validation	2.6293	3.2483	2.8959	0.2321
validation (the whole dataset)			1.5004	3.3826	2.4899	0.4949

shape of the spectral curve in chlorophyll absorption in the red-edge domain. The calculated point separates the convex and concave parts of the spectral curve (in the red-edge part of the spectrum) and lies on the part with the maximum slope. Therefore it also identifies a point where the first derivative of the spectrum exhibits a maximum. To calculate the position of the red-edge inflection point, we used the four-point interpolation technique described in Ref. 60.

Besides the well-known indices, we tested a new index "chlorophyll absorption depth normalized area under curve between 543 and 760 nm ($\mathrm{CADAC}_{543-760}$)" to retrieve the chlorophyll content of the Norway spruce based on similar principles as the $\mathrm{ANMB}_{650-725}$ index.[61] The $\mathrm{CADAC}_{543-760}$ index also utilizes the continuum-removed spectrum and is defined as the area under the reflectance curve between 543 and 760 nm, while each band within this interval is normalized to the maximum depth of the chlorophyll absorption feature (at 675 nm) (Fig. 6):

$$\mathrm{CADAC}_{543-760} = 0.5 \cdot \sum_{j=1}^{n-1} (\lambda_{j+1} - \lambda_j) \cdot \left(\frac{\mathrm{BD}_{j+1}}{\mathrm{BD}_{675}} + \frac{\mathrm{BD}_j}{\mathrm{BD}_{675}} \right) \tag{1}$$

where: $\lambda_j \ldots \lambda_{n-1}$ refers to the central wavelength between 543 to 760 nm and $\mathrm{BD}_j \ldots \mathrm{BD}_{n-1}$ is the band depth (BD) of continuum removed reflectance.

4.3.2 *Stepwise multiple regression models*

In addition to the vegetation indices, we tested two multivariate approaches that utilize the bands between 543 to 760 nm to estimate the chlorophyll content.[62] We used SMR[63] to construct a model defining a relationship between the chlorophyll content and (i) spectral derivatives: the first derivatives of the image spectra between 543 and 760 nm, (ii) BD normalization: the continuum-removal transformation[64] was applied to the spectrum between 543 and 760 nm, and then the BD of each spectral band was divided by the depth maximum of the chlorophyll absorption (675 nm for the HyMap data).

4.3.3 *Ratio indices derived from the first-derivative spectra*

We used two spectral derivative indices based on the ratios of the transformed (first derivation) reflectance D_{718}/D_{704} and D_{718}/D_{747}.[65]

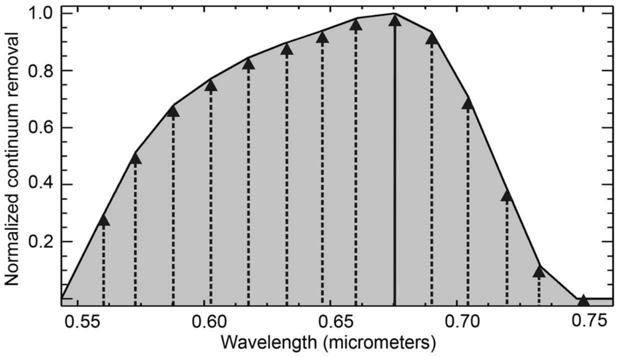

Fig. 6 Chlorophyll absorption and depth normalized area under the curve between 543 to 760 nm ($\text{CADAC}_{543\text{–}760}$).

4.3.4 *Normalized reflectance models*

Another tested approach was based on the normalization of the reflectance to the reflectance minimum at 675 nm (maximal absorption of the chlorophyll) and to the reflectance maximum at 744 nm.[65]

4.4 *Statistical Assessment of the Relationship Between the Canopy Chlorophyll Content and the Spectral Indices Calculated from the HyMap Data*

To test if there is a linear relationship between the chlorophyll content determined in the laboratory for the collected needle samples and the spectral indices derived from the HyMap data, we calculated Pearson's correlation coefficient (see Sec. 5.1) using the training dataset of the group trees (A, C, D, F, G and I). All the independent variables (see 4.3) as well as the dependent variable (laboratory chlorophyll content, C_{ab}) have passed the Shapiro-Wilk normality test[66] (p-value > 0.05) and proved to have normal distributions (Table 4).

After the normal distribution of all the variables was demonstrated, we could test whether the value of the correlation coefficient was large enough to reject the zero-value hypothesis stating the correlation coefficient is equal to 0. By rejecting this hypothesis, we demonstrated that the spectral indicators and the chlorophyll content are not independent. The confidence level was set at 98.5%. Following the statistical testing described above, the linear regression models were then applied to the spectral indices data to predict the canopy chlorophyll content.

Using the training dataset (tree groups A, C, D, F, G, and I), the coefficient of determination (R^2) between each spectral index and the C_{ab} content was calculated (Table 5), describing the amount of data variability explained. The validation dataset (tree groups B, E, H, and J) was then used to validate the accuracy and consistency of the chlorophyll prediction models by calculating the RMSE and coefficients of determination of predicted versus measured C_{ab} values (Rv^2) (Table 6).

4.5 *Vegetation Health Status Classification Method*

The main aim of the study was to develop a statistical method allowing qualitative classification of the forest stands based on their health status. We selected four indicators of vegetation health that are based on the plant/forest spectral property:

1. Total canopy chlorophyll content (C_{ab}) (D_{718}/D_{704})[65]
2. Position of the inflection point of the spectral curve in the red-edge part of spectrum (REP)[42]
3. Photosynthetic reflectance index (PRI)[43]
4. Structure insensitive pigment index (SIPI)[44]

Table 4 Results of the Shapiro-Wilk normality test for chlorophyll content (C_{ab}) values (laboratory determined) and the spectral transformation image products (p-value—significance; W—Shapiro-Wilk test statistic).

Variable	p-value	W
C_{ab}	0.1862	0.8936
NDVI_{705}	0.4348	0.9287
VOG	0.4745	0.9327
REP	0.1667	0.8893
$\text{CADAC}_{543–760}$	0.3900	0.9238
SMR spectral derivative model	0.7879	0.8992
Continuum removal BD normalization model	0.1877	0.8939
D_{718}/D_{701}	0.6273	0.9465
D_{718}/D_{747}	0.7430	0.9563
N_{690}	0.0599	0.8512
N_{704}	0.2197	0.9001
N_{718}	0.2393	0.9035
N_{733}	0.5920	0.9435

Table 5 Training dataset: Pearson's correlation coefficient (r_{xy}), coefficient of determination (R^2) and the t-test results.

Spectral indicator	r_{xy} (Pearson)	Critical value ($\alpha = 0.05$)	t	R^2
NDVI_{705}	0.8517	2.776	3.2509	0.7254
VOG	0.9085	2.776	4.3494	0.8255
REP	0.9397	2.776	5.4932	0.8830
$\text{CADAC}_{543–760}$	0.8899	2.776	3.9026	0.7920
SMR spectral derivative model[a] (D_{632}, D_{661}, D_{544})	−0.9225 −0.6931 0.2558	X	X	0.99998
Continuum removal BD normalization model (R_{CR}norm705)	0.9398	2.776	5.5003	0.8831
D_{718}/D_{704}	0.9555	2.776	6.4782	0.9131
D_{718}/D_{747}	−0.8807	2.776	3.7186	0.7756
N_{690}	−0.9013	2.776	4.1612	0.8124
N_{704}	−0.9306	2.776	5.0847	0.8660
N_{718}	−0.9563	2.776	6.5413	0.9146
N_{733}	−0.8914	2.776	3.9337	0.7946

[a] partial correlation coefficients between canopy chlorophyll content and each variable of the multivariate regressions.

Table 6 Validation dataset: Validation of the total canopy chlorophyll content retrieved from the HyMap image data. Root mean square error (RMSE), Rv^2—coefficient of determination of the predicted versus measured values of the chlorophyll content.

Spectral indicator	RMSE (mg/g)	Rv^2
$NDVI_{705}$	0.2278	0.8960
VOG	0.2269	0.9340
REP	0.3840	0.9050
$CADAC_{543-760}$	0.3395	0.9114
SMR spectral derivative model(D_{632}, D_{661}, D_{544})	0.7962	$1 \cdot 10^{-5}$
continuum removal BD normalization model (R_{CR}norm705)	0.2832	0.9328
D_{718}/D_{704}	0.2055	0.9370
D_{718}/D_{747}	0.2456	0.9880
N_{690}	0.4305	0.8254
N_{704}	0.2833	0.9293
N_{718}	0.2664	0.9440
N_{733}	0.2736	0.9905

The canopy chlorophyll content was estimated using the empirical model that yielded the best results after the validation (see Results, part 5.1).

The amount of green biomass and canopy chlorophyll content primarily determine the position of the inflection point of the spectral curve in the red-edge region. Increasing chlorophyll concentration causes broadening of the major chlorophyll absorption feature around 675 nm and thus causes a shift in the inflection point towards longer wavelengths.[67–71] On the other hand, vegetation stress (e.g., the presence of heavy metals in the soil) might cause a shift in the inflection point to shorter wavelengths.[72] Therefore we also included REP (described in 4.3.1) in the further statistics, as it can serve as an indicator of the vegetation stress.[42,71,73,74]

The PRI was originally defined by Ref. 43 and proposed as an indicator of the de-epoxidation of the carotenoids—xanthophyll pigments; they are related to light-absorption mechanisms and closely linked with light use efficiency and carbon dioxide uptake;[43,75] and Refs. 76 and 77 propose to use this index as an indicator of water stress.

The SIPI was designed by Ref. 44 to maximize the sensitivity of the index to the ratio of bulk carotenoids to chlorophyll while decreasing sensitivity in the canopy structure. Due to the relative low dynamic range of the SIPI values, we used its exponential transformation (expSIPI) in further analysis.

We must emphasize that, except for the canopy chlorophyll content, none of these indices give direct quantitative information on any particular vegetation biochemical parameter. Instead, they are intended to map only relative amounts, which can be further interpreted in terms of the condition of the ecosystem.

The statistical relationship between the estimated canopy chlorophyll content and the selected indicators (e.g., REP, PRI, and SIPI) was assessed (Fig. 7). We found that the value of PRI did not change much for the Norway spruce in the entire area of interest and thus didn't show high enough variability. In addition, the direct relationship of PRI to the chlorophyll content was also relatively weak. Therefore we decided to exclude the PRI index from further investigations.

The values of the three selected indices were transformed into standardized z-scores (Table 7) to ensure their comparability and independence of their physical dimensions (units).

Z-scores generally express how far from the mean the particular value is in terms of the standard deviations (σ). Two products were created using the obtained normalized z-score

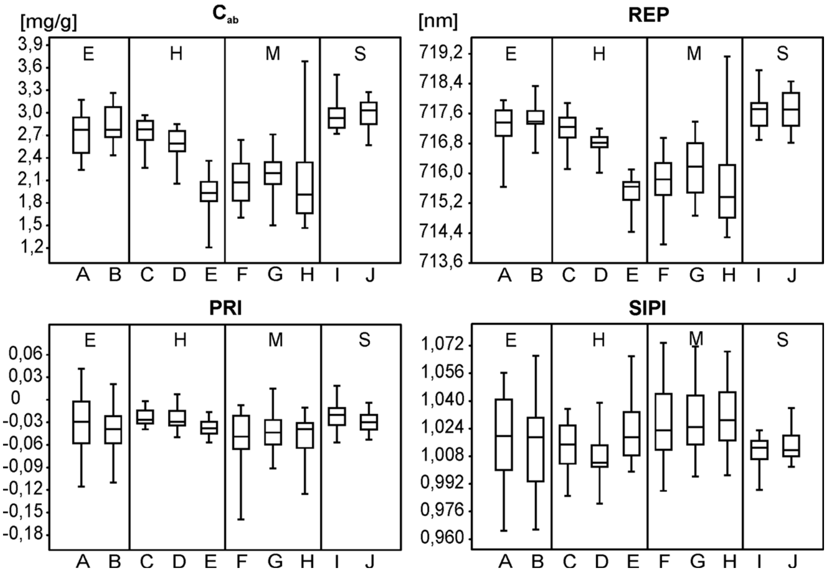

Fig. 7 The selected indicator variability within the studied test sites/groups of trees. C_{ab}—content of chlorophyll $a + b$, REP—position of the inflection point of the spectral curve in the red-edge part of the spectrum; photochemical reflectance index (PRI); structure insensitive pigment index (SIPI); A through J, 10 groups of five sampled trees.

values. First the map of chlorophyll content was classified into five classes defined by the following threshold values (Fig. 8):

Class 1: values $<$ mean $- 1.0\sigma$
Class 2: mean $- 1.0\sigma <$ values $<$ mean $- 0.5\sigma$
Class 3: mean $- 0.5\sigma <$ values $<$ mean $+ 0.5\sigma$
Class 4: mean $- 0.5\sigma <$ values $<$ mean $+ 1.0\sigma$;
Class 5: values $>$ mean $+ 1.0\sigma$.

In addition to the classified chlorophyll content map, we created another raster product that combined the information from both indicators REP and expSIPI. REP has the same directly proportional relationship with the vegetation health as the chlorophyll content, and REP was therefore classified identically. On the other hand, expSIPI needed to be classified in the reverse order as the higher values reflect higher carotenoid-to-chlorophyll contents and thus worse vegetation health (in this case Class 1 was calculate as values $>$ mean $+ 1.0\sigma, \ldots,$ Class 5 as values $<$ mean $- 1.0\sigma$). To create the final raster combining the information from REP and expSIPI, they were both summarized and one raster ranging from 2 to 10 was obtained. These values were finally linearly reclassified into the 1 to 5 range to make this output comparable with the C_{ab} raster (Fig. 9). As a result, in both maps (C_{ab} and REP + exp SIPI) the Class 1 indicates worse health status for the trees without visible damage symptoms and Class 5 represents the values indicating the healthiest trees.

Table 7 Threshold values of selected indicators used for the further health status assessment. Mean (μ) and standard deviation (σ).

Health status indicator	-1.0σ	-0.5σ	$+0.5\sigma$	$+1.0\sigma$	μ
C_{ab}[mg/g]	1.914	2.219	2.828	3.132	2.523
REP [nm]	715.508	716.107	717.306	717.905	716.706
expSIPI	2.683	2.724	2.806	2.847	2.765

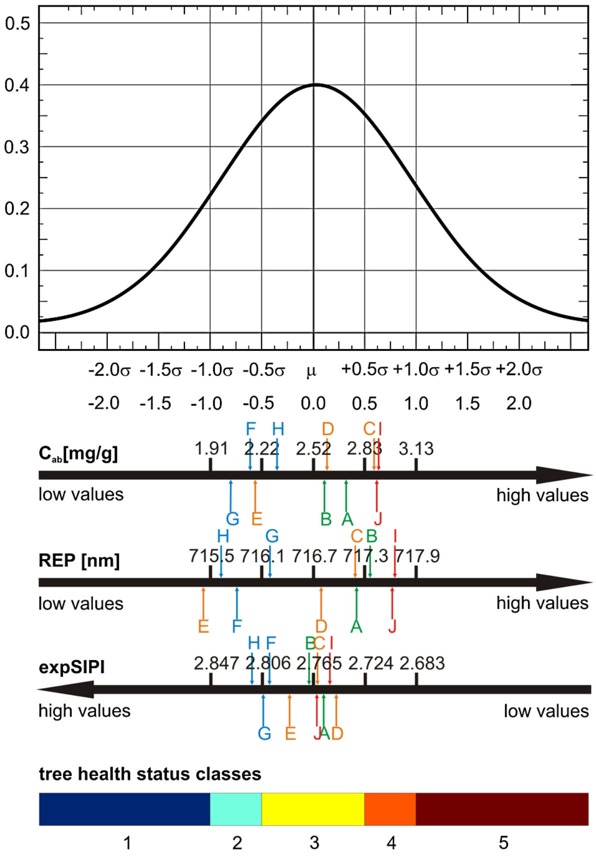

Fig. 8 Scheme showing how the suggested statistical method was constructed. The *z*-normalized values of all three selected indicators are classified into Classes 1 through 5 using the standard deviation (σ) classification method. The studied groups of trees (A through *J*) are projected on an absolute scale for each indicator. The colors correspond with the locations of the studied groups of trees (green A, $B =$ Erika; orange C, D, $E =$ Habartov; blue H, $G =$ Mezihorská; and red I, $J =$ Studenec). C_{ab}—content of chlorophyll $a + b$, REP—Position of the inflection point of spectral curve in red-edge part of spectrum, expSIPI—exponentially transformed structure insensitive pigment index.

5 Results and Discussion

5.1 *Validation and Prediction of the Canopy Chlorophyll Content (C_{ab})*

In both multivariate approaches, the SMR spectral derivative and the continuum removal BD normalization models, the null hypothesis was tested employing SMR. As a result, three different derivative variables (the derivative of the bands with central wavelengths 632, 661, and 544 nm) and only one normalized band ($R_{\mathrm{CRnorm705}}$) passed this test and where further used (Table 5).

Using the training dataset (A, C, D, F, G, and I), we obtained the models that all attained r_{xy} high enough to pass the initial *t*-test (Table 5).

For the validation dataset (groups B, E, H, and J), the statistical parameters, Rv^2 and RMSE (Table 6), were used to test how well the linear models can predict the chlorophyll content, and the image average values were compared with the average values of the chlorophyll content obtained in the laboratory (ground truth).

In general, we obtained rather high coefficients of determination for the linear models calculated between the tested spectral indices and the ground truth dataset (canopy chlorophyll content) on both the training and the validation datasets (R^2, Rv^2). These results confirmed the assumption of a strong dependence between the selected spectral indicators and the canopy

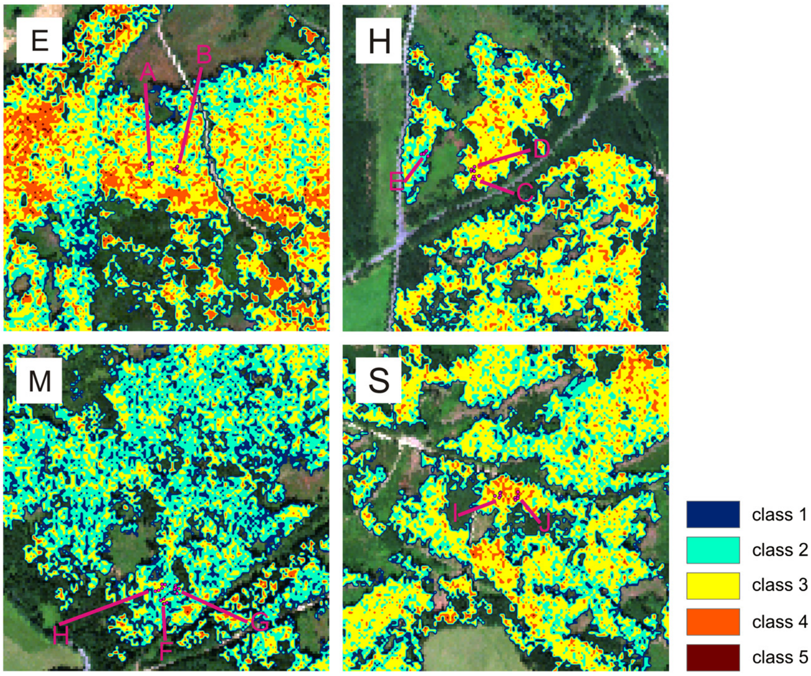

Fig. 9 Statistical classification of the Norway spruce health status by integrating the C_{ab}, REP, and expSIPI. E = Erika; H = Habartov; M = Mezihorská; S = Studenec study sites; A through J; 10 defined tree groups. Color scale 1 through 5—health status classes for the trees without visible damage symptoms; 1 = the worst and 5 = the best result (see Fig. 8).

chlorophyll contents. The scatterplots between ground (laboratory) chlorophyll content value and selected image derived spectral indices are shown in Fig. 10.

For the training dataset (Table 5), the highest correlation coefficients (strongest linear relationship) were obtained for the normalized reflectance (N_{718}) and the derivative ratio (D_{718}/D_{704}) models. The weakest correlation was found for the NDVI_{705} index. The strong negative correlations between the canopy chlorophyll content and the normalized reflectances (N_{690}, N_{704}, N_{718}, and N_{733}) are in accordance with the theoretical background. The higher the chlorophyll concentration, the higher is the absorption of radiation and the lower is the observed reflectance. SMR analysis found a valid result only for the multiple linear regression of spectral derivatives. For this particular case, we were able to calculate only the partial correlation coefficients between each independent variable (spectral index) and the dependent variable chlorophyll content (chlorophyll content). Therefore the general coefficient (r_{xy}) was not defined for this model.

Comparing R^2 (Table 5) to RMSE (Table 6) indicates that the model exhibiting the highest R^2 does not necessarily give the best result. This can be demonstrated on the example of the multiple linear model calculated from the spectral derivatives. Despite the very high value of $R^2(R^2 = 0.99998)$, the model has the highest RMSE ($\mathrm{RMSE} = 0.7962\ \mathrm{mg/g}$, relative $\mathrm{RMSE} = 32\%$). We assume this is due to the rather high noise level, which was multiplied by calculating the first derivatives from the image spectrum.

The variability and the dynamic range of the predicted values for the chlorophyll contents were compared with the ground truth dataset using box plot diagrams. The box plots constructed for the predicted C_{ab} values (D_{718}/D_{708}) and the ground truth C_{ab} data (Fig. 11) exhibit good agreement for the Studenec and Erika sites. In contrast, a worse match was found for the Mezihorská test site, where extremely high variability of the predicted values can be observed. This can be explained by the low radiometric quality of the HyMap line (line No. 9) where the site is located. This particular line No. 9 suffers from a very high noise level compared with the other HyMap lines acquired in 2009 (see Chap. 3, Table 2, Fig. 2).

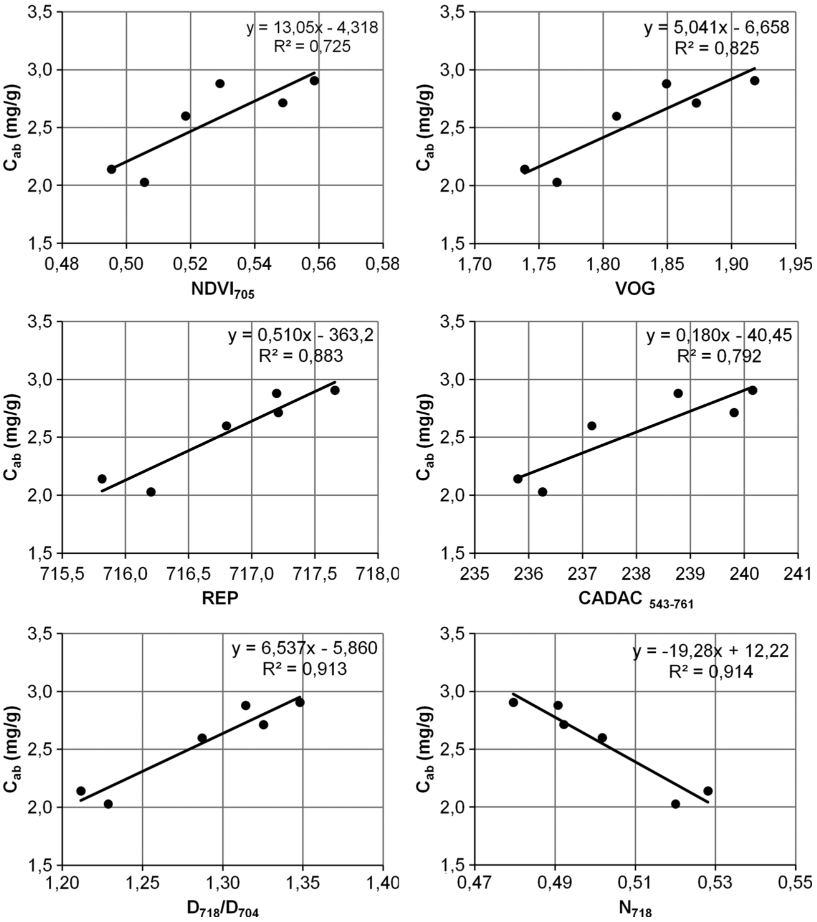

Fig. 10 Scatterplots between ground (laboratory) measured chlorophyll content and selected image derived hyperspectral indices.

The best result taking in account R^2, Rv^2, and RMSE was obtained using the model based on the D_{718}/D_{708} ratios ($R^2 = 0.9131$, $Rv^2 = 0.9370$, $\text{RMSE} = 0.2055$ mg/g, and relative $\text{RMSE} = 8\%$). Therefore the D_{718}/D_{708} model was applied to the all HyMap image data (lines 1 through 9) to retrieve the map of the canopy chlorophyll content (Fig. 12). This output was further used to assess the canopy health status.

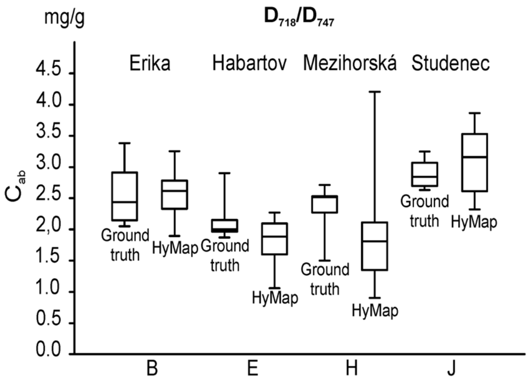

Fig. 11 Box plots of the measured (ground truth) and the predicted (HyMap) canopy chlorophyll contents for the derivative ratio index (D_{718}/D_{708}—content of chlorophyll $a + b$ (g of pigment related to dry mass).

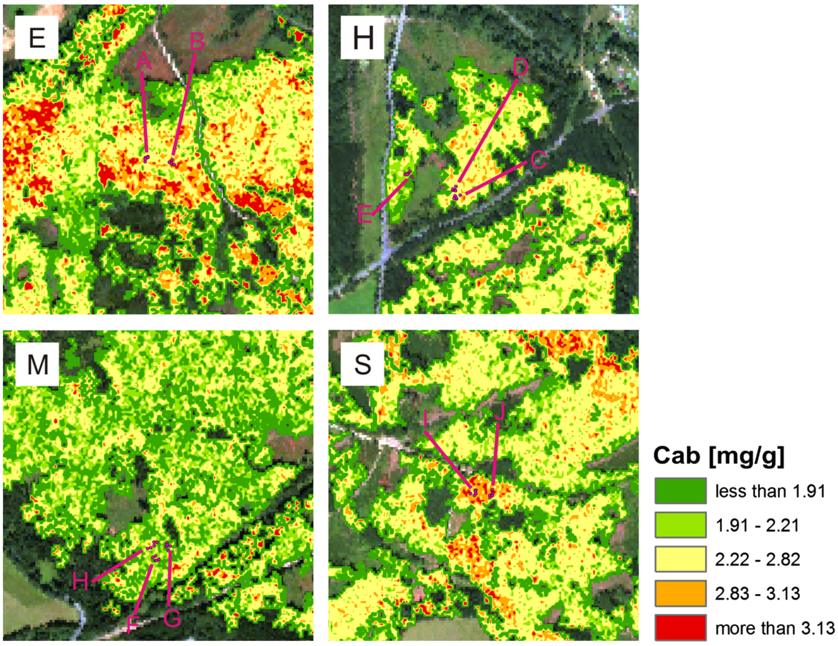

Fig. 12 Map of the Norway spruce canopy chlorophyll content derived by applying the D_{718}/D_{704} regression model. E = Erika; H = Habartov; M = Mezihorská; S = Studenec. C_{ab}—content of chlorophyll $a + b$ (mg of pigment related to dry mass); A through J—10 groups of five sampled trees.

5.2 *Assessment of the Norway Spruce Health Status*

Two statistical scenarios, C_{ab} and REP + exp SIPI, were tested to assess and classify the Norway spruce health status (see Chap. 4.5). Both scenarios were applied to all the pixels classified as homogenous Norway spruce forest in the HyMap image data (lines 1 through 9) (Fig. 9).

In both cases, C_{ab} and REP + exp SIPI, the frequency histograms (Figs. 13 and 14) show rather symmetrical distribution that is close to the Gaussian normal distribution. However, the histograms computed for each test site (Erika, Habartov, Mezihorská, and Studenec) show significant asymmetries. At the Erika site, we can identify slight asymmetry toward the higher-class values, indicating the higher frequencies of average and above-average values. On the other hand, for the Habartov site we can observe slight asymmetry toward the lower-class numbers, indicating the higher frequencies of average and below-average values. For the Mezihorská site, a very strong asymmetry can be observed. The majority (almost 75%) of the pixels were classified into the Classes 1 and 2, while Classes 4 and 5 have very low frequencies. The opposite situation can be observed for the Studenec site, where a strong asymmetry toward the high classes can be observed.

Comparing the two tested classification scenarios (C_{ab} and REP + exp SIPI), the C_{ab} method shows higher data variability. The C_{ab} scenario has higher frequencies of extreme values (Class 1 and Class 5) in contrast with the REP + exp SIPI scenario, where the values are more frequently classified in the average Class 3. This can be explained by the higher variability of the C_{ab} values compared with the expSIPI values.

The laboratory analysis of the Norway spruce needles, collected during the project described in Ref. 61, indicated that higher needle chlorophyll content is not automatically connected with a better health status. Therefore the chlorophyll content itself cannot be the only indicator of damage to the Norway spruce. To take in account this fact, the expSIPI index was used as a correcting factor in the selected model. If the Norway spruce stands have very high C_{ab} and REP values, and the expSIPI values don't indicate any health damage, the pixels fall into average Class 3 instead of being classified in Class 4 or 5.

All the studied sites exhibited soil solution pH values under 3.5 (Table 8), which correspond to low pH threshold for forest soils in the Czech Republic.[46] We assume that soil acidity is the

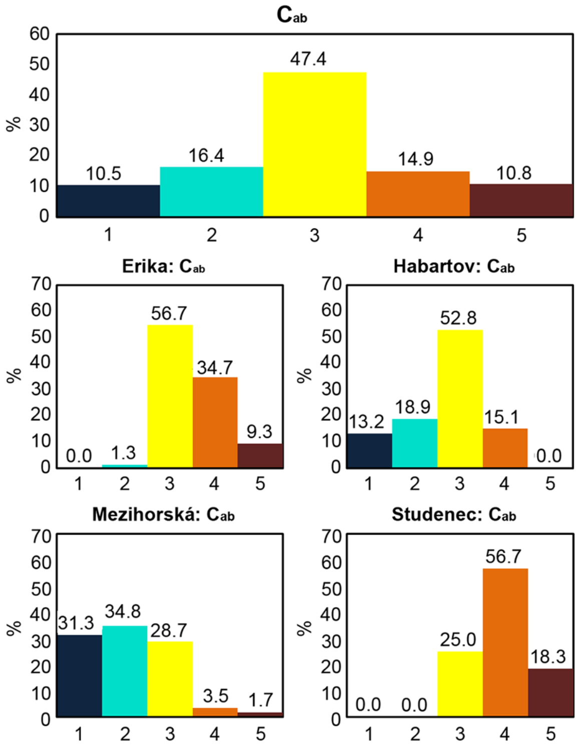

Fig. 13 Relative frequencies (%) of the Norway spruce health status classes obtained for the C_{ab} classification scenario. The entire Sokolov lignite basin area (top) and the individual sites Erika, Habartov, Mezihorská, and Studenec (below).

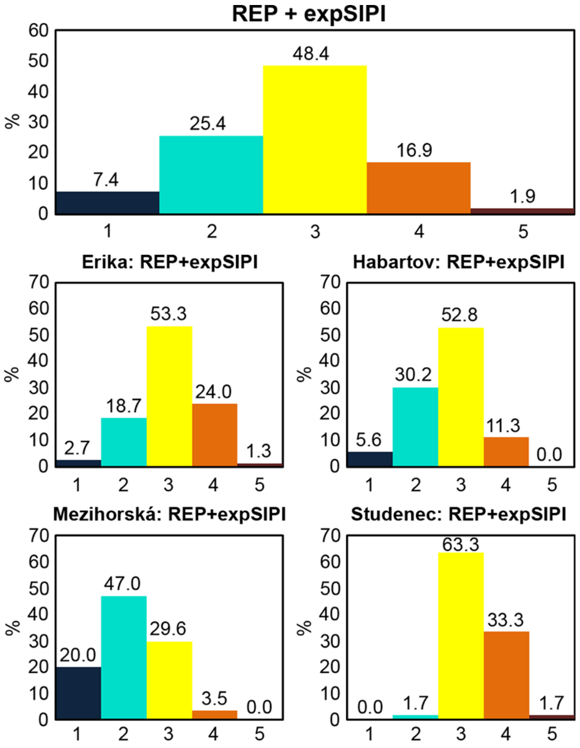

Fig. 14 Relative frequencies (%) of the Norway spruce health status classes obtained by the statistical scenario REP + expSIPI. The entire Sokolov lignite basin area (top) and the individual sites Erika, Habartov, Mezihorská, and Studenec (below).

Table 8 The soil solution pH (in KCl) and $C:N$ ratio for the two organic top horizons. One-way ANOVA.

	pH (KCl)			$C:N$ ratio		
Site	Upper horizons	Lower horizons	Both horizons	Upper horizons	Lower horizons	Both horizons
Erika	2.55^{bb}	$2.50^{d\mathrm{b}}$	$2.53^{d\mathrm{b}}$	$28.06^{ac\mathrm{a}}$	27.10^{ns}	28.40^{ns}
Habartov	$3.18^{ad\mathrm{b}}$	$3.43^{a\mathrm{b}}$	$3.31^{a\mathrm{b}}$	$26.68^{b\mathrm{a}}$	31.80^{ns}	29.24^{ns}
Mezihorská	$2.87^{c\mathrm{b}}$	$2.76^{c\mathrm{b}}$	$2.81^{c\mathrm{b}}$	$28.65^{abc\mathrm{a}}$	27.24^{ns}	27.65^{ns}
Studenec	$3.33^{a\mathrm{b}}$	$2.99^{b\mathrm{b}}$	$3.16^{b\mathrm{b}}$	$29.70^{a\mathrm{a}}$	26.80^{ns}	27.73^{ns}

Different letters indicate significant differences between sites according to Tukey-Krammer multiple comparison test[78]

[a] Significant difference at 0.05.

[b] Significant difference at 0.01.

main stress factor in the studied locality. This finding is supported by the fact that Central Europe and Denmark were considered to be the areas with the highest exceeding of limits for soil acidification indicators, pH and base cations-to-Al ratios in 2010.[79] Soil conditions, especially nutrient availability and balance, determine the physiological status of forest trees. Nutrient imbalances and deficiencies may result in increased susceptibility to a number of stress factors, such as weather extremes or pest invasions.[79] Thus determination of the health status of trees should include evaluation of numerous parameters and should also take into account other factors such as soil pH and the base cations-to-Al ratios, used to estimate the risk of damage to the vegetation from acidified soil (ICP Forests Executive Report, 2010). High values of the organic horizon $C:N$ ratios (above 22) also imply the possibility of lower nitrification[11] and thus slower nutrient turnover or misbalance.

6 Conclusions

According to the ICP Forest methodologies, the main indicators for forest health assessment at Level I consists in evaluation of crown defoliation and foliage discoloration; however several limitations of these indicators have been discussed recently.[6] Although the chlorophyll content could serve as a relevant quantitative forest health indicator, it is not included either in the foliage chemistry indicators of the ICP Forest manual[80] or in the US Forest Service's Forest Inventory and Analysis program.[81] This could be explained by the fact that large-scale assessment of the chlorophyll content could be problematic due to laboriousness and high costs of the needle sampling and biochemical analyses. At the present time, hyperspectral technologies provide an opportunity to retrieve a reliable continuous chlorophyll model while requiring only a reasonable number of samples.

Although the chlorophyll content in foliage is quite often declared to be an indicator of plant physiological status,[82] the uniform classification of chlorophyll contents for Norway spruce needles is not yet very well established. To date, no fixed threshold values of needle chlorophyll content for determination exact classes of forest health status exists. The actual chlorophyll content in the needles of coniferous trees depends on the local and microclimatic conditions, including geographical factors such as latitude and altitude.[83] Particularly the altitude correspond with a combination of several environmental factors, such as irradiance,[17,18] temperature, water, and nutrient availability, which are all factors that influence the chlorophyll content in foliage.[83,84] Oleksyn et al.[83] reported that seedlings of high-altitude Norway spruce populations in colder regions contained higher chlorophyll concentrations in needles than trees at low elevations. According to Ref. 85, the chlorophyll content in needles of healthy mature (60 years and older) Norway spruce (altitude 840 m) ranges between 2.2 to 2.7 mg per gram of dry mass and other authors state even higher chlorophyll contents: 3.21 ± 0.30 mg per gram of dry mass (altitude 400 m)[62] or 4.30 ± 1.06 mg per gram of dry mass (altitude 700 m).[86] Therefore it is necessary in each case to adjust the threshold values of the chlorophyll content to local conditions. We assume that our model could be applied to other spruce or coniferous species, but at least minimal ground truth calibration and laboratory analyses of pigment contents are advisable. It appears that local environmental conditions affect the chlorophyll content even more strongly than the difference between two spruce species. According to Barsi et al.,[84] the difference in chlorophyll content in needles of early succession black spruce (1.6 mg per gram of dry mass) and late succession red spruce (1.44 mg per gram of dry mass), both grown under the same controlled conditions, was on average only 10%.

We evaluated the numerous approaches to determine the chlorophyll content empirically. The individual models were statistically assessed using the ground truth training/validation datasets and the best model based on the spectral derivative ratio (D_{718}/D_{704}, RMSE $= 0.2055$ mg/g, $R^2 = 0.9370$) was chosen to estimate the chlorophyll (C_{ab}) content for the Norway spruce species using the HyMap multiflight line data. Then we developed a new statistical method to assess the physiological status of macroscopically undamaged foliage of Norway spruce. As the chlorophyll content alone may not correspond sufficiently well to the physiological/health status, the suggested method utilizes three indicators (C_{ab}, REP, expSIPI). Thus the suggested method takes in account the two major biochemical parameters that are closely connected with photosynthetic functions (chlorophylls and carotenoids), and it allows assessing of the vegetation stress in a more objective way.

Based on our z-score classification of the needle chlorophyll content, the medium health status class of trees lacking visible damage symptoms (Class 3, chlorophyll content 2.22 to 2.83 mg per gram dry mass) corresponds well with the chlorophyll values reported by Ref. 84. This accordance suggests the possibility of the general applicability of our model after further testing and validation.

Acknowledgments

The research is being undertaken as part of a larger HYPSO scientific research project within the framework of grant No. 205/09/1989 funded by the Czech Science Foundation. Many thanks belong to Dr. Jan Frouz for his technical support of the field campaign and to all the students who participated in sample collection.

References

1. R. B. Jackson et al., "Protecting climate with forests," *En. Re. Lett.* **3**(4), 044006 (2008), http://dx.doi.org/10.1088/1748-9326/3/4/044006.
2. G. B. Bonan, "Forest and climate change: forcing, feedbacks and their climate benefits of forests," *Science* **320**(5882), 1444–1449 (2008), http://dx.doi.org/10.1126/science.1155121.
3. R.Hassan and N. Scholes, Eds., *Ecosystems and Human Well-being: Current State and Trends*, p. 815, Island Press, Washington, DC (2005).
4. J. C. Aznar et al., "Lead exclusion and copper translocation in black spruce needles," *Water Air Soil Poll.* **203**(1–4), 139–145 (2009), http://dx.doi.org/10.1007/s11270-009-9997-8.
5. P. Šebesta et al., "Acidification of primeval forests in the Ukraine Carpathians: vegetation and soil changes over six decades," *Forest Ecology Manag.* **262**(7), 1265–1279 (2011), http://dx.doi.org/10.1016/j.foreco.2011.06.024.
6. J. Johnson and M. Jacob, "Monitoring the effects of air pollution on forest condition in Europe: is crown defoliation an adequate indicator?" *iForest* **3**, 86–88 (2010), http://dx.doi.org/10.3832/ifor0538-003.
7. Large scale forest condition. [on-line], http://icp-forests.net/page/largescale-forest-condition.
8. ICP forest assessment—level II. [on-line], http://icp-forests.net/page/level-ii.
9. S. L. Ustin et al., "Retrieval of foliar information about plant pigment systems from high resolution spectroscopy," *Re. Sens. Envir.* **113**, S67–S77 (2009), http://dx.doi.org/10.1016/j.rse.2008.10.019.
10. R. F. Kokaly et al., "Characterizing canopy biochemistry from imaging spectroscopy and its application to ecosystem studies," *Re. Sens. Envir.* **113**, S78–S91 (2009), http://dx.doi.org/10.1016/j.rse.2008.10.018.

11. S. V. Ollinger et al., “Regional variation in foliar chemistry and N cycling among forests of diverse history and composition,” *Ecology* **83**(2), 339–355 (2002), http://dx.doi.org/10.2307/2680018.
12. J. S. Delegido et al., “Estimating chlorophyll content of crops from hyperspectral data using a normalized area over reflectance curve (NAOC),” *Inter. J. App. Earth Ob. Geoinfo.* **12**(3), 165–174 (2010), http://dx.doi.org/10.1016/j.jag.2010.02.003.
13. D. H. Card, D. L. Peterson, and P. A. Matson, “Prediction of leaf chemistry by the use of visible and near infrared reflectance spectroscopy,” *Re. Sens. Envir.* **26**(3), 123–147 (1988), http://dx.doi.org/10.1016/0034-4257(88)90092-2.
14. D. L. Peterson et al., “Remote sensing of forest canopy and leaf biochemical contents,” *Re. Sens. Envir.* **24**, 85–108 (1988), http://dx.doi.org/10.1016/0034-4257(88)90007-7.
15. A. Gitelson et al., “Remote estimation of canopy chlorophyll content in crops,” *Geophys. Re. Lett.* **32**, 4–7 (2005), http://dx.doi.org/10.1029/2005GL022688.
16. B. Datt, “A new reflectance index for remote sensing of chlorophyll content in higher plants: tests using eucalyptus leaves,” *J. Plant Phy.* **154**(1), 30–36 (1999), http://dx.doi.org/10.1016/S0176-1617(99)80314-9.
17. A. D. Richardson, G. P. Berlyn, and T. G. Gregoire, “Spectral reflectance of Picea rubens (Pinaceae) and Abies balsama (Pinaneae) needles along an elevational gradient, Moosilau-keMt., New Hampshire,” *1. Am. J.Botany* **88**(4), 667–676 (2001), http://dx.doi.org/10.2307/2657067.
18. A. D. Richardson, J. B. Reeves, and T. G. Gregoire, “Multivariate analyses of visible/near infrared (VIS/NIR) absorbance spectra reveal underlying spectral differences among dried, ground conifer needle samples from different growth environments,” *New Phytologist* **161**(1), 291–301 (2004), http://dx.doi.org/10.1046/j.1469-8137.2003.00913.x.
19. P. J. Kramer, “Carbon dioxide concentration, photosynthesis and dry matter production,” *BioScience* **31**(1), 29–33 (1981), http://dx.doi.org/10.2307/1308175.
20. G. A. Blackburn, “Hyperspectral remote sensing of plant pigments,” *J. Exper. Botany* **58**(4), 855–867 (2007), http://dx.doi.org/10.1093/jxb/erl123.
21. C. Wu et al., “Estimating chlorophyll content from hyperspectral vegetation indices: modeling and validation,” *Agr. Forest Meteorol.* **148**(8–9), 1230–1241 (2008), http://dx.doi.org/10.1016/j.agrformet.2008.03.005.
22. B. Demming-Adams and W. W. Adams, “The role of xanthophyll cycle carotenoids in the protection of photosynthesis,” *Trends Plant Sci.* **1**(1), 21–26 (1996), http://dx.doi.org/10.1016/S1360-1385(96)80019-7.
23. J. J. Landsberg et al., “Energy conversion and use in forest: an analysis of forest production in terms of radiation utilization efficiency,” H. L.Gholz, K. Nakane, and H. Shimoda, Eds., *The Use of Remote Sensing in the Modeling of Forest Productivity*, pp. 273–298, Kluver Academic Publishers, Dordrecht, The Netherlands(1996).
24. A. Young and G. Britton, “Carotenoids and stress,” R. G.Alscher and J. R. Cummings, Eds., *Stress Responses in Plants: Adaptation and Aclimation Mechanisms*, pp. 87–112, Willey-Liss, New York (1990).
25. Z. Malenovský et al., “Scaling dimensions in spectroscopy of soil and vegetation,” *Internat. J. App. Earth Ob. Geoinfo.* **9**(2), 137–164 (2007), http://dx.doi.org/10.1016/j.jag.2006.08.003.
26. R. Pu, P. Gong, and Q. Yu, “Comparative analysis of EO-1 ALI and Hyperion, and Landsat ETM+ data for mapping forest crown closure and leaf area index,” *Sensors* **8**(6), 3744–3766 (2008), http://dx.doi.org/10.3390/s8063744.
27. D. R. Peddle et al., “Physically-based inversion modeling for unsupervised cluster labeling, independent forest classification and LAI estimation using MFM-5-scale,” *Can. J. Re. Sens.* **33**(3), 214–225 (2007), http://dx.doi.org/10.5589/m07-026.
28. B. D. Ganapol et al., “LEAFMOD: a new within-leaf radiative transfer model,” *Re. Sens. Envir.* **63**(2), 182–193 (1998), http://dx.doi.org/10.1016/S0034-4257(97)00134-X.
29. S. Jacquemoud and F. Baret, “PROSPECT: a model of leaf optical properties spectra,” *Re. Sens. Envir.* **34**(2), 75–91 (1990), http://dx.doi.org/10.1016/0034-4257(90)90100-Z.
30. C. S. T. Daughtry et al., “Estimating corn leaf chlorophyll concentration from leaf and canopy reflectance,” *Re. Sens. Envir.* **74**(2), 229–239 (2000), http://dx.doi.org/10.1016/S0034-4257(00)00113-9.

31. D. Haboudane et al., “Integrated narrow-band vegetation indices for prediction of crop chlorophyll content for application to precision agriculture,” *Re. Sens. Envir.* **81**(2–3), 416–426 (2002), http://dx.doi.org/10.1016/S0034-4257(02)00018-4.
32. R. A. Jago, M. E. Cutler, and P. J. Curran, “Estimating canopy chlorophyll concentration from field and airborne spectra,” *Re. Sens. Envir.* **68**(3), 217–224 (1999), http://dx.doi.org/10.1016/S0034-4257(98)00113-8.
33. W. Verhoef, “Light-scattering by leaf layers with application to canopy reflectance modeling–the SAIL model,” *Re. Sens. Envir.* **16**(2), 125–141 (1984), http://dx.doi.org/10.1016/0034-4257(84)90057-9.
34. C. van der Tol et al., “An integrated model of soil-canopy spectral radiance observations, photosynthesis, fluorescence, temperature and energy balance,” *Biogeosciences Disc.* **6**, 6025–6075 (2009), http://dx.doi.org/10.5194/bgd-6-6025-2009.
35. V. Demarez and J. P. Gastellu-Etchegorry, “A modeling approach for studying forest chlorophyll content,” *Re. Sens. Envir.* **71**(2), 226–238 (2000), http://dx.doi.org/10.1016/S0034-4257(99)00089-9.
36. S. Jacquemoud, “Inversion of the PROSPECT + SAIL canopy reflectance model from AVIRIS equivalent spectra: theoretical study,” *Re. Sens. Envir.* **44**(2–3), 281–292 (1993), http://dx.doi.org/10.1016/0034-4257(93)90022-P.
37. S. Chaurasia and V. K. Dadhwal, “Comparison of principal component inversion with VI-empirical approach for LAI estimation using simulated reflectance data,” *Inter. ReJ. Sens.* **25**(14) 2881–2887 (2004), http://dx.doi.org/10.1080/01431160410001685018.
38. R. Houborg and E. Boegh, “Mapping leaf chlorophyll and leaf area index using inverse and forward canopy reflectance modeling and SPOT reflectance data,” *Re. Sens. Envir.* **112**(1) 186–202 (2008), http://dx.doi.org/10.1016/j.rse.2007.04.012.
39. C. Atzberger, “Object-based retrieval of biophysical canopy variables using artificial neural nets and radiative transfer models,” *Re. Sens. Envir.* **93**(2–3), 53–67 (2004), http://dx.doi.org/10.1016/j.rse.2004.06.016.
40. C. Atzberger et al., “Retrieval of wheat bio-physical attributes from hyperspectral data and SAILH + PROSPECT radiative transfer mode,” M.Habermayer, A. Müller, and S. Holzwarth, Eds., in *Proc. of the 3rd EARSeL Workshop on Imaging Spectroscopy*, pp. 473–482, Herrchnig, Germany (2003).
41. Annual Tabular Overview, Air Quality Protection Division, Czech Hydrometeorological Institute, [on-line], http://portal.chmi.cz/files/portaldocs/uoco/tab_roc_CZ.html
42. P. J. Curran, W. R. Windham, and H. L. Gholz, “Exploring the relationship between reflectance red edge and chlorophyll concentration in slash pine leaves,” *Tree Physiology* **15**(3), 203–206 (1995).
43. J. A. Gamon, J. Peñuelas, and C. B. Field, “A narrow-wave band spectral index that track diurnal changes in photosynthetic efficiency,” *Re. Sens. Envir.* **41**(1), 35–44 (1992), http://dx.doi.org/10.1016/0034-4257(92)90059-S.
44. J. Peñuelas, F. Baret, and I. Fiella, “Semi-empirical indices to assess carotenoids/chlorophyll-a ratio from leaf spectral reflectance,” *Photosynthetica* **31**(2), 221–230 (1995).
45. P. Rojík, “New stratigraphic subdivision of the tertiary in the Sokolov Basin in Northwestern Bohemia,” *J. Czech Geological Society* **49**(3–4), 173–186 (2003).
46. P. Fabiánek, Forest Condition and Monitoring in the Czech Republic 1984–2003, Ministry of Agriculture of the Czech Republic and Forestry and Game Management Research Institute, ELAN spol. s.r.o., Přerov, Czech Republic, p. 431 (2004).
47. R. Porra, W. Thompson, and P. Kriedemann, “Determination of accurate extinction coefficients and simultaneous equations for assaying chlorophylls a and b extracted with four different solvents: verification of the concentration of chlorophyll standards by atomic absorption spectroscopy,” *Biochimica et Biophysica Acta* **975**(3), 384–394 (1989), http://dx.doi.org/10.1016/S0005-2728(89)80347-0.
48. A. Welburn, “The spectral determination of chlorophyll-a and chlorophyll-b, as well as total carotenoids, using various solvents with spectrophotometers of different resolution,” *J. Plant Phys.* **144**(3), 307–313 (1994), http://dx.doi.org/10.1016/S0176-1617(11)81192-2.

49. G. Schaepman-Strub et al., "Reflectance quantities in optical remote sensing—definitions and case studies," *Re. Sens. Envir.* **103**(1), 27–42 (2006), http://dx.doi.org/10.1016/j.rse.2006.03.002.
50. R. Richter, "Atmospheric/topographic correction for airborne imagery," ATCOR-4 User Guide, Version 5.0, January 2009, DLR-German Aerospace Centre, D-82234 Wessling, Germany, p. 168 (2009).
51. A. Berk, G. P. Anderson, and L. S. Bernstein, "MODTRAN-4 radiative transfer modeling for atmospheric correction, optical spectroscopic techniques and instrumentation for atmospheric and space research III book series," *Proc. SPIE* **3756**, 348–353 (1999).
52. J. Weyermann, A. Damm, and M. Schaepman, "Comparing empirical and semi-empirical approaches for brdf correction in airborne imaging," (in preparation)
53. J. Verrelst et al., "Angular sensitivity analysis of vegetation indices derived from CHRIS/PROBA data," *Re. Sens. Envir.* **112**(5), 2341–2351 (2008), http://dx.doi.org/10.1016/j.rse.2007.11.001.
54. C. B. Schaaf et al., "First operational BRDF, albedo nadir reflectance products from MODIS," *Re. Sens. Envir.* **83**(1–2), 135–148 (2002), http://dx.doi.org/10.1016/S0034-4257(02)00091-3.
55. D. Schläpfer, "Parametric Geocoding, PARGE Using Guide," Version 2.3, ReSe Applications Schläpfer & Remote Sensing Laboratories University of Zurich, PDF/CD-ROM Edition, Wil SG, p. 195
56. F. van der Meer and S. de Jong, "Quality control: signal to noise characterization," chapter 2, part 9, in *Imaging Spectrometry: Basic Principles and Prospective Application*, International Institute for Geo-information Science and Earth Observation (ITC), pp. 1922 (2002).
57. A. A. Green et al., "A transformation for ordering multispectral data in terms of image quality with implications for noise removal," *IEEE Trans. Geosci. Re. Sens.* **26**(1), 65–74 (1988), http://dx.doi.org/10.1109/36.3001.
58. D. A. Sims and J. A. Gamon, "Relationships between leaf pigment content and spectral reflectance across a wide range of species, leaf structures and developmental stages," *Re. Sens. Envir.* **81**(2–3), 337–354 (2002), http://dx.doi.org/10.1016/S0034-4257(02)00010-X.
59. E. Vogelmann, B. N. Rock, and D. M. Moss, "Red edge spectral measurements from sugar maple leaves," *Inter. J. Re. Sens.* **14**(8), 1563–1575 (1993), http://dx.doi.org/10.1080/01431169308953986.
60. J. G. P. Guyot and F. Baret, "Utilisation de la heute resolution spectrale pour suivre l'état des couverts végétaux," *Proceedings of the 4th International colloquium on spectral signatures of object in remote sensing*, ESA SP-287, Assois, France, 279–286 (1988).
61. Z. Malenovský et al., "A New hyperspectral index for chlorophyll estimation of a forest canopy: area under curve normalized to maximal band depth between 650–725 nm," *EARSel eProceedings* **5**(2), 161–172 (2006).
62. M. Schlerf et al., "Retrieval of chlorophyll content and nitrogen in Norway spruce (Picea abies KarstL.) using imaging spectroscopy," *Inter. J. Appl. Earth Ob. Geoinfo.* **12**(1), 17–26 (2010), http://dx.doi.org/10.1016/j.jag.2009.08.006.
63. R. I. Jennrich, "Stepwise regression," K.Enslein, A. Ralston, and S. Wilf, Eds., *Statistical Methods for Digital Computers*, pp. 76–90, Wiley, New York (1977).
64. R. N. Clark and T. L. Roush, "Reflectance spectroscopy: quantitative analysis techniques for remote sensing appélications," *J. Geo. Re.* **89**(B7), 6329–6340 (1984),http://dx.doi.org/10.1029/JB089iB07p06329.
65. P. K. Entcheva-Campbell et al., "Detection of initial damage in Norway spruce canopies using hyperspectral airborne data," *Inter. J. Re. Sens.* **25**(24), 5557–5583 (2004), http://dx.doi.org/10.1080/0143116041000172605.
66. S. S. Shapiro and M. B. Wilk, "An analysis of variance test for normality (complete samples)," *Biometrika* **52**(3–4), 591–611 (1965), http://dx.doi.org/10.1093/biomet/52.3-4.591.
67. D. M. Gates et al., "Spectral properties of plants," *Appl. Optic.* **4**(1), 11–20 (1965), .
68. W. Collins, G. L. Raines, and F. C. Canney, "Airborne spectroradiometer discrimination of vegetation anomalies over sulphide mineralization–a remote sensing technique," in *90th*

Annual Meeting problems and Abstracts, Geological Society of America Seattle, Vol. **9**, pp. 932–933, Washington, DC (1977).

69. N. H. Horler, J. Barber, and A. R. Barringer, "Effects of heavy metals on the absorbance and reflectance spectra of plants," *Inter. J. Re. Sens.* **1**(2), 121–136 (1980), http://dx.doi.org/10.1080/01431168008547550.
70. F. Boochs et al., "Shape of the red edge as vitality indicator for plants," *Inter. J. Re. Sens.* **11**(10), 1741–1753 (1990), http://dx.doi.org/10.1080/01431169008955127.
71. G. P. W. Clevers et al., "Derivation of the red edge index using MERIS standard band setting," *Inter. J. Re. Sens.* **23**(16), 3169–3184 (2002), http://dx.doi.org/10.1080/01431160110104647.
72. B. N. Rock, T. Hoshizaki, and J. R. Miller, "Comparison of in situ and airborne spectral measurement of the blue shift associated with forest decline," *Re. Sens. Envir.* **24**(1), 109–127 (1988), http://dx.doi.org/10.1016/0034-4257(88)90008-9.
73. D. N. H. Horler, M. Dockray, and J. Barber, "The red edge of plant leaf reflectance," *Inter. J. Re. Sens.* **4**(2), 279–288 (1983), http://dx.doi.org/10.1080/01431168308948546.
74. S. H. Chang and W. Collins, "Confirmation of the airborne biogeophysical mineral exploration technique using laboratory methods," *Econ. Geol. Bull. Soc. Econ. Geol.* **78**(4), 723–736 (1983), http://dx.doi.org/10.2113/gsecongeo.78.4.723.
75. J. A. Gamon, L. Serrano, and J. S. Surfus, "The photochemical reflectance index: an optical indicator of photosynthetic radiation use efficiency across species, functional types and nutrient levels," *Oecologia* **112**(4), 492–501 (1997), http://dx.doi.org/10.1007/s004420050337.
76. F. Thenot, M. Méthy, and T. Winkel, "The Photochemical Reflectance Index (PRI) as a water stress index," *Inter. J. Re. Sens.* **23**(23), 5135–5139 (2002), http://dx.doi.org/10.1080/01431160210163100.
77. L. Súarez et al., "Modeling PRI for water stress detection using radiative transfer models," *Re. Sens. Envir.* **113**(4), 730–744 (2009), http://dx.doi.org/10.1016/j.rse.2008.12.001.
78. C. Y. Kramer, "Extension of multiple range test to group means with unequal number of replications," *Biometrics* **12**(3), 307–310 (1956), http://dx.doi.org/10.2307/3001469.
79. ICP Forests Executive Report 2010, [on-line], http://icp-forests.net/page/icp-forests-executive-report
80. ICP Forests Manual, part XII Sampling and Analysis of Leaves and Needles, [on-line], http://icp-forests.org/pdf/FINAL_Foliage.pdf
81. C. W. Woodal et al., "Status and future of the forest health indicators program of the USA," *Environ. Monit. Assess.* **177**(1–4), 419–436 (2011), http://dx.doi.org/10.1007/s10661-010-1644-8.
82. J. Soukupová, B. N. Rock, and J. Albrechtová, "Comparative study of two spruce species in a polluted mountainous region," *New Phytologist* **150**(1), 133–145 (2001), http://dx.doi.org/10.1046/j.1469-8137.2001.00066.x.
83. J. Oleksyn et al., "Growth and physiology of Picea abies populations from elevational transects: common garden evidence for altitudinal ecotypes and cold adaptation," *Funct. Ecol.* **12**(4), 573–590 (1998), http://dx.doi.org/10.1046/j.1365-2435.1998.00236.x.
84. D. Barsi et al., "Generic variation and control of chloroplast pigment concentrations an related needle-level traits in Picea rubens, Picea marina and their hybrids: moisture and light environmental effects," *Trees—Struct. Funct.* **23**(3), 555–571 (2009), http://dx.doi.org/10.1007/s00468-008-0301-0.
85. D. Siefermannharms, "Light and temperature control of season-dependent changes in the alpha-carotene and beta-carotene content of spruce needles," *J. Plant Phys.* **143**(4–5), 488–494 (1994).
86. C. Atzberger and W. Werner, "Needle reflectance of healthy and diseased Spruce stands," *1st EARSeL Workshop on Imaging Spectroscopy*, pp. 271–283, Remote Sensing Laboratories, University of Zurich, Impression Dumas, Saint-Etiene rance (1998).

Biographies and photographs of the authors are not available.

B. Computation of a distributed glacier surface albedo proxy using airborne laser scanning intensity data and in-situ spectro-radiometric measurements

Remote Sensing of Environment 160 (2015) 31–42

Contents lists available at ScienceDirect

Remote Sensing of Environment

journal homepage: www.elsevier.com/locate/rse

Computation of a distributed glacier surface albedo proxy using airborne laser scanning intensity data and in-situ spectro-radiometric measurements

Philip C. Joerg *, Jörg Weyermann, Felix Morsdorf, Michael Zemp, Michael E. Schaepman

Department of Geography, University of Zurich, Winterthurerstrasse 190, CH-8057 Zurich, Switzerland

ARTICLE INFO

Article history:
Received 16 June 2014
Received in revised form 19 December 2014
Accepted 24 December 2014
Available online 7 February 2015

Keywords:
Airborne laser scanning
LiDAR
Signal intensity
Glacier
Albedo
Radiometric calibration
BRDF

ABSTRACT

In recent years, multi-temporal topographic measurements from airborne laser scanning (ALS) have been increasingly used as a source of spatially explicit and accurate information to calculate geodetic glacier mass balances. Simultaneous to collecting topographic data, most ALS instruments record the backscattered intensity for each laser emission and therefore provide additional information on the reflectance characteristics of the surveyed surface. Along with air temperature, the surface albedo of snow and ice was identified as a major driving factor of glacier melt. Consequently, better knowledge on the spatial distribution of the glacier albedo could substantially improve energy balance based glacier melt modeling. In this study, we collected on-glacier spectro-radiometric and albedometer measurements to serve as a ground reference to radiometrically calibrate high resolution ALS intensity data into a distributed albedo proxy map. This method resulted in an albedo proxy with values between 0.6 on the glacier tongue and 0.9 on fresh snow in high altitudes. 99.6% of all values fell within the albedo boundary conditions, i.e. values between 0 and 1. Corrected near-infrared ALS intensity data provided a distributed product that allows simulating albedo in glacier energy and mass balance models more realistically. Remaining challenges are (i) a different surface albedo response in the visual part of the electromagnetic spectrum, (ii) the low radiometric resolution of the ALS system for higher intensity values, and (iii) an insufficient correction of the snow bi-directional reflectance distribution function (BRDF).

1. Introduction

Glacier ablation is primarily driven by air temperature and net solar radiation (e.g. Ohmura, Bauder, Müller, & Kappenberger, 2007). The glacier surface energy balance describes the amount of energy available for melt and depends not only on the incident radiation, but also on the energy uptake efficiency (cf. Wiscombe & Warren, 1980). This important factor is the surface bi-hemispherical reflectance, further on called albedo, defined as the ratio of reflected to incident radiation, and strongly influencing ablation (Oerlemans, Giesen, & Van Den Broeke, 2009; Schaepman-Strub, Schaepman, Painter, Dangel, & Martonchik, 2006). Snow albedo is inversely correlated with snow grain size and the concentration of impurities in the snow pack whereas ice albedo is mostly dependent on the content of debris and smaller sized mineral and biogenic cover (Brock, Willis, & Sharp, 2000; Oerlemans et al., 2009). Typical value ranges for snow (firn, ice) albedo from measurements and used for glacier energy and mass balance modeling range between 0.6 and 0.9 (0.3–0.55, 0.2–0.35) (e.g. Cuffey & Paterson, 2010; Greuell, Knap, & Smeets, 1997; Klok & Oerlemans, 2004; Machguth, Paul, Hoelzle, & Haeberli, 2006).

Current glacier energy and mass balance models rely on single or multiple albedo values which are usually estimated from literature or modeled, e.g. by simulating albedo as a function of aging snow or snow depth, and often assumed to be spatially homogeneous on a larger part on the glacier surface (Klok & Oerlemans, 2004; Machguth et al., 2006). To improve these assumptions, the albedo can either be measured directly on the glacier (Brock et al., 2000; Sugiyama, Yoshizawa, Huss, Tsutaki, & Nishimura, 2011) or derived from remote sensing data (Knap, Brock, Oerlemans, & Willis, 1999; Stroeve et al., 2005). However, the spatial distribution of albedo on a glacier can be highly variable (Sugiyama et al., 2011) and the spatial resolution of a satellite instrument might not be satisfactory for the application on smaller valley type or mountain glaciers. In addition, passive optical measurements depend on the sun as an illumination source and contain directional effects as a result from isotropic, volumetric and geometrical–optical scattering (summarized as bi-directional reflectance distribution function (BRDF) effects; for terminology see Schaepman-Strub et al. (2006)).

In the past decade, the measurements of the geodetic elevation change of glaciers using airborne laser scanning (ALS) provided operational data (e.g. Abermann, Lambrecht, Fischer, & Kuhn, 2009; Geist, 2005; Joerg, Morsdorf, & Zemp, 2012). As a side product to topographic information, most airborne laser scanning systems record the

---

* Corresponding author. Tel.: +41 44 635 6522.
E-mail address: philip.joerg@geo.uzh.ch (P.C. Joerg).

http://dx.doi.org/10.1016/j.rse.2014.12.017

backscattered intensity providing surface reflectance information in one narrow spectral band (e.g. 1 nm sampling width). For glacier laser scanning applications, typically the near-infrared part of the electromagnetic spectrum is used. Lutz, Geist, and Stötter (2003) showed that a near-infrared wavelength is particularly well suited to derive information on snow and ice characteristics. However, to make use of this information, the data has to be radiometrically corrected for different physical effects (Höfle & Pfeifer, 2007; Kaasalainen et al., 2011; Vain, Kaasalainen, Pyysalo, Krooks, & Litkey, 2009). Finally, the ALS measures in a monostatic configuration, having the same illumination and observation geometries.

In this study, we derive a spatially distributed glacier surface albedo derived from radiometrically calibrated ALS intensity data. However, as only one single narrow band in the near-infrared part of the electromagnetic spectrum is provided by our ALS system, the resulting product is seen as an albedo proxy. To provide suitable reference data, we synchronously collected in-situ spectral reflectance and albedo values at different altitudes on the Alpine glacier. We use the on-glacier reference data from spectro-radiometric measurements at four different locations to derive the broadband albedo. Additionally, we correct all-day albedometer measurements at a single location for topographic effects of the inclined glacier surface and perform a sky view correction to eliminate the influence of the surrounding higher regions on the broadband albedo. Furthermore, we physically pre-process ALS intensities to derive a homogeneous data set, including an assessment of two types of bi-directional reflectance distribution functions (BRDF) of snow. Subsequently, we correlate the corrected ALS intensities with the reference in-situ albedo to generate an albedo proxy map. Finally, we assess and discuss the derived albedo map for its validity and some persistent uncertainties, including a comparison with a broadband albedo map derived from a synchronous multi-spectral aerial camera data set.

2. Study site and data

2.1. Study site

Our study site encloses the Findelengletscher (46° N, 7° 52′ E) located in the Canton Valais, Switzerland. This valley-type glacier is one of the larger ones in the Alps with an area of more than 13 km^2 (in 2010). As it covers an elevation range from 2600 m up to 3900 m a.s.l., it is expected to sustain multiple decades from now on, despite the strong retreat in the last decades (cf. Glaciological Reports, 1881–2010). Since 2004/05, glaciological mass balance measurements were available (Machguth, 2008; Machguth et al., 2006) serving as a baseline within a long-term mass balance monitoring program.

Four days before the in-situ and ALS measurements in September 2010, a snowfall event covered the entire Findelengletscher with a layer of fresh snow. The typically present end-of-summer differentiation between snow, firn, and ice including transition zones in between these facies types became consequently indistinct. Snow depth measurements at ablation stakes revealed that at the day of the campaign, about 0.05–0.10 m of snow was still present on the tongue (2600 m a.s.l.), though melting fast. In higher altitudes, the snow depth generally increased with high spatial variability, to a maximum measured snow depth of 0.28 m at 3413 m a.s.l.

2.2. ALS data

On September 29, 2010, the ALS (Optech Inc., ALTM Gemini) was used on board a Pilatus Porter fixed-wing aircraft to retrieve topographic information in order to support the in-situ glaciological mass balance measurements. The weather during data acquisition was cloud-free with an excellent visibility. The built-in surveying system consisted of a pulsed laser, whose emissions were deflected across the flight track using an oscillating mirror. The range distance of each laser emission is calculated by the two way time-of-flight between the ground and the emitter/detector, under the assumption of a constant speed of light. A global positioning system (GPS) coupled with an inertial navigation system (INS) provided position and attitude of the aircraft. These data, together with the range measurement and instantaneous angle of the deflecting mirror, allowed allocating a coordinate in a given reference system for each ground projected field of view (Wehr & Lohr, 1999).

The entire glacier area was surveyed from a nominal flight altitude of 1000 m above ground (cf. Table 1 and Fig. 1). A second acquisition at a lower nominal flying altitude of 600 m above ground and a higher pulse repetition frequency (PRF) and higher resolution was performed as well, but only covered the lower parts of the glacier. Additionally, two flight trajectories at a higher altitude of 2800 m above ground were acquired for a large portion of the glacier area to investigate the effects on the accuracy of this lower point density digital elevation model (DEM) and the behavior of the recorded intensity compared to the standard setup flown at 1000 m above ground.

Point cloud data were available in binary LAS format including intensity values represented as digital numbers (DN) and the flight path data was available as smoothed best estimated trajectory (SBET) data set with a 250 Hz position and attitude recording rate. The emitted laser power was calculated from sensor calibration reports provided by the manufacturer of the scanning system (Optech Inc., data not shown) and the power was assumed to be stable for each respective pulse repetition frequency setting during the entire flight.

2.3. ADS 80 data

On the same day as the ALS data was acquired, an independent flight campaign with an Airborne Digital Sensor (Leica Geosystems AG, ADS 80) was performed by the Federal Office of Topography (swisstopo). The camera collected data in the blue (420–492 nm), green (533–587 nm), red (604–664 nm), and near-infrared (833–920 nm) parts of the electro-magnetic spectrum. Although the camera would provide multi-angular data for photogrammetry purposes, we limited the processing to the nadir multispectral data. Data collection took place on 11:14 UTC at an altitude of 7600 m a.s.l. on an east–west oriented flight trajectory. The flight strip covered most of the Findelengletscher; about 12% in the southernmost part were not covered.

2.4. Ground reference data

To investigate and calibrate the ALS intensity and ADS reflectance measurements, we used a twofold approach. To monitor changes in the snow surface and solar irradiance during the flight campaigns, we installed an albedometer (Kipp & Zonen CM 7B) at 3118 m a.s.l. on a part of the glacier with a gentle slope of approx. 3° to the west. The albedometer consisted of two oppositely mounted zenith and nadir facing pyranometers measuring the broadband radiation between 305 and 2800 nm over each hemisphere. Combining both measurements provides the bi-hemispherical reflectance (BHR), also called the (blue sky) broadband albedo (Schaepman-Strub et al., 2006). The area of the albedometer's location was covered by laser returns from three

Table 1
Data acquisition parameters for the respective flying height.

Date of acquisition	Sept. 29, 2010			
Sensor employed	Optech ALTM Gemini			
Average flying height	[m a.g.l.]	600	1000	2800
Pulse repetition frequency (PRF)	[kHz]	100	71	33
Scanning angle	[degrees]	±15	±15	±20.1
Line scanning frequency	[Hz]	39	39	13.7
Across-track overlap	[%]	40	50	35
Average point density	[Pt/m^2]	14.4	8.2	0.4
Laser wavelength	[nm]	1064	1064	1064
Beam divergence (1/e)	[mrad]	0.25	0.25	0.25

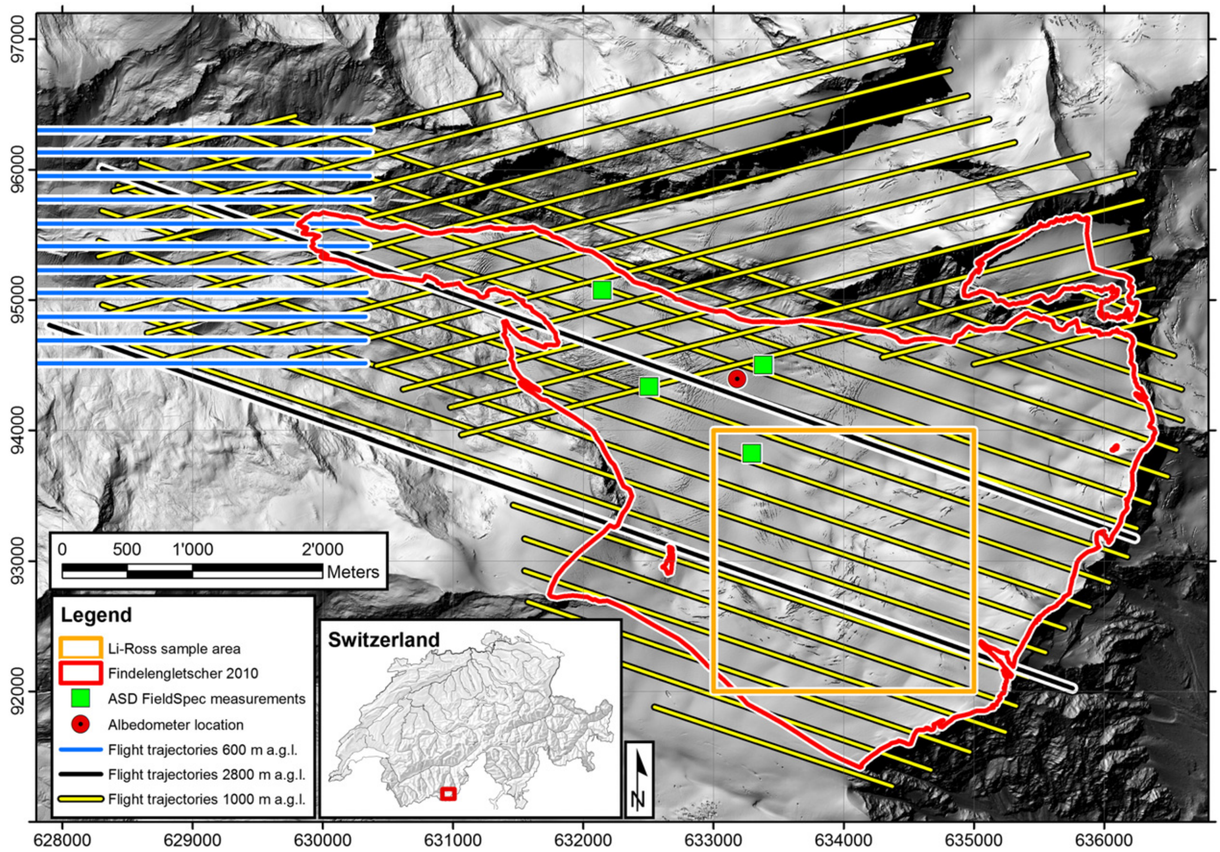

Fig. 1. Shaded relief of the study site with flight trajectories and in-situ reference locations. Coordinates used are in meters in the Swiss national grid (CH1903).

different flight trajectories at different times of the day allowing for a comparison of changes in the measured broadband albedo with changes in the ALS intensity.

In order to expand the reference data set to different locations and surface types at different altitudes, we additionally performed measurements using a spectro-radiometer (Analytical Spectral Devices, Inc., FieldSpec 3 Pro), covering the spectral range between 350 and 2500 nm. We measured at four locations while collecting nadir measurements with a 25° field of view fore optics. Consequently, the applicable scattering concept was hemispherical–conical reflectance factor (HCRF). These HCRFs were then transformed to broadband albedo (cf. Section 3.1.2).

3. Methods

3.1. Ground reference data processing

3.1.1. Albedometer measurements

The albedometer recorded the incident and reflected the hemispherical radiation in W/m^2. The ratio between these two hemispherical radiation measurements is the broadband albedo, describing the integrated surface reflectance ranging between 0 (i.e. no reflectance) and 1 (i.e. 100% reflectance).

Although the albedo was directly deducible from the albedometer measurements, the recorded result was influenced by the local topography and the portion of terrain visible in the upward-looking pyranometer (sky-view factor). The downward-looking pyranometer's FOV was completely looking at terrains. To be able to relate these albedo measurements with the small field of view of the ALS measurements (BCRF), we had to minimize both effects in the albedometer measurements.

In this highly undulated terrain, with nearby peaks towering more than 1000 m over the albedometer position, the sky view correction was of high relevance. Mountains higher than the albedometer elevation on the one hand obstructed diffuse skylight and on the other reflected a portion of the solar radiation back into the upward-looking pyranometer. The area of the hemisphere covered by terrain was calculated with a viewshed analysis based on the position of the albedometer and the surrounding ALS DEM. Bare rock and snow covered different proportions of the visible surface and featured different reflectance characteristics. We adapted the sky view correction factors described in detail by Corripio (2004) by calculating the fraction of direct and diffuse radiation from the sun and the fraction of reflected diffuse radiation from the ground and multiple scattering between the ground and the sky. While the calculation of the radiation from the sun without terrain interaction was straightforward, the terrain reflected radiation depended on the surface properties. We used photos of the surrounding terrain taken at the albedometer location to estimate the fraction of the terrain covered by snow (0.65) and bare rock (0.35), and derived their average albedo from literature: 0.80 for snow (clean fresh and dry snow at high elevations, e.g. Dozier, Green, Nolin, & Painter, 2009; Warren, 1982) and 0.15 for rock (Paul, Machguth, & Kääb, 2005). Additionally, the model contained a factor that was influenced by the fraction of the sunlit and visible ground. We therefore simulated shadowing in our study site over the entire measuring period of the albedometer in 0.1 h steps and calculated the fraction of shaded raster cells in respect to sunlit cells in the area overlapping the albedometer viewshed.

The sum of these four factors (available for each 0.1 h time interval) was subsequently multiplied with the measurement of incoming radiation leading to a correction of incoming radiation and albedo values.

Secondly, we corrected the albedo for the topographic effect of the non-horizontal measuring site by using a Lambertian correction (Law & Nichol, 2004).

$$\alpha_H = \alpha_I \cdot \cos(z)/\cos(i). \tag{1}$$

Eq. (1) uses the solar zenith angle z and the angle of incidence i (the angle between the surface normal and the incident sun vector) to correct the measured albedo on inclined terrain α_I into the horizontal albedo α_H. The angles used were calculated based on the ALS DEM at the location of the albedometer and using the sun trajectory for this day of the year.

3.1.2. ASD FieldSpec transects

During the ALS survey and albedometer data acquisition, we measured four glacier surface plots with a spectro-radiometer at different locations (Fig. 1). Each plot of approx. 15 × 20 m consisted of three parallel transects, separated by 10 m and oriented parallel to the solar principal plane. Before and after each surface measurement, we calibrated the instrument for changes in the solar irradiance using a white reference Spectralon panel (Labsphere, Inc.).

We then transformed the narrowband reflectance (expressed as HCRF) $r(\lambda)$ into broadband albedo α_{ASD} by weighting the reflectance with the incident spectral irradiance $L_\downarrow(\lambda)$ (Liu, Liu, Wen, & Li, 2010; Negi & Kokhanovsky, 2011; Warren, 1982).

$$\alpha_{ASD} = \frac{\int r(\lambda) \cdot F_\downarrow(\lambda) d\lambda}{\int F_\downarrow(\lambda) d\lambda.} \tag{2}$$

Subsequently, we corrected the broadband albedo values for the influence of the local topography using the solar angles at the time of each plot measurement and the local surface normal as described in Eq. (1). As the spectro-radiometer provided HCRF instead of BHR, and a different spectral range compared to the albedometer's broadband albedo, we decided to account for these effects by introducing a correction factor. One in-situ spectro-radiometer measurement location was chosen to be only 200 m away from the albedometer location at a similar altitude. Similar environmental variables (altitude, location, exposition, slope, snow cover) present at these two nearby locations allowed the assumption of similar albedo and subsequent calculation of an albedo offset from the corrected albedometer values and the corresponding spectro-radiometer broadband albedo measurements. The correction factor was then applied to all four measurements.

3.2. ALS intensity data pre-processing

ALS intensity information is usually defined as the total energy per return and is either provided as single unit-less digital numbers for multiple-return (also discrete return) systems or as discrete series of DNs containing the whole return waveform for each emitted pulse for full-waveform systems (e.g. Mallet & Bretar, 2009; Wagner, 2010). The instrument type we used was a discrete digitizing system. In discrete return systems, the term intensity is sometimes not clearly defined and a waveform analysis to derive a well-defined intensity is not possible. Therefore, we performed tests using intensity data of the same surface location from all different flying heights to correct the discrete return intensity data: once under the assumption of a true intensity value (i.e. return energy), and once under the assumption that the recorded intensity is the maximum amplitude of the signal power. These tests have revealed that we are provided with the peak power and not the return energy.

The entire returned pulse energy was assumed to be reflected from a single scatterer larger than the laser footprint (the so called extended target), i.e. we excluded multiple echoes. In addition, we assumed a stable laser emission level per PRF and a constant system transmission factor for the entire flight campaign (Höfle & Pfeifer, 2007). Spatially distributed point observations were mapped into a regular grid with 1 × 1 m cell size by averaging all enclosed intensity values with a local angle of incidence smaller than 40°.

3.2.1. Range correction

An important factor influencing the returned signal strength is the range distance between scanner and target. The range distance is influenced by topography, by the flight altitude and by different scanning angles across the flight track (Luzum, Starek, & Slatton, 2004). The reduction of the intensity is based on the LiDAR equation and is inversely proportional to the 2nd power of the range (Baltsavias, 1999). The intensity correction for a scatterer larger than the laser footprint size at a given range R is R^2/R_{ref}^2, with R_{ref} being an arbitrary reference range to normalize the output values (Höfle & Pfeifer, 2007; Luzum et al., 2004; Vain, Liba, & Sepp, 2011).

3.2.2. Pulse power correction

The ALS intensity values are not only affected by processes occurring after the pulse was emitted, but as well as directly by the emitted signal power. The signal power for a given laser source is a function of the pulse repetition frequency, i.e. the more pulses per second, the weaker the emitted pulse. The intensity values of discrete returns from a full-waveform system can be calculated by Gaussian decomposition methods and integration of the full width at half maximum (FWHM) or standard deviation of each derived Gaussian (Heinzel & Koch, 2011; Mallet & Bretar, 2009). In that case, the term intensity is equivalent to the power of the return pulse. To correct for different power levels, two parameters of the scanner have to be known: the width of the emitted pulses and the pulse energy, the latter varies with PRF. This information is available from calibration reports of the scanner manufacturer and only valid for the particular scanner used (pers. comm. Optech Inc.). Knowing these values, one can calculate the peak power of the emitted laser pulse for each PRF by dividing the pulse energy by the pulse width. Finally, the chosen reference PRF power P_{ref} is divided by the actual PRF power P_{PRF} (similar to Vain et al. (2009) but using power instead of energy).

3.2.3. Topographic correction

A secondary effect of the intensity being proportional to the peak power is the dependence of the angle of incidence at the target. An inclined target surface relative to the emitted laser pulse vector leads to receiving an elongated version of the sent pulse with reduced peak amplitude. If the scattering behavior of the target's surface is assumed to be Lambertian, the peak power is reduced by $1/\cos(i)$ with i as the local angle of incidence. However, the scattering of snow is known to be non-Lambertian, i.e. has a distinctive directional scattering behavior (e.g. Li, Stamnes, Eide, & Spurr, 2007; Lyapustin et al., 2010). Due to the monostatic measurement setup, an ALS system always measures light exactly reflected into the direction of illumination (a configuration typically denoted as “hot spot” in optical remote sensing). Surface roughness leading to the distinct hotspot effect in passive remote sensing applications does not affect ALS intensities, however. The geometrical–optical scattering concept of ALS can therefore be described by the bi-conical reflectance function (BCRF) using a single wavelength at 1064 nm. Snow reflectance measurements are thus characterized by high backscatter and a large single (direct) scattering component. We employed a kernel-based approach for normalization of the anisotropic reflectance behavior of snow. Li–Ross kernels (Roujean, Leroy, & Deschamps, 1992; Wanner, Li, & Strahler, 1995) model the individual influence of volume- and geometric–optical scattering effects on the angular reflectance behavior of surfaces. Initially designed for vegetation, these functions were shown to be applicable to a multitude of natural surface types, including snow (e.g. Stroeve et al., 2005). Derived from physical principles, such an approach dramatically reduces the degrees of freedom over purely statistical–empirical approaches (Wanner et al., 1995). The present work shows the applicability also in the case of the ALS measurements.

We used a patch of 2 × 2 km of snow on the higher part of the Findelengletscher to train a Li–Ross based correction method dependent on the intensities with their respective angle of incidences (also

Fig. 1). A combination of the Li-sparse geometric–optical kernel and the Ross-thick volumetric kernel provided a good fit to the measured ALS intensities in the used range of local incidence angles from 0 to 40°. The local incidence angle was employed as angular offset between illumination and observation direction, assuming observation in the forward scatter direction and solar principle plane.

3.2.4. Atmospheric correction

Atmospheric effects like scattering and absorption further reduce the received signal strength (Höfle & Pfeifer, 2007). We calculated the atmospheric attenuation values at the laser's wavelength using MODTRAN (Berk et al., 2006). Settings in MODTRAN were set to 50 km visibility, dry air and rural aerosol content to match the clear high Alpine conditions present at the day of the campaign. As we were working with three different ALS mission settings (Table 1) with different elevations above sea level and above ground, we calculated three different attenuation coefficients a: for the 600 m range R (1000 m; 2800 m) of the campaign, we assumed a mean flight altitude of 2600 m (4200 m; 6000 m) above sea level and a mean target elevation of 2000 m (3200 m; 3200 m). The resulting attenuation coefficients used for the atmospheric correction were 0.12, 0.11, and 0.06 dB/km, respectively. These values were considerably lower than those reported for similar ranges by Höfle and Pfeifer (2007), due to the better visibility at the high elevation above sea level of our signal paths. The resulting atmospheric condition η_{atm} used is (Höfle & Pfeifer, 2007)

$$\eta_{atm} = 10^{-2 \cdot R \cdot a / 10000}. \tag{3}$$

3.3. From intensity values to an albedo proxy

The resulting correction equation for the Lambertian case of the ALS intensities used is

$$I_{cor} = I_{ori} \cdot \frac{R^2}{R_{ref}^2} \cdot 10^{2 \cdot R \cdot a / 10000} \cdot \frac{P_{ref}}{P_{PRF}} \cdot \frac{1}{\cos(i)} \tag{4}$$

where I_{cor} and I_{ori} are corrected and originally recorded DNs of intensity for each laser return. In the case of the Li–Ross method, the cosine part of the equation is substituted by a correction factor taken from a lookup table for the respective angle of incidence.

In the next step, the corrected intensity data were linked to the corrected spectro-radiometric and albedometer measurements. For the spectro-radiometric measurements, we clipped the ALS intensity point cloud to the same area as the patch defined by in-situ GPS measurements. To minimize the temporal influence of changes of the snow surface between ground and aerial measurements, we used only those ALS intensity values that were closest in time to the in-situ measurements. In the albedometer case, three ALS intensities from different times were available to compare with the synchronous broadband albedo. To homogenize the ALS intensities, we used the averaged data from a 10 × 10 m patch around the albedometer position.

To finally link the ALS intensities with the albedo data, we used the seven available reference albedo values to derive slope and offset values based on a linear regression (Fig. 2). Subsequently, these values were used to correct all ALS intensities in order to produce a glacier-wide albedo map.

3.4. ADS 80 data processing

The digital image strip from ADS 80 was orthorectified using ERDAS LPS 2013 (Intergraph Corp.) and the ALS DEM from the same day. Subsequently, the data were processed to atmospherically corrected reflectance using the ATCOR-4 software (Richter & Schläpfer, 2002) and a rural standard aerosol model. Then, the data were corrected for BRDF effects by utilizing data from goniometer measurements on snow from different locations than our field measurements, taken from the spectral data base Specchio (Hueni, Nieke, Schopfer, Kneubühler, & Itten, 2009). Due to the north–south viewing direction of the ADS 80 sensor and the current solar azimuth angle of 175°, we extracted only the goniometer measurements in the solar principal plane. The measurements were available in 15° sensor zenith angle steps from 75° in the backscatter to 75° in the forward scattering region of the solar principal plane and for solar zenith angles between 56° and 78°. The spectro-radiometric measurements were convolved for the spectral response functions of the four ADS 80 bands and subsequently, a lookup table with the bidirectional reflectance factors (BRF) was generated. To account for solar zenith angles not covered in the BRF lookup table, we extrapolated all the measurements from the same sensor zenith angle using a linear model. Subsequently, the solar and sensor geometry for each surface pixel was calculated using the ALS DEM and corrected for BRDF effects using the BRF lookup table factors. Finally, a multiple linear regression was performed using the in-situ albedo data and the four BRDF corrected band reflectance values in an area of 10 m around the measurement positions. Then, a narrowband to broadband albedo conversion was performed using these factors according to Eq. (5).

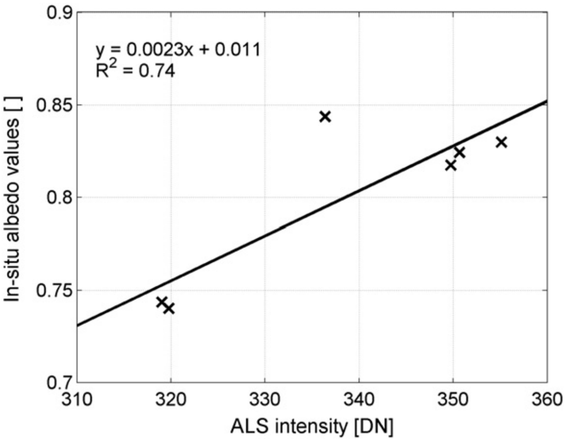

Fig. 2. Corrected ALS intensity and in-situ broadband albedo measured at transect locations and albedometer position (see Fig. 1). The linear regression was used for converting all ALS intensities (Fig. 4b) to a distributed albedo proxy map (Fig. 6a).

$$\alpha_{broad} = 2.41 \cdot \alpha_{blue} - 0.66 \cdot \alpha_{green} - 0.93 \cdot \alpha_{red} + 0.09 \cdot \alpha_{nir}. \tag{5}$$

The conversion to broadband albedo α_{broad} contains the four ADS 80 band reflectances (e.g. α_{blue} for the blue band) and weighting factors derived in the regression. Note that our conversion is optimized for snow and has not been tested on other surface types. A similar method was applied e.g. for Landsat TM (Knap, Reijmer, & Oerlemans, 1999) and other instruments (Liang, 2001).

4. Results

4.1. Correcting in-situ data for geometric–optical effects

Using the uncorrected radiance values provided by the albedometer to directly calculate the broadband albedo resulted in a strongly changing albedo over time, starting at a value of 0.65 at 9:30 a.m. local time and ending with an albedo of 0.80 at 4:00 p.m. (Fig. 3). Although the snow reflectance was expected to change slightly, i.e. decrease, over the course of the measuring period due to suspected melt and increasing snow grain size (e.g. Wiscombe & Warren, 1980), the calculated diurnal albedo values were far off the anticipated range and demanded correction (Jonsell, Hock, & Holmgren, 2003; Mannstein, 1985).

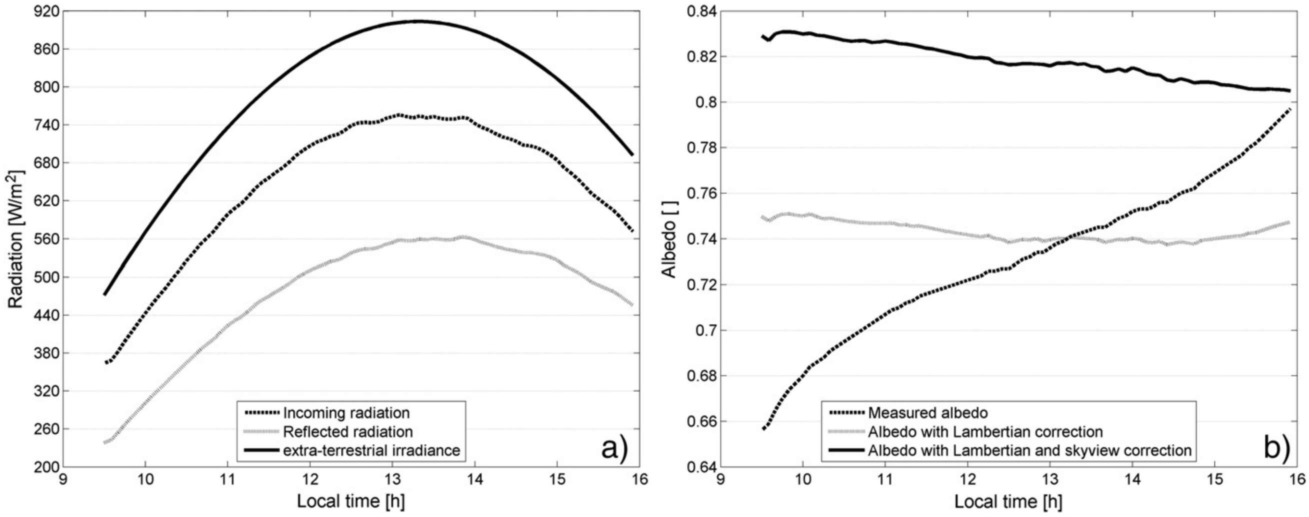

Fig. 3. Measured incoming and reflected radiation from albedometer measurements as well as modeled extra-terrestrial irradiance at top of atmosphere for that day (a). The smooth shape of the measured curves, similar to the extra-terrestrial one, demonstrates the clear atmospheric conditions during the day of the survey. The derived albedo values from these measurements (b) show the need to correct for topographic effects using a Lambertian and a sky view correction.

The horizontal albedo with the Lambertian correction applied already exhibited a much improved shape, although in the afternoon, the values still increased to unrealistic values (Fig. 3). We then applied the sky view correction with a measured terrain covered fraction of 0.20 of the upward-looking pyranometer's hemisphere. Consequently, one fifth of the “sky” was obstructed by terrain consisting of bare rock and snow. The resulting sky view correction factors ranged between 1.11 for the earliest measurement and 1.07 for the last one in the afternoon. This results in generally higher albedo values decreasing over the course of the entire day in a linear way. The corrected albedo values finally ranged between 0.83 in the morning and 0.81 in the afternoon.

The derived broadband albedo from the FieldSpec's first plot was adjusted to match the albedometer measurement at the time of the FieldSpec measurements. The derived offset of 0.08 was subsequently applied to all FieldSpec measurements. The adjusted spectro-radiometric broadband albedo then ranged between 0.74 and 0.84, increasing with altitude.

4.2. Physical correction of ALS intensity data

We used four pre-processing steps on the ALS intensity data to reduce physical and sensor-dependent effects before converting the intensity data into albedo proxy values. Additionally, to qualitatively check the influence of each correction step on the generated intensity maps (Fig. 4), we calculated the standard deviation of all intensity values within a raster cell. As the correction steps in the processing chain also changed the mean value in a raster cell, we normalized the standard deviations with the mean of the raster cell and therefore present the standard deviations as a percentage of the mean value. The changes from raw, uncorrected intensity values to a fully corrected, more homogeneous intensity raster can be seen in Fig. 4. In the corresponding Table 2, we present the changes in average per raster cell standard deviations for snow-free terrain, the area of the glacier tongue and the glacier area excluding the tongue for a number of corrections applied. For example, after range normalization, the relative standard deviation at the glacier tongue was reduced to 59% of the initial standard deviation, meaning that the influence of the range accounts for 41% of the originally present variability. Further corrections for different PRFs, atmospheric influences and two types of topographic corrections showed an additional decrease of the relative standard deviations in most cases. The lowest variability of intensity values for the glacier tongue and snow-free area was achieved when applying all correction steps, including the Lambertian topographic correction. On the other hand, for the higher glacier area only, the topographic corrections did not further decrease the standard deviations.

Fig. 5 shows the influence of variations of the angle of incidence on the recorded intensity of snow, after being corrected for range, PRF, and atmospheric effects for a 2 × 2 km snow area (Li–Ross sample area in Fig. 1). As expected, with increasing angles of incidence, the values of the return intensity were decreasing. After a perfect topographic correction, the new average was expected to be a horizontal line. However, after the Lambertian correction was applied, the resulting average values per degree angle of incidence exhibited an increasing trend, showing an overcorrection of the data. Having trained Li–Ross kernels on the same test area provided a better correction of the mean values, i.e. produced an almost horizontal line.

4.3. Spatially distributed albedo proxy derived from intensity values

A linear regression was used to correlate the normalized ALS intensity values with the corrected in-situ measurements of the albedo (Fig. 2). The seven value pairs showed a good agreement, with a resulting coefficient of determination (R^2) of 0.74. The linear model was then used to generate a distributed albedo proxy map. In the resulting converted raster, 80% of all values on the glacier were in between 0.7 and 0.9, 50% of all albedo values were within the range of the ground reference albedo measurements (0.74 to 0.84). The empirical model fulfilled the physical boundary conditions of the albedo definition, i.e. values ranging between 0 and 1, for 99.6% of all values. The derived glacier albedo proxy map (Fig. 6a) revealed a mean of 0.79 for the entire Findelengletscher, with average values at the tongue of 0.66 (0.05–0.10 m of snow) and 0.8 in higher areas (up to 0.28 m of snow). These results are in good agreement with measurements of snow depths and corresponding albedo values from an automated weather station on the Morteratschgletscher (Oerlemans & Knap, 1998).

The high sensitivity of the ALS wavelength concerning different snow grain sizes (Dozier & Painter, 2004) is nicely shown in the halo pattern of helicopter landing sites (inset in Fig. 6a), showing the redistribution of fine snow grains (high albedo halo) and residual larger grains (center). Redistributed snow grain sizes are also visible in the glacier's accumulation area, where areas downwind from small crests were filled with redistributed small diameter snow grains. Crevasses are visible as dark linear features, as the fresh snow cover was not sufficient to cover the bare ice surface beneath.

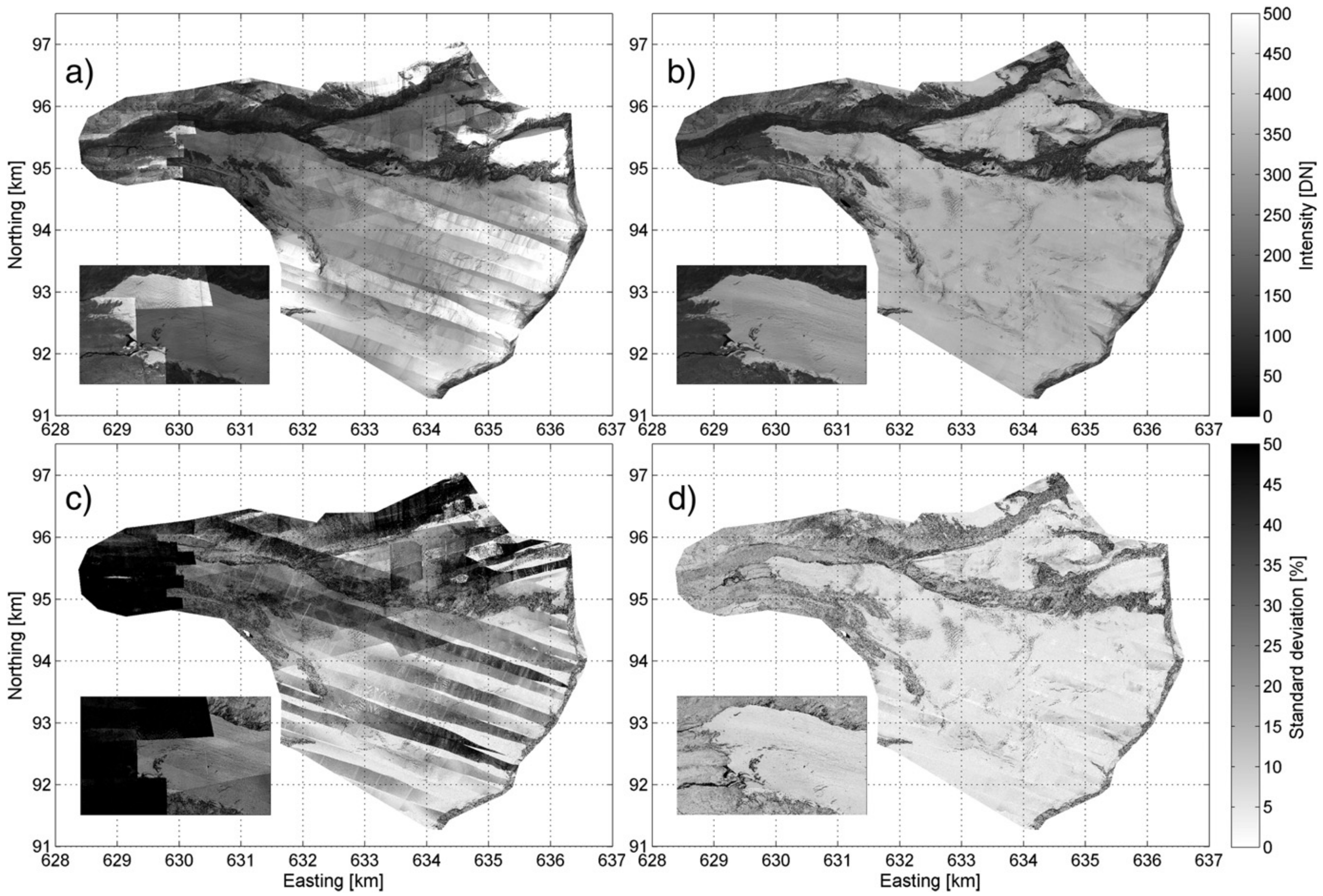

Fig. 4. Raw (a) and physically corrected ALS intensity data (b, topography correction: Li–Ross) show the need for intensity corrections. The corrected intensity (b) presents an albedo proxy where different surface characteristics and features (e.g. crevasses, see insets of the tongue) are visible. The relative change in the per raster cell standard deviations is visualized before (c) and after (d) the intensity corrections. Note that the lowest standard deviations in the corrected raster (d) are areas where only data from one flight strip are present. Values exceeding the color bar range are reduced to the maximum values' color to preserve a high contrast in the image. Coordinates used are in kilometers in the Swiss national grid (CH1903).

Where only the ALS measurements from flight transects from one direction were present (mostly in the southwest of the Findelengletscher), a linear artifact persisted in the map (cf. Section 5.2).

4.4. Spatially distributed broadband albedo derived from ADS 80

ADS 80 multispectral imagery has served to derive broadband albedo (Fig. 6b) as a reference to the ALS albedo proxy map (Fig. 6a). Comparing the statistics for the entire glacier, the mean albedo values differ by only 0.01, with the ALS derived values being slightly higher. The standard deviations are 0.09 in the ADS 80 case and 0.13 in the case of the ALS. Differencing the ALS and ADS 80 albedo maps led to a high agreement for large regions for albedo values within ± 0.1, with larger differences at the tongue. For that region, the statistical agreement is again high with the ADS 80 measuring a mean albedo of 0.69, 0.03 higher than from the ALS data, and the standard deviations are similar. However, a visual inspection of the differences shows that the ALS overestimated albedo at locations where darker glacier debris showed through the thin layer of snow and underestimated albedo at areas with a higher snow cover. In north-exposed slopes of the accumulation area and around large crevasses, the ALS overestimated the albedo compared to the reference albedo.

5. Discussion

5.1. Measurement and correction of in-situ data

To provide accurate and absolute in-situ reference albedo data, multiple corrections of the raw albedometer and spectro-radiometric data were required. Without these corrections, the values measured on the ground contained a strong topographic bias because of the

Table 2
Standard deviations of raw ALS intensity values with a combination of corrections applied. The relative variation with respect to the uncorrected intensity standard deviations is shown for snow-free terrain, snow at the lower glacier tongue as well as higher elevation snow.

Corrections applied					Terrain only	Glacier snow (tongue)	Glacier snow
Range normalization	PRF	Atmospheric	Topographic (Lambertian)	Topographic (Li–Ross)	Standard deviation [%]	Standard deviation [%]	Standard deviation [%]
					100.00	100.00	100.00
X					63.31	59.16	75.59
X	X				36.84	29.04	30.23
X	X	X			36.20	28.14	29.89
X	X	X	X		34.52	28.00	29.96
X	X	X		X	36.94	28.16	30.49

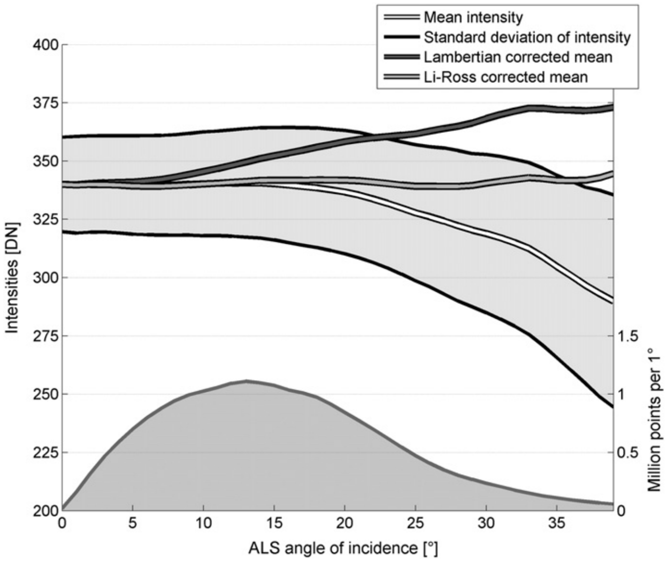

Fig. 5. Effects of the topographic correction for a 2 × 2 km sample patch of snow (cf. Fig. 1). The mean intensity and standard deviation show the decline of intensity with larger angles of incidence before the topographic correction was applied. Correcting for the topography using the Lambertian approach shows an overcorrection, while the Li–Ross correction was able to shift the average intensities to a similar value independent of the angle of incidence. The number of points per degree (angle of incidence) is shown below.

measurement setup and could not be compared with the ALS measurements.

Calculation of the broadband albedo from the albedometer's measured incident and reflected radiation led to a strongly changing albedo (+0.14) over the course of the day as consequence of the inclined local surface and the horizontal measurement setup (Jonsell et al., 2003; Mannstein, 1985). Although the evolution of the albedo values over time was improved by this first correction step, a temporal trend remained, showing an increase of the albedo in the afternoon over the initial values present in the morning. Taking the influence of the terrain into account, at the same time obstructing the diffuse irradiance from the sky and reflecting radiation back into the upward-looking pyranometer, led to a more reasonable result. In this second correction step, the sunlit fraction of the raster cells within the viewshed of the top pyranometer was the dominating factor: Due to the highly undulated topography present in our study site, the ratio of visible cells illuminated by the sun was 0.97 at the beginning of the measurements and decreased to 0.70 at the end of the measurements, with a more rapid decrease towards the end. In the late afternoon, the high mountain range to the southwest of the albedometer position started to cast shadows onto areas in the viewshed of the instrument, reducing the incident radiation. The evolution of this shadow fraction was therefore responsible for the increase in albedo in the afternoon.

The high proportion of the snow covered part of the terrain with a corresponding high albedo led to the sky view correction factors larger than 1. This indicated that the amount of radiation reflected from the snow covered terrain was larger than the amount of diffuse radiation obscured by the mountains. Consequently, the measured incident radiation was too high compared to the topography corrected result. Accordingly, the corrected albedo values increased after the sky view correction.

The conversion of spectro-radiometric field measurements to broadband albedo depended on more assumptions. Applying Eq. (2) is not fully correct as we integrate the spectral reflectance (HCRF) rather than the spectral albedo (BHR). Furthermore, the spectral irradiance is taken from the white reference measurements also based on the HCRF measurement setup. As the albedo is defined as a BHR property, one should measure and integrate the reflectance values from all possible incidence angles at a single location. However, this is only possible using either a BRDF snow model or in-situ goniometer measurements, which were not available. Hemispherical snow measurements available at different locations and dates were not used, as multiple assumptions to fit the model to our measurements would have been needed. Instead, we assumed a Lambertian behavior of the surface and corrected the spectro-radiometer derived albedo topographically using Eq. (1), as for the albedometer measurements. Additionally, the spectral ranges of the FieldSpec (350–2500 nm) and the albedometer (305–2800 nm) were not entirely the same. Consequently, to further homogenize the resulting albedo, we calculated the albedo difference between the spatially closest FieldSpec measurement and the albedo value of the albedometer taken at the same time. Due to similar environmental variables (altitude, location, exposition, slope, snow cover) at the two sites, we assumed the snow properties to be similar and therefore shifted the values of the FieldSpec based measurements to the ones of the albedometer and applied this offset to all other FieldSpec albedo values.

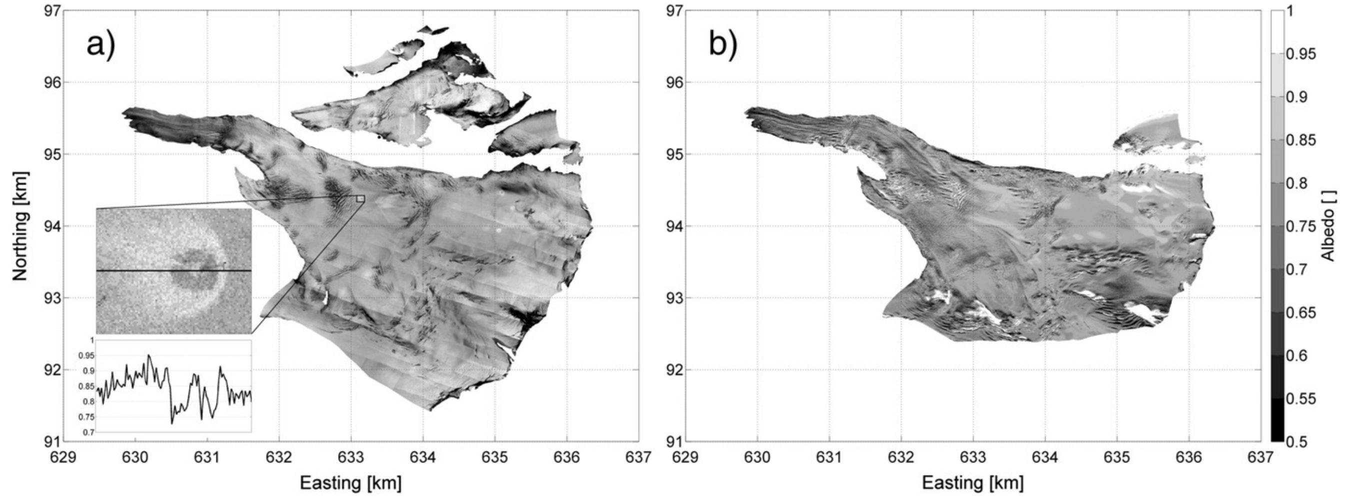

Fig. 6. Distributed albedo proxy map derived from ALS intensity values and ground reference measurements (a; topographic correction: Li–Ross) of Findelengletscher (south) and a contributing glacier (Adlergletscher, north). The inset shows a detail of the halo pattern where the helicopter landed (approaching from the west). Below are the albedo proxy values of the transect across the landing site. Note the areas of the deposition of fine grained snow (high albedo), the dark circular area where the fine grained snow was blown away, and the center part showing a higher albedo again, possibly due to the protected zone directly below the helicopter's fuselage. The ADS 80 reference albedo of Findelengletscher (b) is shown for comparison. Shadow areas were excluded and are therefore visible as gaps in the map, as is an area to the south, which was not covered by the sensor. Coordinates used are in kilometers in the Swiss national grid (CH1903).

5.2. Remaining intensity patterns after corrections

We homogenized the ALS intensity data using multiple physically based correction steps (cf. Section 3.2). Despite these correction steps, which homogenized the ALS intensity values considerably, a striped pattern of intensity values remained, most apparent in the accumulation area (Fig. 6a). This pattern was likely due to a combination of effects that it is most apparent in the south-west area of the glacier and could be attributed to the low point density and to the lower overlap of different flight strips with different viewing geometries. Therefore, the corrected intensity values per raster cell in these areas were only a mean of the returns observed with the same laser geometry (i.e. incidence angle and range distance), whereas in all other cases, the ground returns stemmed from at least two different flight paths and consequently, incidence angles. Thus, the deficiency in the result is most likely to be associated with the recorded raw intensity values or the insufficiencies in the physical correction process.

When examining the raw intensity values, we found that the ALS instrument recorded weak intensity returns in increments of 1 DN, whereas stronger return intensities were sampled in increments of 20 DN. In our data set, all low- to mid-altitude flight configurations produced data with a majority of increments of 20 DN. Although this instrument setup facilitates to cover a broad range of intensities, it resulted in only a few unique values, e.g. only about 10 different intensity values were recorded on a homogeneous part of the glacier. Values that would have been situated in between the unique interval numbers were rounded to the next increment. Consequently, small changes in the measured intensity might have resulted in large differences when registered. This effect was therefore impossible to correct for. Lutz et al. (2003) reported that the use of the maximum intensity value per raster cell evaded the striped pattern. However, extensive experiments with the highest and lowest values per raster cell did not improve the result, most likely due to the aforementioned influence of the sampling intervals.

5.3. Remaining intensity variability in single raster cells

We found that not all corrected intensity values in a single raster cell were the same. The possible sources of these differences are a) the local snow BRDF, b) possible stray light from the sun reflected into the sensor (in particular in the forward scattering domain), and c) variations in the energy of the emitted laser pulse. To quantify the influence of the BRDF, we applied two BRDF models: the first by assuming a Lambertian reflection behavior and the second by training Li–Ross kernels on a test site of snow. The Lambertian model overcorrected the average intensities for increasing angles of incidence (Fig. 5). Although the Li–Ross correction performed better than the Lambertian correction in the snow sample area (Fig. 1), it is based on the assumption of a specific BRDF for a test site, which may not be correct for different regions or snow types, hindering the transferability of the method. As the snow properties were expected to change from higher to lower altitudes (e.g., as indicated by snow grain size measurements), applying the model to regions exhibiting a different snow surface will result in a bias. Therefore, the Li–Ross correction did not outperform the Lambertian correction according to our statistical analysis (Table 2). However, the amount of variance explained by the topographic corrections remained small or even impaired the standard deviations compared to the considerable amount of variance attached to the range and PRF corrections. Note that the remaining standard deviation of for example 30% (glacier snow with Li–Ross correction) is not to be evaluated worse than the 28% of the glacier tongue. This difference in standard deviations is due to the remaining natural variations inherent to the different surface areas and therefore not comparable. Furthermore, after an additional correction was applied, the changes could lead to a qualitative improvement of the raster representation, although the change in standard deviation was small.

Based on a qualitative visual inspection of single ALS flight strips, the influence of sun-induced snow BRDF effects seemed possible, though extensive simulation with solar stray light did not improve the results. The ALS intensity values were therefore assumed to be not affected by solar radiation which is in support of the findings by Wagner, Ullrich, Ducic, Melzer, and Studnicka (2006).

The emitted laser pulse energy was assumed to be stable over the period of the surveys. However, the measurements of the emitted intensity recorded in full-waveform digitizing systems suggest a considerable variation of the pulse energy in between pulses. Due to the discrete digitizing system used, which did not record the outgoing laser pulse, this additional uncertainty remained in the data but is considered to be small.

5.4. From intensity to a spatially distributed albedo proxy

Correlating the ALS intensity values with in-situ measured albedo values showed a coefficient of determination (R^2) of 0.74. The small number of in-situ measurements ($N = 7$) were limiting us from testing other possible correlation functions, as the range of different in-situ albedo values was small and the use of a higher order function (e.g. a polynomial) to fit the data would likely result in overfitting. The small spatial variation of the measured albedo values was due to a snowfall event a few days prior the campaign and limited melt thereafter. Snow characteristics were therefore similar on larger parts of the glacier area and did not exhibit the characteristic end-of-summer facies types such as snow, firn, and bare ice. Due to the size of the glacier, it was not possible to collect more in-situ reference measurements, e.g. on the partially melted snow parts on the glacier tongue. However, precisely because the glacier surface was rather homogeneous in large areas, most ALS intensity values are in close agreement with the field reference measurements and mitigate the challenge of converting ALS intensities to an albedo proxy outside the interval of the reference measurements. Overall, the resulting values were within the expected range, e.g. around 0.6 on the glacier tongue with partially molten and aged snow, along with mineral and biogenic dust starting to show through the snow and values up to 0.9 in the accumulation area with greater snow depths. This is in line with the results comparing snow depth, snow age and albedo on another glacier in the Swiss Alps (Morteratschgletscher; Oerlemans and Knap (1998)).

5.5. Cross-comparison of ALS albedo proxy with ADS 80 broadband albedo

Finally, we compared the ALS albedo proxy with a broadband albedo from synchronous multispectral ADS 80 airborne imagery (Fig. 6). The statistical results, as well as a first qualitative assessment, look generally promising. The mean difference of the albedo values is only 0.01 with a slightly larger difference at the tongue due to the impure surface being visible through the thin snow layer. The albedo difference in the accumulation area, where the ALS proxy is higher than the ADS 80 reference albedo, could be explained by the large local solar zenith angle on the north-exposed slopes, being an indication that the BRDF correction of ADS 80 imagery did not perform adequately at extreme solar angles.

At the survey date, the glacier was still entirely snow covered. However, for a typical end-of-summer situation with one third or more of the glacier being snow-free, the narrowband to broadband conversion becomes more challenging. At the near-infrared wavelength of the ALS, the reflectance is mostly dependent on the snow grain size. The broadband albedo, though, is dominated by impurities in the visible part of the electro-magnetic spectrum. Fig. 7 demonstrates the challenge by providing the results from a simulation of hemispheric albedo based on fine (0.1 mm radius) and coarse grained snow (1 mm), each without, with moderate, and with high dust concentrations (based on the SNICAR simulator, Flanner et al., 2007). In the case of surface impurities, the relationship between broadband albedo and reflectance at 1064 nm becomes non-linear. Therefore, at the tongue, the ALS albedo

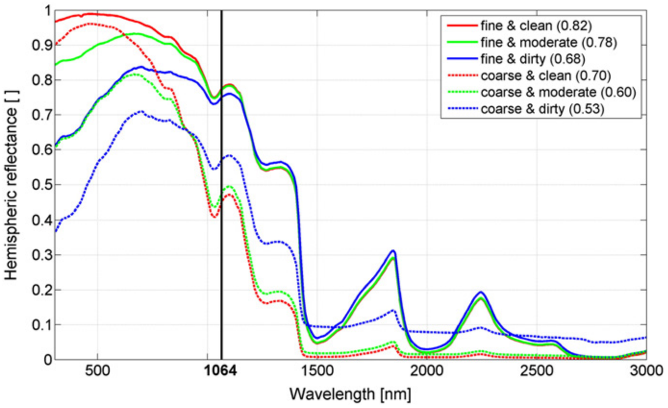

Fig. 7. Simulation of broadband albedo influenced by two snow grain sizes and three dust concentrations based on the SNICAR model (Flanner, Zender, Randerson, & Rasch, 2007). Note the non-linear relationship between the ALS reflectance (vertical line at 1064 nm) and the broadband albedo (in brackets in the legend) when dust concentrations increase.

proxy was not entirely able to mimic the influence of debris being visible through the thin snow layer and overestimated albedo. Our study has therefore limited transferability. To overcome this limitation in the narrowband to broadband conversion, more in-situ measurements on the different surface types must be conducted or additional multi-spectral imaging is required.

In addition, the physical effects in snow backscattering such as shadows and coherent backscatter are not fully understood. Therefore, there remain uncertainties in the scattering models in this regard.

5.6. Implications for glacier modeling

Literature references of glacier surface albedo used for energy and mass balance modeling usually consist of assumed values for snow, firn, and ice (e.g. Machguth et al., 2006). Some models allow snow albedo to evolve with time using a snow aging function partly including the growing influence of underlying facies types (e.g. Oerlemans & Knap, 1998). However, these approaches do not take into account the local variability of albedo. In the case of Findelengletscher, a snowfall took place only four days prior to the in-situ and ALS measurements; the modeled albedo will thus result in snow albedo values very similar to the assumed initial snow albedo. Consequently, a bias between the calculated albedo in this study and the modeled values exists. Table 3 shows the snow albedo value from Machguth et al. (2006), as used for Findelengletscher (among other glaciers), compared to the calculated snow albedo for different regions from this study. The average albedo for the entire Findelengletscher derived from in-situ and ALS measurements is 0.09 higher than the model value, leading to slower melting of the fresh snow surface compared to the model. At the same time, the tongue's albedo is lower, leading to increased melting and finally being snow-free earlier than calculated by the model. Subsequently, the melt will be even faster due to this albedo feedback mechanism.

As in-situ albedo measurements are only available on few glaciers, the direct application of the proposed method on a different glacier is difficult. However, assuming the average corrected ALS intensity represented the snow albedo from the literature and using the median absolute deviation (MAD, used in Table 3) or another suitable measure of statistical dispersion of the ALS values, enables one to attribute a variability value to the literature albedo and consequently allows deriving a distributed albedo map. In the case of a glacier with multiple facies types visible, local maxima in the ALS intensity's histogram for snow and ice surfaces could be used to link intensity with albedo values from the literature. Therefore, the ALS intensity data could be used to map the variation of albedo for an entire glacier without in-situ measurements. The resulting albedo can then be checked for validity when the albedo ranges between 0 and 1. From the three albedo products, the radiometrically calibrated ALS intensity (Table 3, c) provided the best albedo product for modeling purposes.

6. Conclusions and outlook

We measured and corrected on-glacier spectro-radiometric and albedometer measurements to serve as reference broadband albedo in preparation for deriving a glacier-wide spatially distributed albedo proxy map based on the ALS intensity data. First, we show that it is essential to correct in-situ measurements for topographic biases. For instrument inter-comparison, a transformation to the broadband albedo is required. Second, the ALS intensity data — once corrected for range, PRF, atmospheric, and topographic artifacts — can be combined with literature values to a distributed, relative albedo proxy. Third, the ALS intensity data, radiometrically calibrated with in-situ measurements, provided a distributed albedo proxy for snow. However, care must be taken on bare ice and impure surface regions.

Nowadays, the ALS is increasingly used to map topographic changes in glaciology, in order to derive a geodetic glacier mass balance. As these measurements are usually only performed in a decadal interval, the mass balance in between this interval has to be calculated using either in-situ glaciological mass balance measurements or by modeling, relying on meteorological measurements. However, one of the most important factors for glacier melt is the surface albedo which is spatially and temporally highly variable. Being able to complement glacier volume change measurements from ALS with a calibrated albedo proxy provides an important input variable for glacier mass balance models. It enables using the high resolution albedo information as a starting point of models by using only a few in-situ albedo measurements and data provided by the ALS anyway. As ALS is an active instrument measuring in the hotspot configuration, the ALS reflectance is not affected by shadowing and to a lesser degree subject to directional effects than passive optical imagery.

For future applications, we recommend using albedometer measurements on all surface types present as the measurements can be performed quickly and evade the transformation of the spectro-radiometric measurements into broadband albedo. Still, all of these measurements must be carefully evaluated and corrected for potential topographic influences. On the airborne side, the use of combined ALS and passive optical imagery, preferentially imaging spectrometry, will lead to better products in cryospheric applications. An example of such a system in operation is the new NASA Airborne Snow Observatory (ASO; http://aso.jpl.nasa.gov).

Although provided with only one narrow spectral band, the spectral response of glacial surfaces at this wavelength enabled one to distinguish areas with a different albedo. Overall, the results obtained in this

Table 3
Comparison of three albedo products. The literature snow albedo (a) is taken from Machguth and others (2006). Product (b) is an albedo normalized to the literature values using the average corrected ALS intensity and the median absolute deviation (MAD). The last column (c) shows average and MAD of the radiometrically calibrated ALS intensity.

Area	a) Literature albedo	b) Scaled ALS variability	c) Measured ALS variability
Findelengletscher, tongue	0.70 ± 0	0.70 ± 0.04	0.66 ± 0.06
Findelengletscher, main part	0.70 ± 0	0.70 ± 0.02	0.79 ± 0.04
Entire Findelengletscher	0.70 ± 0	0.70 ± 0.03	0.79 ± 0.04
Northern side glacier (Adlergletscher)	0.70 ± 0	0.70 ± 0.06	0.77 ± 0.09

study encourage exploiting the intensity information present in the ALS data to support glacier energy and mass balance modeling.

Acknowledgments

We thank Jeff Dozier and an anonymous reviewer for their constructive and helpful comments, Alexander Damm for providing atmospheric attenuation values, Andreas Hueni for providing data from the Specchio data base, Hendrik Wulf for valuable advice, and Optech Inc. for laser scanner calibration values. We acknowledge BSF Swissphoto for the acquisition of the ALS data and continued support. Karl Schroff from the Institute for Atmospheric and Climate Science (ETH Zurich) provided the albedometer and technical support. We are grateful to Wilfried Haeberli for his valuable support. This project was supported by the Swiss energy utility Axpo.

References

Abermann, J., Lambrecht, A., Fischer, A., & Kuhn, M. (2009). Quantifying changes and trends in glacier area and volume in the Austrian Ötztal Alps (1969–1997–2006). *The Cryosphere*, *3*, 415–441. http://dx.doi.org/10.5194/tc-3-205-2009.

Baltsavias, E. P. (1999). Airborne laser scanning: Basic relations and formulas. *ISPRS Journal of Photogrammetry and Remote Sensing*, *54*, 199–214. http://dx.doi.org/10.1016/s0924-2716(99)00015-5.

Berk, A., Anderson, G. P., Acharya, P. K., Bernstein, L. S., Muratov, L., Lee, J., et al. (2006). MODTRAN™ 5: 2006 update. *Proceedings of SPIE — The International Society for Optical Engineering. Kissimmee, FL, USA.*

Brock, B. W., Willis, I. C., & Sharp, M. J. (2000). Measurement and parameterization of albedo variations at Haut Glacier d'Arolla, Switzerland. *Journal of Glaciology*, *46*, 675–688. http://dx.doi.org/10.3189/172756500781832675.

Corripio, J. G. (2004). Snow surface albedo estimation using terrestrial photography. *International Journal of Remote Sensing*, *25*, 5705–5729. http://dx.doi.org/10.1080/01431160410001709002.

Cuffey, K. M., & Paterson, W. S. B. (2010). *The physics of glaciers* (4th ed.). Oxford: Butterworth-Heinemann.

Dozier, J., Green, R. O., Nolin, A. W., & Painter, T. H. (2009). Interpretation of snow properties from imaging spectrometry. *Remote Sensing of Environment*, *113*, 25–37. http://dx.doi.org/10.1016/j.rse.2007.07.029.

Dozier, J., & Painter, T. H. (2004). Multispectral and hyperspectral remote sensing of Alpine snow properties. *Annual Review of Earth and Planetary Sciences*, *32*, 465–494. http://dx.doi.org/10.1146/annurev.earth.32.101802.120404.

Flanner, M. G., Zender, C. S., Randerson, J. T., & Rasch, P. J. (2007). Present-day climate forcing and response from black carbon in snow. *Journal of Geophysical Research, D: Atmospheres*, *112*, D11202. http://dx.doi.org/10.1029/2006JD008003.

Geist, T. (2005). Application of airborne laser scanner technology in glacier research. *Faculty of Geo- and Atmospheric Sciences, Institute of Geography* (pp. 118). Innsbruck: University of Innsbruck.

Glaciological Reports (1881–2010). The Swiss glaciers. *Yearbooks of the Cryospheric Commission of the Swiss Academy of Sciences (SCNAT) published since 1964 by the Laboratory of Hydraulics, Hydrology and Glaciology (VAW) of ETH Zürich*.

Greuell, W., Knap, W. H., & Smeets, P. C. (1997). Elevational changes in meteorological variables along a midlatitude glacier during summer. *Journal of Geophysical Research, D: Atmospheres*, *102*, 25941–25954. http://dx.doi.org/10.1029/97JD02083.

Heinzel, J., & Koch, B. (2011). Exploring full-waveform LiDAR parameters for tree species classification. *International Journal of Applied Earth Observation and Geoinformation*, *13*, 152–160. http://dx.doi.org/10.1016/j.jag.2010.09.010.

Höfle, B., & Pfeifer, N. (2007). Correction of laser scanning intensity data: Data and model-driven approaches. *ISPRS Journal of Photogrammetry and Remote Sensing*, *62*, 415–433. http://dx.doi.org/10.1016/j.isprsjprs.2007.05.008.

Hueni, A., Nieke, J., Schopfer, J., Kneubühler, M., & Itten, K. I. (2009). The spectral database SPECCHIO for improved long-term usability and data sharing. *Computers and Geosciences*, *35*, 557–565. http://dx.doi.org/10.1016/j.cageo.2008.03.015.

Joerg, P. C., Morsdorf, F., & Zemp, M. (2012). Uncertainty assessment of multi-temporal airborne laser scanning data: A case study on an Alpine glacier. *Remote Sensing of Environment*, *127*, 118–129. http://dx.doi.org/10.1016/j.rse.2012.08.012.

Jonsell, U., Hock, R., & Holmgren, B. (2003). Spatial and temporal variations in albedo on Storglaciären, Sweden. *Journal of Glaciology*, *49*, 59–68. http://dx.doi.org/10.3189/172756503781830980.

Kaasalainen, S., Pyysalo, U., Krooks, A., Vain, A., Kukko, A., Hyyppä, J., et al. (2011). Absolute radiometric calibration of ALS intensity data: Effects on accuracy and target classification. *Sensors*, *11*, 10586–10602. http://dx.doi.org/10.3390/s111110586.

Klok, E. J., & Oerlemans, J. (2004). Modelled climate sensitivity of the mass balance of Morteratschgletscher and its dependence on albedo parameterization. *International Journal of Climatology*, *24*, 231–245. http://dx.doi.org/10.1002/joc.994.

Knap, W. H., Brock, B. W., Oerlemans, J., & Willis, I. C. (1999). Comparison of Landsat TM-derived and ground-based albedos of Haut Glacier d'Arolla, Switzerland. *International Journal of Remote Sensing*, *20*, 3293–3310. http://dx.doi.org/10.1080/014311699211345.

Knap, W. H., Reijmer, C. H., & Oerlemans, J. (1999). Narrowband to broadband conversion of Landsat TM glacier albedos. *International Journal of Remote Sensing*, *20*, 2091–2110. http://dx.doi.org/10.1080/014311699212362.

Law, K. H., & Nichol, J. (2004). Topographic correction for differential illumination effects on IKONOS satellite imagery. *Proceedings of the XXth ISPRS Congress, Istanbul, Turkey*.

Li, W., Stamnes, K., Eide, H., & Spurr, R. (2007). Bidirectional reflectance distribution function of snow: Corrections for the Lambertian assumption in remote sensing applications. *Optical Engineering*, *46*, 066201. http://dx.doi.org/10.1117/1.2746334.

Liang, S. (2001). Narrowband to broadband conversions of land surface albedo I algorithms. *Remote Sensing of Environment*, *76*, 213–238. http://dx.doi.org/10.1016/S0034-4257(00)00205-4.

Liu, S., Liu, Q., Wen, J., & Li, X. (2010). The angular and spectral kernel model for BRDF and albedo retrieval. *IEEE Journal of Selected Topics in Applied Earth Observations and Remote Sensing*, *3*, 241–256. http://dx.doi.org/10.1109/JSTARS.2010.2048745.

Lutz, E., Geist, T. H., & Stötter, J. (2003). Investigations of airborne laser scanning signal intensity on glacial surfaces — Utilizing comprehensive laser geometry modeling and orthophoto surface modeling (a case study: Svartisheibreen, Norway). *International archives of photogrammetry, remote sensing and spatial information sciences* (pp. 143–148).

Luzum, B. J., Starek, M., & Slatton, K. C. (2004). Normalizing ALSM intensities. *Geosensing engineering and mapping (GEM) center report no. Rep 2004-07-001* (pp. 8). Civil and Coastal Engineering Department, University of Florida.

Lyapustin, A., Gatebe, C. K., Kahn, R., Brandt, R., Redemann, J., Russell, P., et al. (2010). Analysis of snow bidirectional reflectance from ARCTAS spring-2008 campaign. *Atmospheric Chemistry and Physics*, *10*, 4359–4375. http://dx.doi.org/10.5194/acp-10-4359-2010.

Machguth, H. (2008). On the use of RCM Data and gridded climatologies for regional scale glacier mass balance modeling in high mountain topography; the example of the Swiss Alps. *Department of Geography* (pp. 176). Zurich: University of Zurich.

Machguth, H., Paul, F., Hoelzle, M., & Haeberli, W. (2006). Distributed glacier mass-balance modelling as an important component of modern multi-level glacier monitoring. *Annals of Glaciology*, *43*, 335–343. http://dx.doi.org/10.3189/172756406781812285.

Mallet, C., & Bretar, F. (2009). Full-waveform topographic LiDAR: State-of-the-art. *ISPRS Journal of Photogrammetry and Remote Sensing*, *64*, 1–16. http://dx.doi.org/10.1016/j.isprsjprs.2008.09.007.

Mannstein, H. (1985). The interpretation of albedo measurements on a snowcovered slope. *Archives for Meteorology, Geophysics, and Bioclimatology Series B*, *36*, 73–81. http://dx.doi.org/10.1007/BF02269458.

Negi, H. S., & Kokhanovsky, A. (2011). Retrieval of snow albedo and grain size using reflectance measurements in Himalayan basin. *The Cryosphere*, *5*, 203–217. http://dx.doi.org/10.5194/tc-5-203-2011.

Oerlemans, J., Giesen, R. H., & Van Den Broeke, M. R. (2009). Retreating Alpine glaciers: Increased melt rates due to accumulation of dust (Vadret da Morteratsch, Switzerland). *Journal of Glaciology*, *55*, 729–736. http://dx.doi.org/10.3189/002214309789470969.

Oerlemans, J., & Knap, W. H. (1998). A 1 year record of global radiation and albedo in the ablation zone of Morteratschgletscher, Switzerland. *Journal of Glaciology*, *44*, 231–238.

Ohmura, A., Bauder, A., Müller, H., & Kappenberger, G. (2007). Long-term change of mass balance and the role of radiation. *Annals of Glaciology*, *46*, 367–374. http://dx.doi.org/10.3189/172756407782871297.

Paul, F., Machguth, H., & Kääb, A. (2005). On the impact of glacier albedo under conditions of extreme glacier melt: The summer of 2003 in the Alps. *EARSeL eProceedings* (pp. 139–149).

Richter, R., & Schläpfer, D. (2002). Geo-atmospheric processing of airborne imaging spectrometry data. Part 2: Atmospheric/topographic correction. *International Journal of Remote Sensing*, *23*, 2631–2649. http://dx.doi.org/10.1080/01431160110115834.

Roujean, J. L., Leroy, M., & Deschamps, P. Y. (1992). A bidirectional reflectance model of the Earth's surface for the correction of remote sensing data. *Journal of Geophysical Research*, *97*, 20455–20468. http://dx.doi.org/10.1029/92JD01411.

Schaepman-Strub, G., Schaepman, M. E., Painter, T. H., Dangel, S., & Martonchik, J. V. (2006). Reflectance quantities in optical remote sensing—Definitions and case studies. *Remote Sensing of Environment*, *103*, 27–42. http://dx.doi.org/10.1016/j.rse.2006.03.002.

Stroeve, J., Box, J. E., Gao, F., Liang, S., Nolin, A., & Schaaf, C. (2005). Accuracy assessment of the MODIS 16-day albedo product for snow: Comparisons with Greenland in situ measurements. *Remote Sensing of Environment*, *94*, 46–60. http://dx.doi.org/10.1016/j.rse.2004.09.001.

Sugiyama, S., Yoshizawa, T., Huss, M., Tsutaki, S., & Nishimura, D. (2011). Spatial distribution of surface ablation in the terminus of Rhonegletscher, Switzerland. *Annals of Glaciology*, *52*, 1–8. http://dx.doi.org/10.3189/172756411797252185.

Vain, A., Kaasalainen, S., Pyysalo, U., Krooks, A., & Litkey, P. (2009). Use of naturally available reference targets to calibrate airborne laser scanning intensity data. *Sensors*, *9*, 2780–2796. http://dx.doi.org/10.3390/s90402780.

Vain, A., Liba, N., & Sepp, K. (2011). Factors affecting the airborne laser scanning intensity data. *Environmental Engineering, 8th International Conference.* Vilnius, Lithuania: Vilnius Gediminas Technical University.

Wagner, W. (2010). Radiometric calibration of small-footprint full-waveform airborne laser scanner measurements: Basic physical concepts. *ISPRS Journal of Photogrammetry and Remote Sensing*, *65*, 505–513. http://dx.doi.org/10.1016/j.isprsjprs.2010.06.007.

Wagner, W., Ullrich, A., Ducic, V., Melzer, T., & Studnicka, N. (2006). Gaussian decomposition and calibration of a novel small-footprint full-waveform digitising airborne laser scanner. *ISPRS Journal of Photogrammetry and Remote Sensing*, *60*, 100–112. http://dx.doi.org/10.1016/j.isprsjprs.2005.12.001.

Wanner, W., Li, X., & Strahler, A. H. (1995). A new class of geometric –optical semiempirical kernels for global BRDF and albedo modeling. *Geoscience and Remote Sensing Symposium, IGARSS '95* (pp. 15–17).

Warren, S. G. (1982). Optical properties of snow. *Reviews of Geophysics and Space Physics*, *20*, 67–89. http://dx.doi.org/10.1029/RG020i001p00067.

Wehr, A., & Lohr, U. (1999). Airborne laser scanning—An introduction and overview. *ISPRS Journal of Photogrammetry and Remote Sensing*, *54*, 68–82. http://dx.doi.org/10.1016/s0924-2716(99)00011-8.

Wiscombe, W. J., & Warren, S. G. (1980). A model for the spectral albedo of snow. I: Pure snow. *Journal of the Atmospheric Sciences*, *37*, 2712–2733. http://dx.doi.org/10.1175/1520-0469(1980)037<2712:AMFTSA>2.0.CO;2.

C. Bayesian object-based estimation of LAI and chlorophyll from a simulated Sentinel-2 top-of-atmosphere radiance image

Remote Sensing of Environment 140 (2014) 318–329

Contents lists available at ScienceDirect

Remote Sensing of Environment

journal homepage: www.elsevier.com/locate/rse

Bayesian object-based estimation of LAI and chlorophyll from a simulated Sentinel-2 top-of-atmosphere radiance image

Valérie C.E. Laurent [a,c,*], Michael E. Schaepman [a], Wout Verhoef [b], Joerg Weyermann [a], Roberto O. Chávez [c]

[a] Remote Sensing Laboratories, University of Zurich, Winterthurerstrasse 190, CH-8057 Zurich, Switzerland
[b] Faculty of Geo-Information Science and Earth Observation (ITC), University of Twente, P.O. Box 217, 7500 AE Enschede, The Netherlands
[c] Laboratory of Geo-Information Science and Remote Sensing, Wageningen University, P.O. Box 47, 6700 AA Wageningen, The Netherlands

ARTICLE INFO

Article history:
Received 11 January 2013
Received in revised form 4 September 2013
Accepted 6 September 2013
Available online 1 October 2013

Keywords:
Top-of-atmosphere radiance
Sentinel-2
APEX
Variable estimation
Bayesian optimization
Object-based
Coupled model
Radiative transfer
SLC
MODTRAN4
Li–Ross
Nadir-normalization

ABSTRACT

Leaf area index (LAI) and chlorophyll content (Cab) are important vegetation variables which can be monitored using remote sensing (RS). Physically-based approaches have higher transferability and are therefore better suited than empirically-based approaches for estimating LAI and Cab at global scales. These approaches, however, require the inversion of radiative transfer (RT) models, which is an ill-posed and underdetermined problem. Four regularization methods have been proposed, allowing finding stable solutions: 1) model coupling, 2) using a priori information (e.g. Bayesian approaches), 3) spatial constraints (e.g. using objects), and 4) temporal constraints. For mono-temporal data, only the first three methods can be applied.

In an earlier study, we presented a Bayesian object-based algorithm for inverting the SLC-MODTRAN4 coupled canopy-atmosphere RT model, and compared it with a Bayesian LUT inversion. The results showed that the object-based approach provided more accurate LAI estimates. This study, however, heavily relied on expert knowledge about the objects and vegetation classes. Therefore, in this new contribution, we investigated the applicability of the Bayesian object-based inversion of the SLC-MODTRAN4 model to a situation where no such knowledge was available.

The case study used a 16 × 22 km^2 simulated top-of-atmosphere image of the upcoming Sentinel-2 sensor, covering the area near the city of Zurich, Switzerland. Seven APEX radiance images were nadir-normalized using the parametric Li–Ross model, spectrally and spatially resampled to Sentinel-2 specifications, geometrically corrected, and mosaicked. The atmospheric effects between APEX flight height and top-of-atmosphere level were added based on two MODTRAN4 simulations. The vegetation objects were identified and delineated using a segmentation algorithm, and classified in four levels of brightness in the visible domain. The LAI and Cab maps obtained from the Bayesian object-based inversion of the coupled SLC-MODTRAN4 model presented realistic spatial patterns. The impact of the parametric Li–Ross nadir-normalization was evaluated by comparing 1) the angular signatures of the SLC-MODTRAN4 and Li–Ross models, and 2) the LAI and Cab maps obtained from a Li–Ross nadir-normalized image (using nadir viewing geometry) and from the original image (using the original viewing geometry). The differences in angular signatures were small but systematic, and the differences between the LAI and Cab maps increased from the center towards the edges of the across-track direction. The results of this study contribute to preparing the RS community for the arrival of Sentinel-2 data in the near future, and generalize the applicability of the Bayesian object-based approach for estimating vegetation variables to cases where no field data are available.

1. Introduction

Global climate and carbon cycles are strongly influenced by the Earth's biosphere, and in particular by its vegetation component. Vegetation variables, such as leaf area index (LAI) and leaf chlorophyll content (Cab), are therefore important inputs in dynamic global vegetation models (DGVM) (Foley, Levis, Costa, Cramer, & Pollard, 2000). These vegetation inputs can be provided in a spatially continuous way and at global scale by satellite remote sensing (Bacour, Baret, Béal, Weiss, & Pavageau, 2006; Baret et al., 2007; Myneni et al., 2002).

Usually, remote sensing data are first atmospherically corrected to top-of-canopy (TOC) reflectance data before they are used for estimating the vegetation variables. The variables can be estimated by using two main approaches. Empirical approaches rely on statistical relationships between the vegetation variables and the TOC reflectance data. The

---

* Corresponding author at: Irstea, UMR TETIS, Maison de la Télédétection, 500 rue J.F. Breton, 34093 Montpellier Cedex 5, France. Tel.: +33 467558615; fax: +33 467548700.

E-mail addresses: valerie.laurent@geo.uzh.ch, valerie.laurent@teledetection.fr (V.C.E. Laurent), michael.schaepman@geo.uzh.ch (M.E. Schaepman), w.verhoef@utwente.nl (W. Verhoef), joerg.weyermann@geo.uzh.ch (J. Weyermann), roberto.chavez@wur.nl (R.O. Chávez).

0034-4257/$ – see front matter © 2013 Elsevier Inc. All rights reserved.
http://dx.doi.org/10.1016/j.rse.2013.09.005

statistical relationships, however, require extensive field data collection and are only valid for the specific conditions for which they were developed, including sensor, acquisition geometry, and vegetation type (Dorigo et al., 2007; Ustin et al., 2009). Physically based approaches rely on vegetation canopy reflectance models, which are mostly based on radiative transfer (RT) theory, and are therefore more general because they can be adapted for different sensors, acquisition geometry and be parameterized for various vegetation types (Gemmell, Varjo, Strandstrom, & Kuusk, 2002; Malenovský et al., 2008).

1.1. Physically-based estimation of vegetation variables

To estimate the vegetation variables from the TOC reflectance data, however, the canopy RT model has to be inverted. This inverse problem is ill-posed (Combal et al., 2002; Jacquemoud et al., 2009), and four types of regularization methods have been proposed (Baret & Buis, 2008): 1) coupling models, 2) using a priori data, 3) using spatial constraints and 4) using temporal constraints, or combinations of these.

Model coupling allows reducing the number of input parameters, thereby reducing the under-determined nature of the inversion (Baret & Buis, 2008). The maximum model coupling set-up involves soil, leaf, canopy, and atmosphere RT models. Using such a coupled model allows working directly with the top-of-atmosphere (TOA) radiance data, skipping the atmospheric correction step (Laurent, Verhoef, Clevers, & Schaepman, 2011a). The atmospheric correction requires inverting the atmospheric RT model, whereas, when working at TOA level, the atmospheric RT model is used in forward mode, which is more accurate and allows for better inclusion of canopy directional effects (Laurent, Verhoef, Clevers, & Schaepman, 2011b), topography and adjacency effects in the coupled canopy-atmosphere model. Despite the higher model complexity, the traditional inversion techniques can be used, and the same knowledge of the atmospheric parameters as in the atmospheric correction is sufficient.

A priori information allows restricting the variable space to a smaller subspace, thus facilitating the inversion (Combal et al., 2002). Bayesian approaches use the a priori data directly in the cost function, and have been widely used for estimating vegetation variables (Lavergne et al., 2007; Li, Gao, Wang, & Strahler, 2001; Pinty et al., 2007). Spatial constraints allow using the information contained in the neighbouring pixels in the inversion (Atzberger, 2004; Atzberger & Richter, 2012; Houborg, Anderson, & Daughtry, 2009), while temporal constraints allow using the information contained in a time series of remote sensing observations (Kötz, Baret, Poilve, & Hill, 2005; Lauvernet, Baret, Hascoët, Buis, & Le Dimet, 2008).

For a single RS image, the maximum regularization set-up involves a coupled canopy-atmosphere RT model, a priori information, and spatial constraints (Laurent, Verhoef, Damm, Schaepman, & Clevers, 2013).

1.2. Sentinel-2

Sentinel-2 is a scheduled multispectral and high spatial resolution mission which is part of the Global Monitoring for Environment and Security (GMES) program (Berger, Moreno, Johannessen, Levelt, & Hanssen, 2012; Drusch et al., 2012; Malenovský et al., 2012). The spectral and spatial characteristics for the Sentinel-2 mission have been specified so as to provide enhanced continuity for SPOT and Landsat missions in the visible (VIS), near infrared (NIR) and short-wave infrared (SWIR) spectral domains. The Multi Spectral Instrument (MSI) onboard Sentinel-2 will have 13 spectral bands in the range from 400 to 2400 nm, with pixel sizes of 10, 20, or 60 m, depending on the spectral band (Drusch et al., 2012; Sentinel-2 PDGS Project Team, 2011). The first of two satellites is planned to be launched in 2014. Until Sentinel-2 data are available, several studies have investigated the potential of Sentinel-2 for vegetation applications.

Most of the Sentinel-2 exploratory studies focussed on the spectral dimension, selecting appropriate bands from surrogate sensors such as CHRIS (Atzberger & Richter, 2012; Delegido, Verrelst, Alonso, & Moreno, 2011) and HyMap (Richter, Hank, Vuolo, Mauser, & D'Urso, 2012), or convolving the bands of hyperspectral sensors such as CASI (Richter, Atzberger, Vuolo, & D'Urso, 2011a; Richter, Atzberger, Vuolo, Weihs, & D'Urso, 2009) or field spectrometers (Clevers & Gitelson, 2013; Herrmann et al., 2011) to the Sentinel-2 bands. Limited by the spectral range of the surrogate sensor used, most of these studies were not able to simulate the blue and the SWIR Sentinel-2 bands in full.

Further, few studies included the varying pixel size in their simulated Sentinel-2 data (Richter, Wang, Bachmann, & Schläpfer, 2011b), and even fewer investigated the potential of the spatial characteristics of the Sentinel-2 data (Hedley, Roelfsema, Koetz, & Phinn, 2012; Verrelst et al., 2012). Only two studies made use of top-of-atmosphere simulated Sentinel-2 data, and they focussed on cloud detection and correction (Hagolle, Huc, Pascual, & Dedieu, 2010; Richter et al., 2011b), but not on vegetation.

Therefore, despite its potential use for supporting the development of (pre)processing algorithms in advance, a full TOA simulated image compliant with all spectral and spatial characteristics of the Sentinel-2 mission so far was still missing.

1.3. Objectives

The two main objectives of this study were to: 1) build a realistic TOA Sentinel-2 image with full spectral and spatial characteristics as specified in the Sentinel-2 documentation, and 2) estimate LAI and Cab from the Sentinel-2 image by inverting a coupled canopy-atmosphere RT model.

The particular spatial and spectral characteristics of Sentinel-2 can only be simulated using high resolution airborne imaging spectrometer data. APEX was chosen for this purpose because of its unprecedented spectral, spatial and radiometric resolution. Its continuous spectral coverage of the range 380 to 2500 nm (Jehle et al., 2010) allowed simulating all 13 Sentinel-2 bands. Each band was simulated with at least three APEX bands (D'Odorico, Gonsamo, Damm, & Schaepman, 2013), and each Sentinel-2 pixel was covered by at least nine APEX pixels. The signal-to-noise ratio (SNR) of APEX is also well above the expected SNR of Sentinel-2. Seven APEX images were normalized to nadir viewing before being spatially and spectrally resampled and mosaicked. The simulated Sentinel-2 image covers an area of 16 × 22 km^2 around the city of Zurich, Switzerland, which includes a wide range of land cover types (e.g., agriculture, forest, lakes, an airport and urban areas). In order to obtain the most accurate LAI and Cab estimates as possible from this single image, the Bayesian object-based approach of Laurent et al. (2013) was chosen, because it combines the strengths of model coupling, a priori data and spatial constraints regularization methods. This latter study, however, relied on manual digitization of the objects used to apply the spatial constraints and was based on extensive field data on vegetation classes and their associated a priori data. Therefore, two specific objectives were added to the main objectives: 1) evaluate the effect of the normalization to nadir viewing of the APEX images, and 2) propose an image-based approach for extracting objects, and a general vegetation classification associated with a priori data which does not require field data.

The results of this study contribute to preparing the RS community for the arrival of Sentinel-2 data in the near future, and generalize the applicability of the Bayesian object-based approach for estimating vegetation variables to cases where no field data are available, as is generally the case for studies in less accessible regions as well as global studies.

2. Materials and methods

2.1. Study area and APEX data

The study area covered the city of Zurich, Switzerland (+47° 22′ 2″ N, +8° 32′ 40″ E) and its surrounding rural areas. A wide range of land covers and land uses are present in the area: buildings, urban parks, an airport, lakes, rivers, forests, and crop fields at various phenological stages. The lake is framed by two hill slopes, with altitudes varying between 392 and 871 m a.s.l. The average altitude of the area was 485 m a.s.l.

The remote sensing data were acquired on June 26th, 2011, under cloud-free conditions, with the APEX instrument. APEX is a dispersive push broom imaging spectrometer which records 1000 pixels per scan line with a field of view (FOV) of 28°. It covers the spectral region between 380 nm and 2500 nm in 313 spectral bands with a sampling interval varying between 0.4 and 10 nm (Hüni et al., 2009; Jehle et al., 2010). The flight pattern consisted of seven flight lines with headings alternating between north (34.2°) and south (214.2°). The data were acquired at an altitude of about 6400 m a.s.l., resulting in a raw across-track ground sampling distance of approximately 3.0 m. The solar zenith angle varied between 34.7 and 43.2°, with an average of 38.6°, and the solar azimuth angle varied between 107.6 and 122.7°, with an average of 115.3°. The seven resulting APEX images were radiometrically calibrated to obtain at-sensor radiance images.

2.2. Simulated Sentinel-2 image

Each APEX radiance image was pre-processed individually before mosaicking. The pre-processing included: nadir-normalization, spectral resampling, geometric correction, and spatial resampling.

First, the APEX images were normalized to nadir viewing by applying a Li–Ross BRDF (bidirectional reflectance distribution function) correction based on a land cover classification (Weyermann, Damm, Kneubühler, & Schaepman, 2013). Each image was classified into five land cover types (two vegetation structural classes, soil, water and urban surfaces) using spectral angle mapping, with reference signatures extracted from the images. The angular signature of each land cover type was modelled by a linear combination of three kernels: a constant kernel for isotropic scattering, a Li kernel for geometric scattering (intra-pixel shading effects), and a Ross kernel for volumetric scattering. The Li and Ross kernels are non-linear functions of the illumination and observation geometry (Roujean, Leroy, & Deschamps, 1992; Wanner, Xiaowen, & Strahler, 1995). Variants of these functions were designed to account for variations of LAI in the Li kernel ("thick" or "thin"), and of canopy density in the Ross kernel ("sparse" or "dense"). For each land cover type, the Li and Ross kernel types and the three kernel weights were chosen by minimizing the root mean square error (RMSE) between angular observations and simulations.

To account for the Sentinel-2 spectral characteristics, the nadir-normalized data were spectrally convolved to the Sentinel-2 sensor response functions. The convolved images were then geo-corrected and ortho-rectified to the Swiss National Grid (CH1903) with a ground sampling distance of 10 m, using bi-linear interpolation, and mosaicked. To account for the Sentinel-2 spatial characteristics, bands 5, 6, 7, 8b, 11 and 12 of the mosaic were resampled to 20 m, and bands 1, 9 and 10 were resampled to 60 m.

Finally, the Sentinel-2 TOA radiances were calculated from the radiances in the mosaic that correspond to measurements at the height of the APEX flight (L_{APEX}) using the following equation (Green, Pavri, & Chrien, 2003):

$$L = L_{\mathrm{path}} + T_{\mathrm{atm}} L_{\mathrm{APEX}}, \tag{1}$$

where L_{path} is the atmospheric path radiance, and T_{atm} is the total atmospheric upward transmittance between the APEX flight height and the top of the atmosphere. These two variables were calculated using MODTRAN4 as described in (Guanter, Richter, & Kaufmann, 2009) for surface albedo values of 0 and 0.5. The MODTRAN4 runs were performed with a "ground altitude" of 6 km, the maximum allowed in MODTRAN4, instead of the APEX flight height of 6.4 km. The water column was estimated, using the method of (Richter & Schläpfer, 2002), to values higher than the maximum allowed in MODTRAN4, and the maximum water column of 0.36308 g/cm^2 was therefore used. The final image spatially and spectrally corresponds to a Sentinel-2 level 1c product.

2.3. Objects segmentation and classification

The simulated Sentinel-2 image was segmented in spectrally homogeneous objects using the multi-resolution segmentation algorithm as implemented in eCognition (version 8.0.1). This algorithm is the most frequently used object-based studies (Blaschke, 2010) and has been successfully used for identification and classification of operational vegetation units (Johansen, Coops, Gergel, & Stange, 2007; Lamonaca, Corona, & Barbati, 2008; Massada et al., 2012; Wang, Sousa, & Gong, 2004). It is a region-growing algorithm which minimizes the internal spectral and spatial heterogeneity of the objects. The segmentation is performed using three user-defined parameters: the scale parameter (*scale*) which controls the internal homogeneity and therefore the size of the objects, the shape parameter (*shape*) which weights the importance of the spatial information versus the spectral information, and the compactness parameter (*compact*) which weights the importance of the compactness versus the smoothness of the object within the shape weight (Benz, Hofmann, Willhauck, Lingenfelder, & Heynen, 2004).

To obtain the highest spatial accuracy, the segmentation was performed on the bands having the smallest pixel size of 10 m: band 2 (blue, B), band 3 (green, G), band 4 (red, R), and band 8 (near infra-red, NIR). The three segmentation parameters were chosen by trial and error, paying attention to keeping agricultural fields and forest stands as individual objects. They were set as follows: *scale* = 8, *shape* = 0.2 and *compact* = 0.5.

Because of the lack of field data, the objects were classified into only five general land cover classes: no vegetation, and four vegetation classes (see Table 1). The normalized difference vegetation index (NDVI) was used to discriminate vegetated and non-vegetated objects. The vegetated objects were then classified in four classes having similar radiative transfer regime, as related to their structural complexity. The structural complexity is inversely related to the brightness in the visible domain and the four vegetation classes (VB1 to VB4) were therefore defined using the sum of the R, G, and B bands (R + G + B). For this proof of concept, the NDVI and R + G + B thresholds were chosen based on expert knowledge.

Table 1
Decision rules used for classifying the objects.

NDVI (–)	R + G + B (mW/(m^2 sr nm))	Class
NDVI > 0.3	R + G + B ≤ 86	VB1
	86 < R + G + B ≤ 100	VB2
	100 < R + G + B < 130	VB3
	R + G + B ≥ 130	VB4
NDVI ≤ 0.3		No vegetation

2.4. Bayesian object-based estimation of LAI and Cab

2.4.1. Estimation algorithm

LAI and Cab were estimated directly from the TOA radiance data using a Bayesian object-based algorithm (Laurent et al., 2013). This algorithm consists of two steps which are briefly described below.

In the first step, six to seven variables, including LAI and Cab, are estimated for each object, using a Bayesian optimization algorithm. This algorithm seeks to find the maximum likelihood estimate by minimizing the cost function χ^2 (Tarantola, 2005):

$$\chi^2 = {}^{1}\!/_{2}(\mathbf{L_o}-\mathbf{L})^{\mathrm{T}}\mathbf{C_o^{-1}}(\mathbf{L_o}-\mathbf{L}) + {}^{1}\!/_{2}(\mathbf{v_a}-\mathbf{v})^{\mathrm{T}}\mathbf{C_a^{-1}}(\mathbf{v_a}-\mathbf{v}), \tag{2}$$

where $\mathbf{L_o}$ is the vector of observed radiance, averaged for the object and including all 13 Sentinel-2 bands, $\mathbf{L}$ is the vector of simulated radiance, $\mathbf{C_o}$ is the covariance matrix containing the observation and model uncertainties in each spectral band, $\mathbf{v_a}$ is the vector of a priori variable values, $\mathbf{v}$ is the vector of variable values, $\mathbf{C_a}$ is the covariance matrix of the a priori variables, and T represents the matrix transposition operator. The first term of Eq. (2) is the radiometric cost, and the second term is the a priori cost.

The update vector $\mathbf{\Delta v}$ to apply to $\mathbf{v}$ in each iteration of the optimization is given by:

$$\mathbf{\Delta v} = \left[\mathbf{J^T C_o^{-1} J} + \mathbf{C_a^{-1}} + \mu\mathbf{J^T J}\right]^{-1}\left[\mathbf{J^T C_o^{-1}}(\mathbf{L_o}-\mathbf{L}) + \mathbf{C_a^{-1}}(\mathbf{v_a}-\mathbf{v})\right], \tag{3}$$

where $\mathbf{J}$ is the Jacobian matrix, and μ is the damping factor. $\mathbf{J}$ contains the partial derivatives of the model, obtained by varying each variable, by 1% of its allowed range (Laurent et al., 2011a). The damping factor was introduced to avoid the occasional cost increase which can happen with the Gauss–Newton-like formula by rotating $\mathbf{\Delta v}$ towards the direction of steepest descent, similarly to the Levenberg–Marquardt algorithm. It is set to zero at the beginning of each iteration. In case of increasing cost, μ is set to one, and subsequently multiplied by 10, until a decrease in cost is obtained, or until μ reaches 10^{10}.

Each variable v is constrained between its a priori minimum ($v_{\min}$) and maximum ($v_{\max}$) values by a transformation into a variable u:

$$u = \arcsin\left(2\frac{v-v_{\min}}{v_{\max}-v_{\min}}-1\right). \tag{4}$$

The optimization is performed in the transformed variable space, so the $\mathbf{C_a}$ and $\mathbf{J}$ matrices are also expressed in the transformed variables. At the end of the optimization, the optimized variable values are transformed back into the original variable space.

In the second step, LAI and Cab are estimated for each pixel in the object using a LUT, constrained by the outputs of the Bayesian optimisation at the object level. All variables, except LAI and Cab are fixed to their optimized values. The LAI range is chosen by optimizing LAI for the two pixels having the minimum and maximum radiance in the NIR bands (bands 8 and 9), using the Bayesian optimization algorithm of the first step. LAI is then uniformly sampled within the obtained range, increasing the number of samples with increasing LAI range. For each sampled LAI, the range for Cab was chosen according to the LAI value. Cab was then sampled in its range using steps of 10 μg/cm². Finally, the coupled model was run for all LAI–Cab combinations to populate the LUT. The estimates were then found in the LUT by minimizing Eq. (2).

2.4.2. Coupled canopy-atmosphere model

The vegetation canopy was modelled with the soil-leaf-canopy model SLC (Verhoef & Bach, 2007). It was chosen because it is a hybrid RT model with good accuracy and fast running time for use in the optimization algorithm. SLC couples the soil model 4SOIL with the leaf model PROSPECT and the canopy model 4SAIL2.

PROSPECT simulates the leaf optical properties based on the leaf concentrations in chlorophyll (Cab), dry matter (Cdm), water (Cw), and on the leaf mesophyll parameter (N) (Jacquemoud & Baret, 1990). The refractive index of leaf material and the specific absorption coefficients of chlorophyll, dry matter and water at 1 nm resolution were taken from Feret et al. (2008). In addition, the model was extended to include the concentration in brown pigments (Cs) (Verhoef & Bach, 2003).

4SAIL2 is based on the SAIL model (Verhoef, 1984), which assumes arbitrarily inclined leaves, as described by the leaf inclination distribution (LIDF). 4SAIL2 allows for two horizontal canopy layers, which can have different proportions of brown and green leaves in their total leaf area (fB). The vertical distribution of the brown and green leaves is controlled by the dissociation parameter (D): if D = 0, the brown and green leaves are homogeneously distributed, if D = 1, the brown leaves are all in the bottom layer of the canopy, and the green leaves in the top layer. The crown-level clumping is modelled assuming spherical crown shapes and is controlled by the canopy cover (Cv), and the crown shape parameter (Zeta), defined as the ratio of the crown diameter to the height of the crown center above ground (Verhoef & Bach, 2007). The crown clumping is an interesting feature to model open canopies. Finally, the hot spot parameter (Hot) controls the width of the hot spot reflectance peak in the angular domain.

The atmosphere was simulated using the MODTRAN4 RT model (Berk et al., 2003). It is a state-of-the-art model with rather high computational demands. The canopy-atmosphere coupling approach of Laurent et al. (2011a, 2011b), however, requires only three runs for surface albedo values of 0, 0.5, and 1 (Verhoef & Bach, 2003) which can be performed in advance. Because the atmospheric parameters were considered constant, this allowed using the coupled SLC-MODTRAN4 model in the optimization. The canopy-atmosphere coupling relies on the 4-stream theory, and allows making full use of the four directional components of the canopy reflectance provided by SLC.

2.4.3. Parameterization of the model and estimation algorithm

A soil spectrum measured with an ASD spectroradiometer in a neighbouring test site with similar soil type (Oensingen, Switzerland, +47° 16′ 44″ N, +7° 43′ 53″ E) was used, instead of using the 4SOIL model, and it was considered constant in the study area. The SLC parameters were fixed independently for each vegetation class, using expert knowledge (Table 2). The three MODTRAN4 runs were conducted for a visibility of 60 km, a water vapour column of 1.3 g/cm², between the average height of the study area and TOA level, using the 1 cm^{-1} band model. The visibility of 60 km and water vapour column of 1.3 g/cm² were obtained by averaging the values calculated for the atmospheric correction of the individual flight lines. The SLC and MODTRAN4 simulations were performed at 1 nm spectral resolution, and the final radiance output signature was convolved to the Sentinel-

Table 2
Fixed parameter values for the SLC model for the four vegetation classes.

	Parameter	Unit	Vegetation class			
			VB1	VB2	VB3	VB4
Canopy	LIDF	–	Spherical	Spherical	Spherical	Spherical
	D	–	0	0	0	0
	Zeta	–	0.5	0.5	1	1
	Hot	–	0.01	0.05	0.05	0.05
Brown leaves	Cab	μg/cm²	10	5	5	5
	Cw	cm	0	0.001	0.001	0.001
	Cdm	g/cm²	0.5	0.005	0.005	0.005
	Cs	–	15	1	1	1
	N	–	10	2	2	2
Green leaves	Cs	–	0.05	0.05	0.05	0.05

2 bands using the spectral response functions as defined in Drusch et al. (2012).

LAI and Cab were estimated using the Bayesian object-based estimation algorithm (Section 2.4.1) for all vegetated objects whose size was larger than 1000 m^2 (ten pixels of 10 m). The free variables in the object-based Bayesian optimization were: LAI, Cv, Cab, Cw, Cdm, N (of the green leaves), and additionally fB for the VB1 and VB2 objects, which correspond to forest or mature crop fields. The a priori data for these six or seven variables for each vegetation class were chosen using expert knowledge (Table 3). The initial values of all the variables were set to the middle of their a priori variation range, except LAI whose initial value was 2. The optimization was terminated when the update changes (Eq. (3)) for all the variables were smaller than 1% of their a priori variable range, or when ten iterations had been performed. The measurement uncertainties for the a priori data and the Sentinel-2 observations were assumed to be uncorrelated, so the two covariance matrices were both diagonal. The diagonal of the $\mathbf{C_a}$ matrix was filled with the a priori variance of the variables, calculated from Table 3. Following Laurent et al. (2013), the model uncertainties were ignored, and a constant uncorrelated noise of 1 [mW/(m^2 sr nm)]^2 was assumed for all spectral bands, resulting in the $\mathbf{C_o}$ matrix being equal to the identity matrix. This choice is discussed in Section 4.5.

2.5. Evaluation of the effects of the parametric nadir-normalization

There is a conceptual issue when using a parametric RT model, like the Li–Ross model, to normalize the radiance data to nadir viewing, and then estimating the variables from the nadir-normalized data using a physically-based RT model, like the coupled SLC-MODTRAN4 model. Indeed, the radiance values are corrected to nadir-viewing according to the angular behaviour of the parametric model, which may differ from that of the physically-based model, and therefore reduce the performance of the inversion of the physically-based model. First, the discrepancy between the Li–Ross and SLC-MODTRAN4 angular signatures was investigated, and second the impact of the Li–Ross nadir-normalization on the LAI and Cab estimates was evaluated. These two analyses were performed at APEX flight height, before applying Eq. (1). The results are easily transferred to TOA level, because the TOA radiance is a linear transformation of the radiance at APEX flight height (Eq. (1)). The westernmost image (flight line 9, FL9) was selected because it had the most vegetation. The solar zenith angle for FL9 was 34.7° and the solar azimuth angle was 122.7°. MODTRAN4 was run in advance, between the average altitude of the study area and the APEX flight height, for viewing zenith angles (VZA) between $-14°$ and $+14°$ (APEX FOV) in steps of 2°. The outputs were stored in an atmospheric database. Positive VZA values indicate viewing directions opposite to the sun (forward direction).

Table 3
A priori mean, standard deviation, minimum and maximum values of the canopy and green leaves variables for the four vegetation classes.

Variable	Unit	Vegetation class			
		VB1	VB2	VB3	VB4
LAI	–	**4** (2) [2, 8]	**3** (2) [1, 8]	**1** (2) [0, 4]	**0.5** (2) [0, 2]
Cv	–	**1** (0.2) [0.7, 1]	**1** (0.2) [0.5, 1]	**0.8** (0.2) [0.3, 1]	**0.3** (0.2) [0, 0.5]
Cab	μg/cm^2	**40** (20) [10, 100]	**40** (20) [10, 100]	**40** (20) [10, 100]	**40** (20) [10, 100]
Cw	cm	**0.02** (0.01) [0.005, 0.05]	**0.02** (0.01) [0.005, 0.05]	**0.02** (0.01) [0.005, 0.05]	**0.02** (0.01) [0.005, 0.05]
Cdm	g/cm^2	**0.005** (0.001) [0.001, 0.01]	**0.005** (0.001) [0.001, 0.01]	**0.005** (0.001) [0.001, 0.01]	**0.005** (0.001) [0.001, 0.01]
N	–	**1.8** (0.5) [1, 2.5]	**1.8** (0.5) [1, 2.5]	**1.8** (0.5) [1, 2.5]	**1.8** (0.5) [1, 2.5]
fB	–	**0.2** (0.1) [0, 0.5]	**0.2** (0.1) [0, 0.5]	**0** (n/a) [n/a]	**0** (n/a) [n/a]

2.5.1. Angular signatures

The angular signatures simulated by the SLC-MODTRAN4 and Li-Ross models were compared for the four vegetation classes for the four 10 m bands of Sentinel-2. For each class, the SLC-MODTRAN4 was run using the default parameter values (Table 2) and the a priori values (Table 3), for each of the 1000 across-track APEX pixels, interpolating the MODTRAN4 outputs from the atmospheric database. The obtained angular signatures were then fed to the Li–Ross nadir-normalization algorithm (see Section 2.2). The kernels and associated weights chosen by the algorithm were then used to simulate the Li–Ross angular signatures.

2.5.2. LAI and Cab estimates

The impact of the parametric Li–Ross nadir-normalization on the LAI and Cab estimates was evaluated by comparing the LAI and Cab maps obtained by the Bayesian object-based inversion of the SLC-MODTRAN4 model (Section 2.4) from:

1) the nadir-normalized image, using nadir viewing geometry in the simulations (NN approach)
2) the original image, using the original viewing geometry in the simulations (OG approach)

The objects and associated classes needed to apply the Bayesian object-based estimation algorithm to FL9 were obtained by taking a spatial subset of the objects and associated vegetation classes obtained for the Sentinel-2 image (Section 2.3). For the OG approach, an image containing the original viewing geometry (zenith and azimuth angles) for each pixel was created in raw APEX geometry, and then geometrically corrected in the same way as FL9. The average viewing geometry for each object were then calculated and used in the SLC-MODTRAN4 simulations.

3. Results

3.1. Simulated Sentinel-2 image

The simulated Sentinel-2 image has an extent of 16 × 22 km^2. It has full spectral and spatial characteristics of the future Sentinel-2 satellite. True and false colour composites of the 10 m resolution bands are presented in Fig. 1. Despite the nadir-normalization applied to each of the seven APEX images, a brighter vertical stripe appears on the west side of the image, and there is a general trend of increasing brightness from east to west. This is discussed in Section 4.3.

3.2. Objects identification and classification

The objects and classes for a small area in the south west of the image are presented in Fig. 2. The size of the objects is related to the heterogeneity of the area. Small objects are predominantly found in urban areas where many types of surfaces can be found within a few pixels, while larger objects are found in forested areas, which possess lower spectral and spatial internal variability. Agricultural fields are spectrally and spatially more homogenous than forest patches, but objects in agricultural areas are smaller because of the sharp transition from one crop to the next at the edges of the small Swiss fields.

The classification criteria (Table 1) efficiently discriminated vegetated and non vegetated objects such as urban areas and bare fields. As expected, most forest objects were classified as VB1, and brown field objects having low vegetation cover were classified as VB4. Vegetated objects located within urban areas and larger than 1000 m^2 were included in the LAI and Cab estimation.

3.3. Bayesian object-based estimation

The object-level maps of the estimates of the seven free variables in the Bayesian optimization algorithm are presented in Fig. 3, as well as

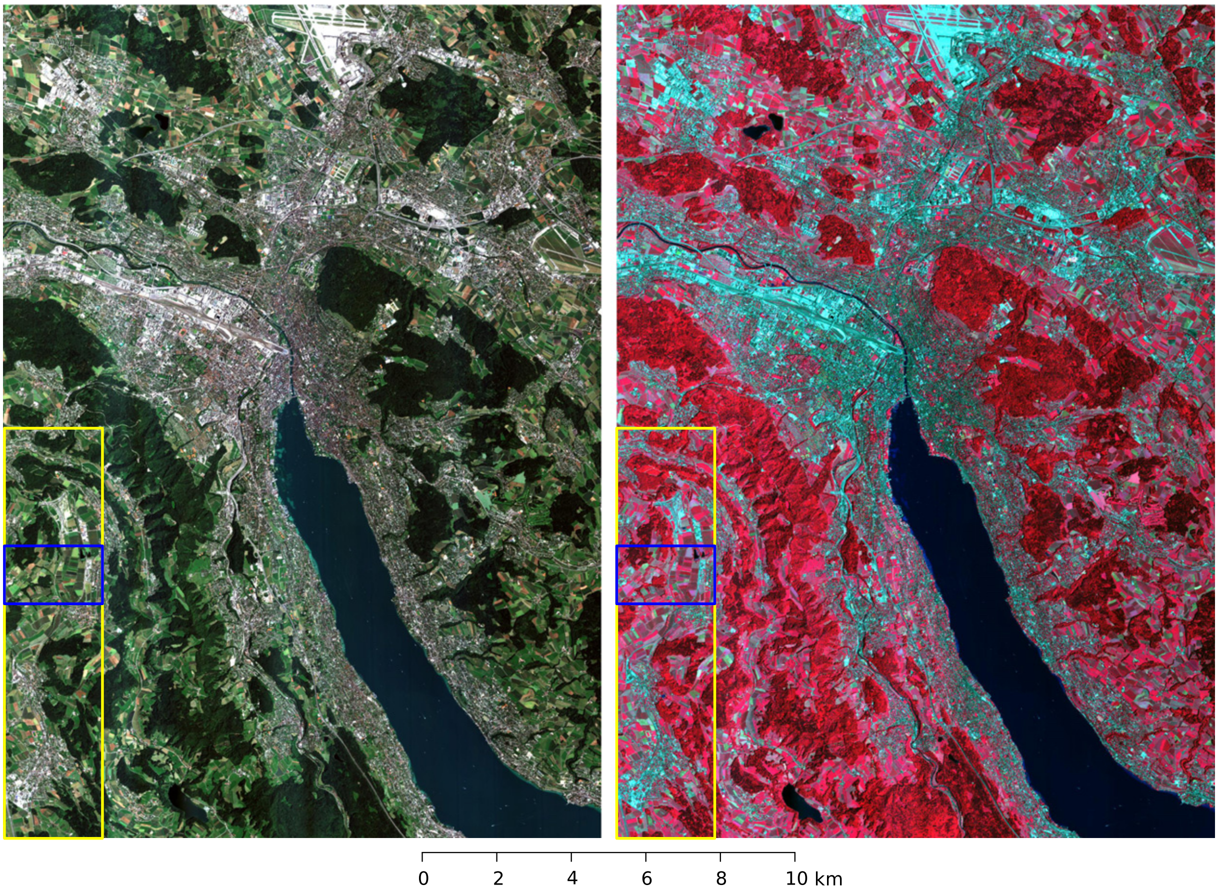

Fig. 1. True (R: band 4, G: band 3, B: band 2) and false (R: band 8, G: band 4, B: band 3) colour composites of the simulated Sentinel-2 image with 10 m resolution. The blue rectangle indicates the area used for Figs. 2 and 4, and the yellow rectangle indicates the area of FL9 used for Fig. 6.

the full vegetation classification map, and the cost map. Most objects had high Cv values, except for VB4 objects and a few VB3 objects, accordingly to the Cv ranges used in the a priori data (Table 3). The highest LAI values were found in VB1 objects. These objects also had higher Cab and higher fB than the objects classified as VB2 to VB4. The differences between object classes were less marked for Cdm, Cw, and N. The unitless cost values were represented using the value range from 8 to 100. To give the reader an idea of the meaning of the cost values, ignoring the negligible a priori part of the cost, this range corresponds to an average radiance mismatch of 1.1 to 3.9 mW/(m^2 sr nm) per band. This mismatch can be related to the magnitude of the radiance values, which is usually in the range of 20 to 50 mW/(m^2 sr nm) in the visible, and in the range of 40 to 200 mW/(m^2 sr nm) in the NIR for vegetation. Most objects had cost values smaller than 100, but there was a

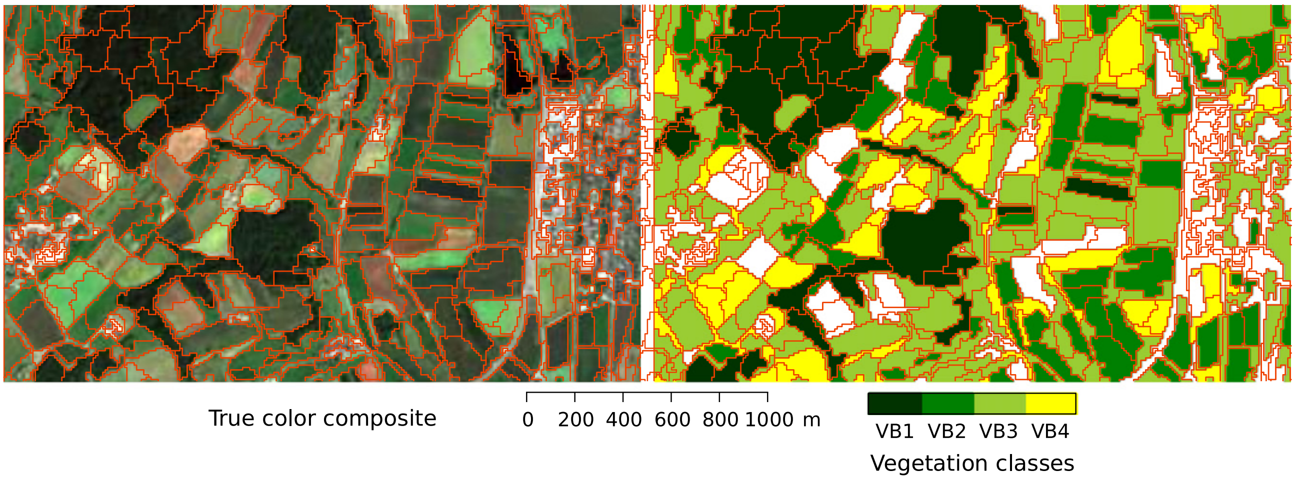

Fig. 2. Objects (red polygons) with the true colour composite (left) and with the vegetation classes (right) for a zoomed area (blue rectangle on Fig. 1). The white areas were classified as no vegetation.

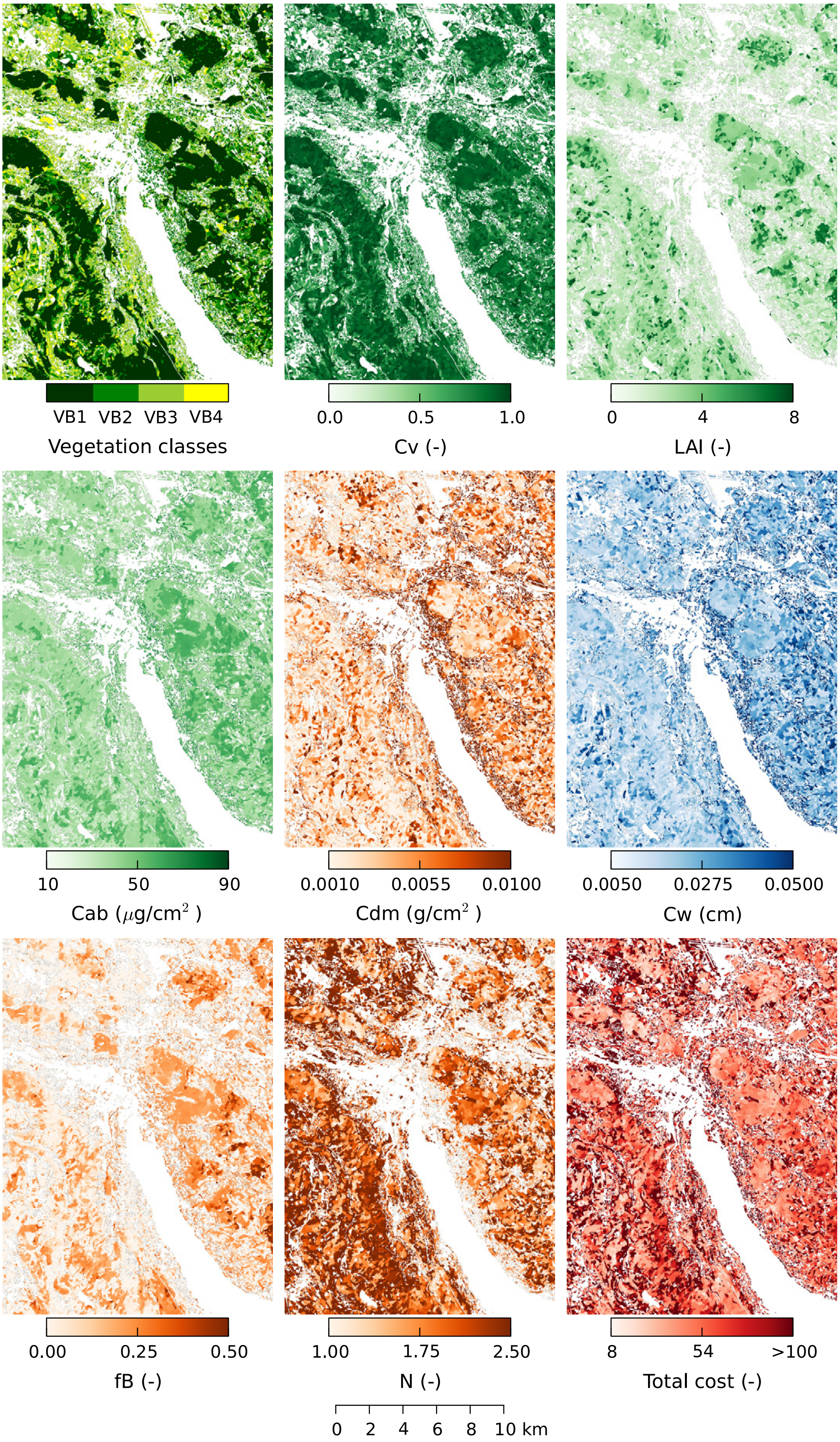

Fig. 3. Object-based maps of vegetation classes, LAI, Cv, fB, Cab, Cdm, Cw, N, and cost values obtained from the simulated Sentinel-2 image.

trend to higher cost values towards the west of the image. The brighter vertical stripe on the west side of the image translated into visible stripes on the object-level maps of LAI, Cdm, fB, and cost.

The pixel-level maps of LAI and Cab (not shown) show the same spatial patterns of higher values in VB1 objects, the values were higher than those obtained at the object level. Most pixels still had cost values smaller than 100, but much higher cost values than at object level were reached locally, especially in very high VB1 objects.

The LAI and Cab estimates at object and pixel levels are presented in more detail for a small area in the south west of the image (Fig. 4). The object and pixel maps of each variable have similar spatial patterns, with more details appearing in the pixel maps. The added variability at the pixel level concerns mostly the VB1 and VB2 objects (see vegetation classes on Fig. 2). From object to pixel level, the maximum values increased from 7.6 to 8 for LAI, and from 57 to 100 for Cab.

3.4. Effects of the parametric nadir normalization

3.4.1. Angular signatures

For the Li–Ross simulations, the nadir normalization algorithm selected the same kernels for all four vegetation classes and for all four 10 m resolution bands: Ross-thin for the volumetric scattering and Li-dense for the geometric scattering (see Section 2.2). For all bands and vegetation classes, the spectral profiles of the kernel weights were similar (not shown). The weights of the isotropic scattering kernel were the highest, while the weights of the geometric kernel were close to zero, and the weights for the volumetric kernel were negative.

The relative differences between the Li-Ross and SLC-MODTRAN4 angular signatures for the four 10 m resolution bands are presented in Fig. 5. The difference curves for all four vegetation classes present the same sinusoidal shape for the four bands, revealing systematic differences between the two models. The Li–Ross simulations were lower than the SLC-MODTRAN4 simulations for $VZA < -11°$ and for $VZA \in [1°, 12°]$, and higher than the SLC-MODTRAN4 simulations for $VZA \in [-11°, 1°]$ and $VZA > 12°$. The Li–Ross simulations therefore differed from the SLC-MODTRAN4 simulations for nadir viewing. For the VB1 and VB2 vegetation classes, the relative differences were lower in the NIR than in the visible bands, whereas for the VB3 and VB4 vegetation classes, the relative differences were lowest in the red bands. All absolute difference values were smaller than 0.15 mW/(m^2 sr nm) in absolute value.

3.4.2. LAI and Cab estimates

The LAI, Cab and cost maps obtained from the NN and OG approaches (not shown) had R^2 values of 0.96 for LAI, 0.98 for Cab and 0.93 for the cost, showing a good consistency between the two approaches. The difference maps (Fig. 6) show the spatial patterns of the differences between the two approaches. The objects are much more visible on the LAI and cost difference maps than on the Cab difference map, which appears more scattered. For all three maps, as expected, the differences are smallest in the across-track center of the image, and increase towards the edges. The highest LAI differences are found in objects having very high structural complexity (VB1, very low brightness in the visible), where LAI values are higher. The spatial pattern of very high cost differences roughly follows the pattern of the VB1 and VB2 objects.

4. Discussion

4.1. Objects and spatial constraints

The area of the city of Zurich and its surroundings presented discrete landscape units with clear boundaries, favouring object-based approaches. Objects of various sizes were efficiently delineated thanks to the *scale* parameter, which limits both spectral and spatial heterogeneity. If this threshold is reached early in the segmentation process, as in urban areas, the object will be small (Fig. 2). On the contrary, if the threshold is reached later, as in forested areas, the object will be bigger (Fig. 2). For this reason, careful tuning of the *scale* parameter is

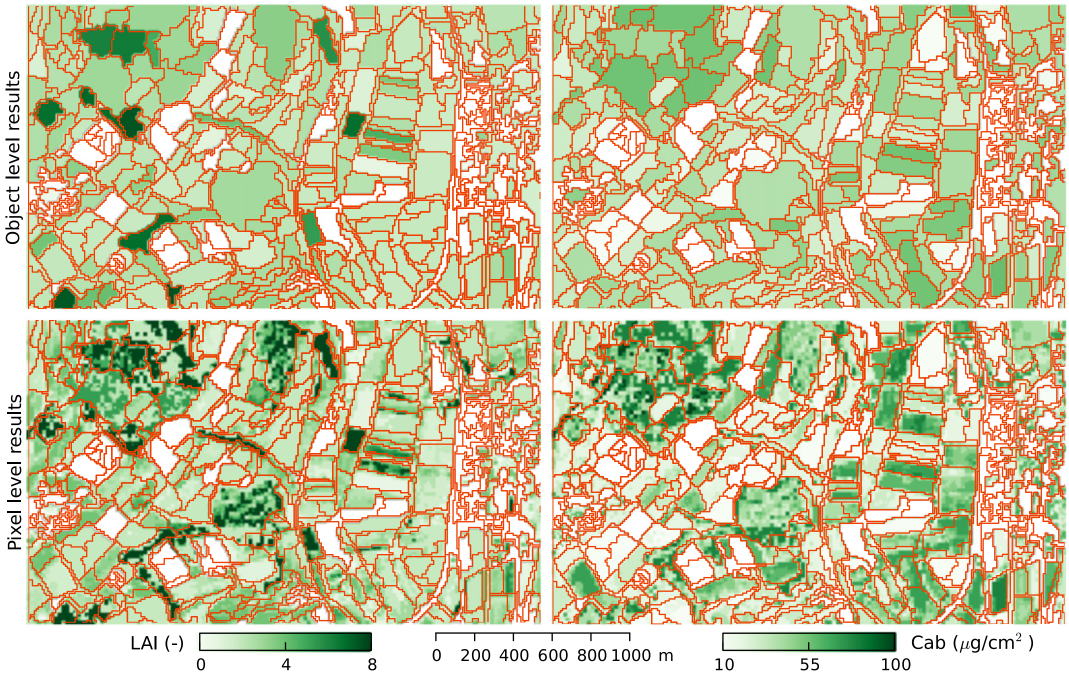

Fig. 4. Object- and pixel-level maps of LAI and Cab for a zoomed area (blue rectangle on Fig. 1), with objects boundaries (red polygons).

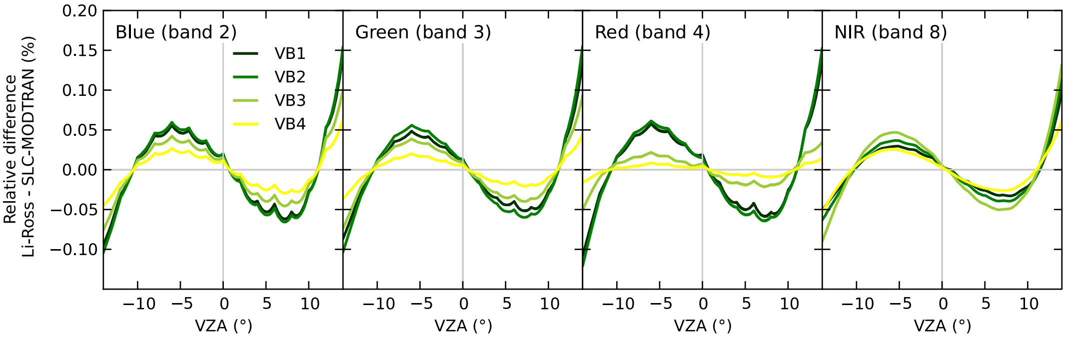

Fig. 5. Relative difference between the Li–Ross and SLC-MODTRAN4 angular signatures for the four 10 m bands and for the four vegetation classes.

important in order to obtain objects homogenous enough to apply the spatial constraints and to obtain accurate estimates of LAI and Cab at the pixel level. Indeed, in this study, the smoothness principle (Wang, Yang, & Li, 2008) was applied strictly, fixing the object-level variables to their optimized values for all pixels in the object. If, for example, an object consists of pixels belonging to two vegetation classes, the object-level variables will be optimized to match the area-weighted average signature of the two classes. The obtained values will not be suitable for either of the two classes, and will lead to inaccurate LAI and Cab estimates at the pixel level. Multi-level image segmentation yields a hierarchical object network (Benz et al., 2004), which allows obtaining meaningful objects (Blaschke, 2010) such as agricultural fields and urban tree lines. For implementation of the spatial constraints, however, the homogeneity of the objects is primordial, and single-level segmentation was more adapted, as it was preferred to have several objects in a single field rather than two fields in the same object.

The 10 m resolution of four of the Sentinel-2 bands was appropriate for deriving objects using multi-resolution segmentation. Contrary to the study of Laurent et al. (2013), the mixed pixels at the edges of the objects were not discarded, because of the spatial resolution of Sentinel-2 was not as fine.

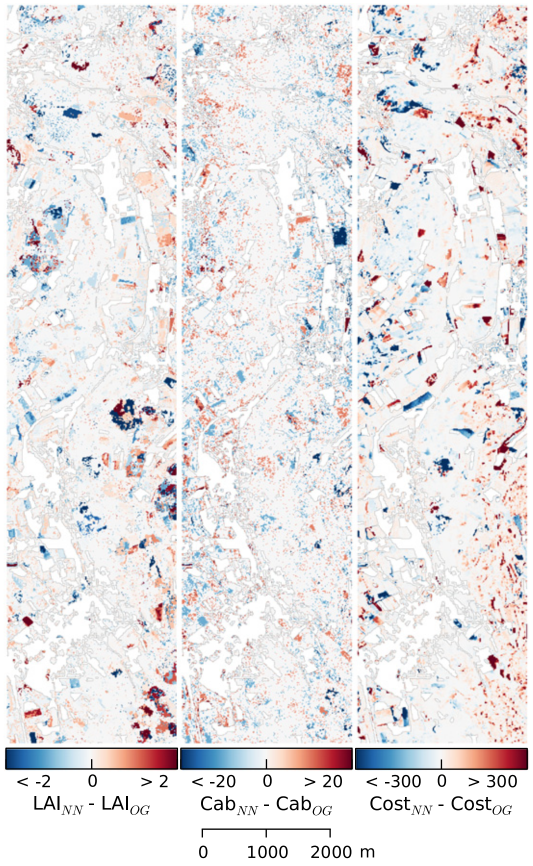

Fig. 6. Maps of the difference between the LAI, Cab, and cost obtained from the NN and OG approaches for the south part of FL9 (area in the yellow rectangle of Fig. 1). Blue colours indicate areas where the NN approach gave lower values than the OG approach.

4.2. Vegetation classes and a priori data

A general, straightforward to apply, vegetation classification was adopted because, contrary to the study of Laurent et al. (2013), no extensive land cover data was available. The R + G + B threshold values of Table 1 are specific to the present study because they depend on the atmospheric conditions. In the general case, one could use top-of-canopy reflectance thresholds and transfer them to radiance using Eq. (1), or derive the vegetation classification from existing land cover maps. The four levels of brightness in the visible domain were related to vegetation vertical structure, and general expert knowledge could then be used to define the a priori data (Table 3). Because of the broadness of the classes, the confidence in the a priori values was low. This was reflected by large values for the a priori standard deviations. This classification is therefore applicable without the need of labour- (or cost-) intensive generation of a priori data.

4.3. Li–Ross modelling and nadir normalization

Both Li–Ross and SLC-MOSTRAN4 models are simplified representations of the BRDF effects. In the parametric Li–Ross model each wavelength is treated independently, which may result in different kernels and kernel weights for each band, whereas the physically-based SLC-MODTRAN4 model uses the same values of the canopy parameters for all bands. In addition, the volume scattering component of the Li–Ross model is based on the assumption of a spherical LIDF and equal leaf reflectance and transmittance. The latter assumption is better satisfied in the NIR than in the visible domain, so one would expect smaller angular deviations between Li–Ross and SLC-MODTRAN4 in the NIR than in the visible bands. This expectation was only fulfilled for the VB1 and VB2 vegetation classes. The deviations between the SLC-MODTRAN4 and Li–Ross model were expected to be small because the spherical LIDF assumption used in the Li–Ross volumetric scattering component matches the spherical LIDF used for defining the vegetation classes (Table 2). Although the deviations between the two models were small in radiance units, they were systematic, which might be due to the much smaller number of degrees of freedom of the Li–Ross model.

These systematic deviations may have impacted the quality of the nadir-normalization of the APEX images. The main limitation, however, was that the changes in solar geometry over the two-hour acquisition period were not accounted for in the Li–Ross BRDF correction algorithm. This explains the trend of increasing brightness from the east to the west (Fig. 1) of the Sentinel-2 mosaic. Another important issue is that the nadir-normalization algorithm relies on a 5-classes land cover classification, only two of which concerning vegetation. This implies that the quality of the results depend on the spatial distribution of pixels of each class over the sensor's FOV. If observations of a scattering type are rather sparse and not well distributed over the FOV, the Li–Ross kernel weights can be less stable and correction may become less reliable. Another interfering effect is caused by topography, which is not accounted for in the algorithm. The brighter vertical stripe in the western part may be due to a combination of the described uncertainties. The Li–Ross BRDF correction cannot distinguish between the anisotropy of the surface and that of the atmosphere, and therefore corrected them both simultaneously. This is consistent with the nadir viewing convention used for creating the simulated Sentinel-2 image. Enhancements on the BRDF correction approach are subject to current work. A more robust correction could be achieved by inverting the model on a set of observations generated from several flight lines if not from all. Applying different error metrics than least-RMSE for the inversion process, e.g. the least median of error squares (Susaki, Hara, Kajiwara, & Honda, 2004) or least variance of white-sky albedo (Gao, Schaaf, Strahler, & Lucht, 2001) could further enhance the quality of the mosaic.

4.4. Simulated Sentinel-2 TOA image

4.4.1. Sources of error

The main pitfall is the 2-hour duration of the APEX acquisition, which resulted in variation of the solar geometry (zenith: 34.7 to 43.2°, azimuth: 107.6 to 122.7°). This impacted the nadir normalization as discussed in Section 4.3. The fact that the nadir-normalization ignored the atmospheric and topographic effects, however, means that these effects were included in the final simulated Sentinel-2 image, as would be the case in real imagery. The very high spectral resolution of the APEX data allowed limiting the inaccuracies related to the spectral convolution, and its high spatial resolution allowed for precise geometric correction and spatial resampling. The mosaicking process averaged the radiance values from up to three nadir-normalized APEX images, but which still included directional effects related to the solar geometry. The use of Eq. (1) to add the atmospheric effects above the APEX flight height also introduced some inaccuracies because it ignored adjacency effects, whereas the atmosphere above 6.4 km still contains scattering particles. In addition, the values for the atmospheric parameters at APEX flight height were not known, so the surface values were used when possible, or replaced by the maximum value allowed in MODTRAN4. Finally, each step of the processing described in Section 2.2 introduced inaccuracies, all of which propagated in the simulated Sentinel-2 TOA image. Although the final level of inaccuracy could not be evaluated, because of current lack of reference Sentinel-2 data, it was most probably far from negligible and it was therefore not considered appropriate to add noise to the simulated Sentinel-2 image.

4.4.2. Aspects not included

The simulated Sentinel-2 image has an extent of 16 × 22 km^2, which is smaller than the 290 km swath and than the 100 × 100 km^2 tiles planned for the Sentinel-2 mission. Despite its restricted extent, however, the Zurich simulated image covers a wide range of land cover types including agricultural fields, pastures, forests, water bodies, urban areas and even an airport. This variety makes this image an interesting dataset for preparing and/or testing operational algorithms for Sentinel-2. Cirrus correction methods, however, cannot be tested on this simulated Sentinel-2 image, because the APEX flight altitude was not high enough to see cirrus clouds.

The simulated image consists of a mosaic of nadir-normalized APEX images and therefore contains nadir-normalized radiance data. If the image would be at the centre of the Sentinel-2 swath, the VZA would vary between $-0.6°$ and $+0.6°$, which is small enough to assume that all pixels are viewed from nadir. The geometry of the Sentinel-2 MSI is relatively complex because it involves 12 detector modules, each recording the radiance in 13 spectral bands. Each detector module and spectral band has a slightly different viewing angle, which causes a significant parallax effect. This parallax effect, however, was ignored because it will only be visible for targets which are not at the ground altitude, such as clouds, and will therefore not be ortho-rectified properly.

4.5. LAI and Cab estimates

Unfortunately, no field data was available for evaluating the accuracy of the LAI and Cab estimates. It would be possible to perform an indirect validation using independent remote sensing products such as MODIS or MERIS LAI and Cab products. These products, however, have very different pixel sizes and are also subject to uncertainties. In the context of this proof of concept study for applying the Bayesian object-based approach in areas without field data, it was not considered necessary to implement such an indirect validation.

The accuracy of the LAI and Cab estimates is limited by the accuracy of the simulated Sentinel-2 data, as discussed above, and by the performance of the estimation method, which includes the segmentation (see Section 4.1), the SLC-MODTRAN4 model and the Bayesian object-based approach. The Bayesian object-based approach was shown to be more accurate than a LUT with Bayesian cost function approach by a previous study where the results were extensively discussed (Laurent et al., 2013).

In theory, the $\mathbf{C_o}$ matrix should contain model and observation uncertainties (Kimes, Knyazikhin, Privette, Abuelgasim, & Gao, 2000). In practice, however, the model uncertainties were ignored because they are difficult to assess, and the constant noise of 1 $[\mathrm{mW}/(\mathrm{m}^2\ \mathrm{sr\ nm})]^2$ used for the observation uncertainties does not correspond to actual noise behaviour. The most common approach, however, is to avoid the noise issue by summarizing the $\mathbf{C_o}$ and $\mathbf{C_a}$ matrices in a vector containing subjective weight factors (Combal et al., 2002; Meroni, Colombo, & Panigada, 2004). Another approach is to approximate $\mathbf{C_o}$ using the covariance matrix of the vegetated pixels (Dorigo, Richter, Baret, Bamler, & Wagner, 2009). Vegetated pixels have higher variance in the VNIR than in the SWIR. Therefore, this approach gives smaller weights to the VNIR bands, thus leading to a poor fit in this spectral range, and, consequently, to poor estimates of LAI and Cab. For an extensive discussion on the Co matrix and noise model, see Laurent et al. (2013).

An indication on the performance of the estimation method is given by the cost values: higher cost values correspond to less reliable estimates. At the object level, most cost values were under 100 (Fig. 3). At the pixel-level, however, the cost values increased, especially in VB1 objects. This may be related to the 10 m pixel size of the simulated Sentinel-2 data, which is too small for SLC to model forest environments: there are not enough trees in a pixel for the spatial distribution of crowns and empty spaces to be homogenous. Therefore, the object-level LAI and Cab estimates for VB1 vegetation are more reliable than those at pixel level. Indeed, the lower LAI values obtained at object level are more realistic because the forests around Zurich are regularly thinned. Spherical LIDF represents randomly oriented leaves and was chosen as a compromise to account for the broadness of the vegetation classes in terms of possible LIDFs. This assumption, however, may severely impact the quality of the estimates in cases where the species' LIDF is not spherical. Finally, the spatial variations of the atmospheric parameters related to elevation, and the adjacency and topography effects were ignored in the coupled canopy-atmosphere RT modelling.

5. Conclusions

Thanks to an image-based multi-resolution segmentation to identify vegetation objects and to a general vegetation classification based on four levels of brightness in the visible domain, the Bayesian object-based approach was successfully applied to estimate LAI and Cab from a simulated Sentinel-2 image for which no field data was available. The results of this study therefore extend the applicability of the Bayesian object-based approach to cases where no field data is available, which is essential for large-scale environmental studies relying on RS-based LAI and Cab maps. Another important contribution of this study is the demonstration of systematic, although small, differences between the angular simulations of the physically-based SLC-MODTRAN4 model and the parametric Li–Ross model. Therefore, nadir-normalization of the data should be avoided, and it should be preferred to use original data, including the original geometry for each object, as was demonstrated here. Although the simulated Sentinel-2 image built in this study has a number of limitations, it is the most realistic simulation available so far. We have made the image available for download at http://www.apex-esa.org/content/sentinel-2-simulation for the scientific community to further investigate the capabilities of the multi-resolution band set-up of Sentinel-2.

Acknowledgements

We acknowledge support from the University of Zurich through the University Research Priority Programme on Global Change and Biodiversity (URPP GCB). We thank Peter Roosjen for performing the processing to build the simulated Sentinel-2 image, Ferran Gascon for helpful comments on the manuscript, and VITO for hosting the simulated Sentinel-2 image on its web pages. We appreciate helpful comments from the reviewers to improve the manuscript.

References

Atzberger, C. (2004). Object-based retrieval of biophysical canopy variables using artificial neural nets and radiative transfer models. *Remote Sensing of Environment*, *93*(1–2), 53–67.

Atzberger, C., & Richter, K. (2012). Spatially constrained inversion of radiative transfer models for improved LAI mapping from future Sentinel-2 imagery. *Remote Sensing of Environment*, *120*, 208–218.

Bacour, C., Baret, F., Béal, D., Weiss, M., & Pavageau, K. (2006). Neural network estimation of LAI, fAPAR, fCover and LAI × Cab, from top of canopy MERIS reflectance data: Principles and validation. *Remote Sensing of Environment*, *105*(4), 313–325.

Baret, F., & Buis, S. (2008). Estimating canopy characteristics from remote sensing observations: Review of methods and associated problems. In S. Liang (Ed.), *Advances in Land Remote Sensing: System, Modeling, Inversion and Application* (pp. 173–201). : Springer.

Baret, F., Hagolle, O., Geiger, B., Bicheron, P., Miras, B., Huc, M., et al. (2007). LAI, fAPAR and fCover CYCLOPES global products derived from VEGETATION. Part 1: Principles of the algorithm. *Remote Sensing of Environment*, *110*(3), 275–286.

Benz, U. C., Hofmann, P., Willhauck, G., Lingenfelder, I., & Heynen, M. (2004). Multi-resolution, object-oriented fuzzy analysis of remote sensing data for GIS-ready information. *ISPRS Journal of Photogrammetry and Remote Sensing*, *58*(3–4), 239–258.

Berger, M., Moreno, J., Johannessen, J. A., Levelt, P. F., & Hanssen, R. F. (2012). ESA's sentinel missions in support of Earth system science. *Remote Sensing of Environment*, *120*, 84–90.

Berk, A., Anderson, G. P., Acharya, P. K., Hoke, M. L., Chetwynd, J. H., Bernstein, L. S., et al. (2003). *MODTRAN4 Version 3 Revision 1 User's manual.* Hanscom, MA, USA: Airforce Research Laboratory (97 pp.).

Blaschke, T. (2010). Object based image analysis for remote sensing. *ISPRS Journal of Photogrammetry and Remote Sensing*, *65*(1), 2–16.

Clevers, J. G. P. W., & Gitelson, A. A. (2013). Remote estimation of crop and grass chlorophyll and nitrogen content using red-edge bands on sentinel-2 and-3. *International Journal of Applied Earth Observation and Geoinformation*, *23*(1), 344–351.

Combal, B., Baret, F., Weiss, M., Trubuil, A., Mace, D., Pragnère, A., et al. (2002). Retrieval of canopy biophysical variables from bidirectional reflectance using prior information to solve the ill-posed inverse problem. *Remote Sensing of Environment*, *84*(1), 1–15.

Delegido, J., Verrelst, J., Alonso, L., & Moreno, J. (2011). Evaluation of sentinel-2 red-edge bands for empirical estimation of green LAI and chlorophyll content. *Sensors*, *11*(7), 7063–7081.

D'Odorico, P., Gonsamo, A., Damm, A., & Schaepman, M. E. (2013). Experimental evaluation of Sentinel-2 spectral response functions for NDVI time-series continuity. *IEEE Transactions on Geoscience and Remote Sensing*, *51*(3), 1336–1348.

Dorigo, W., Richter, R., Baret, F., Bamler, R., & Wagner, W. (2009). Enhanced automated canopy characterization from hyperspectral data by a novel two step radiative transfer model inversion approach. *Remote Sensing*, *1*(4), 1139–1170.

Dorigo, W. A., Zurita-Milla, R., de Wit, A. J. W., Brazile, J., Singh, R., & Schaepman, M. E. (2007). A review on reflective remote sensing and data assimilation techniques for enhanced agroecosystem modeling. *International Journal of Applied Earth Observation and Geoinformation*, *9*(2), 165–193.

Drusch, M., Del Bello, U., Carlier, S., Colin, O., Fernandez, V., Gascon, F., et al. (2012). Sentinel-2: ESA's optical high-resolution mission for GMES operational services. *Remote Sensing of Environment*, *120*, 25–36.

Feret, J. B., François, C., Asner, G. P., Gitelson, A. A., Martin, R. E., Bidel, L. P. R., et al. (2008). PROSPECT-4 and 5: Advances in the leaf optical properties model separating photosynthetic pigments. *Remote Sensing of Environment*, *112*(6), 3030–3043.

Foley, J. A., Levis, S., Costa, M. H., Cramer, W., & Pollard, D. (2000). Incorporating dynamic vegetation cover within global climate models. *Ecological Applications*, *10*(6), 1620–1632.

Gao, F., Schaaf, C. B., Strahler, A. H., & Lucht, W. (2001). Using a multikernel least-variance approach to retrieve and evaluate albedo from limited bidirectional measurements. *Remote Sensing of Environment*, *76*(1), 57–66.

Gemmell, F., Varjo, J., Strandstrom, M., & Kuusk, A. (2002). Comparison of measured boreal forest characteristics with estimates from TM data and limited ancillary information using reflectance model inversion. *Remote Sensing of Environment*, *81*(2–3), 365–377.

Green, R. O., Pavri, B. E., & Chrien, T. G. (2003). On-orbit radiometric and spectral calibration characteristics of EO-1 hyperion derived with an underflight of AVIRIS and In situ measurements at Salar de Arizaro, Argentina. *IEEE Transactions on Geoscience and Remote Sensing*, *41*(6 PART I), 1194–1203.

Guanter, L., Richter, R., & Kaufmann, H. (2009). On the application of the MODTRAN4 atmospheric radiative transfer code to optical remote sensing. *International Journal of Remote Sensing*, *30*(6), 1407–1424.

Hagolle, O., Huc, M., Pascual, D.V., & Dedieu, G. (2010). A multi-temporal method for cloud detection, applied to FORMOSAT-2, VENμS, LANDSAT and SENTINEL-2 images. *Remote Sensing of Environment*, *114*(8), 1747–1755.

Hedley, J., Roelfsema, C., Koetz, B., & Phinn, S. (2012). Capability of the Sentinel 2 mission for tropical coral reef mapping and coral bleaching detection. *Remote Sensing of Environment*, *120*, 145–155.

Herrmann, I., Pimstein, A., Karnieli, A., Cohen, Y., Alchanatis, V., & Bonfil, D. J. (2011). LAI assessment of wheat and potato crops by VENμS and Sentinel-2 bands. *Remote Sensing of Environment*, *115*(8), 2141–2151.

Houborg, R., Anderson, M., & Daughtry, C. (2009). Utility of an image-based canopy reflectance modeling tool for remote estimation of LAI and leaf chlorophyll content at the field scale. *Remote Sensing of Environment*, *113*(1), 259–274.

Hüni, A., Bieseman, J., Dell'Endice, F., Alberti, E., Meuleman, K., & Schaepman, M. (2009). The structure of the APEX (airborne prism experiment) Processing and Archiving Facility. *First Workshop on Hyperspectral Image and Signal Processing: Evolution in Remote Sensing (WHISPERS '09)* (pp. 1–4).

Jacquemoud, S., & Baret, F. (1990). PROSPECT: A model of leaf optical properties spectra. *Remote Sensing of Environment*, *34*(2), 75–91.

Jacquemoud, S., Verhoef, W., Baret, F., Bacour, C., Zarco-Tejada, P. J., Asner, G. P., et al. (2009). PROSPECT + SAIL models: A review of use for vegetation characterization. *Remote Sensing of Environment*, *113*(Suppl. 1), S56–S66.

Jehle, M., Hueni, A., Damm, A., D'Odorico, P., Weyermann, J., Kneubühler, M., et al. (2010). APEX - Current status, performance and validation concept. *IEEE Sensors 2010 Conference, Waikoloa, HI, USA* (pp. 533–537).

Johansen, K., Coops, N. C., Gergel, S. E., & Stange, Y. (2007). Application of high spatial resolution satellite imagery for riparian and forest ecosystem classification. *Remote Sensing of Environment*, *110*(1), 29–44.

Kimes, D. S., Knyazikhin, Y., Privette, J. L., Abuelgasim, A. A., & Gao, F. (2000). Inversion methods for physically-based models. *Remote Sensing Reviews*, *18*(2), 381–439.

Kötz, B., Baret, F., Poilve, H., & Hill, J. (2005). Use of coupled canopy structure dynamic and radiative transfer models to estimate biophysical canopy characteristics. *Remote Sensing of Environment*, *95*(1), 115–124.

Lamonaca, A., Corona, P., & Barbati, A. (2008). Exploring forest structural complexity by multi-scale segmentation of VHR imagery. *Remote Sensing of Environment*, *112*(6), 2839–2849.

Laurent, V. C. E., Verhoef, W., Clevers, J. G. P. W., & Schaepman, M. E. (2011a). Estimating forest variables from top-of-atmosphere radiance satellite measurements using coupled radiative transfer models. *Remote Sensing of Environment*, *115*(4), 1043–1052.

Laurent, V. C. E., Verhoef, W., Clevers, J. G. P. W., & Schaepman, M. E. (2011b). Inversion of a coupled canopy-atmosphere model using multi-angular top-of-atmosphere radiance data: A forest case study. *Remote Sensing of Environment*, *115*(10), 2603–2612.

Laurent, V. C. E., Verhoef, W., Damm, A., Schaepman, M. E., & Clevers, J. G. P. W. (2013). A Bayesian object-based approach for estimating vegetation biophysical and biochemical variables from at-sensor APEX data. *Remote Sensing of Environment*, *139*, 6–17.

Lauvernet, C., Baret, F., Hascoët, L., Buis, S., & Le Dimet, F. X. (2008). Multitemporal-patch ensemble inversion of coupled surface–atmosphere radiative transfer models for land surface characterization. *Remote Sensing of Environment*, *112*(3), 851–861.

Lavergne, T., Kaminski, T., Pinty, B., Taberner, M., Gobron, N., Verstraete, M. M., et al. (2007). Application to MISR land products of an RPV model inversion package using adjoint and Hessian codes. *Remote Sensing of Environment*, *107*(1–2), 362–375.

Li, X., Gao, F., Wang, J., & Strahler, A. (2001). A priori knowledge accumulation and its application to linear BRDF model inversion. *Journal of Geophysical Research D: Atmospheres*, *106*(D11), 11925–11935.

Malenovský, Z., Martin, E., Homolová, L., Gastellu-Etchegorry, J. P., Zurita-Milla, R., Schaepman, M. E., et al. (2008). Influence of woody elements of a Norway spruce canopy on nadir reflectance simulated by the DART model at very high spatial resolution. *Remote Sensing of Environment*, *112*(1), 1–18.

Malenovský, Z., Rott, H., Cihlar, J., Schaepman, M. E., García-Santos, G., Fernandes, R., et al. (2012). Sentinels for science: Potential of Sentinel-1, -2, and -3 missions for scientific observations of ocean, cryosphere, and land. *Remote Sensing of Environment*, *120*, 91–101.

Massada, A.B., Kent, R., Blank, L., Perevolotsky, A., Hadar, L., & Carmel, Y. (2012). Automated segmentation of vegetation structure units in a Mediterranean landscape. *International Journal of Remote Sensing*, *33*(2), 346–364.

Meroni, M., Colombo, R., & Panigada, C. (2004). Inversion of a radiative transfer model with hyperspectral observations for LAI mapping in poplar plantations. *Remote Sensing of Environment*, *92*(2), 195–206.

Myneni, R. B., Hoffman, S., Knyazikhin, Y., Privette, J. L., Glassy, J., Tian, Y., et al. (2002). Global products of vegetation leaf area and fraction absorbed PAR from year one of MODIS data. *Remote Sensing of Environment*, *83*(1–2), 214–231.

Pinty, B., Lavergne, T., Vossbeck, M., Kaminski, T., Aussedat, O., Giering, R., et al. (2007). Retrieving surface parameters for climate models from Moderate Resolution Imaging Spectroradiometer (MODIS)-Multiangle Imaging Spectroradiometer (MISR) albedo products. *Journal of Geophysical Research D: Atmospheres*, *112*(10).

Richter, K., Atzberger, C., Vuolo, F., & D'Urso, G. (2011a). Evaluation of Sentinel-2 spectral sampling for radiative transfer model based LAI estimation of wheat, sugar beet, and maize. *IEEE Journal of Selected Topics in Applied Earth Observations and Remote Sensing*, *4*(2), 458–464.

Richter, K., Atzberger, C., Vuolo, F., Weihs, P., & D'Urso, G. (2009). Experimental assessment of the Sentinel-2 band setting for RTM-based LAI retrieval of sugar beet and maize. *Canadian Journal of Remote Sensing*, *35*(3), 230–247.

Richter, K., Hank, T. B., Vuolo, F., Mauser, W., & D'Urso, G. (2012). Optimal exploitation of the sentinel-2 spectral capabilities for crop leaf area index mapping. *Remote Sensing*, *4*(3), 561–582.

Richter, R., & Schläpfer, D. (2002). Geo-atmospheric processing of airborne imaging spectrometry data. Part 2: Atmospheric/topographic correction. *International Journal of Remote Sensing*, *23*(13), 2631–2649.

Richter, R., Wang, X., Bachmann, M., & Schläpfer, D. (2011b). Correction of cirrus effects in Sentinel-2 type of imagery. *International Journal of Remote Sensing*, *32*(10), 2931–2941.

Roujean, J. -L., Leroy, M., & Deschamps, P. -Y. (1992). A bidirectional reflectance model of the Earth's surface for the correction of remote sensing data. *Journal of Geophysical Research-Atmospheres*, *97*(D18), 20455–20468.

Sentinel-2 PDGS Project Team (2011). *GMES space component, Sentinel-2 payload data ground segment (PDGS), Products definition document.* : ESA (93 pp.).

Susaki, J., Hara, K., Kajiwara, K., & Honda, Y. (2004). Robust estimation of BRDF model parameters. *Remote Sensing of Environment*, *89*(1), 63–71.

Tarantola, A. (2005). *Inverse problem theory and methods for model parameter estimation.* Philadelphia, USA: Society for Industrial and Applied Mathematics.

Ustin, S. L., Gitelson, A. A., Jacquemoud, S., Schaepman, M., Asner, G. P., Gamon, J. A., et al. (2009). Retrieval of foliar information about plant pigment systems from high resolution spectroscopy. *Remote Sensing of Environment*, *113*(Suppl. 1), S67–S77.

Verhoef, W. (1984). Light scattering by leaf layers with application to canopy reflectance modeling: The SAIL model. *Remote Sensing of Environment*, *16*(2), 125–141.

Verhoef, W., & Bach, H. (2003). Simulation of hyperspectral and directional radiance images using coupled biophysical and atmospheric radiative transfer models. *Remote Sensing of Environment*, *87*(1), 23–41.

Verhoef, W., & Bach, H. (2007). Coupled soil-leaf-canopy and atmosphere radiative transfer modeling to simulate hyperspectral multi-angular surface reflectance and TOA radiance data. *Remote Sensing of Environment*, *109*(2), 166–182.

Verrelst, J., Muñoz, J., Alonso, L., Delegido, J., Rivera, J. P., Camps-Valls, G., et al. (2012). Machine learning regression algorithms for biophysical parameter retrieval: Opportunities for Sentinel-2 and -3. *Remote Sensing of Environment*, *118*, 127–139.

Wang, L., Sousa, W. P., & Gong, P. (2004). Integration of object-based and pixel-based classification for mapping mangroves with IKONOS imagery. *International Journal of Remote Sensing*, *25*(24), 5655–5668.

Wang, Y. F., Yang, C., & Li, X. (2008). Regularizing kernel-based BRDF model inversion method for ill-posed land surface parameter retrieval using smoothness constraint. *Journal of Geophysical Research D: Atmospheres*, *113*(13).

Wanner, W., Xiaowen, L., & Strahler, A. H. (1995). A new class of geometric-optical semiempirical kernels for global BRDF and albedo modeling. *Geoscience and Remote Sensing Symposium, 1995. IGARSS '95. 'Quantitative Remote Sensing for Science and Applications', International*, *Vol. 11*. (pp. 15–17).

Weyermann, J., Damm, A., Kneubühler, M., & Schaepman, M. E. (2013). Correction of reflectance anisotropy effects of vegetation on airborne spectroscopy data and derived products. *IEEE Transactions on Geoscience and Remote Sensing*, *PP*(99), 1–12.

D. Curriculum Vitae

CURRICULUM VITAE JÖRG WEYERMANN

PERSONAL DETAILS

Date of birth:	6. July 1977
Place of birth:	Düren, Germany
Nationality:	German
Residence permit:	“C”
Family status:	married, 1 daughter
Present Address:	Longchamps 5 2534 Orvin Switzerland
Mobile phone:	+41 76 308 13 79
Private:	+41 52 202 28 55
E-mail:	joerg.weyermann@gmail.com

EDUCATION

04/2008 – present	PhD studies in Optical Remote Sensing, University of Zurich, Switzerland
12.9.2008	Master of Advanced Studies in Software Engineering (Masters thesis as team project: ‘*opnMind – web-based mind mapping tool with Java technologies’*)
09/2006 – 09/2008	Master of Advanced Studies in Software Engineering, University of Applied Sciences Rapperswil, Switzerland (Diploma thesis: *opnMind – web based mind mapping tool.* Team project, Java technologies)
28.10.2005	Dipl.-Geograph (MSc Geography) Diploma Thesis: *2-D Phase Unwrapping: Verfahren für die SAR- Interferometrie*
1999 – 2005	Studies in Physical Geography and Remote Sensing, University Erlangen, Germany and University of Zurich, Switzerland
05/1998 – 04/1999	Studies in Construction, RWTH Aachen, Germany

07/1997 – 04/1998	Military Service
16.6.1997	Abitur, Stiftisches Gymnasium Düren, Germany
08/1988 – 06/1997	Stiftisches Gymnasium Düren, Germany
08/1984 – 07/1988	Katholische Grundschule Kreuzau, Germany

PROFESSIONAL EXPERIENCE

04/2008 – present	Research Assistant and PhD student at the University of Zurich, optical remote sensing group
01/2006 – 03/2008	Research Assistant at the University of Zurich, Radar remote sensing group
10/2004 – 12/2004	Internship at SARMAP, Purasca, Switzerland (OO-Programming, Image Matching in SAR data)
12/2003 – 03/2004	GIS Development for the University of Erlangen-Nürnberg (Sports science department)
07/2003 – 08/2003	Internship at the German Aerospace Center DLR (Geometric error budget analysis for geocoding, ASAR WS data, SIBERIA II project)
03/2003 – 02/2004	Internship and Freelancer with GIBS Geologen, Nürnberg, Germany
02/2002 – 10/2002	Scientific work in Loja/Ecuador (rain forest ecology)
05/1998 – 09/1998	Internship for construction studies, former Kelzenberg GmbH and Simons Metallguss GmbH, Düren, Germany

SOFTWARE TECHNOLOGIES

Programming languages

- C++, Matlab (> 6 Jahre, near-daily usage)
- Java, SQL (> 6 Jahre, periodically)
- C#, Objective-C, JavaScript, PHP, HTML4/5, Python, Perl, Shell-Script (basic knowledge)

Methods, Technologies

- RUP, Scrum
- Requirements Engineering, Use Case definition
- OOA, OOD, UML, XML

Tools

- Eclipse IDE (> 80% of all development work)
- Microsoft Visual Studio (10%)
- NetBeans IDE (5%)
- Apple XCode (5%)
- Enterprise Architect with MDG-Link for Eclipse (CASE tool)
- Trac, SVN, Eclipse WTP
- Apache/Tomcat servers, Apache Struts web application framework
- JUnit
- Oracle, MySQL

FURTHER SKILLS

Course Leading, Teaching

- Leading a seminar on airborne spectroscopy data handling for surveyors (Fort-de-France, Martinique)
- Co-leading students excursion to the United States and preparatory seminar
- MSc thesis co-supervision
- Internship supervision

Graduate School Classes

- Effective Scientific Presentations
- Scientific Writing
- Statistics in R

Languages

- German (mother tongue)
- English (fluid in speaking and writing)
- French (basic knowledge)
- Spanish (basic knowledge)

Other

- Experience in planning/organizing field and flight campaigns
- Driving license level B, C1 and D1

PUBLICATIONS

Peer-reviewed Journal Articles

Weyermann, Jörg; Schläpfer, Daniel; Kneubühler, Mathias; Schaepman, Michael E (2015). *Minimizing reflectance anisotropy effects in airborne spectroscopy data using Ross-Li model inversion with continuous field land cover stratification*. IEEE Transactions on Geoscience and Remote Sensing, 53(11): 5814-5823.

Weyermann, Jörg; Damm, Alexander; Kneubühler, Mathias; Schaepman, Michael E (2013). *Correction of reflectance anisotropy effects of vegetation on airborne spectroscopy data and derived products*. IEEE Transactions on Geoscience and Remote Sensing, 52(1): 616-627.

Joerg, Philip Claudio; **Weyermann, Jörg**; Morsdorf, Felix; Zemp, Michael; Schaepman, Michael E (2015). *Computation of a distributed glacier surface albedo proxy using airborne laser scanning intensity data and in-situ spectro-radiometric measurements*. Remote Sensing of Environment, 160: 31-42.

Schaepman, Michael E.; Jehle, Michael; Hueni, Andreas; D'Odorico, Petra; Damm, Alexander; **Weyermann, Jörg**; Schneider, Fabian D.; Laurent, Valérie; Popp, Christoph; Seidel, Felix C.; Lenhard, Karim; Gege, Peter; Küchler, Christoph; Brazile, Jason; Kohler, Peter; De Vos, Lieve; Meuleman, Koen; Meynart, Roland; Schläpfer, Daniel; Kneubühler, Mathias; Itten, Klaus I.; *et al.* (2015). *Advanced radiometry measurements and Earth science applications with the Airborne Prism Experiment (APEX)*. Remote Sensing of Environment, 158: 207-215.

Laurent, Valérie C.E.; Schaepman, Michael E.; Verhoef, Wout; **Weyermann, Jörg**; Chávez, Roberto O.*A.* (2014). *Bayesian object-based estimation of LAI and chlorophyll from a simulated Sentinel-2 top-of-atmosphere radiance image.* Remote Sensing of Environment, 140: 318-329.

Mulder, V.L.; de Bruin, S.; **Weyermann, Jörg**.; Kokaly, R.; Schaepman, Michael E. (2013). *Characterizing regional soil mineral composition using spectroscopy and geostatistics*. Remote Sensing of Environment, 139: 415-429.

Misurec, Jan; Kopačková, Veronika; Lhotáková, Zuzana; Hanuš, Jan; **Weyermann, Jörg**; Entcheva-Campbell, Petya; Albrechtová, Jana (2012).

Utilization of hyperspectral image optical indices to assess the Norway spruce forest health status. Journal of Applied Remote Sensing, 6(1).

Conference Proceedings

Weyermann, Jörg; Hueni, Andreas; Kneubühler, Mathias; Schaepman, Michael E. (2010). *Capabilities and limitations of methods for BRDF characterization in imaging spectrometry data*. In: Hyperspectral Workshop 2010, Frascati, IT, 17 March 2010 - 19 March 2010, 1-5.

Weyermann, Jörg; Schläpfer, Daniel; Hueni, Andreas; Kneubühler, Mathias; Schaepman, Michael E. (2009). *Spectral Angle Mapper (SAM) for anisotropy class indexing in imaging spectrometry data*. In: SPIE Optics and Photonics 2009, San Diego, US, 2 - 6 August 2009, 74570B.

Weyermann, J; Schläpfer, D; Hueni, A; Kneubühler, M; Itten, K I (2009). *Land cover classification concept for anisotropy correction in hyperspectral imagery*. In: 6th Workshop on Imaging Spectroscopy, Tel Aviv, Israel, 16 - 19 March 2009, 1-6.

Monographs

Weyermann, Jörg (2005). *2-D Phase Unwrapping: Verfahren für die SAR-Interferometrie*. Diploma thesis at the Institute of Geography, University of Erlangen-Nürnberg, Germany

PERSONAL INTERESTS

Photography, Alpine Sports

Orvin, 17 November 2015

ISBN Nr. 978-3-906894-02-7